THE MINISTRY OF SCIENCE AND HIGHER EDUCATION OF THE RUSSIAN FEDERATION

ST. PETERSBURG STATE POLYTECHNICAL UNIVERSITY JOURNAL

Physics and Mathematics

VOLUME 15, No. 3, 2022

Peter the Great St. Petersburg
Polytechnic University
2022

**ST. PETERSBURG STATE POLYTECHNICAL UNIVERSITY JOURNAL.
PHYSICS AND MATHEMATICS**

The journal is included in the List of leading peer-reviewed scientific journals and other editions to publish major findings of theses for the research degrees of Doctor of Sciences and Candidate of Sciences.

The publications are presented in the VINITI RAS Abstract Journal and Ulrich's Periodical Directory International Database.

The journal is published since 2008 as part of the periodical edition 'Nauchno-tekhnicheskie vedomosti SPb-GPU'.

The journal is registered with the Federal Service for Supervision in the Sphere of Telecom, Information Technologies and Mass Communications (ROSKOMNADZOR). Certificate ПИ № ФС77-52144 issued December 11, 2012.

The journal is distributed through the CIS countries catalogue, the «Press of Russia» joint catalogue and the «Press by subscription» Internet catalogue. The subscription index is **71823.**

The journal is in the **Web of Science** (Emerging Sources Citation Index), **Scopus**, the **Russian Science Citation Index** (RSCI) and the **Directory of Open Access Journals** (DOAJ) databases.

Address: 195251 Politekhnicheskaya St. 29, St. Petersburg, Russia.

Phone: (812) 294-22-85.
http://ntv.spbstu.ru/physics

МИНИСТЕРСТВО НАУКИ И ВЫСШЕГО ОБРАЗОВАНИЯ РОССИЙСКОЙ ФЕДЕРАЦИИ

НАУЧНО-ТЕХНИЧЕСКИЕ ВЕДОМОСТИ

САНКТ-ПЕТЕРБУРГСКОГО ГОСУДАРСТВЕННОГО ПОЛИТЕХНИЧЕСКОГО УНИВЕРСИТЕТА

Физико-математические науки

ТОМ 15, № 3

2022

Санкт-Петербургский политехнический
университет Петра Великого
2022

НАУЧНО-ТЕХНИЧЕСКИЕ ВЕДОМОСТИ САНКТ-ПЕТЕРБУРГСКОГО ГОСУДАРСТВЕННОГО ПОЛИТЕХНИЧЕСКОГО УНИВЕРСИТЕТА. ФИЗИКО-МАТЕМАТИЧЕСКИЕ НАУКИ

Журнал с 2002 г. входит в Перечень ведущих рецензируемых научных журналов и изданий, в которых должны быть опубликованы основные результаты диссертаций на соискание ученых степеней доктора и кандидата наук.

Сведения о публикациях представлены в Реферативном журнале ВИНИТИ РАН, в международной справочной системе «Ulrich's Periodical Directory».

С 2008 года выпускается в составе сериального периодического издания «Научно-технические ведомости СПбГПУ».

Журнал зарегистрирован Федеральной службой по надзору в сфере информационных технологий и массовых коммуникаций (Роскомнадзор). Свидетельство о регистрации ПИ № ФС77-52144 от 11 декабря 2012 г.

Распространяется по Каталогу стран СНГ, Объединенному каталогу «Пресса России» и по Интернет-каталогу «Пресса по подписке». Подписной индекс **71823**.

Журнал индексируется в базе данных **Web of Science** (Emerging Sources Citation Index), **Scopus**, а также включен в базы данных **«Российский индекс научного цитирования»** (РИНЦ), размещенную на платформе Научной электронной библиотеки на сайте http://www.elibrary.ru, и **«Directory of Open Access Journals»** (DOAJ)

Адрес редакции и издательства:
Россия, 195251, Санкт-Петербург, ул. Политехническая, д. 29.
Тел. редакции (812) 294-22-85.
http://ntv.spbstu.ru/physics

Contents

Condensed matter physics

Simulation of physical processes

Physical electronics

Physical materials technology

Radiophysics

Mechanics

Содержание

Физика конденсированного состояния

Математическое моделирование физических процессов

Физическая электроника

Физическое материаловедение

Радиофизика

Механика

CONDENSED MATTER PHYSICS

Original article
DOI: https://doi.org/10.18721/JPM.15301

STABILIZATION OF THE FERROELECTRIC PHASE OF POTASSIUM NITRATE IN COMPOSITES CONTAINING METALLIC MICROPARTICLES

Yu. Milinskiy[1], *S. V. Baryshnikov*[1], *E. V. Stukova*[2]✉

[1] Blagoveshchensk State Pedagogical University

[2] Amur State University

✉ lenast@bk.ru

Abstract. In the paper, the temperature dependences of the differential thermal analysis signal, permittivity, and amplitude of the third harmonic of the $(KNO_3)_{1-x}/Sn_x$ composites have been studied. It was shown that the temperature of the α → β phase transition decreased by 2 – 3 K in the potassium nitrates being parts of the composites, and the temperature of the γ → α phase transition decreased up to 360 K. This result can be explained within the framework of the Landau – Ginzburg theory, taking into account the shielding of potassium nitrate particles by tin metal particles.

Keywords: ferroelectric, composite, permittivity, phase transition

Citation: Milinskiy A. Yu., Baryshnikov S. V., Stukova E. V., Stabilization of the ferroelectric phase of potassium nitrate in composites containing metallic microparticles, St. Petersburg Polytechnical State University Journal. Physics and Mathematics. 15 (3) (2022) 9–16. DOI: https://doi.org/10.18721/JPM.15301

Научная статья
УДК 537.226
DOI: https://doi.org/10.18721/JPM.15301

СТАБИЛИЗАЦИЯ СЕГНЕТОЭЛЕКТРИЧЕСКОЙ ФАЗЫ НИТРАТА КАЛИЯ В КОМПОЗИТАХ, СОДЕРЖАЩИХ МЕТАЛЛИЧЕСКИЕ МИКРОЧАСТИЦЫ

А. Ю. Милинский[1], *С. В. Барышников*[1], *Е. В. Стукова*[2]✉

[1] Благовещенский государственный педагогический университет

[2] Амурский государственный университет

✉ lenast@bk.ru

Аннотация. Исследованы температурные зависимости сигнала дифференциального термического анализа, диэлектрической проницаемости и амплитуды третьей гармоники композитов $(KNO_3)_{1-x}/Sn_x$. Показано, что у нитрата калия в этих соединениях происходит понижение температуры фазового перехода α → β на 3 – 2 K, а температура фазового перехода γ → α понижается вплоть до 360 K. Полученный результат можно объяснить в рамках теории Ландау – Гинзбурга с учетом экранирования частиц нитрата калия металлическими частицами олова.

Ключевые слова: сегнетоэлектрик, композит, диэлектрическая проницаемость, фазовый переход

Ссылка для цитирования: Милинский А. Ю., Барышников С. В., Стукова Е. В. Стабилизация сегнетоэлектрической фазы нитрата калия в композитах, содержащих металлические микрочастицы // Научно-технические ведомости СПбГПУ. Физико-математические науки. 2022. Т. 3 № .15. С. 9–16. DOI: https://doi.org/10.18721/JPM.15301

Introduction

Ferroelectrics are the focus of much attention as materials for producing ultra-high density non-volatile memory, due to high values of the dielectric constant, their capability to change the polarization direction and store energy [1]. Research efforts are currently concentrated both on synthesizing new ferroelectric compounds [2] and improving the polar properties of existing materials. One of the approaches to modifying the ferroelectric properties of substances is producing composites based on them [3–5]. Ferroelectric composites can have different structures (depending on the nature and compatibility of components), formed in the polar matrix by different particles: polar, non-polar, metal, etc.

A promising ferroelectric for applications in microelectronic devices is potassium nitrate Kno_3, since it has a sufficiently high value of spontaneous polarization $P_s \approx 10$ μC/cm²[6]. However, potassium nitrate has several drawbacks, limiting its applications for these purposes: it does not have spontaneous polarization at room temperature, and the polar phase of this compound is stable only in a narrow temperature range, under cooling from 397 to ~373 K [6]. Numerous studies have been dedicated to attempts to expand the temperature range where the ferroelectric phase of KNO_3 exists to room temperature [7–10]. Thin films [7], composites [8] and nanocomposites [9,10] were prepared from potassium nitrate. An expansion of the domain where the polar phase exists in KNO_3 was detected in all of these studies.

This paper reports on the study of thermal and dielectric properties of $(KNO_3)_{1-x}/Sn_x$ composites (x = 0, 0.10 and 0.20), obtained upon mixing of potassium nitrate powder and tin microbeads with a size of 20–38 μm.

Samples and experimental procedure

Potassium nitrate KNO_3 is in paraelectric state under standard conditions and has the space group *Pmcn* [6]. This phase is customarily denoted by α. As potassium nitrate is heated to 401 K, a structural phase transition occurs to another, paraelectric β-phase, which has the $R\bar{3}m$ structure. Upon subsequent cooling from 453 K, phase I is transformed into an intermediate, ferroelectric γ-phase with the three-dimensional $R\bar{3}m$ symmetry, and, finally, this γ-phase is transformed into the α-phase near 373K. Spontaneous polarization P_s of the γ-phase is approximately 1–2 μC/cm² at 393 K [6]. It was established in [11] that the temperature range for stability of the polar state in potassium nitrate depends on the thermal history and cooling rate.

The $(KNO_3)_{1-x}/Sn_x$ $(KNO_3)_{1-x}/Sn_x$ composites were prepared from chemically pure KNO_3 and Sn microbeads 20–38 μm in size. Potassium nitrate powder was mixed with Sn microbeads indifferent ratios (x=0.1 and 0.2 (x is the volume fraction)) in an agate mortar for 10minutes. Next, the samples were pressed from the obtained powder into disks with a thickness of 1 mm and a radius of 5 mm under 7500 kg/cm². Fig. 1 shows a micrograph of the sample prepared from a mixture of potassium nitrate powder and tin microbeads with a volume fraction of x = 0.2.

Indium-gallium paste was applied to the samples as electrodes to measure the electrophysical characteristics.

The temperature dependences of dielectric permittivity ε′ were obtained with an E7-25 meter. Nonlinear dielectric measurements of $(KNO_3)_{1-x}/Sn_x$ composites were carried out with the setup described in [12]. The electric field strength in the sample was about 100 V/mm during the temperature measurements of the coefficient $\gamma_{3\omega} = U_{3\omega}/U_{1\omega}$. The temperature was determined with an accuracy up to 0.1 K using a Chromel/Alumel thermocouple and a TS-6621 thermometer.

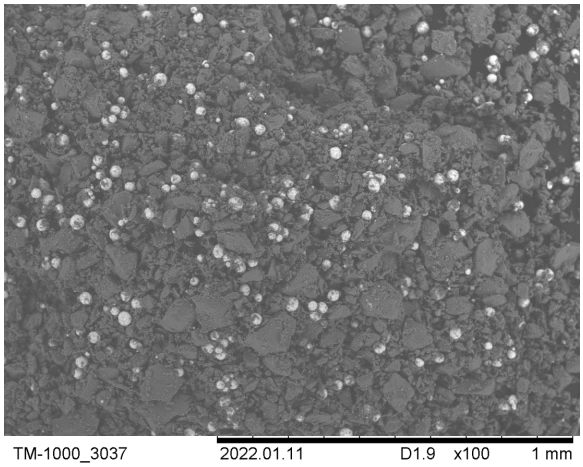

Fig. 1. SEM micrograph of $(KNO_3)_{0.8}/Sn_{0.2}$ mixture

Differential thermal analysis (DTA) was conducted for the$((KNO_3)_{1-x}/Sn_x$ samples using a Linseis STA PT 1600 simultaneous thermal analyzer (Linseis, USA), enabling combined gravimetry and DTA.

Measurements of the quantities ε′ and $\gamma_{3\omega}$ were carried out in the temperature range from 300 to 453 K at a rate of 2 K/min. The maximum heating temperature of 453 K is chosen because the ferroelectric phase is not formed in bulk potassium nitrate heated to lower temperatures.

Experimental results

Fig. 2 shows the ε′(*T*) dependences for $(KNO_3)_{1-x}/Sn_x$ (x = 0, 0.10, 0.20) composites obtained under heating and cooling. A sharp increase in the ε′(*T*) dependence is observed in pure KNO_3 (x = 0) under heating to 401–410 K, induced by the α → β phase transition. An additional step is detected in the curve upon cooling, suggesting that an intermediate ferroelectric γ-phase emerges [6].

The ε′(*T*) dependences for $(KNO_3)_{1-x}/Sn_x$ (x = 0.10, 0.20) composites are strongly smeared (see Fig. 2). Theα → β phase transition between 1 and 2 K is the same as the phase transition in pure potassium nitrate. Upon cooling, the ε′(*T*) curve obtained during heating starts coinciding with the corresponding curve obtained during cooling at lower temperatures than for pure potassium nitrate. This indirectly points to a decrease in the temperature of the γ → α structural transition. Aside from this, the values of dielectric permittivity ε′ increase with increasing volume fraction of tin microparticles.

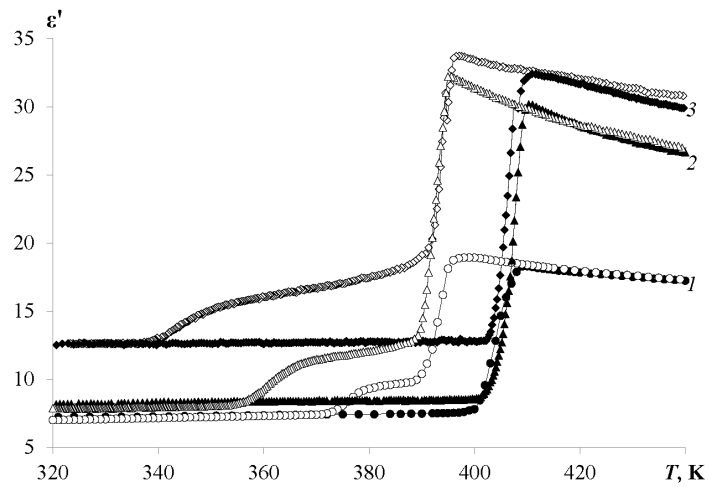

Fig. 2. Temperature dependences of ε′(*T*) for the $(KNO_3)_{1-x}/Sn_x$ composite for different values of *x*: 0 (*1*), 0.1 (*2*), 0.2 (*3*); shaded symbols correspond to heating, empty symbols to cooling

According to DTA for pure KNO_3 (Fig. 3), one phase transition is observed in the heating mode: β → α around 407 K. Two phase transitions detected during cooling: the first one, α → γ, is observed at about 394 K, and the second one, γ → β, at about 371 K, which corresponds to the data known from the literature [6].

Measurements of the DTA signal in$(KNO_3)_{1-x}/Sn_x$ composites (see Fig. 3) indicate the presence of one phase transition during heating at 406 and 405 K for $x = 0.10$ and 0.20 respectively. The temperatures of the α → γ transition during cooling are 392 and 391 K, and temperatures of the γ → β transition are 368 and 361 K for $x = 0.10$ and 0.20, respectively.

To determine the boundaries within which the ferroelectric phase exists in $(KNO_3)_{1-x}/Sn_x$ (x = 0, 0.10, 0.20) samples, we examined the temperature dependence of the third harmonic coefficient $\gamma_{3\omega}$. An increase in the third harmonic coefficient $\gamma_{3\omega}$ was observed under cooling for $(KNO_3)_{1-x}/Sn_x$ samples in the temperature ranges of 397–373 K, 394–362 K and 394–353 K (Fig. 4).

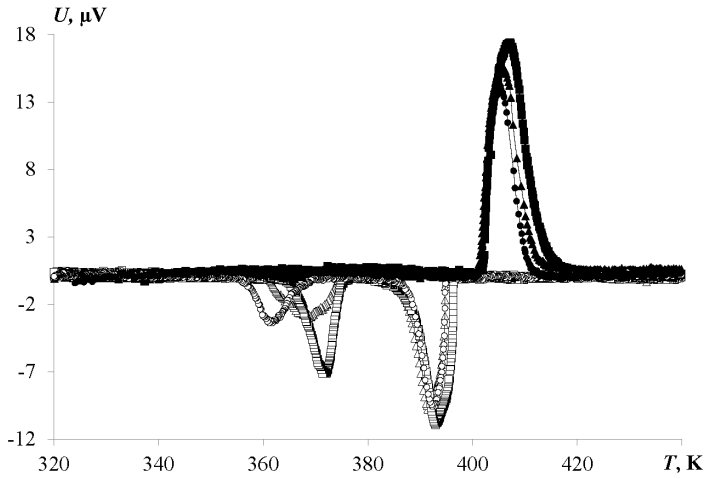

Fig. 3. Temperature dependences of DTA signal for $(KNO_3)_{1-x}/Sn_x$ composite for $x = 0$ (■), 0.1 (▲) and 0.2 (●); shaded symbols correspond to heating, empty symbols to cooling

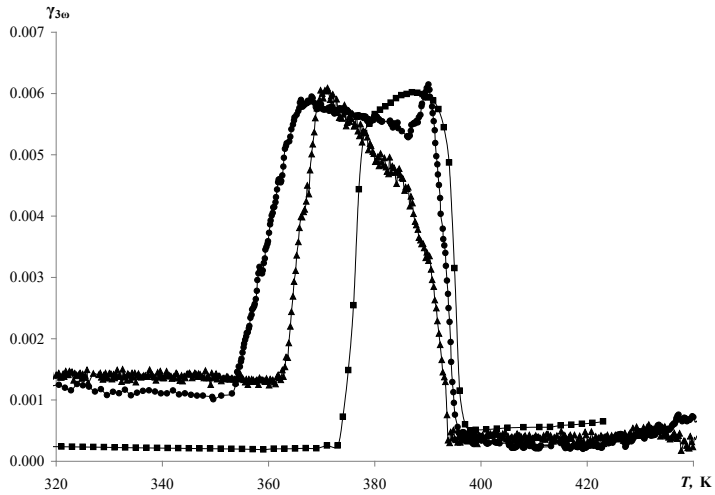

Fig. 4. Temperature dependences of $\gamma_{3\omega}$ for the $(KNO_3)_{1-x}/Sn_x$ composite for $x = 0$ (■), 0.1 (▲) and 0.2 (●); shaded symbols correspond to heating, empty symbols to cooling

Results and discussion

To interpret the results obtained, in particular, the decrease in the Curie temperature of potassium nitrate, which is part of the $(KNO_3)_{1-x}/Sn_x$ composite, let us consider an array of particles located at a certain distance from each other. We write the free energy F of the composite as the sum of the energy of KNO_3 particles and the interaction energy between KNO_3 and Sn particles:

$$F = \sum_i \left(F_{0i} + \frac{1}{2}\alpha P_i^2 + \frac{1}{4}\beta P_i^4 + \frac{1}{2}\delta(\nabla P_i)^2) \right) dv_i + \sum_i \int_{S_i} \Delta F_{S_i} dS_i, \quad (1)$$

where P_i is the polarization of KNO_3 particles, which is a function of temperature and coordinates; α, β, δ are the decomposition coefficients, generally dependent on temperature; v_i, S_i are the volume and surface areas of the ith particle, respectively; ΔF_{Si} is the surface free energy.

Integration of surface free energy over the area S_i takes the form

$$\sum_i \int_{S_i} \Delta F_{S_i} dS_i = \int_{S_i} \sigma_i dS_i + \int_{S_i} \varphi_i dS_i + \int_{S_i} \mu_i dN_i,$$

where σ_i is the surface tension, φ_i is the electrical potential, δ_i is the surface charge density, μ_i is the chemical potential, N_i is the number of particles.

The first term in expression (1) takes into account the so-called baric effect. It can manifest as either an increase or a decrease in the temperature of the structural transition, depending on the sign of the baric coefficient and the ratio of thermal expansion coefficients characterizing the composite components. The second term accounts for the energy from shielding of KNO_3 particles by Sn metal particles. The third term accounts for the energy of the electric field resulting from different electron work functions from KNO_3 and from Sn metal particles.

The phase boundaries in$(KNO_3)_{1-x}/Sn_x$ have a large surface, making a substantial contribution to the composite energy and to a decrease in the effective field of KNO_3particles. This can lead to a change in the Curie temperature and spontaneous polarization. According to Landau–Ginsburg theory, the change in the Curie temperature accounting for ΔF_s is expressed as

$$\tilde{T}_C = T_C - \frac{1}{\alpha_0} \int_{AS} \Delta F_{S_i} dS.$$

The greatest contribution to the temperature shift of the ferroelectric phase transition can be made by shielding fields, inducing a rearrangement in the domain structure and production of oppositely oriented domains.

As established in [13, 14], the presence of free charge carriers in ferroelectrics tends tomodify the dielectric properties, Curie temperature, spontaneous polarization, etc. It was reported in [14] that the additional energy generated by excitation of non-equilibrium charge carriers leads to a decrease in the temperature of ferroelectric phase transition by ΔT_s:

$$\Delta T_C = \Delta E_g Cn/\pi P_s^2,$$

where ΔE_g is the variation in the bandgap width upon a first-order phase transition, is the Curie–Weiss constant.

Conclusion

We can conclude from analysis of dielectric measurements and differential thermal analysis that a decrease by 2–3 K is observed in the temperature of the α → β phase transition in $(KNO_3)_{1-x}/Sn_x$ composites, while the temperature of the phase transition γ → α decreases up to 360 K. The result can be explained within the Landau-Ginsburg theory, taking into account the shielding of potassium nitrate particles by tin metal particles.

REFERENCES

1. **Tanaka K., Kurihashi Y., Uda T., et al.,** Scanning nonlinear dielectric microscopy nano-science and technology for next generation high density ferroelectric data storage, Jap. J. Appl. Phys. 47 (5R) (2008) 3311.

2. **Acharya M., Mack S., Fernandez A., et al.,** Searching for new ferroelectric materials using high-throughput databases: An experimental perspective on $BiAlO_3$ and $BiInO_3$, Chem. Mater. 32 (17) (2020) 7274–7283.

3. **Pierangeli D., Ferraro M., Di Mei F., et al.,** Super-crystals in composite ferroelectrics, Nat. Commun. 7(2016) 10674.

4. **Milinskiy A. Yu., Baryshnikov S. V., Charnaya E. V., et al.,** Phase transitions in bulk and confined organic ferroelectric DIPAI, Res. Phys. 17 (June) (2020) 103069.

5. **Yan Z., Yang Y., Cai X.,** Preparation of a ferroelectric composite film metal-organic framework/ PVDF, J. Polm. Res. 27 (12) (2020) 377.

6. **Chen A., Chernow F.** Nature of ferroelectricity in KNO_3, Phys. Rev. 154 (2) (1967) 493–505.

7. **Scott J. F., Duiker H. M., Beale P. D., et al.,** Properties of ceramic KNO_3 thin-film memories, Physica. B. 150 (1–2) (1988) 160–167.

8. **Stukova E. V., Baryshnikov S. V.,** Stabilization of the ferroelectric phase in $(KNO_3)_{1-x}$-$(BaTiO_3)_x$ composites, Inorg. Mater. Appl. Res. 2-I (5) 434–438.

9. **Naberezhnov A. A., Vanina P. Yu., Sysoeva A. A., et al.,** Effect of restricted geometry on the structure and phase transitions in potassium nitrate nanoparticles, Phys. Solid State. 60 (3) (2018) 442–446.

10. **Milinskii A. Y., Baryshnikov S. V., Stukova E. V., et al.,** Dielectric and thermal properties of KNO_3 encapsulated in carbon nanotubes, Phys. Solid State. 63 (6) (2021) 872–876.

11. **Deshpande V. V., Karkhanavala M. D., Rao U. R. K.,** Phase transitions in potassium nitrate, J. Therm. Anal. Calorim. 6 (6) (1974) 613–621.

12. **Ikeda S., Kominami H., Koyama K., Wada Y. J.,** Nonlinear dielectric constant and ferroelectric-to-paraelectric phase transition in copolymers of vinylidenefluo-ride and trifluoroethylene, Appl. Phys. 62 (8) (1987) 3339–3342.

13. **Fridkin V. M.,** Ferroelectrics semiconductors (Translation from Russian), Consultants Bureau, New York, USA, 1980.

14. **Fridkin V. M.,** Photoferroelectrics, Springer, Berlin, Heidelberg, New York, 1979.

СПИСОК ЛИТЕРАТУРЫ

1. **Tanaka K., Kurihashi Y., Uda T., Daimon Y., Odagawa N., Hirose R., Hiranaga Y., Cho Y.** Scanning nonlinear dielectric microscopy nano-science and technology for next generation high density ferroelectric data storage // Japanese Journal of Applied Physics. 2008. Vol. 47. No. 5R. P. 3311.

2. **Acharya M., Mack S., Fernandez A., Kim J., Wang H., Eriguchi K., Meyers D., Gopalan V., Neaton J., Martin L. W.** Searching for new ferroelectric materials using high-throughput databases: An experimental perspective on $BiAlO_3$ and $BiInO_3$// Chemistry Materials. 2020. Vol. 32. No. 17. Pp. 7274–7283.

3. **Pierangeli D., Ferraro M., Di Mei F., Di Domenico G., de Oliveira C. E. M., Agranat A.J., DelRe E.** Super-crystals in composite ferroelectrics // Nature Communications. 2016. Vol.7. P. 10674.

4. **Milinskiy A. Yu., Baryshnikov S. V., Charnaya E. V., Egorova I. V., Sarnatskii V. M.** Phase transitions in bulk and confined organic ferroelectric DIPAI // Results in Physics. 2020. Vol. 17. June.P. 103069.

5. **Yan Z., Yang Y., Cai X.** Preparation of a ferroelectric composite film metal-organic framework/ PVDF // Journal of Polymer Research. 2020. Vol. 27. No.12. P. 377.

6. **Chen A., Chernow F.** Nature of feroelectricity in KNO_3 // Physical Review. 1967. Vol. 154. No. 2. Pp. 493–505.

7. **Scott J. F., Duiker H. M., Beale P. D., Pouligny B., Dimmler K., Parris M., Butler D., Eaton S.** Properties of ceramic KNO_3 thin-film memories // Physica B. 1988. Vol. 150. No. 1–2. P. 160–167.

8. **Stukova E. V., Baryshnikov S. V.** Stabilization of the ferroelectric phase in $(KNO_3)_{1-x}$-$(BaTiO_3)_x$ composites // Inorganic Materials: Applied Research. 2011. Vol. 2. Part I. No. 5. Pp. 434–438.

9. **Набережнов А. А., Ванина П. Ю., Сысоева А. А., Cizman A., Rysiakiewicz-Pasek E., Hoser A.** Влияние ограниченной геометрии на структуру и фазовые переходы в наночастицах нитрата калия // Физика твердого тела. 2018. Т. 60. № 3. С. 439–442.

10. **Милинский А. Ю., Барышников С. В., Стукова Е. В., Чарная Е. В., Чернечкин И. А., Ускова Н. И.** Диэлектрические и тепловые свойства KNO_3, внедренного в углеродные нанотрубки // Физика твердого тела. 2021. Т. 63. № 6. С. 767–771.

11. **Deshpande V. V., Karkhanavala M. D., Rao U. R. K.** Phase transitions in potassium nitrate // Journal of Thermal Analysis and Calorimetry. 1974. Vol. 6. No. 6. Pp. 613–621.

12. **Ikeda S., Kominami H., Koyama K., Wada Y. J.** Nonlinear dielectric constant and ferroelectric-to-paraelectric phase transition in copolymers of vinylidenefluoride and trifluoroethylene // Applied Physics. 1987. Vol. 62. No. 8. Pp. 3339–3342.

13. **Фридкин В. М.** Сегнетоэлектрики – полупроводники. М.: Наука, 408 ,1976 с.

14. **Фридкин В. М.** Фотосегнетоэлектрики. М.: Наука, 1979. 464 с.

THE AUTHORS

MILINSKIY Alexey Yu.
Blagoveshchensk State Pedagogical University
104, Lenina St., Blagoveshchensk, 675000, Russia
a.milinskiy@mail.ru
ORCID: 0000-0001-7525-4396

BARYSHNIKOV Sergey V.
Blagoveshchensk State Pedagogical University
104, Lenina St., Blagoveshchensk, 675000, Russia
svbar2003@list.ru
ORCID: 0000-0002-3362-8975

STUKOVA Elena V.
Amur State University
21 Ignatievskoe Ave., Blagoveshchensk, 675027, Russia
lenast@bk.ru
ORCID: 0000-0002-7981-7456

СВЕДЕНИЯ ОБ АВТОРАХ

МИЛИНСКИЙ Алексей Юрьевич – *доктор физико-математических наук, доцент кафедры физического и математического образования Благовещенского государственного педагогического университета.*

675000, Россия, г. Благовещенск, ул. Ленина, 104
a.milinskiy@mail.ru
ORCID: 0000-0001-7525-4396

БАРЫШНИКОВ Сергей Васильевич – *доктор физико-математических наук, профессор кафедры физического и математического образования Благовещенского государственного педагогического университета.*

675000, Россия, г. Благовещенск, ул. Ленина, 104
104svbar2003@list.ru
ORCID: 0000-0002-3362-8975

СТУКОВА Елена Владимировна – *доктор физико-математических наук, профессор, заведующая кафедрой физики Амурского государственного университета.*

675027, Россия, г. Благовещенск, Игнатьевское шоссе, 21
lenast@bk.ru
ORCID: 0000-0002-7981-7456

Received 24.03.2022. Approved after reviewing 31.05.2022. Accepted 31.05.2022.

Статья поступила в редакцию 24.03.2022. Одобрена после рецензирования 31.05.2022. Принята 31.05.2022.

Original article
DOI: https://doi.org/10.18721/JPM.15302

EFFECT OF INTERFACE MODIFICATION BY TITANIUM DIOXIDE ON DIELECTRIC PROPERTIES OF SODIUM NITRITE NANOCOMPOSITE BASED ON POROUS GLASS

A. Yu. Molokov[1]✉, *A. A. Sysoeva*[1], *A. A. Naberezhnov*[1], *E. Yu. Koroleva*[1,2]

[1] Ioffe Institute, St. Petersburg, Russia;

[2] Peter the Great St. Petersburg Polytechnic University, St. Petersburg, Russia

✉ antonmol@mail.ru

Abstract. Dielectric properties and structure of initial nanocomposite based on porous glass with embedded ferroelectric $NaNO_2$ and nanocomposite identical to that but having a TiO_2-modified pore surface, have been studied over a temperature range 300 – 450 K (on cooling) and frequency one 0.1 – $3 \cdot 10^6$ Hz. X-ray spectroscopy of the samples exhibited that $NaNO_2$ was in the ferroelectric phase in both composites and the percentage of crystalline $NaNO_2$ increased in the pores of the modified one. An increase in permittivity and conductivity was observed in the TiO_2-modified nanocomposite. Two relaxation processes were identified and their nature was established. The charge polarization at the interfaces was found to make the main contribution to the dielectric response of the both nanocomposites. The DC-conductivity of both composites was estimated and its activation energies were determined. An activation energy change observed in a vicinity of 400 K was attributed to the phase transition to the low-temperature phase of $NaNO_2$. The possibility to control the properties of nanocomposites through modifying the interfaces was shown.

Keywords: nanocomposite, ferroelectric, sodium nitrate, titanium oxide, porous glass, dielectric spectroscopy

Funding: The reported study was funded by Russian Science Foundation (Russian Federation), DST (Republic of India) & NRF (Republic of South Africa) within the framework of the Scientific Project No. 19-52-80019 BRICS.

Citation: Molokov A. Yu., Sysoeva A. A., Naberezhnov A. A., Koroleva E. Yu., Effect of interface modification by titanium dioxide on dielectric properties of sodium nitrite nanocomposite based on porous glass, St. Petersburg State Polytechnical University Journal. Physics and Mathematics. 15 (3) (2022) 17–27. DOI: https://doi.org/10.18721/JPM.***15302***

Научная статья
УДК 538.956
DOI: https://doi.org/10.18721/JPM.15302

ВЛИЯНИЕ МОДИФИКАЦИИ ИНТЕРФЕЙСА ДИОКСИДОМ ТИТАНА НА ДИЭЛЕКТРИЧЕСКИЕ СВОЙСТВА НАНОКОМПОЗИТА НА ОСНОВЕ ПОРИСТОГО СТЕКЛА С НИТРИТОМ НАТРИЯ

А. Ю. Молоков[1]✉, *А. А. Сысоева*[1], *А. А. Набережнов*[1], *Е. Ю. Королева*[1,2]

[1] Физико-технический институт им. А.Ф. Иоффе РАН, Санкт-Петербург, Россия;

[2] Санкт-Петербургский политехнический университет Петра Великого, Санкт-Петербург, Россия

✉ antonmol@mail.ru

Аннотация. Исследованы диэлектрические свойства и структура исходного нанокомпозита на основе пористого стекла с внедренным $NaNO_2$ и такого же нанокомпозита, но с поверхностью пор, модифицированной диоксидом титана (температурный диапазон – 300 – 450 K, частотный – 0,1 – $3 \cdot 10^6$ Гц), при охлаждении. Структурные исследования показали, что в обоих композитах $NaNO_2$ находится в сегнетоэлектрической фазе. При модификации поверхности процент кристаллического $NaNO_2$ в порах возрастает. В модифицированном композите наблюдается увеличение диэлектрической проницаемости и проводимости. Идентифицированы два релаксационных процесса и установлена их природа. Установлено, что основной вклад в диэлектрический отклик НКМ вносит зарядовая поляризация на границах раздела. Оценена проводимость на постоянном токе обоих композитов и определены соответствующие энергии активации. Изменение энергии активации, наблюдаемое в районе 400 K, связано с фазовым переходом в низкотемпературную фазу $NaNO_2$. Показана возможность управления свойствами нанокомпозитов через модификацию интерфейса.

Ключевые слова: нанокомпозит, сегнетоэлектрик, нитрит натрия, пористое стекло, оксид титана, диэлектрическая спектроскопия

Финансирование: Исследование выполнено при финансовой поддержке РФФИ (Российская Федерация), DST (Республика Индия) и NRF (Южно-Африканская Республика) в рамках научного проекта 80019-52-19 БРИКС.

Ссылка для цитирования: Молоков А. Ю., Сысоева А. А., Набережнов А. А., Королева Е. Ю. Влияние модификации интерфейса диоксидом титана на диэлектрические свойства нанокомпозита на основе пористого стекла с нитритом натрия // Научно-технические ведомости СПбГПУ. Физико-математические науки. 2022. Т. 15. № 3. С. 17–27. DOI: https://doi.org/10.18721/ JPM.**15302**

Introduction

Nanocomposite materials (NCM) based on nanoporous matrices with embedded ferroelectrics are of undoubted interest due to broad prospects for practical applications in novel approaches in electronics, information storage devices, applied medicine and biology, etc. It is known that the dimensional effect can fundamentally change the physical properties of materials, especially when the characteristic sizes of the nanoparticles become comparable to the correlation length of critical fluctuations in the order parameter. There are various methods for preparing NCM; one of them is embedding substances into nanoporous glasses (referred to as porous glasses, or PG).

The advantages of PG is that modifying the parameters of pure (non-porous) alkali borosilicate glass allows to obtain matrices with different mean pore parameters, controllable from 3 nm to approximately 300–400 nm [1, 2].

At the same time, aside from the dimensional effect, the properties of NCM are significantly affected by the presence of the interface between the matrix and the embedded material. Modifications to the interface can also be used to tailor the overall macroscopic properties of the NCM; this approach has been adopted in several studies [3–5].

Sodium nitrite ($NaNO_2$) is a model ferroelectric, whose macroscopic properties and phase transitions have been thoroughly analyzed [6, 7]. This compound has an orthorhombic structure at room temperature (space group *Im2m*) with the parameters of the crystal cell a = 3.55 E, b = 5.56 E and c = 5.37 E [8]. Sodium nitrite passes into the high-temperature orthorhombic phase *Immm* above 438 K [9]. The dielectric properties of sodium nitrite in porous glass with a mean pore diameter of 7(1) nm (PG7 + $NaNO_2$ system) were considered in [10 – 12]. The authors observed an exponential increase in the dielectric response at low measuring frequencies with increasing temperature, and the presence of frequency dispersion. In this case, not only the phase transition temperature decreased to 427 K, but the type of phase transition (PS) changed [12, 13]. One of the possible reasons for this major change in the physical properties of sodium nitrite embedded in PG7 may be the influence of the interface between the matrix and the embedded material, so modifying the surface of the pores (channels) in porous glass should be expected to produce a change in the overall properties of the NCM. We used titanium dioxide TiO_2 wetting the surface of the porous glass to modify the interface in our study.

Our goal was to establish the effect that modifying the interface between the matrix and the embedded material with titanium dioxide has on the dielectric properties of the PG6 + $NaNO_2$ nanocomposite.

Samples and experimental procedure

The following group of samples was considered:

porous glass with an average pore diameter of 6(1) nm (PG6);

porous glass with titanium dioxide (PG6 + TiO_2);

sodium nitrite in porous glass (PG6 + $NaNO_2$);

sodium nitrite in porous glass with titanium dioxide (PG6 + TiO_2 + $NaNO_2$).

Porous PG6 glasses were prepared by etching borosilicate glasses. The diameter of the pores obtained was determined via mercury porometry. The pure porous glass was held in a 20% solution of tetraisopropylortitanate $Ti[OCH(CH_3)_2]_4$ (TTIP) in isopropanol for a day at 60 °C. This PG6 glass was then hydrolyzed in air at room temperature. Annealing was carried out at 450 °C for 4 hours. The measurements indicate that the degree of filling with titanium oxide was 11% of the pore volume. To embed sodium nitrite, porous glass samples were placed in a saturated aqueous solution of $NaNO_2$ at 130 °C until the water evaporated completely. The degree of filling with sodium nitrite in both samples was 59% of the pore volume.

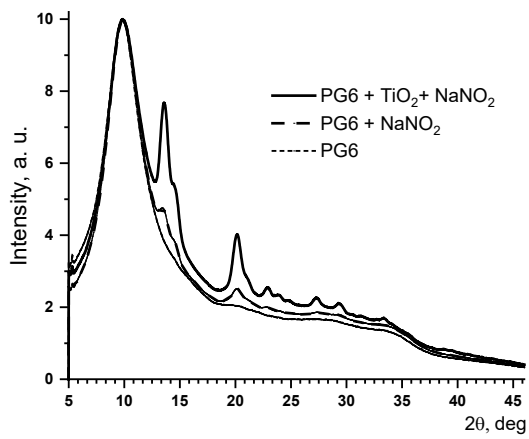

Fig. 1. Experimental X-ray patterns for PG6 + $NaNO_2$, PG6 + TiO_2 + $NaNO_2$ and unfilled PG6 samples at room temperature

The finished samples were rectangular plates measuring 8.0 × 5.0 × 0.6 mm. Dielectric studies were carried out depositing gold electrodes about 80 nm thick with a 4 nm thick chromium sublayer (for better adhesion) onto the surface of the samples.

The dielectric response was measured with a Novocontrol BDS 80 wideband dielectric spectrometer (Germany) in the frequency range of $0.1–3.0 \cdot 10^6$ Hz and in the temperature range of 300–440 K under cooling at a rate of 1 K/min after preheating to 440 K. The phase state of $NaNO_2$ the NCM prepared was determined after the first heating-cooling cycle via analysis of PG6 + $NaNO_2$ and PG6 + TiO_2 + $NaNO_2$ NCM structures with a Oxford Diffraction SuperNova X-ray diffractometer (USA) at a wavelength λ = 0.70926 E (Mo $K_{\alpha 1}$ radiation) in the range of angles 2Θ = 5°–43° at room temperature. Measurements were carried out in transmission geometry, the illuminated area of the samples and their thickness was the same in all cases. The contribution of the background from amorphous silica SiO_2 comprising the framework joints was determined from the XRD pattern from the empty framework.

Experimental results and discussion

Fig. 1 shows the XRD patterns for three models (unfilled PG6, PG6 + TiO_2 + $NaNO_2$ and PG6 + $NaNO_2$). The XRD pattern for PG6 + TiO_2 (not shown in Fig. 1) does not contain any elastic peaks corresponding to the titanium oxide structure; moreover, the XRD patterns for the PG6 and PG6 + TiO_2 samples are almost identical. A broad peak is observed in the vicinity of the angle $2\theta \approx 10°$, associated with scattering by the amorphous material of the SiO_2 framework. Fig. 1 shows that the diffraction spectra are similar for NCM with sodium nitrite but the integral intensities of the peaks differ significantly.

The phase state of sodium nitrite in NCM was determined by subtracting the background from scattering by the amorphous framework from the spectra of PG6 + $NaNO_2$ and PG6 + TiO_2 + $NaNO_2$ samples; the data were then compared with the model spectrum for bulk sodium nitrite at this wavelength (Fig. 2).

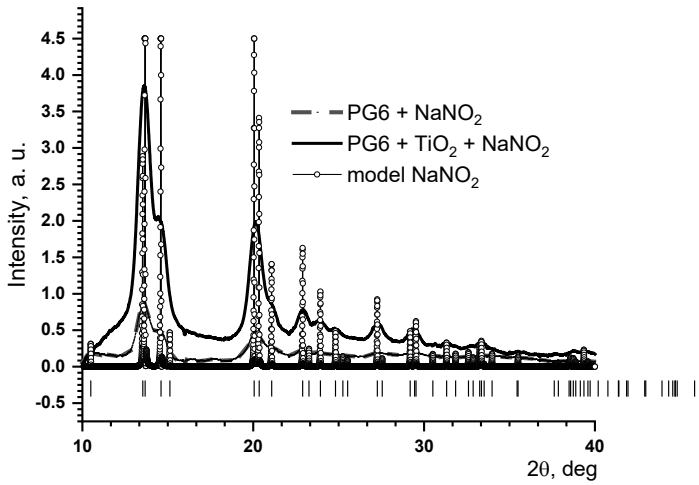

Fig. 2. Comparison of XRD patterns from Fig. 1, subtracting the background from the framework (amorphous SiO_2), with the model spectrum of bulk $NaNO_2$ at room temperature (vertical bars indicate the positions of elastic Bragg peaks)

Due to a number of considerations, we did not conduct a detailed quantitative analysis for the crystalline structure of these NCM, but comparing the data presented with the model spectrum for bulk material allows to draw some conclusions about the phase state of sodium nitrite in the framework pores.

As seen from Fig. 2, the spectrum of the PG6 + $NaNO_2$ sample contains all the main peaks characteristic for the low-temperature orthorombic phase of sodium nitrite, which is even more pronounced in the corresponding spectrum for the sample with titanium dioxide. In addition, the integral intensity of the peaks significantly increased when sodium nitrite was embedded into the titanium dioxide glass, even though both PG6-based NCM had the same degree of filling with

sodium nitrite. This result can be associated with an increase in the fraction of the crystalline phase in the pores upon crystallization of sodium nitrite in porous glass with titanium dioxide. The remaining sodium nitrite is most likely in an amorphous state. The presence of a significant fraction of the amorphous phase, along with the crystalline phase in the NCM based on porous glasses, is unsurprising, since it was observed earlier for nanocomposites with embedded selenium [14] and low-melting+point metals [15].

Fig. 3 shows the temperature dependences of dielectric permittivity ε′ (left) and conductivity σ′ (right) at frequencies of 1 kHz and 0.1 Hz during cooling. Comparing these dependences, we can conclude that adding titanium dioxide increases the magnitudes of ε′ and σ› in these glasses throughout the temperature range considered. The σ′ values in glass with TiO_2 increase by almost an order of magnitude, compared to PG6 at low frequencies. Unfortunately, it was not possible to measure σ′ in the entire temperature range in empty porous glass at high frequencies. It is clear from the given temperature dependences of σ′ for PG6 and PG6+TiO_2 that titanium dioxide increases the conductivity of the porous matrix.

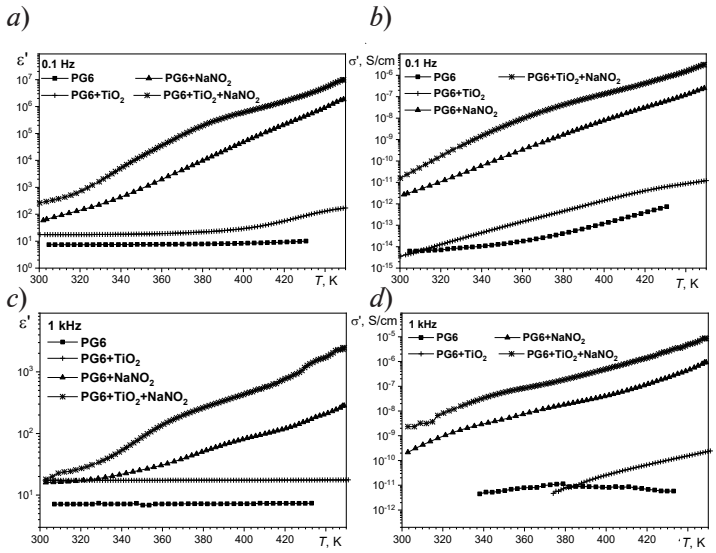

Fig. 3. Temperature dependences of dielectric permittivity ε′ (*a*, *c*) and conductivity σ′ (*b*, *d*) for PG6, PG6 + TiO_2, PG6 + $NaNO_2$ and PG6 + TiO_2 + $NaNO_2$ NCM at 0.1 Hz (*a*, *b*) and 1 kHz (*c*, *d*)

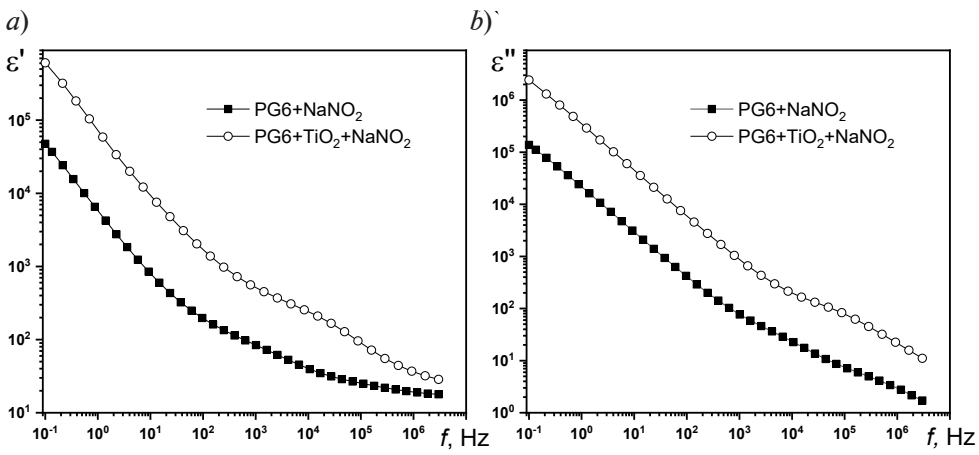

Fig. 4. Frequency dependences of dielectric permittivity ε′ (*a*) and dielectric losses ε″ (*b*) for PG6 + $NaNO_2$ and PG6 + TiO_2 + $NaNO_2$ samples at 400 K

In the next step, we analyzed the behavior of dielectric response in composites with embedded sodium nitrite. Comparing the behavior of the curves related to the temperature dependences of ε′ and σ′ for these nanocomposites, we can see that the level of ε′ and σ′ values in the NCM with TiO_2 is higher than for the samples without it both at low (0.1 Hz) and high (1 kHz) frequencies in the entire measured temperature range. The ε′ and σ′ values of the PG6 + TiO_2 + $NaNO_2$ composite at high temperatures (above 400 K) are an order of magnitude greater than those of PG6 + $NaNO_2$. The difference in ε′ values is small at low temperatures (near room temperature). This behavior of the dielectric response in NCM with titanium dioxide confirms our assumption based on the results of structural studies that the percentage of crystalline sodium nitrite is higher in PG6 + TiO_2 + $NaNO_2$ than in PG6 + $NaNO_2$ samples.

The respective frequency dependences were obtained and investigated to analyze the physical nature of the dielectric response. These dependences at 400 K are shown in Fig. 4.

Notably, no rigorous theory has been formulated this far for describing the relaxation contributions other than from Debye relaxation [16, 17], so empirical distributions are used to analyze the results, characterizing the dispersion dependences for a large number of substances sufficiently well. Expression (1) is used as a model function; consisting of the following terms: the sum of the empirical Cole–Cole functions, describing relaxation processes, the term from the contribution of phonon modes, and the term responsible for DC conductivity:

$$\varepsilon^*(\omega) = \varepsilon_\infty + \sum_j \frac{\Delta\varepsilon_j}{1+(i\omega\tau_j)^\alpha} + \frac{i\sigma_{DC}}{\varepsilon_0\omega}, \quad (1)$$

where Δε is the dielectric strength of the relaxation process, τ is the mean relaxation time, α is the exponent characterizing the broadening of the spectrum relative to Debye behavior, ε_∞ is the contribution of phonon modes and electron polarization, ω is the angular frequency, ε_0 is the dielectric constant of vacuum, σ_{DC} is the DC conductivity.

The dispersion curves can be described by expression (1), if we first carry out nonlinear approximation of the frequency dependences of the dielectric permittivity and dielectric losses. Approximation was performed by the Levenberg–Marquardt algorithm [18]. The curves of the ε′ and ε′ dependences were simultaneously fitted, allowing to significantly reduce the error. Two relaxation processes were detected in the frequency and temperature ranges considered. The contribution of DC conductivity was found, consequently yielding the temperature dependences for the parameters of relaxation processes, Δε and τ (Fig. 5).

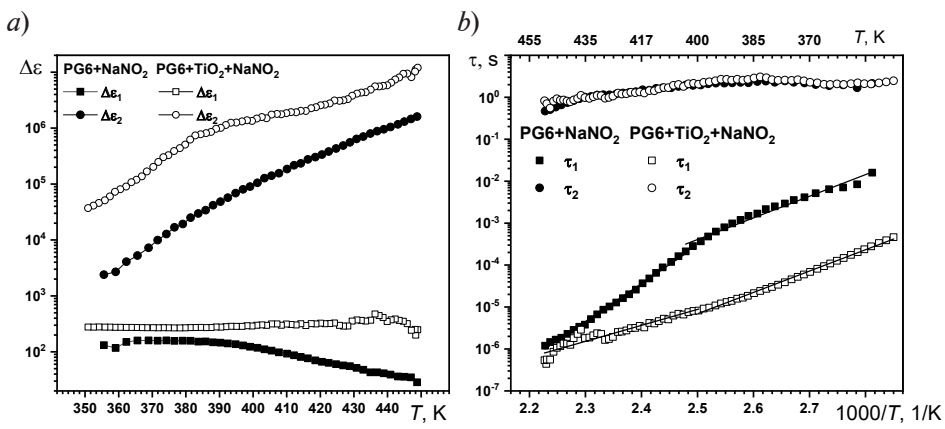

Fig. 5. Temperature dependences for dielectric strength of the relaxation process Δε (*a*) and the characteristic values of mean relaxation time τ (*b*) for two relaxation processes (denoted by subscripts 1 and 2) for PG6 + $NaNO_2$ and PG6 + TiO_2 + $NaNO_2$ samples

The main contribution to the dielectric response of both composites is made by the quantity $\Delta\varepsilon_2$, and this contribution increases with increasing temperature. The characteristic relaxation times of this process for both composites are equal to about a second, and their temperature dependences are almost identical throughout the temperature region considered. This confirms that these processes are equivalent, even though the strength of the process is higher in modified NCM than in the one not modified with TiO_2 (this may be due to a higher percentage of the crystalline phase of sodium nitrite in the given NCM). We associate this process with charge polarization at the grain (nanoparticle) boundaries of sodium nitrite.

The magnitude of $\Delta\varepsilon_1$ is virtually independent of temperature in modified NCM. The process is somewhat weaker in unmodified NCM, and its value of $\Delta\varepsilon$ decreases within the same order of magnitude with increasing temperature. Relaxation times vary from 10^{-2} s (at 350 K) to 10^{-6} s (at 450 K) for unmodified NCM and from 10^{-3} to 10^{-7} s for the NCM modified with TiO_2. Such values and temperature behavior observed for the parameters of the relaxation process allow to relate ot to hopping conductivity of sodium ions, which has already been detected earlier in the PG7 + $NaNO_2$ NCM [19, 20]. This process is faster by an order of magnitude faster in the NCM with a modified surface, i.e. it can be assumed that modification of the pore surface with titanium dioxide facilitates the hoping conductivity of sodium ions. The dependences of relaxation time for the second type of processes exhibit a thermally activated behavior in both NCM. Two regions with different activation energies (with a change in the slope of the curves) can be detected for each dependence near 400 K, which may be due to a PT to the low-temperature phase of sodium nitrite, shifting in temperature due to the size effect.

Estimates of DC conductivity in both NMCs were also obtained by fitting the experimental data using Eq. (1). The temperature dependences of conductivity for PG6 + $NaNO_2$ and PG6 + TiO_2 + $NaNO_2$ samples are shown in Fig. 6 in Arrhenius coordinates. Modifying the surface with titanium dioxide produces an increases in the DC conductivity of the NCM by an order of magnitudein the entire temperature range considered. The conductivity has a thermally activated nature; two regions with different activation energies can be observed on each curve, while the change in activation energy is observed at about 400 K. This correlates well with the data obtained for relaxation times. The activation energy of the composite containing TiO_2turns out to be somewhat lower, i.e., the modification of the surface seems to facilitate the hopping conductivity of sodium ions.

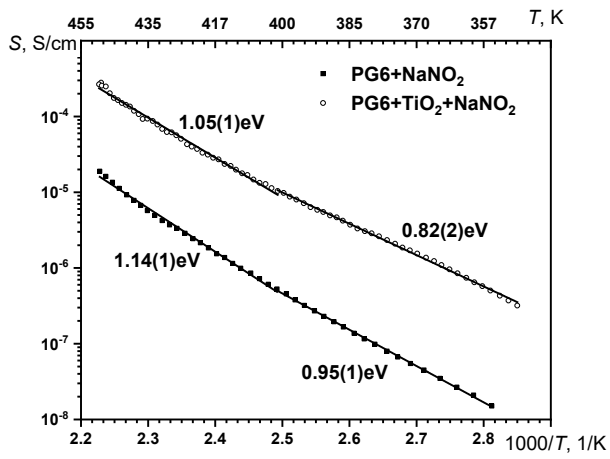

Fig. 6. Dependences of DC conductivity on inverse temperature (the corresponding values of T are given on the upper scale) for PG6 + $NaNO_2$ and PG6 + TiO_2 + $NaNO_2$ samples. Straight lines correspond to Arrhenius approximations (the corresponding activation energies are also given)

Conclusion

We have investigated the electrical and structural properties of nanocomposite materials based on pure porous glasses with an average pore diameter of 6(1) nm, porous glasses with the pores modified with titanium dioxide and filled with a ferroelectric (sodium nitrite). Structural studies revealed a crystalline phase of sodium nitrite in the samples (no peaks from TiO_2 were detected), so there is reason to believe that TiO_2 is in amorphous state. It was established from XRD patterns that the integral intensity of the diffraction peaks is significantly higher for the PG6 + TiO_2 + $NaNO_2$ sample than for PG6 + $NaNO_2$. This suggests an increase in the percentage of sodium nitrite crystalline phase in the pores of modified NCM, compared to the content of this phase in the NCM without titanium dioxide.

We have found an increase in the dielectric permittivity and conductivity of the modified NCM compared to the unmodified sample. The dielectric response of both composites was analyzed, with two relaxation processes observed in the selected temperature and frequency ranges. Evidently, the main contribution to the dielectric response of NCM is made by a relaxation process associated with charge polarization at grain (nanoparticle) boundaries, and this relaxation process is more pronounced in the NCM with titanium dioxide, due to increased volume of crystalline sodium nitrite in NCM pores. We attributed the second relaxation process to hopping conductivity of sodium ions along the channels. This process is as intense in the NCM containing TiO_2 but it proceeds much faster, pointing to a possible increase in the number of conduction channels and/or a decrease in the hopping length due to modification of the pore surface with titanium dioxide.

Thus, it is confirmed that modifying the surface allows to control the dielectric properties of nanocomposite materials based on porous matrices.

REFERENCES

1. **Enke D., Janowski F., Schwieger W.,** Porous glasses in the 21st century – a short review, Microp. Mesopor. Mat. 60 (1–3) (2003) 19–30.

2. **Elmer T. H., Nordberg M. E., Carrier G. B., Korda E. J.,** Phase separation in borosilicate glasses as seen by electron microscopy and scanning electron microscopy, J. Am. Ceram. Soc. 53 (4) (1970) 171–175.

3. **Kikukawa T., Kuraoka K., Kawabe K., et al.,** Preparation of an organic-inorganic hybrid ionic conductive material with thermal and chemical stability, J. Am. Ceram. Soc. 87 (3) (2004) 504–506.

4. **Yazawa T.**, **Miyamoto S., Yusa S., et al.,** Preparation of pH responsive porous glass by surface modification with COOH group, Mater. Res. Bull. 48 (10) (2013) 4267–4270.

5. **Dvoyashkin M.**, **Romanova E. E., Einicke W,-D., et al.,** Diffusion of cyclohexane in native and surface-modified mesoporous glasses, Adsorption. 17 (1) (2011) 93–99.

6. **Sawada S., Nomura S., Asao Y.,** Dielectric properties of ferroelectric $NaNO_2$, J. Phys. Soc. Jap. 16 (11) (1961) 2207–2212.

7. **Kay M. I.,** The structure of sodium nitrite at 150°, 185°, 225°C, Ferroelectrics. 4 (1) (1972) 235–243.

8. **Ravindran P., Delin A., Johansson B., et al.,** Electronic structure, chemical bonding, and optical properties of ferroelectric and antiferroelectric $NaNO_2$, Phys. Rev. B. 59 (3) (1999) 1776–1785.

9. **Yamada Y., Shibuya I., Hoshino S.,** Phase transition in $NaNO_2$, J. Phys. Soc. Jap. 18 (11) (1963) 1594–1603.

10. **Colla E. V., Koroleva E. Y., Kumzerov Yu. A., Savenko B. N.,** Ferroelectric phase transitions in materials embedded in porous media, Ferroelectrics Lett. 20 (5–6) (1996) 143–147.

11. **Kinka M., Banys J., Naberezhnov A.,** Dielectric properties of sodium nitrite confined in porous glass, Ferroelectrics. 348 (1) (2007) 67–74.

12. **Kutnjak Z., Vodopivec B., Blinc R., et al.,** Calorimetric and dielectric studies of ferroelectric sodium nitrite confined in a nanoscale porous glass matrix, J. Chem. Phys. 123 (8) (2005) 084708.

13. **Naberezhnov A., Fokin A., Kumzerov Yu., et al.,** Structure and properties of confined sodium nitrite, Eur. Phys. J. E. 12 (Suppl. 1) (2003) 21–24.

14. **Golosovsky I. V., Smirnov O. P., Delaplane R. G., et al.,** Atomic motion in Se nanoparticles embedded into a porous glass matrix, Eur. Phys. J. B. 54 (2) (2006) 211–216.

15. **Naberezhnov A. A., Borisov S. A., Fokin A. V., et al.,** SANS studies of nanostructured low-melting metals at room temperature, Nanosystems: Phys. Chem. Math. 11 (6) (2020) 690–697.

16. **Jonscher A. K.,** Dielectric relaxation in solids, J. Phys. D. 1999. Vol. 32 (14) (1999) R57–.

17. **Kremer F., Schönhals A.** (Eds.), Broadband dielectric spectroscopy, Springer, Berlin, Heidelberg, 2003.

18. **Moré J. J.,** The Levenberg – Marquardt algorithm: Implementation and theory, In book: Numerical Analysis. Lecture notes in Mathematics, Vol. 630. Ed. by G. A. Watson, Springer, Berlin, Heidelberg (1978) 105–116.

19. **Vakhrushev S. B., Kumzerov Yu. A., Fokin A., et al.,** ^{23}Na spin-lattice relaxation of sodium nitrite in confined geometry, Phys. Rev. B. 70 (13) 132102.

20. **Naberezhnov A. A., Vakhrushev S. B., Kumzerov Yu. A., Fokin A. V.,** Mechanism of ferroelectric phase transition in ultra-dispersed sodium nitrite particles, Ferroelectrics. 575 (1) (2021) 75–83.

СПИСОК ЛИТЕРАТУРЫ

1. **Enke D., Janowski F., Schwieger W.** Porous glasses in the 21st century – a short review // Microporous and Mesoporous Materials. 2003. Vol. 60. No. 1–3. Pp. 19–30.

2. **Elmer T. H., Nordberg M. E., Carrier G. B., Korda E. J.** Phase separation in borosilicate glasses as seen by electron microscopy and scanning electron microscopy // Journal of the American Ceramic Society. 1970. Vol. 53. No. 4. Pp. 171–175.

3. **Kikukawa T., Kuraoka K., Kawabe K., Yashida K., Hirao K., Yazawa T.** Preparation of an organic-inorganic hybrid ionic conductive material with thermal and chemical stability // Journal of the American Ceramic Society. 2004. Vol. 87. No. 3. Pp. 504–506.

4. **Yazawa T.**, **Miyamoto S., Yusa S., Jin T., Mineshige A.** Preparation of pH responsive porous glass by surface modification with COOH group // Materials Research Bulletin. 2013. Vol. 48. No. 10. Pp. 4267–4270.

5. **Dvoyashkin M.**, **Romanova E. E., Einicke W.-D., Gläser R., Kärger J., Valiulin R.** Diffusion of cyclohexane in native and surface-modified mesoporous glasses // Adsorption. 2011. Vol. 17. No. 1. Pp. 93–99.

6. **Sawada S., Nomura S., Asao Y.** Dielectric properties of ferroelectric $NaNO_2$ // Journal of the Physical Society of Japan. 1961. Vol. 16. No. 11. Pp. 2207–2212.

7. **Kay M. I.** The structure of sodium nitrite at 150°, 185°, 225°C // Ferroelectrics. 1972. Vol. 4. No. 1. Pp. 235–243.

8. **Ravindran P., Delin A., Johansson B., Ericsson O., Wills J. M.** Electronic structure, chemical bonding, and optical properties of ferroelectric and antiferroelectric $NaNO_2$ // Physical Review B. 1999. Vol. 59. No. 3. Pp. 1776–1785.

9. **Yamada Y., Shibuya I., Hoshino S.** Phase transition in $NaNO_2$ // Journal of the Physical Society of Japan. 1963. Vol. 18. No. 11. Pp. 1594–1603.

10. **Colla E. V., Koroleva E. Y., Kumzerov Yu. A., Savenko B. N.** Ferroelectric phase transitions in materials embedded in porous media // Ferroelectrics Letters Section. 1996. Vol. 20. No. 5–6. Pp. 143–147.

11. **Kinka M., Banys J., Naberezhnov A.** Dielectric properties of sodium nitrite confined in porous glass // Ferroelectrics. 2007. Vol. 348. No. 1. Pp. 67–74.

12. **Kutnjak Z., Vodopivec B., Blinc R., Fokin A. V., Kumzerov Y. A., Vakhrushev S. B.** Calorimetric and dielectric studies of ferroelectric sodium nitrite confined in a nanoscale porous glass matrix // Journal of Chemical Physics. 2005. Vol. 123. No. 8. P. 084708.

13. **Naberezhnov A., Fokin A., Kumzerov Yu., Sotnikov A., Vakhrushev S., Dorner B.** Structure and properties of confined sodium nitrite // The European Physical Journal E. 2003. Vol. 12. Supplement No. 1. Pp. 21–24.

14. **Golosovsky I. V., Smirnov O. P., Delaplane R. G., Wannberg A., Kibalin Y. A., Naberezhnov A., Vakhrushev S.** B. Atomic motion in Se nanoparticles embedded into a porous glass matrix // The European Physical Journal B. 2006. Vol. 54. No. 2. Pp. 211–216.

15. **Naberezhnov A. A., Borisov S. A., Fokin A. V., Islamov A. Kh., Kuklin A. I., Kumzerov Yu. A.** SANS studies of nanostructured low-melting metals at room temperature // Nanosystems: Physics, Chemistry, Mathematics. 2020. Vol. 11. No. 6. Pp. 690–697.

16. **Jonscher A. K.** Dielectric relaxation in solids // Journal of Physics D. 1999. Vol. 32. No. 14. Pp. R57–.

17. **Kremer F., Schönhals A.** (Eds.). Broadband dielectric spectroscopy. Berlin, Heidelberg: Springer, 2003. 729 p.

18. **Moré J. J.** The Levenberg – Marquardt algorithm: Implementation and theory // Numerical Analysis. Lecture notes in Mathematics. Vol. 630. Ed. by G. A. Watson. Berlin, Heidelberg: Springer, 1978. Pp. 105–116.

19. **Vakhrushev S. B., Kumzerov Yu. A., Fokin A., Naberezhnov A. A., B. Zalar, Lebar A., Blinc R.** ^{23}Na spin-lattice relaxation of sodium nitrite in confined geometry // Physical Review B. 2004. Vol. 70. No. 13. P. 132102.

20. **Naberezhnov A. A., Vakhrushev S. B., Kumzerov Yu. A., Fokin A. V.** Mechanism of ferroelectric phase transition in ultra-dispersed sodium nitrite particles // Ferroelectrics.

THE AUTHORS

MOLOKOV Anton Yu.
Ioffe Institute, RAS;
26 Polytekhnicheskaya St., St. Petersburg, 194021, Russia
antonmol@mail.ru
ORCID: 0000-0001-5254-3806

SYSOEVA Anna A.
Ioffe Institute, RAS
26 Polytekhnicheskaya St., St. Petersburg, 194021, Russia
annasysoeva07@mail.ru
ORCID: 0000-0002-8876-9185

NABEREZHNOV Aleksandr A.
Ioffe Institute, RAS
26 Polytekhnicheskaya St., St. Petersburg, 194021, Russia
alex.nabereznov@mail.ioffe.ru
ORCID: 0000-0003-1929-032X

KOROLEVA Ekaterina Yu.
Ioffe Institute, RAS;
Peter the Great St. Petersburg Polytechnic University
29 Politechnicheskaya St., St. Petersburg, 195251, Russia
e.yu.koroleva@mail.ioffe.ru
ORCID: 0000-0003-4370-5417

СВЕДЕНИЯ ОБ АВТОРАХ

МОЛОКОВ Антон Юрьевич – *лаборант лаборатории нейтронных исследований Физико-технического института имени А. Ф. Иоффе РАН.*
194021, Россия, г. Санкт-Петербург, Политехническая ул., 26
antonmol@mail.ru
ORCID: 0000-0001-5254-3806

СЫСОЕВА Анна Августовна – *научный сотрудник лаборатории нейтронных исследований Физико-технического института имени А. Ф. Иоффе РАН.*
194021, Россия, г. Санкт-Петербург, Политехническая ул., 26
annasysoeva07@mail.ru
ORCID: 0000-0002-8876-9185

НАБЕРЕЖНОВ Александр Алексеевич – *доктор физико-математических наук, старший научный сотрудник лаборатории нейтронных исследований Физико-технического института имени А. Ф. Иоффе РАН.*
194021, Россия, г. Санкт-Петербург, Политехническая ул., 26
alex.naberezn ov@mail.ioffe.ru
ORCID: 0000-0003-1929-032X

КОРОЛЕВА Екатерина Юрьевна – *кандидат физико-математических наук, старший научный сотрудник лаборатории нейтронных исследований Физико-технического института имени А. Ф. Иоффе РАН, старший научный сотрудник научно-образовательного центра «Физика нанокомпозитных материалов электронной техники Санкт-Петербургского политехнического университета Петра Великого.*
195251, Россия, г. Санкт-Петербург, Политехническая ул., 29
e.yu.koroleva@mail.ioffe.ru
ORCID: 0000-0003-4370-5417

Received 07.07.2022. Approved after reviewing 12.07.2022. Accepted 12.07.2022.
Статья поступила в редакцию 07.07.2022. Одобрена после рецензирования 12.07.2022. Принята 12.07.2022.

SIMULATION OF PHYSICAL PROCESSES

Original article
DOI: https://doi.org/10.18721/JPM.15303

COMPARATIVE EVALUATION OF RANS EDDY-VISCOSITY TURBULENCE MODELS FOR CALCULATING THE SILICON MELT CONVECTION IN CRYSTAL GROWTH SYSTEMS

D. V. Borisov✉, *V. V. Kalaev*

STR Group, Inc. – Soft-Impact, Ltd., St. Petersburg, Russia

✉ dmitriy.borisov@str-soft.com

Abstract. In the paper, the results of RANS calculations of turbulent convection in silicon melt, obtained using several eddy-viscosity turbulence models, have been compared with previously published ILES eddy-resolving calculation data for similar conditions. A turbulence model was chosen for its subsequent problem-oriented modification with the algebraic introduction of factors that could produce the required anisotropy of the Reynolds stress tensor and the turbulent heat flux vector including in the Reynolds-averaged equations of momentum and energy. As applied to the problems of calculating the convection in crystal growth furnace crucibles using the Czochralski method, it was shown the expediency of taking either the one-equation k-model or the two-equation k-ε model as the initial RANS-model for modification.

Keywords: Czochralski method, ILES, RANS, Reynolds stress tensor, turbulent heat transfer

Citation: Borisov D. V., Kalaev V. V., Comparative evaluation of RANS eddy-viscosity turbulence models for calculating the silicon melt convection in crystal growth systems, St. Petersburg Polytechnical State University Journal. Physics and Mathematics. 15 (3) (2022) 28–42. DOI: https://doi.org/10.18721/JPM.15303

Научная статья
УДК 532.5
DOI: https://doi.org/10.18721/JPM.15303

СРАВНИТЕЛЬНАЯ ОЦЕНКА RANS-МОДЕЛЕЙ ТУРБУЛЕНТНОСТИ С ИЗОТРОПНОЙ ВЯЗКОСТЬЮ ДЛЯ РАСЧЕТА КОНВЕКЦИИ РАСПЛАВА КРЕМНИЯ В УСТАНОВКАХ ВЫРАЩИВАНИЯ КРИСТАЛЛОВ

Д. В. Борисов✉, *В. В. Калаев*

АО «Группа СТР» – ООО «Софт-Импакт», Санкт-Петербург, Россия

✉ dmitriy.borisov@str-soft.com

Аннотация. В работе сопоставляются результаты RANS-расчетов турбулентной конвекции в расплаве кремния, полученные по нескольким моделям турбулентности с изотропной вязкостью, с ранее опубликованными данными вихреразрешающих ILES-вычислений для аналогичных условий. Выбирается модель турбулентности для ее последующей проблемно-ориентированной модификации с алгебраическим введением факторов, которые могут продуцировать нужную анизотропию тензора Рейнольдсовых напряжений и вектора турбулентного теплового потока, входящих в осредненные по Рейнольдсу уравнения движения и энергии. Показано, что применительно к задачам расчета конвекции в тиглях установок, где используют метод Чохральского, целесообразно взять для модификации либо однопараметрическую k-модель, либо двухпараметрическую k-ε модель в качестве исходной RANS-модели.

Ключевые слова: метод Чохральского, ILES, RANS, тензор Рейнольдсовых напряжений, турбулентный теплоперенос, конвекция

Ссылка для цитирования: Борисов Д. В., Калаев В. В. Сравнительная оценка RANS-моделей турбулентности с изотропной вязкостью для расчета конвекции расплава кремния в установках выращивания кристаллов // Научно-технические ведомости СПбГПУ. Физико-математические науки. 2022. Т. 15. № 3. С. 28–42. DOI: https://doi.org/10.18721/JPM.15303

Introduction

The Czochralski method is one of the main techniques for producing semiconductor silicon crystals, widely used in the electronics industry [1–3]. High-quality can be achieved in single crystals by controlling the mass transfer of impurities in the melt that are assimilated into the crystal during the growth process. As a rule, the flow of silicon melt is turbulent, which is due to the growing conditions even for crystals with a relatively small diameter (10 cm) in laboratory systems. The presence of turbulent structures with different sizes in crucibles for industrial growth of crystals of 20–30 cm in diameter makes it difficult to control the concentration of impurities; it can also trigger a transition from monocrystalline to polycrystalline growth [4]. Experimental studies into turbulent flow of silicon melt are hindered by both high temperatures of the processes and the requirements imposed on the precision of the equipment used to measure turbulent fluctuations. In view of this, numerical modeling seems to be the most promising method for studying turbulent flow and the processes of heat and mass transfer in silicon melt.

The most accurate method for computations of turbulent flows is direct numerical simulation (DNS), aimed at resolving all spatio-temporal scales of turbulence without resorting to additional hypotheses to close equations [2, 3]. However, this method requires significant computational resources, making it impossible to use in practical engineering calculations. The most popular and relatively economical approach is based on Reynolds-averaged Navier–Stokes equations (RANS), allowing, in particular, to perform computations in an axisymmetric formulation.

The k-ε turbulence model was adopted in [5] to numerically study the effect of crucible rotation on heat transfer in silicon melt based on the RANS approach. The computational results showed a general qualitative agreement with the experimental data. The computations in [6] were performed using a low-Reynolds-number k-ε model, finding, in particular, enhanced heat and mass transfer with an increase in the crucible rotation rate. Similar results could not be achieved with previous computations assuming laminar convection, which did not involve any turbulence model. The computed distributions for the melt temperature and the interface shape also yielded good agreement with the experimental data. Three turbulence models were tested in [7] to calculate turbulent convection in the melt: the 'standard' k-ε model using near-wall functions; the two-layer k-ε model combined with the one-equation model near solid boundaries; the Launder–Jones low-Reynolds-number k-ε model [8]. An apparent advantage detected for the third model was that it could to produce solutions close to laminar ones for weakened turbulence. Turbulent characteristics of silicon melt in an idealized cylindrical crucible were considered in [9] using the unsteady RANS (URANS) approach in a three-dimensional formulation. The computations adopted the Launder–Sharma k-ε model [10], as well as Menter's k-ω SST model [11, 12]. These URANS computations confirm the advantage of the SST model, providing the best resolution of the flow structure and near-wall temperature gradients, as well as generating more intense flow on the free surface of the melt.

Numerical modeling of silicon melt convection in industrial crucibles (by the Czochralski method) based on axisymmetric RANS formulation met with moderate success. However, a number of important characteristics of heat and mass transfer in the melt could not be reproduced within this approach. For example, to correctly model the thermal stresses and point defects in the crystal volume, it is necessary to accurately predict the shape of the crystallization front, which largely depends on the flow structure and heat transfer in the melt. For instance, the experimental and calculated curvatures of the interfaces obtained in [13–16] in simulations of heat transfer in the melt by the RANS approach differed by 2–3 times. The key reason for this discrepancy for crystals with a diameter of 100 mm is that RANS computations predict strong downward flow in the vicinity of the crucible's symmetry axis, which is not observed experimentally [17]. Modifications were introduced in [16] to the RANS turbulence model to more accurately predict the shape of the crystallization front in simulations of the growth processes for crystals 300 mm in diameter, produced by the Czochralski method. However, the authors specify that these modifications were introduced to artificially overcome the particular deficiency of the RANS turbulence model in the region below the crystal rather than improve the model itself.

Another important characteristic of convection in the silicon melt that affects the properties and quality of the crystal is the oxygen concentration in the melt. The results obtained in early attempts to use the RANS turbulence model to predict the level of oxygen concentration in a wide range of parameters controlling the operation of a Czochralski furnace were inconsistent with the experimental data [6, 18].

Most RANS models are based on the Boussinesq hypothesis assuming isotropic turbulent viscosity, and on the standard gradient diffusion hypothesis (SGDH) closing Reynolds-averaged equations for transport of temperature.

We investigated the local applicability of the Boussinesq and SGDH hypotheses to simulations of the Reynolds stress tensor and the turbulent heat flux vector in silicon melt in our previous study [19]. For this purpose, we used a specialized technique to process and analyze the results of computations based on the implicit eddy-resolving method (ILES). Furthermore, it was found that the strong anisotropy of the Reynolds stress tensor in the vicinity of the crucible wall, the crystallization interface and free surface of the melt is not reproduced by the Boussinesq hypothesis; the latter was exclusively designed to describe shear stresses. In addition, pronounced anisotropy of turbulent heat transfer near the free surface is also not described within the SGDH hypothesis.

The main objectives of this study are formulated as follows:

compare the results of RANS computations of turbulent convection in silicon melt, obtained by several turbulence models with isotropic viscosity, with the data obtained based on the ILES approach, published earlier in [19];

select RANS turbulence models for subsequent modification with adjustments introduced based on the data from ILES computations.

The results of RANS computations of conjugate heat transfer presented in this paper were obtained with the Flow Module software package, which is part of the CGSim code developed by the STR Group for simulation of heat and mass transfer during crystal growth by various methods [20].

We used the following low-Reynolds-number turbulence models: Wolfshtein k-model [21]; Chien k-ε model [22]; Menter k-ω SST model [11, 12].

Using the Flow Module and ANSYS Fluent packages for the Menter model, we also conducted cross-verification for a simplified problem, simulating turbulent convection in the melt only.

Mathematical model

Numerical modeling for growing silicon crystals by the Czochralski method includes turbulent convection and heat transfer in the melt and in inert gas (argon) circulated above the melt. Thermal conductivity is computed in quartz and graphite crucibles, as well as in silicon single crystal. The mathematical model based on the RANS approach incorporates steady-state equations for mass, momentum and temperature balance:

$$\nabla\cdot\left(\rho\overline{\mathbf{u}}\right)=0, \tag{1}$$

$$\nabla\cdot\left(\rho\overline{\mathbf{u}}\overline{\mathbf{u}}\right)=-\nabla\overline{p}+\nabla\cdot\left(\boldsymbol{\tau}-\rho\overline{\mathbf{u}'\mathbf{u}'}\right)+\left(\rho-\rho_0\right)\mathbf{g}, \tag{2}$$

$$\boldsymbol{\tau}=\mu\left(\nabla\overline{\mathbf{u}}+\left(\nabla\overline{\mathbf{u}}\right)^T\right)-\frac{2}{3}\mu\left(\nabla\cdot\overline{\mathbf{u}}\right)\mathbf{E}, \tag{3}$$

$$\nabla\cdot\left(\rho c_p\overline{\mathbf{u}T}\right)=\nabla\cdot\left(\lambda\nabla\overline{T}-\rho c_p\overline{\mathbf{u}'T'}\right), \tag{4}$$

$$\rho=\left[\begin{array}{l}\rho\left(T\right),\ \text{for melt or solid region}\\ \dfrac{p_0M}{R_gT},\ \text{for gas,}\end{array}\right. \tag{5}$$

Here ρ, ρ_0, kg/m^3, are the local and steady-state densities, respectively; **u,** m/s, is the velocity vector; p, p_0, Pa, are the local pressure and the gas pressure in the furnace, respectively; **g** is the gravitational acceleration; τ is the viscous stress tensor, **E** is the unit tensor; μ, Pa·s, is the dynamic viscosity; c_p, J/(kg·K), is the specific heat capacity at constant pressure; T, K, is the temperature, λ, W/(m·K), is the thermal conductivity; M, amu, is the molecular weight; R_g, J/(kmol·K), is the universal gas constant.

The overbar denotes Reynolds averaging of the quantity, the prime corresponds to a fluctuating component; $\overline{\mathbf{u}'\mathbf{u}'}$ and $\overline{\mathbf{u}'T'}$ denote the Reynolds stress tensor and the turbulent heat flux vector, respectively.

Turbulent transport of momentum and heat is simulated assuming turbulent eddy viscosity and SGDH:

$$\overline{\mathbf{u}'\mathbf{u}'}=\frac{2}{3}k\mathbf{E}-\nu_t\left(\nabla\overline{\mathbf{u}}+\left(\nabla\overline{\mathbf{u}}\right)^T-\frac{2}{3}\left(\nabla\cdot\overline{\mathbf{u}}\right)\mathbf{E}\right); \tag{6}$$

$$\overline{\mathbf{u}'T'}=-\frac{\nu_t}{\mathrm{Pr}_t}\nabla\overline{T}, \tag{7}$$

where ν_t, m^2/s, is the kinematic turbulent viscosity, determined in accordance with the turbulence model; Pr_t is the turbulent Prandtl number.

System of equations (1)–(5) is complemented with one or two equations for transport: turbulent kinetic energy k, m^2/s^2 (for all models used), dissipation rate ε, m^2/s^3 (for Chien's model) and specific dissipation rate ω, 1/s (for Menter's model).

According to the Wolfshtein and Chien models, turbulent viscosity is determined as follows:

$$\nu_t = C_\mu f_\mu \frac{k^2}{\varepsilon}, \tag{8}$$

where C_μ is the empirical constant, f_μ is the damping function.

According to Menter's SST model, turbulent viscosity is determined as

$$\nu_t = \frac{a_1 k}{\max\left(a_1\omega, SF_2\right)}, \tag{9}$$

where a_1 is the model constant; S, 1/s, is the magnitude of the strain rate tensor, F_2 is the model function introduced in [11].

Computational tools

Computations of turbulent heat transfer in the melt were carried out in the two-dimensional/axisymmetrical configuration of the Flow Module package. The finite volume method was used to discretize system of equations (1)–(5). The discretized equations were solved by the SIMPLEC algorithm. The convective terms of heat flux and velocity components were approximated by the QUICK scheme, and the turbulent kinetic energy and specific dissipation were computed using a first-order upwind scheme. Diffusion fluxes were computed with second-order accuracy.

A two-dimensional/axisymmetric version of the ANSYS Fluent software package was also used in benchmark computations for the simplified model problem presented below. The SIMPLEC algorithm was used to solve the discretized equations, the convective terms in the equations for velocity components and temperature were treated by the QUICK scheme, the convective terms in the equations for k and ω were computed by a first-order upwind scheme.

Model problem

The computational domain of the model problem only covered the region of the melt (Fig. 1). The crucible radius R_c = 170 mm, the crystal radius R_s = 50 mm, the melt height H = 97 mm.

The following boundary conditions were imposed: no slip on the crucible wall and the crystallization front; zero shear stress on the free surface of the melt; temperature dependence on the radius-to-depth ratio of the melt, obtained from the experimental values [17]. The crystallization front was taken at a constant temperature equal to the melting point of silicon; the free surface was considered adiabatic.

The properties of liquid silicon used in the computations are given in Table 1. The model problem was solved without accounting for the Marangoni effect. The rotational speeds of the crucible wall ω_c and the crystal wall ω_s amounted to 5 and 20 rpm, respectively (see Fig. 1).

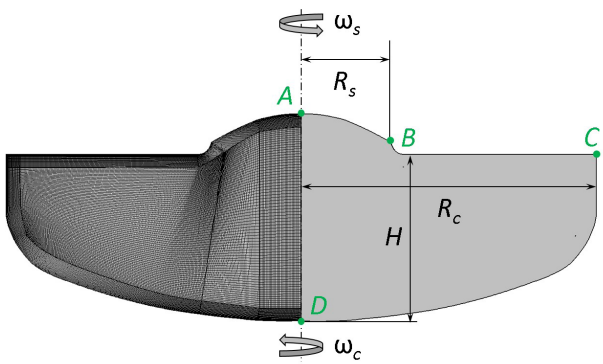

Fig. 1. Computational domain (right) and mesh (left) of the model problem:
AB is the melt/crystal interface; *BC*, *CD* are the melt/gas (free) and melt/crucible interfaces;
DA is the axis of symmetry; R_c, R_s are the melt and crystal radii, respectively; H is the melt height;
ω_c, ω_s are the angular velocities of crucible and crystal rotation, respectively

The computational mesh contained about 72,000 cells, the size of the first near-surface cell was about 0.12 mm, the size of the cell in the volume was about 1.8 mm. The dimensionless coordinate y^+ in the first near-wall cell did not exceed unity.

Fig. 2 shows a comparison of the radial temperature distributions, velocity components and turbulent viscosity for melt depths of 1 and 3 cm, obtained using Flow Module and ANSYS Fluent. Evidently, the results obtained in both packages are in good agreement. Small differences can be observed in the distributions of the axial and radial velocity components in the vicinity of the symmetry axis, which can be due to different approximations of the terms inversely proportional to the radial coordinate; the terms appear in the equation for balance of momentum written in cylindrical coordinates.

Table 1

Parameter values of liquid silicon used in the computations

Parameter	Notation	Unit	Value
Density	ρ	kg/m^3	$3{,}194–0.3701\cdot T$
Equilibrium density	ρ_0	kg/m^3	2,570
Thermal conductivity	λ	W/(m·K)	66.5
Heat capacity	c_p	J/(kg·K)	915
Dynamic viscosity	μ	Pa·s	$8\cdot10^{-4}$
Melting temperature	T_m	K	1,685
Marangoni coefficient	$\partial\sigma/\partial T$	N/(m·K)	$-1\cdot10^{-4}$
Emissivity factor	ε_{rad}	–	0.3

Note. The data given in the last two rows will be used below.

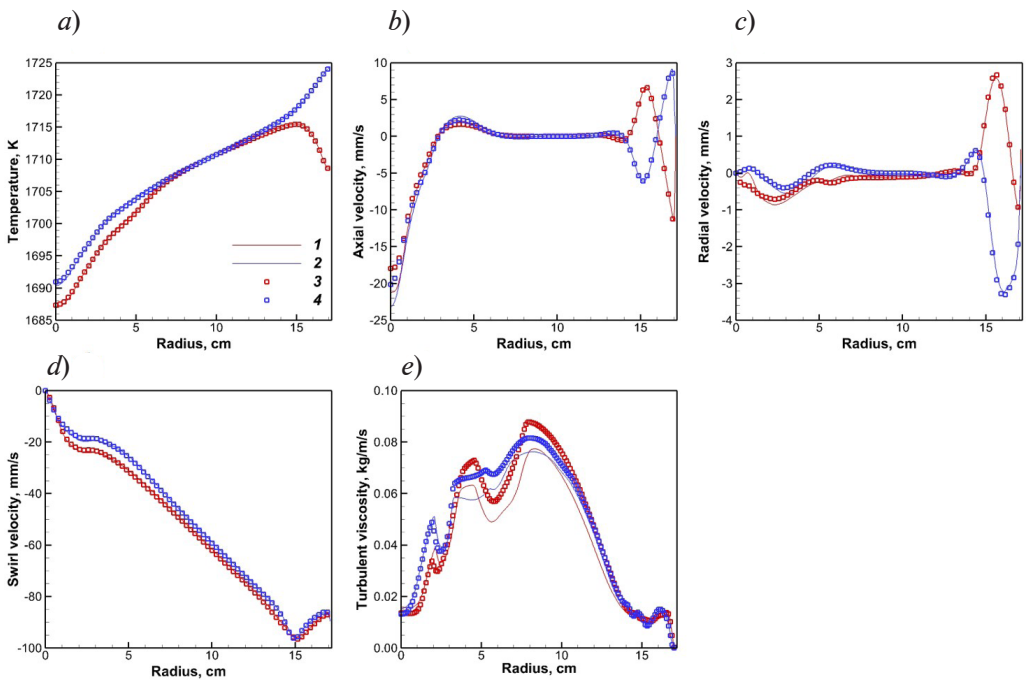

Fig. 2. Comparison of radial temperature distributions (*a*); axial (*b*), radial (*c*), circumferential (*d*) velocity components, and turbulent viscosity (*e*) computed at different melt depths: 1 cm (*1*, *3*) and 3 cm (*2*, *4*), using ANSYS Fluent (*1*, *2*) and Flow Module (*3*, *4*)

Fig. 3 compares the heat flux density distributions along the crucible wall obtained with the Flow Module and ANSYS Fluent packages. The difference between the distributions increases as it approaches the symmetry axis, which may due to the differences in the flow structure. Despite the slight discrepancy between the results obtained by both codes, we can conclude that the Menter model is implemented correctly in the Flow Module package.

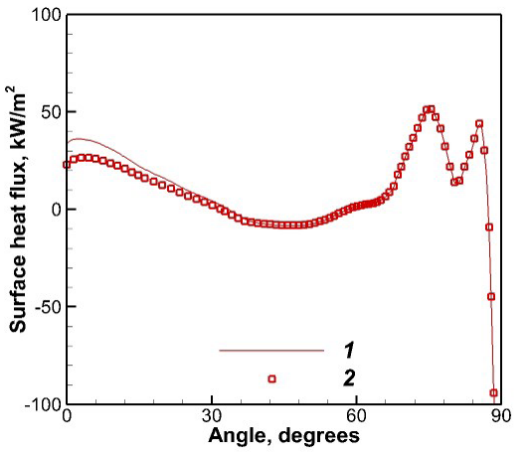

Fig. 3. Heat flux density distributions along the crucible obtained with ANSYS Fluent (*1*) and Flow Module (*2*)

Statement of the conjugate problem

The computational domain of the conjugate problem, formulated based on the data for the EKZ-1300 system [23], includes the melt, the crystal, the quartz and graphite crucibles, as well as a part of the gas region above the melt. The scheme of the computational domain is shown in Fig. 4. The crucible radius R_c = 170 mm, the crystal radius R_s = 50 mm, the melt height H = 97 mm.

The following boundary conditions are imposed: no slip at the melt/crucible and melt/crystal

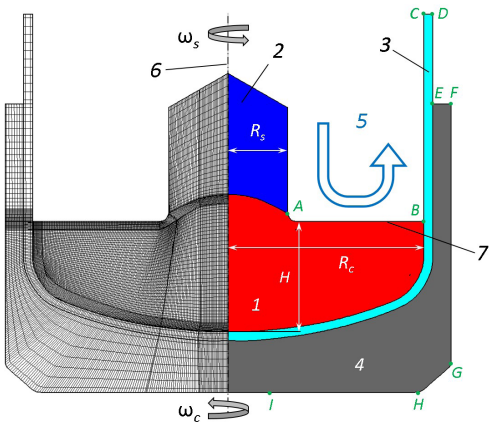

Fig. 4. Schemes of computational domain (right) and mesh (left) for the conjugate problem: melt *1*; crystal *2*; quartz and graphite crucibles *3* and *4*, respectively; argon flow *5*; symmetry axis *6*; free surface *7* (the remaining notations are the same as in Fig. 1)

interfaces, zero outlet pressure at the outlet boundary.

The boundary condition on the free surface of the melt takes into account the thermocapillary Marangoni effect:

$$\left(\mu\frac{\partial u_\tau}{\partial n}\right)_{melt} = \left(\mu\frac{\partial u_\tau}{\partial n}\right)_{gas} + \frac{\partial\sigma}{\partial T}\frac{\partial T}{\partial\tau}, \tag{10}$$

τ corresponds to the direction tangential to the free surface, and n to the normal; the subscripts *melt* and *gas* denote the melt and the gas, respectively.

The crystallization front is maintained at a constant temperature equal to the melting point of silicon.

The following condition is imposed at the outer boundaries:

$$\left(\lambda \frac{\partial T}{\partial n}\right)_{ext} = \left(\lambda \frac{\partial T}{\partial n}\right)_{gas} + \sigma_{SB}\varepsilon_{rad}T_{ext}^4 - Q_{rad}^{in}, \tag{11}$$

where σ_{SB} is the Stefan–Boltzmann constant; ε_{rad} is the emissivity Q^{in}_{rad} is the incident radiant heat flux obtained from the solution to the problem on global heat transfer for the EKZ-1300 system (Fig. 5); the subscript *ext* corresponds to the outer boundary, the subscript *gas* to the adjacent gas region.

A constant gas flow rate $v = 0.66$ m/s is given at the inlet boundary. The rotation rates of the crucible, ω_c, and the crystal, ω_s, amounted to 5 and 20 rpm, respectively (see Fig. 1). The properties of the materials used in the computations are given in Table 2.

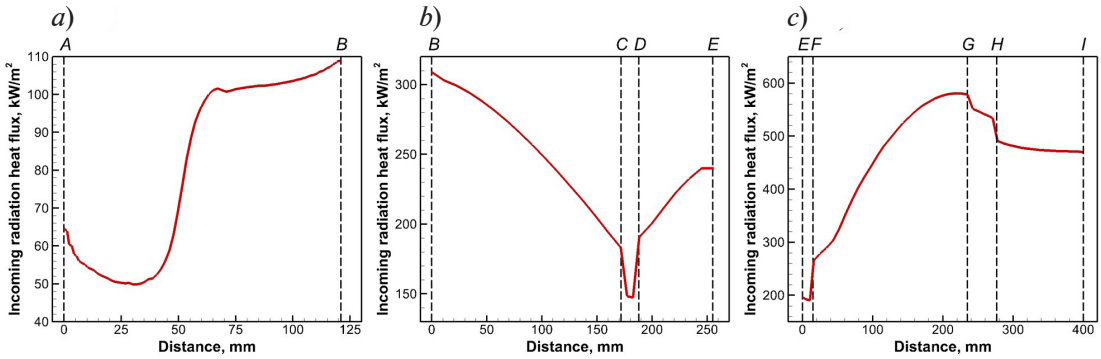

Fig. 5. Distributions of incident radiant heat flux along the free surface (*a*), along the quartz (*b*) and graphite (*c*) crucibles
Vertical dashes highlight the behavior of the curves specific to each type of crucible (see Fig. 4)

Table 2

Characteristics of substances used in the computations for the conjugate problem

Substance	Parameter value			
	ρ kg/m³	λ, W/(m·K)	c_p, J/(kg·K)	ε_{rad}
Solid silicon	2330	$44–0.0138\cdot T$	$687–0.236\cdot T$	$0.9016–0.00026208\cdot T$
Quartz	2650	4	1,232	0.85
Graphite	2000	$70.7–0.0191\cdot T$	2,019	0.80
Argon	$\frac{p_0 M}{R_g T}$	$0.01–2.5\cdot 10^{-5}\,T$	532	–
	$\mu = 8.466\cdot 10^{-6} + 5.365\cdot 10^{-6}\cdot T - 8.682\cdot 10^{-12}T^2$ Pa·s; $\rho_0 = 0.01$ kg/m³; $p_0 = 3000$ Pa; $M = 40$ AU			

Note. The properties of liquid silicon are given above in Table 1.

Notations: p_0 is the gas pressure in the furnace; M is the molecular weight; the rest correspond to those given in Table 1.

The governing parameters of this problem were the Prandtl number Pr, the Grashof number Gr, the Rayleigh number Ra, the rotational Reynolds numbers Re_c (crucible) and Re_s (crystal), the Marangoni number Ma, and the number DN characterizing the influence of shear stress in gas on the melt flow along the free surface. They are defined as follows:

$$\mathrm{Pr} = \frac{\mu c_p}{\lambda} = 1.1 \cdot 10^{-2}, \tag{12}$$

$$\mathrm{Gr} = \frac{g\beta \Delta T_{bulk} H^3}{\nu^2} = 3.4 \cdot 10^8, \tag{13}$$

$$\mathrm{Ra} = \mathrm{Gr} \cdot \mathrm{Pr} = 3.7 \cdot 10^6, \tag{14}$$

$$\mathrm{Re}_c = \frac{\omega_c R_c^2}{\nu} = 4.9 \cdot 10^4, \tag{15}$$

$$\mathrm{Re}_s = \frac{\omega_s R_s^2}{\nu} = 1.7 \cdot 10^4, \tag{16}$$

$$\mathrm{Ma} = -\frac{\partial \sigma}{\partial T} \frac{H^2 \Delta T_{fs}}{L \mu a} = 6.7 \cdot 10^3, \tag{17}$$

$$\mathrm{DN} = \frac{\langle \tau_g \rangle H^2 \rho}{\mu^2} = 2.6 \cdot 10^6. \tag{18}$$

Here ΔT_{bulk} = 25.2 K is the temperature difference between the point where the crystallization front intersects the symmetry axis and the point where melt/crucible interface intersects the symmetry axis; ν, m^2/s, is the kinematic viscosity, $\nu = \mu/\rho$; ΔT_{fs} = 19.3 K is the temperature difference between the triple points corresponding to melt/gas/crystal and melt/gas/crucible; L, m, is the characteristic length of the free surface, $L = R_c - R_s$; a, m^2/s, is the thermal conductivity, $a = \nu/\mathrm{Pr}$; $\langle \tau_g \rangle$, Pa, is the average value of the gas shear stress along the free surface.

Computations were carried out on three meshes (using the Wolfshtein model) to study mesh sensitivity. The basic mesh contained about 20,000 cells, the size of the first near-surface cell was about 0.3 mm, the size of the cell in the melt was about 3.6 mm (see Fig 4). The coarse and the refined mesh were obtained by decreasing and increasing the number of cells by 2 times in each direction in the melt and by 1–2 times in the remaining blocks.

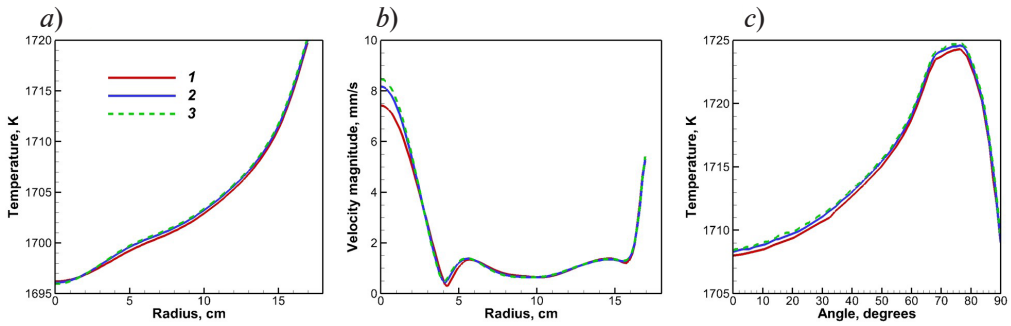

Fig. 6. Comparison of radial temperature profiles (*a*) and the magnitude of the meridional velocity component (*b*) at a depth of 2 cm from the free surface of the melt with an angular temperature distribution along the melt/crucible interface (*c*). The results obtained with coarse (*1*), basic (*2*) and refined (*3*) meshes are also compared.
Angles of 0° and 90° correspond to the points where the crucible wall intersects with the symmetry axis and the free surface of the melt, respectively

Computational results for conjugate problem

Fig. 6 shows the radial temperature profiles, the magnitude of the meridional velocity component at a depth of 2 cm from the free surface of the melt, as well as the temperature distribution along the melt/crucible interface, obtained in computations on three meshes. As can be seen from the distributions, the differences between the results obtained on the basic and the refined mesh are smaller than when between the results obtained on the coarse and the basic mesh, so we mesh convergence can be established for the computations performed. Due to the small difference between the solutions obtained on the basic and refined mesh, subsequent computations were carried out on the basic mesh.

Fig. 7 compares the temperature fields, the magnitude of the meridional velocity component, as well as the velocity vectors obtained by the ILES and RANS approaches. The temperature difference closest to the ILES data is predicted by the Wolfshtein model, while the Chien model predicts an underestimated difference, and the Menter model an overestimated one. The vortical structure in the vicinity of the crucible's vertical wall, clearly manifested in the ILES solution, is also reproduced by the models of Wolfshtein and Menter, while the Chen model predicts a different flow structure: with relatively low velocities at the edges of the melt.

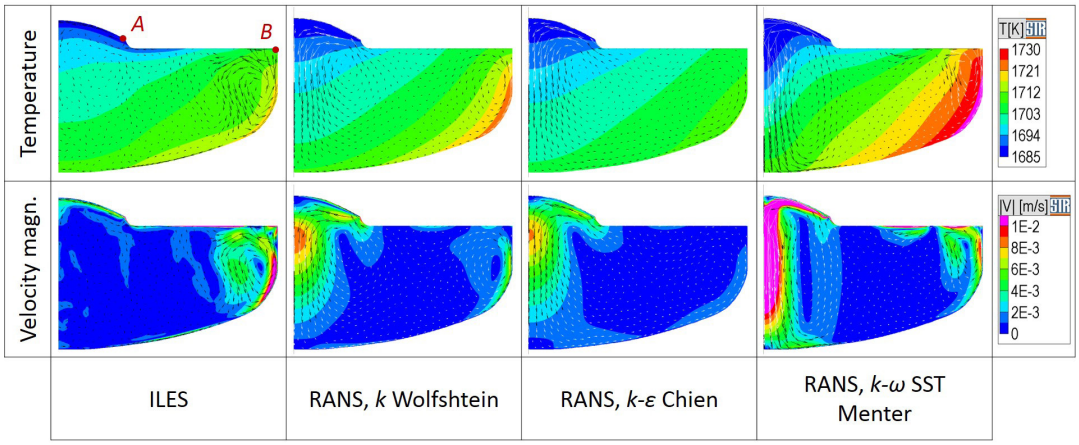

Fig. 7. Distributions of temperature (top row), magnitude of the meridional velocity component (bottom row) over the melt; vector velocity fields (marked by arrows), obtained by ILES and RANS computations based on the Wolfshtein, Chien and Menter models (from left to right)

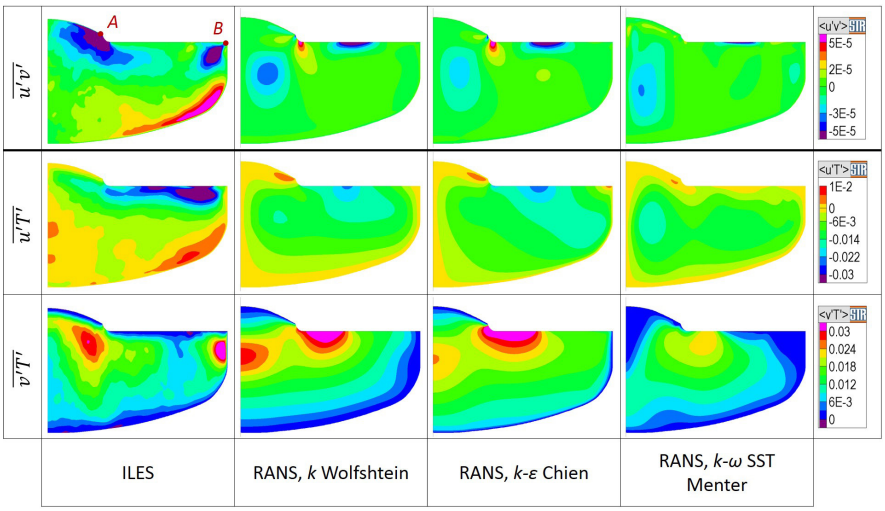

Fig. 8. Distributions of shear component $\overline{u'v'}$ of Reynolds stress tensor (top row) and components of turbulent heat flux vector (middle and bottom rows) obtained in ILES and RANS computations based on the Wolfshtein, Chien and Menter models (from left to right)

It should be noted that all turbulence models considered predict a pronounced downward flow of the melt in the vicinity of the symmetry axis, which contradicts the results of ILES computations, where high melt velocities are not observed under the crystal. The strongest downward flow is predicted by the Menter model, which also gives the lowest level of turbulent viscosity.

Fig. 8, *a* shows a comparison of the shear component $\overline{u'v'}$ of the Reynolds stress tensor obtained by ILES and RANS computations. Here u' corresponds to radial fluctuations of velocity and v' to the axial ones. Qualitative disagreement can be observed in the distributions of components $\overline{u'v'}$ predicted by ILES and RANS approaches. The highest absolute values in ILES computations $\overline{u'v'}$ are observed in the vicinity of the meniscus, near the gas/crucible/melt triple point and near the rounded part of the crucible wall. As established in [19], this feature is associated with the anisotropy of velocity fluctuations, which consists in stronger damping of normal fluctuations, compared with longitudinal fluctuations near the solid wall, as well as damping of only normal fluctuations at a free surface.

Thus, the reason for the qualitative difference in the distributions of the component $\overline{u'v'}$ in ILES and RANS computations is that the eddy viscosity assumption does not include a factor producing surface anisotropy.

Fig. 8,*b* compares the components of the turbulent heat flux vector. The ILES approach predicts the drop in the component $\overline{v'T'}$ near the horizontal part of the free surface, while high negative values are observed for the the component $\overline{u'T'}$. The average level of turbulent heat flux is consistent in ILES and RANS computations. If special modifications accounting for the effect of the free surface on turbulence are not introduced, the level of turbulent viscosity obtained on the free surface is of the same order of magnitude as in the volume of the melt. This, in turn, produces high values of both the horizontal and vertical components of the flow, which contradicts the results of ILES computations predicting pronounced anisotropy of heat transfer and attributing the decrease in the values of the component $\overline{v'T'}$ to damping of normal velocity fluctuations.

Conclusion

The results of RANS computations of turbulent convection in silicon melt obtained by several turbulence models with isotropic viscosity were compared with the data for ILES computations carried out for similar conditions.

In what concerns the temperature distributions the models of isotropic turbulent viscosity reflect the heat transfer characteristics in the melt of Czochralski furnaces for growing crystals. However, isotropic viscosity models cannot correctly account for the details of heat and mass transfer in the melt that are important for studying the influence of growth parameters in order to optimize the growing process. At the same time, we can conclude that models with two differential equations for predicting the flow structure and temperature field do not offer any advantages compared to the model with only one equation. The strongest differences in the predictions of the three RANS models for the convection structure compared to the ILES data are observed for the k-ω SST-model.

The disadvantages of RANS models with isotropic viscosity can be overcome by using models of Reynolds stress transfer, requiring to additionally solve several substantially nonlinear differential equations. However, this can lead to numerical difficulties in obtaining a steady-state solution [24]. Another approach is problem-oriented modification of the initial models of isotropic viscosity, algebraically introducing factors that, as we established in [25], can produce the required anisotropy of the Reynolds stress tensor and the turbulent heat flux vector included in the Reynolds-averaged equations of motion and energy. Comparing the results of RANS and ILES computations presented in this paper, we can conclude that either a one-parameter k-model or a two-parameter k-ε model is preferable as the initial RANS model for modification in problems dedicated to simulation of convection in the crucibles of Czochralski furnaces.

REFERENCES

1. **Vegad M., Bhatt N. M.,** Review of some aspects of single crystal growth using Czochralski crystal growth technique, Procedia Technol. 14 (2nd Int. Conf. on Innovations in Automation and Mechatronics Engin. (ICIAME 2014)) (2014) 438–446.

2. **Wagner C., Friedrich R.,** Direct numerical simulation of momentum and heat transport in idealized Czochralski crystal growth configurations, Int. J. Heat & Fluid Flow. 25 (3) (2004) 431–443.

3. **Raufeisen A., Breuer M., Botsch T., Delgado A.,** DNS of rotating buoyancy- and surface tension-driven flow, // Int. J. Heat & Mass Transfer. 51 (25–26) (2008) 6219–6234.

4. **Gräbner O., Mühe A., Müller G., et al.,** Analysis of turbulent flow in silicon melts by optical temperature measurement, Mater. Sci. Eng. B. 73 (1–3) (2000) 130–133.

5. **Kobayashi S., Miyahara S., Fujiwara T., et al.,** Turbulent heat transfer through the melt in silicon Czochralski growth, J. Cryst. Growth. 109 (1–4) (1991) 149–154.

6. **Kinney T. A., Brown R. A.,** Application of turbulence modeling to the integrated hydrodynamic thermal-capillary model of Czochralski crystal growth of silicon, J. Cryst. Growth. 132 (3–4) (1993) 551–574.

7. **Lipchin A., Brown R. A.,** Comparison of three turbulence models for simulation of melt convection in Czochralski crystal growth of silicon, J. Cryst. Growth. 205 (1–2) (1999) 71–91.

8. **Jones W. P., Launder B. E.,** The prediction of laminarization with a two-equation model of turbulence, Int. J. Heat & Mass Transfer. 15 (2) (1972) 301–314.

9. **Verma S., Dewan A.,** Thermofluid characteristics of Czochralski melt convection using 3D URANS computations, ASME J. Therm. Sci. Eng. Appl. 11 (6) (2019) 061017.

10. **Launder B. E., Sharma B. I.,** Application of the energy-dissipation model of turbulence to the calculation of flow near a spinning disc, Lett. Heat & Mass Transfer. 1 (2) (1974) 131–137.

11. **Menter F. R.** Zonal two equation k-ω turbulence models for aerodynamic flows, Proc. 24th Fluid Dynamics Conf., July 6 – 9, 1993, Orlando, Florida, USA, American Institute of Aeronautics & Astronautics (AIAA), 1993. Paper 1993–2906.

12. **Menter F. R., Kuntz M., Langtry R.,** Ten years of industrial experience with the SST turbulence model, In book: "Turbulence, Heat and Mass Transfer 4". Proc. Symp. on Turbulence, Heat & Mass Transfer. 12–17 Oct., 2003, Antalya, Turkey. Ed. by Hanjalić K., Nagano Y., Tummers M. J., Book Ser. Turbulence, Heat & Mass Transfer. Vol. 4, Begell House Inc., USA (2003) 625–632.

13. **Lipchin A., Brown R. A.,** Hybrid finite-volume/finite-element simulation of heat transfer and melt turbulence in Czochralski crystal growth of silicon, J. Cryst. Growth. 216 (1–4) (2000) 192–203.

14. **Kalaev V. V., Lukanin D. P., Zabelin V. A., et al.,** Prediction of bulk defects in CZ Si crystals using 3D unsteady calculations of melt convection, Mater. Sci. Semicond. Proc. 5 (4–5) (2002) 369–373.

15. **Kalaev V. V., Lukanin D. P, Zabelin V. A., et al.,** Calculation of bulk defects in CZ Si growth impact of melt turbulent fluctuations, J. Cryst. Growth. 250 (1–2) (2003) 203–208.

16. **Wetzel T., Virbulis J., Muiznieks A., et al.,** Prediction of the growth interface shape in industrial 300 mm CZ Si crystal growth, J. Cryst. Growth. 266 (1–3) (2004) 34–39.

17. **Gräbner O., Müller G., Virbulis J., et al.,** Effects of various magnetic field configurations on temperature distributions in Czochralski silicon melts, Microelectr. Eng. 56 (1–2) (2001) 83–88.

18. **Müller G, Mühe A., Backofen R., et al.,** Study of oxygen transport in Czochralski growth of silicon, Microelectr. Eng. 1999. Vol. 45 (2–3) (1999) 135–147.

19. **Borisov D. V., Kalaev V. V.,** ILES of melt turbulent convection with conjugated heat transfer in the crucible and gas flow for Czochralski silicon crystal growth system, J. Cryst. Growth. 573 (1 November) (2021) 126305.

20. Software package CGSim [Electronic resource]. URL: http://www.str-soft.com/products/CGSim/ (Last accessed date: March 29, 2022).

21. **Wolfshtein M.,** The velocity and temperature distribution in one-dimensional flow with turbulence augmentation and pressure gradient, Int. J. Heat & Mass Transfer. 12 (3) (1969) 301–318.

22. **Chien K.-Y.,** Predictions of channel and boundary-layer flows with a low-Reynolds number turbulence model, AIAA J. 20 (1) (1982) 33–38.

23. **Kalaev V., Sattler A., Kadinski L.,** Crystal twisting in Cz Si growth, J. Cryst. Growth. 413 (1 March) (2015) 12–16.

24. **Ristorcelli J. R., Lumley J. L.,** A second-order turbulence simulation of the Czochralski crystal growth melt: the buoyantly driven flow, J. Cryst. Growth. 129 (1–2) (1993) 249–265.

25. **Kalaev V., Borisov D., Smirnov A.,** A modified hypothesis of Reynolds stress tensor modeling for mixed turbulent convection in crystal growth, J. Cryst. Growth. 580 (15 February) (2022) 126464.

СПИСОК ЛИТЕРАТУРЫ

1. **Vegad M., Bhatt N. M.** Review of some aspects of single crystal growth using Czochralski crystal growth technique // Procedia Technology. 2014. Vol. 14. 2nd International Conference on Innovations in Automation and Mechatronics Engineering (ICIAME 2014). Pp. 438–446.

2. **Wagner C., Friedrich R.** Direct numerical simulation of momentum and heat transport in idealized Czochralski crystal growth configurations // International Journal of Heat and Fluid Flow. 2004. Vol. 25. No. 3. Pp. 431–443.

3. **Raufeisen A., Breuer M., Botsch T., Delgado A.** DNS of rotating buoyancy- and surface tension-driven flow // International Journal of Heat and Mass Transfer. 2008. Vol. 51. No. 25–26. Pp. 6219–6234.

4. **Gräbner O., Mühe A., Müller G., Tomzig E., Virbulis J., Ammon W. V.** Analysis of turbulent flow in silicon melts by optical temperature measurement // Materials Science and Engineering. B. 2000. Vol. 73. No. 1–3 Pp. 130–133.

5. **Kobayashi S., Miyahara S., Fujiwara T., Kubo T., Fujiwara H.** Turbulent heat transfer through the melt in silicon Czochralski growth // Journal of Crystal Growth. 1991. Vol. 109. No. 1–4. Pp. 149–154.

6. **Kinney T. A., Brown R. A.** Application of turbulence modeling to the integrated hydrodynamic thermal-capillary model of Czochralski crystal growth of silicon // Journal of Crystal Growth. 1993. Vol. 132. No. 3–4. Pp. 551–574.

7. **Lipchin A., Brown R. A.** Comparison of three turbulence models for simulation of melt convection in Czochralski crystal growth of silicon // Journal of Crystal Growth. 1999. Vol. 205. No. 1–2. Pp. 71–91.

8. **Jones W. P., Launder B. E.** The prediction of laminarization with a two-equation model of turbulence // International Journal of Heat and Mass Transfer. 1972. Vol. 15. No. 2. Pp. 301–314.

9. **Verma S., Dewan A**. Thermofluid characteristics of Czochralski melt convection using 3D URANS computations // ASME Journal of Thermal Science and Engineering Applications. 2019. Vol. 11. No. 6. P. 061017.

10. **Launder B. E., Sharma B. I.** Application of the energy-dissipation model of turbulence to the calculation of flow near a spinning disc // Letters in Heat and Mass Transfer. 1974. Vol. 1. No. 2. Pp. 131–137.

11. **Menter F. R.** Zonal two equation k-ω turbulence models for aerodynamic flows // Proceedings of the 24th Fluid Dynamics Conference. July 6 – 9, 1993, Orlando, Florida, USA. American Institute of Aeronautics & Astronautics (AIAA). 1993. Paper 1993–2906.

12. **Menter F. R., Kuntz M., Langtry R.** Ten years of industrial experience with the SST turbulence model // "Turbulence, Heat and Mass Transfer 4". Proceedings of the Symposium on Turbulence, Heat and Mass Transfer. 12 – 17 October, 2003. Antalya, Turkey. Ed. by Hanjalić K., Nagano Y., Tummers M. J. Book Series: Turbulence, Heat and Mass Transfer. Vol. 4. USA: Begell House Inc., 2003. Pp. 625–632.

13. **Lipchin A., Brown R. A.** Hybrid finite-volume/finite-element simulation of heat transfer and melt turbulence in Czochralski crystal growth of silicon // Journal of Crystal Growth. 2000. Vol. 216. No. 1–4. Pp. 192–203.

14. **Kalaev V. V., Lukanin D. P., Zabelin V. A., Makarov Y. N., Virbulis J., Dornberger E., Ammon W. V**. Prediction of bulk defects in CZ Si crystals using 3D unsteady calculations of melt convection // Materials Science in Semiconductor Processing. 2002. Vol. 5. No. 4–5. Pp. 369–373.

15. **Kalaev V. V., Lukanin D. P, Zabelin V. A., Makarov Y. N., Virbulis J., Dornberger E., Ammon W. V.** Calculation of bulk defects in CZ Si growth impact of melt turbulent fluctuations // Journal of Crystal Growth. 2003. Vol. 250. No. 1–2. Pp. 203–208.

16. **Wetzel T., Virbulis J., Muiznieks A., Ammon W. V., Tomzig E., Raming G., Weber M.** Prediction of the growth interface shape in industrial 300 mm CZ Si crystal growth // Journal of Crystal Growth. 2004. Vol. 266. No. 1–3. Pp. 34–39.

17. **Gräbner O., Müller G., Virbulis J., Tomzig E., Ammon W. V.** Effects of various magnetic field configurations on temperature distributions in Czochralski silicon melts // Microelectronic Engineering. 2001. Vol. 56. No. 1–2. Pp. 83–88.

18. **Müller G, Mühe A., Backofen R., Tomzig E., Ammon W. V**. Study of oxygen transport in Czochralski growth of silicon // Microelectronic Engineering. 1999. Vol. 45. No. 2–3. Pp. 135–147.

19. **Borisov D. V., Kalaev V. V.** ILES of melt turbulent convection with conjugated heat transfer in the crucible and gas flow for Czochralski silicon crystal growth system // Journal of Crystal Growth. 2021. Vol. 573. 1 November. P. 126305.

20. Программный пакет CGSim [Электронный ресурс]. URL: http://www.str-soft.com/products/CGSim/ (Дата обращения: 29.03.2022).

21. **Wolfshtein M.** The velocity and temperature distribution in one-dimensional flow with turbulence augmentation and pressure gradient // International Journal of Heat and Mass Transfer. 1969. Vol. 12. No. 3. Pp. 301–318.

22. **Chien K.-Y.** Predictions of channel and boundary-layer flows with a low-Reynolds number turbulence model // American Institute of Aeronautics & Astronautics (AIAA) Journal. 1982. Vol. 20. No. 1. Pp. 33–38.

23. **Kalaev V., Sattler A., Kadinski L.** Crystal twisting in Cz Si growth // Journal of Crystal Growth. 2015. Vol. 413. 1 March. Pp. 12–16.

24. **Ristorcelli J. R., Lumley J. L.** A second-order turbulence simulation of the Czochralski crystal growth melt: the buoyantly driven flow // Journal of Crystal Growth.1993. Vol. 129. No. 1–2. Pp. 249–265.

25. **Kalaev V., Borisov D., Smirnov A.** A modified hypothesis of Reynolds stress tensor modeling for mixed turbulent convection in crystal growth // Journal of Crystal Growth. 2022. Vol. 580. 15 February. P. 126464.

THE AUTHORS

BORISOV Dmitry V.
STR Group, Inc. – Soft-Impact, Ltd.
64, Bolshoi Sampsonievskii Ave., St. Petersburg, 194044, Russia
dmitriy.borisov@str-soft.com
ORCID: 0000-0002-7481-8265

KALAEV Vladimir V.
STR Group, Inc. - Soft-Impact, Ltd.
64, Bolshoi Sampsonievskii Ave., St. Petersburg, 194044, Russia
vladimir.kalaev@str-soft.com
ORCID: 0000-0001-9231-0740

СВЕДЕНИЯ ОБ АВТОРАХ

БОРИСОВ Дмитрий Витальевич – *инженер-программист АО «Группа СТР» – ООО «Софт-Импакт».*
194044, Россия, г. Санкт-Петербург, Большой Сампсониевский пр., 64
dmitriy.borisov@str-soft.com
ORCID: 0000-0002-7481-8265

КАЛАЕВ Владимир Владимирович – *кандидат физико-математических наук, технический директор АО «Группа СТР» – ООО «Софт-Импакт».*
194044, Россия, г. Санкт-Петербург, Большой Сампсониевский пр., 64
vladimir.kalaev@str-soft.com
ORCID: 0000-0001-9231-0740

Received 29.03.2022. Approved after reviewing 30.05.2022. Accepted 30.05.2022.
Статья поступила в редакцию 29.03.2022. Одобрена после рецензирования 30.05.2022. Принята 30.05.2022.

Original article
DOI: https://doi.org/10.18721/JPM.15304

EXPERIENCE OF USING SEMIEMPIRICAL DIFFERENTIAL MODELS OF TURBULENCE FOR CALCULATION OF LIQUID-METAL CONVECTION IN A BOTTOM HEATED CYLINDER

S. I. Smirnov✉, *E. M. Smirnov*

Peter the Great St. Petersburg Polytechnic University, St. Petersburg, Russian Federation

✉ sergeysmirnov92@mail.ru

Abstract. The paper deals with assessments of ability of the three RANS turbulence models (k-ω SST, k-ε RNG and one of the differential RSM formulations) to predict local and integral characteristics of the statistically 3D Rayleigh – Bénard liquid-metal convection with a key role of large-scale circulation (LSC). URANS-based calculations at the Rayleigh number of 10^6 and the Prandtl number of 0.025 have been performed for a bottom heated cylindrical container with equal diameter to height, using computational grids of varied cell sizes. The case of the slightly tilted container was considered where the LSC azimuth position being fixed. The suitability of the used turbulence models was evaluated by comparing the obtained results with the direct numerical simulation data obtained earlier for the same conditions.

Keywords: Rayleigh – Bénard convection, large scale circulation, RANS model, turbulence, cylinder

Funding: The research has been funded in part by the Ministry of Science and Higher Education of the Russian Federation, within the framework of strategic academic leadership "Priority 2030" (Agreement No. 075-15-2021-1333 dated September 30, 2021)

Citation: Smirnov S. I., Smirnov E. M., Experience of using semiempirical differential models of turbulence for calculation of liquid-metal convection in a bottom heated cylinder, St. Petersburg Polytechnical State University Journal. Physics and Mathematics. 15 (3) (2022) 43–60. DOI: https://doi.org/10.18721/JPM.15304

Научная статья
УДК 536.25
DOI: https://doi.org/10.18721/JPM.15304

ОПЫТ ПРИМЕНЕНИЯ ПОЛУЭМПИРИЧЕСКИХ ДИФФЕРЕНЦИАЛЬНЫХ МОДЕЛЕЙ ТУРБУЛЕНТНОСТИ ДЛЯ РАСЧЕТА КОНВЕКЦИИ ЖИДКОГО МЕТАЛЛА В ПОДОГРЕВАЕМОМ СНИЗУ ЦИЛИНДРЕ

С. И. Смирнов✉, *Е. М. Смирнов*

Санкт-Петербургский политехнический университет Петра Великого,

Санкт-Петербург, Россия

✉ sergeysmirnov92@mail.ru

Аннотация. Статья содержит оценку возможностей трех известных RANS-моделей турбулентности (k-ω SST, k-ε RNG и одной из дифференциальных RSM-моделей) по предсказанию локальных и интегральных характеристик статистически трехмерной рэлей-бенаровской конвекции жидкого металла с определяющей ролью крупномасштабной циркуляции (КМЦ). Расчеты на основе Unsteady-RANS-подхода на различных по измельченности сетках проведены при числе Рэлея 10^6 и числе Прандтля 0,025 для подогреваемой снизу цилиндрической емкости при равенстве ее диаметра высоте. Рассмотрен случай слабого наклона объекта, когда в нем КМЦ принимает «зафиксированное» азимутальное положение. Работоспособность использованных моделей турбулентности оценивается через сопоставление результатов с ранее полученными данными прямого численного моделирования для тех же условий.

Ключевые слова: конвекция Рэлея – Бенара, крупномасштабная циркуляция, турбулентность, осредненные по Рейнольдсу уравнения

Финансирование: Исследование частично финансировалось Министерством науки и высшего образования Российской Федерации в рамках программы стратегического академического лидерства «Приоритет 2030» (Соглашение 075-15-2021-1333 от 30.09.2021).

Ссылка для цитирования: Смирнов С. И., Смирнов Е. М. Опыт применения полуэмпирических дифференциальных моделей турбулентности для расчета конвекции жидкого металла в подогреваемом снизу цилиндре // Научно-технические ведомости СПбГПУ. Физико-математические науки. 2022. Т. 15. № 3. С. 43–60. DOI: https://doi.org/10.18721/JPM.15304

Introduction

A characteristic feature of free convective flow developing in cylindrical containers heated from below is the presence of large-scale vortex structures occupying the entire domain (see, for example, reviews [1, 2]). In particular, if the diameter of the cylinder is equal to its height, the predominant structure of convective flow is a single vortex, also called a convection cell, or large-scale circulation (LSC) [3–7]. LSC in a strictly vertically oriented container with axially symmetric boundary conditions does not have a dedicated azimuthal position and, accordingly, nothing prevents it from occasionally making random movements in the azimuthal direction. This is confirmed by both experimental [8–11] and numerical [12–15] studies of turbulent Rayleigh–Bénard convection in cylindrical containers. The specific azimuthal behavior of LSC is determined in experimental studies by small deviations from axial symmetry that are difficult

to control, inevitably present in laboratory models. The azimuthal instability of a convection cell is also generally manifested in numerical studies, where the 'external' factor affecting the random oscillations of LSC is the asymmetry of the computational grid or the peculiarities of numerical algorithms.

The random azimuthal movements of the convection cell make it incredibly difficult to obtain statistical data on its three-dimensional structure, including the quantities characterizing the 'background' turbulence: fields of Reynolds stresses and turbulent heat flux. However, these low-frequency movements can be suppressed, thus 'locking' the LSC in a certain azimuthal position if a stabilizing external factor is artificially introduced; this can be achieved, for example, by slightly tilting the container. This method for 'locking' the LSC is used in experimental [8, 16–20] and numerical [20–24] studies.

The Direct Numerical Simulation (DNS) method is widely used to describe turbulent Rayleigh-Bénard convection in regions with relatively simple geometry. This approach assumes that all scales of turbulent fluid flow are resolved, consequently proving to be the most informative (see, for example, [25–30] for the case of a vertically oriented cylinder and [23, 24] for the case of a slightly tilted container). However, large computational costs are required for resolving the entire spectrum, increasing very quickly with increasing Rayleigh numbers.

The Large Eddy Simulation (LES) method allows reducing the costs, in particular, in its 'simplified' version, the Implicit LES (ILES), where subgrid-scale turbulent viscosity is not introduced explicitly into the transport equations, and the dissipative properties of the numerical scheme play the role of physical viscosity on a small scale. The experience of adopting the ILES approach for modeling the turbulent Rayleigh–Bénard convection in cylindrical containers is described in [22, 31, 32]. A recent paper [33] applied the ILES method to studying anisotropy of turbulent transfer in mixed convective flow developing in the crucible of a Czochralski furnace for growing silicon crystals.

It is well known, however, that as the Rayleigh number increases, computations of convective flow by the LES method require progressively refining the grids in the near-wall layers, with the refinements introduced in all spatial directions. As a result, obtaining reliable numerical data for a wide range of practical problems characterized by high Rayleigh numbers also involves very high computational costs.

In view of this, strong interest persists in numerical modeling of turbulent free and mixed-convection flows based on Reynolds-averaged Navier–Stokes (RANS) equations, closed by some semi-empirical differential model of turbulence. It should be borne in mind, however, that the options for obtaining a steady RANS solution are very limited in the case of Rayleigh–Bénard convection, depending on the turbulence model applied. It is therefore worthwhile to explore a problem statement developed to incorporate computations based on unsteady Reynolds equations. This approach is interpreted as Unsteady RANS (URANS) or Transient RANS (TRANS).

Refs. [34–36] thoroughly analyze the applications of the URANS approach to reproducing unsteady coherent structures and the intensity of turbulent transfer in the 'classical' statistically one-dimensional case of free convection between two differently heated horizontal plates. The authors emphasize the presence of two different scales in the motion: large amplitudes associated with plumes, thermals and convection cells, as well as turbulence arising mainly in the near-wall boundary layers and carried by large-scale structures. This makes turbulent Rayleigh–Bénard convection very convenient for computations based on unsteady Reynolds equations. The computational results [34–36] obtained by the URANS method closed by a three-parameter turbulence model indicate that the averaged temperature profile, second-order moments and integral heat transfer are in good agreement with the data of most DNS calculations and experimental data on convection between horizontal plates.

Recent years saw growing interest towards RANS simulations of free convective flows, closed by some model from the RSM family (Reynolds Stress Model) based on either steady or unsteady statements [37–41]. In general, the RSM model solves differential equations for transport of all components of the Reynolds stress tensor and the turbulent heat flux vector. Efforts to somewhat simplify the model, lowering the computational costs, are concentrated on 'reduced' formulations where differential transport equations are solved only for Reynolds stresses, and the turbulent heat flux is computed based on the gradient hypothesis in terms of averaged flow parameters.

The experience of using Reynolds stress models to computing turbulent free-convection flows in the gravitational field presented in the literature mainly covers model configurations with differently heated vertical walls or the case of a boundary layer near a vertical heated surface [37–41].

This paper adopts one of the well-known RSM models (implemented, in particular, in the ANSYS Fluent software package) for URANS simulations of mercury convection in a slightly tilted cylinder heated from below. Similar simulations are also carried out for two turbulence models with isotropic viscosity from the k-ω and k-ε families. The computed statistical characteristics of the first and second orders are compared with the data in [23] obtained earlier for the given configuration based on the DNS approach.

Problem statement and mathematical model

We consider turbulent convection of fluid in a bottom-heated cylindrical container with a single aspect ratio ($\Gamma = D/H = 1$). The container is tilted by a small angle ($\varphi = 2°$) with respect to the gravity vector **g** (Fig. 1,*a*).

No-flow and no-slip conditions are imposed on all boundaries of the container. Horizontal walls are assumed to be isothermal: the temperature T_h of the top wall is higher than that of the bottom wall (T_c). The side wall is treated as adiabatic.

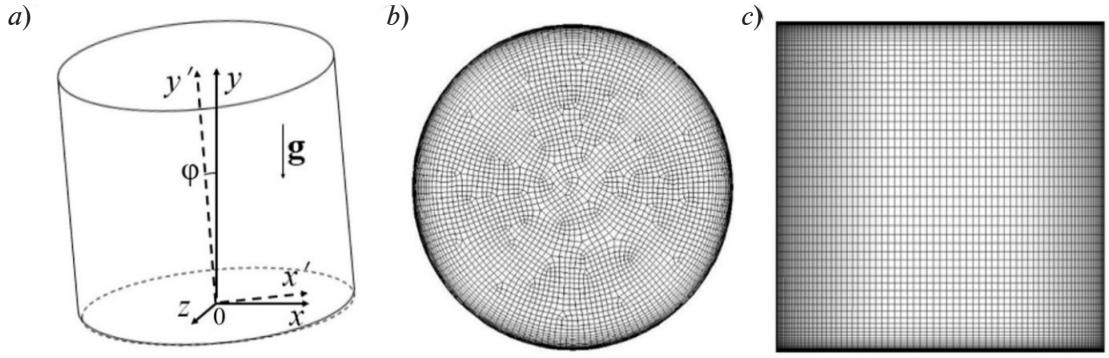

Fig. 1. Images of cylindrical container for the problem statement: *a* corresponds to the geometry of the computational domain; *b*, *c* show characteristic views of the computational grids in horizontal (*b*) and central vertical (*c*) planes

The dimensionless governing parameters of the problem were the Prandtl number $\mathrm{Pr} = \mu C_p/\lambda$ and the Rayleigh number

$$\mathrm{Ra} = \mathrm{Pr}\cdot(\rho^2 g\beta\Delta T H^3/\mu^2),$$

where μ is the dynamic viscosity; C_p is the specific heat at constant pressure; λ is the thermal conductivity; ρ is the density; β is the volumetric expansion coefficient; g is the gravity acceleration; ΔT is the temperature difference between the hot and cold walls, $\Delta T = T_h - T_c$.

The characteristic (large-scale) velocity of the flow (buoyant velocity) is the quantity $V_b = (g\beta\Delta T H)^{0.5}$. The time scale is the characteristic convective time $t_b = H/V_b$.

The computations presented were carried out for the values of hydrodynamic numbers $\mathrm{Pr} = 0.025$ and $\mathrm{Ra} = 10^6$.

Convective motion is calculated from a system of unsteady Reynolds-averaged equations of dynamics and heat transfer (1)–(3), which includes the Navier–Stokes equations written in the Bussinesq approximation to account for buoyancy effects in the gravitational field, the continuity equation and the energy equation:

$$\frac{\partial V_j}{\partial x_j} = 0, \tag{1}$$

$$\rho\frac{\partial V_i}{\partial t} + \rho V_j\frac{\partial V_i}{\partial x_j} = -\frac{\partial p}{\partial x_i} + \frac{\partial\left(\tau_{ij} + \tau_{t,ij}\right)}{\partial x_j} - \rho\beta\left(T - T_0\right)g_i, \tag{2}$$

$$\rho C_p \frac{\partial T}{\partial t} + \rho C_p V_j \frac{\partial T}{\partial x_j} = \frac{\partial}{\partial x_j}\left(q_j + q_{t,j}\right). \quad (3)$$

The equations are solved in the coordinate system associated with the cylindrical container $x_j = (x', y', z' = z)$ shown in Fig. 1,*a*. The notations V_i and T correspond to the components of Reynolds-averaged velocity ($i(j) = 1, 2, 3$) and temperature; τ_{ij}, q_j are the components of the viscous stress tensor and the diffusive heat flux calculated in terms of the Reynolds-averaged values:

$$\tau_{ij} = \mu\left(\frac{\partial V_i}{\partial x_j} + \frac{\partial V_j}{\partial x_i}\right), \quad (4)$$

$$q_j = -\lambda \frac{\partial T}{\partial x_j}. \quad (5)$$

The quantities $\tau_{t,ij}$, $q_{t,j}$ entering Eqs. (2), (3) are the components of the turbulent (Reynolds) stress tensor and the turbulent heat flux vector arising from Reynolds averaging and reflecting the presence of relatively high-frequency fluctuations of velocity v_i and the temperature θ in the instantaneous motion.

Respectively,

$$\tau_{t,ij} = -\rho \overline{v_i v_j}, \quad (6)$$

$$q_{t,j} = -\rho C_p \overline{v_j \theta}, \quad (7)$$

where the overbar indicates Reynolds averaging.

The system of equations (1)–(3) is not closed. To close the system, we should determine the method (model) for calculating the quantities $\tau_{t,ij}$ and $q_{t,j}$.

The calculated data presented in this paper are obtained when the system (1)–(3) is closed with respect to three models.

The *k*-ε RNG and *k*-ω SST models. These models belong to the class of two-parameter differential turbulence models based on the concept of isotropic turbulent viscosity (the Bussinesq hypothesis). According to this concept, the components of the turbulent stress tensor and the turbulent heat flux vector are related to the Reynolds-averaged flow parameters as follows:

$$\tau_{t,ij} = \mu_t\left(\frac{\partial V_i}{\partial x_j} + \frac{\partial V_j}{\partial x_i}\right) - \frac{2}{3}k\delta_{ij}, \quad (8)$$

$$q_{t,j} = -\lambda_t \frac{\partial T}{\partial x_j}, \quad (9)$$

where μ_t is the turbulent viscosity determined from the calculated turbulence parameters (k, ε or ω); λ_t is the turbulent thermal conductivity, $\lambda_t = C_p\mu_t/\mathrm{Pr}_t$ (Pr_t is the turbulent Prandtl number (taken equal to 0.8 in this calculation)); k is the turbulent kinetic energy.

The complete formulation for the k-ε RNG and k-ω SST models is given in [42] and [43, 44], respectively.

Reynolds stress model. The differential model of Reynolds stresses implemented in the ANSYS Fluent 18.2 package was used in this study. Transport equations are only solved for turbulent stresses within the model, while the components of turbulent heat flux are calculated in terms of the averaged flow parameters based on the gradient hypothesis.

The transport equations for Reynolds stresses equations are generally formulated as follows:

$$\rho\frac{\partial\left(\overline{v_i v_j}\right)}{\partial t}+\rho V_j\frac{\partial\left(\overline{v_i v_j}\right)}{\partial x_j}=D_{ij}^m+D_{ij}^t+R_{ij}+G_{ij}+\varphi_{ij}-\varepsilon_{ij}, \quad (10)$$

where D_{ij}^m, D_{ij}^t are the terms reflecting molecular (m) and turbulent (t) diffusive transport; R_{ij}, G_{ij} are the terms characterizing the kinetic energy generated by averaged motion and by buoyancy forces, respectively; φ_{ij} is the quantity responsible for the redistribution of energy between stress and strain velocity tensors; ε_{ij} is the dissipative term.

A differential equation for transport of the quantity ω (the specific dissipation rate of kinetic energy used to close Eq. (10)) is solved together with the equations for the Reynolds stresses. The Stress Omega option was selected during the computations from the options available in the ANSYS Fluent package and defining the specific form of this equation.

The components of turbulent heat flux $\overline{v_i\theta}$ are calculated by the formulas:

$$\overline{v_i\theta}=\frac{\mu_t}{\rho\,\mathrm{Pr}_t}\frac{\partial T}{\partial x_i},\ \mu_t=\frac{\rho k}{\omega},\ k=\frac{1}{2}\overline{v_i v_i}, \quad (11)$$

where $\mathrm{Pr}_t = 0.8$ (the same as above).

The components of the Reynolds stress model are described in [45–47], as well as in the user documentation for the ANSYS Fluent 18.2 software package.

Specifics of computations and data processing

Comparative computations based on the ANSYS Fluent finite volume method were carried out on two grids consisting of hexagonal elements containing 0.47 million (C1 grid) and 3.7 million cells (C2 grid). The structure of the grids in transverse and longitudinal (central) planes is illustrated in Fig. 1, *b*, *c*. The grids were clustered to the walls, while the size of the near-wall element was $1.5\cdot10^{-4}$ N. A characteristic feature of the grids was the presence of a central 'unstructured' (asymmetric) subdomain about $0.8D$ in diameter (see Fig. 1, *b*).

Preliminary computations led us to conclude that none of the turbulence models applied is capable of providing a steady-state solution to the problem. All subsequent computations were performed in an unsteady formulation. The non-iterative fractional step method with second-order accuracy was applied to advance in physical time. The time step was about one hundredth of the large-scale time t_b of the problem, which was about 10 times higher than that used in [23] for computations by the DNS method.

The spatial approximation of convective terms in the transport equations was carried out by the QUICK scheme with nominally third-order accuracy. Diffusion terms were approximated by a central-difference scheme with second-order accuracy.

All computations started from a zero initial velocity field and uniform temperature field taken as $(T_c + T_h)/2$. Samples for the time averaging performed after a transition region were equal to $3000t_b$ in all computations.

The computational data were processed to obtain the first-order and second-order statistical characteristics based on the following assumptions.

First, it was assumed that the instantaneous velocities and temperatures present in the real current (marked with an asterisk) can be decomposed into low- and high-frequency components:

$$V_i^*=V_i+v_i,\ T^*=T+\theta. \quad (12)$$

Secondly, it was assumed that Reynolds-averaged motion contains only low-frequency 'large-scale' components of velocity and temperature fields, i.e.,

$$\overline{V_i^*}=V_i,\ \overline{T^*}=T, \quad (13)$$

which, in turn, can be decomposed into mean values t_{avr} obtained by averaging over a sufficiently large time sample and fluctuation components:

$$V_i = \langle V_i \rangle + V_i', \; T = \langle T \rangle + T'. \tag{14}$$

The angle brackets ⟨…⟩ here indicate time averaging, and the prime indicates the fluctuations. In this case,

$$\langle V_i^* \rangle = \langle V_i \rangle, \langle T^* \rangle = \langle T \rangle. \tag{15}$$

Let us introduce further notations for second-order statistical characteristics (second moments):

$$P_{ij}^t = \langle V_i^* V_j^* \rangle - \langle V_i^* \rangle \langle V_j^* \rangle, \tag{16}$$

$$Q_i^t = \langle V_i^* T^* \rangle - \langle V_i^* \rangle \langle T^* \rangle, \tag{17}$$

which are the components of the total turbulent stress tensor (taken with the reverse sign) and the total heat flux vector.

Taking into account the decompositions (12), (14), we obtain:

$$P_{ij}^t = \langle V_i' V_j' \rangle + \langle \overline{v_i v_j} \rangle + \langle V_i' v_j \rangle + \langle v_i V_j' \rangle, \tag{18}$$

$$Q_i^t = \langle V_i' T' \rangle + \langle \overline{v_i \theta} \rangle + \langle V_i' \theta \rangle + \langle v_i T' \rangle. \tag{19}$$

The first terms in the right-hand sides of expressions (18) and (19) reflect the contribution from numerically resolved components of the motion, the second ones reflect the contribution from simulated components, the third and fourth ones are the so-called cross terms which we are forced to discard (as it was done in [34–36]), due to the assumption of weak correlation between the low- and high-frequency components of motion. It is generally estimated *a posteriori* whether such an assumption is acceptable for a continuous fluctuation spectrum in instantaneous turbulent flow, that is, by comparison with 'reference' data of numerical and experimental studies.

Thus, for comparison with the data from [23], obtained earlier by the DNS method, the values of total turbulent stresses, the components of the total turbulent heat flux and the total kinetic energy of oscillatory motion were calculated as

$$P_{ij}^t = \langle V_i' V_j' \rangle + \langle \overline{v_i v_j} \rangle, \tag{20}$$

$$Q_i^t = \langle V_i' T' \rangle + \langle \overline{v_i \theta} \rangle, \tag{21}$$

$$K^t = \frac{1}{2} P_{ii}^t. \tag{22}$$

The computations by the Reynolds stress model determined the contribution from the simulated component of P_{ij}^t by averaging the Reynolds stresses obtained during the time t_{avr} by solving transport equations (10).

The contribution of the simulated component to the total turbulent heat flux was estimated as follows:

$$\langle \overline{v_i \theta} \rangle = \left\langle \frac{\mu_t}{\rho \, \mathrm{Pr}_t} \frac{\partial T}{\partial x_i} \right\rangle \approx \frac{\langle \mu_t \rangle}{\rho \, \mathrm{Pr}_t} \frac{\partial \langle T \rangle}{\partial x_i}. \tag{23}$$

This expression is obtained based on the gradient hypothesis (11) assuming a weak correlation between the fluctuations of turbulent viscosity and numerically resolved fluctuations of temperature.

Computational results and discussion

The computational results are given below in dimensionless form. The coordinate values are taken relative to container height H. This implies the following correspondence:

$$x_{i(j)} = x', y', z' \text{ for } i(j) = 1, 2, 3.$$

The velocity components are taken relative to the buoyant velocity V_b, the turbulent stresses P^t_{ij} and kinetic energy K^t to the square of buoyant velocity; the components of turbulent heat flux Q^t_i are normalized by the product $V_b \Delta T$.

Time-averaged flow fields and local heat transfer. Fig. 2, *a* illustrates an averaged picture of mercury convection in a bottom-heated cylinder with pronounced LSC predicted from URANS computations for different turbulence models.

Fig. 2,*b* shows the field of time-averaged axial velocity component $\langle V_{y'} \rangle$ in the central vertical plane of the cylinder. Evidently, when LSC is 'locked' in this azimuthal position, the flow is symmetrical relative to the plane $x'0y'$. Distributions of the averaged axial velocity along the coordinate x' in the same plane (Fig. 2,*c*), computed for different RANS-models, are almost identical and very close to the distribution obtained in our previous study [23] by the DNS method.

The mean temperature distributions along the central container axis, computed for the three RANS models, are compared with each other and with the DNS data in Fig. 2,*d*. There is generally good agreement between the results obtained by different models/approaches: in particular, all of them predict an extended central zone with an inverse temperature gradient. On the other hand, more detailed analysis of the distributions in the area adjacent to the end wall (see the enlarged fragment in Fig. 2,*d*) allows us to conclude that in the case of the *k*-ε RNG model, the temperature gradient in this area, and therefore the local heat flux on the wall, is somewhat lower (by 2–3%) than in the case of the other two RANS models, which predict gradient values that virtually coincide with the result of the DNS computations.

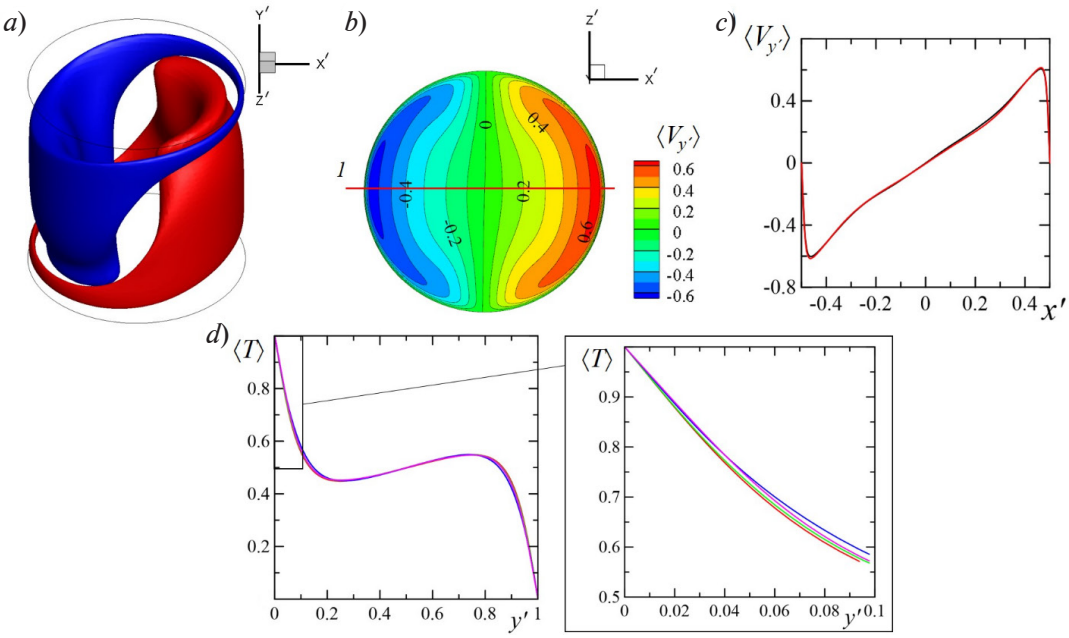

Fig. 2. Comparison of the curves for the computed quantities of the problem, obtained using different models: URANS (*a, b*), URANS, DNS (*c*), DNS, RSM, *k*-ω SST, *k*-ε RNG (*d*).

The figure shows isosurfaces of time-averaged axial velocity component of upward (red) and downward (blue) flow, $|\langle V_{y'} \rangle| = 0.3$ (*a*); the field of averaged axial velocity component in the central plane (*b*), as well as the distribution of this velocity along line *1* (the two curves coincide) (*c*); the distribution of averaged temperature along the container axis by the DNS (red curves), RSM (green), *k*-ω SST (blue), *k*-ε RNG (lilac) (*d*) models

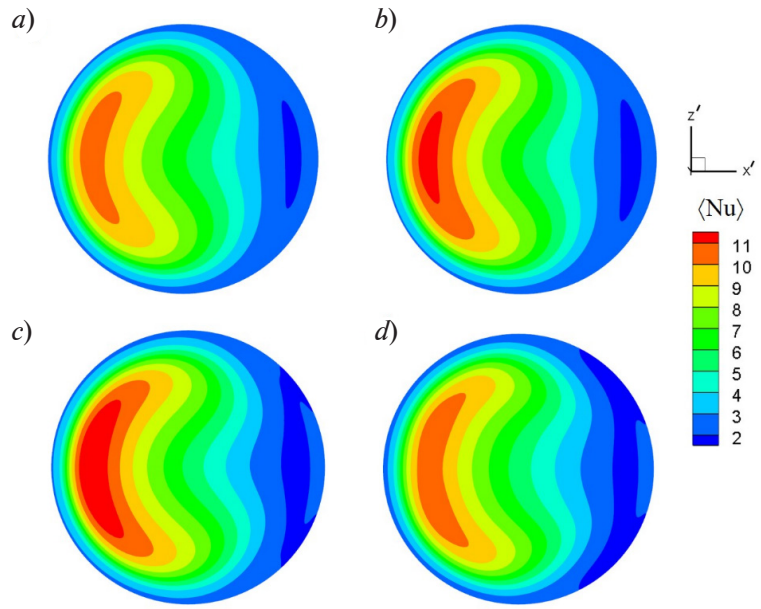

Fig. 3. Distributions of the time-averaged local Nusselt number on the lower cylinder wall, obtained using different models: DNS [23] (*a*), RSM (*b*), *k*-ω SST (*c*) and *k*-ε RNG (*d*)

Fig. 3 shows the distributions of the time-averaged local Nusselt number on the lower wall, illustrating, in particular, strong spatial non-uniformity of this quantity due to the presence of LSC. The results of RANS computations show very satisfactory agreement with the DNS data, especially for the RSM model: in this case, not only a crescent-shaped zone of maximum heat transfer is reproduced, but also a well-defined region of the lowest values of the Nusselt number.

Averaging of the distributions shown in Fig. 3 over the wall surface yields the integral Nusselt numbers given in the table. Apparently, these values obtained by different RNS models differ from the DNS data by no more than 3.6%; a deviation towards lower values is observed for the *k*-ε RNG model, and towards higher values for the other two models. The Reynolds stress model gives the result closest to the one obtained by the DNS method.

Concluding this subsection, we should note that the URANS computations presented in it were obtained using the C1 grid. Similar computations were performed on a C2 grid which contained more cells (almost by an order of magnitude). Time-averaged distributions/profiles of velocity, temperature and local Nusselt number computed on two grids were found to be virtually the same (up to the thickness of the visualized curves). The integral Nusselt numbers differed only in the fourth digit. Thus, we can conclude for a related family of problems on three-dimensional Rayleigh-Bénard convection of liquid metal that the grid size of about half a million cells is sufficient to predict first-order statistical data based on the URANS approach at Rayleigh numbers of the order of 10^6.

Table

Comparison of integral Nusselt numbers, obtained from different RANS models, with DNS data

Model	*k*-ε RNG	*k*-ω SST	RSM	DNS [23]
Nu	5.46	5.84	5.78	5.64

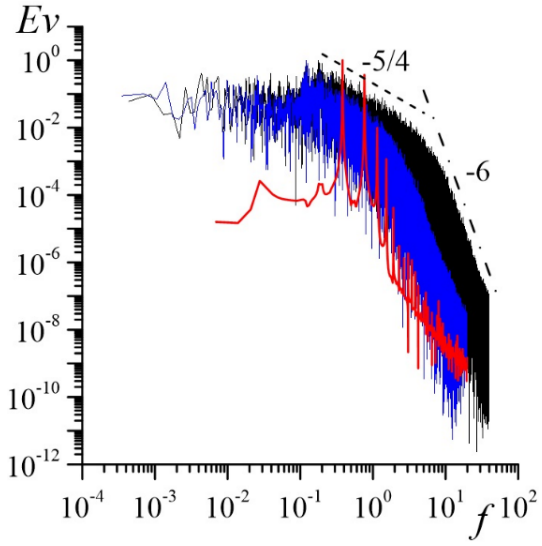

Fig. 4. Energy spectra for fluctuations of the axial velocity component $V_{y'}$ at the point located at $x' = 0.35$ at the intersection of the plane $x'0y'$ and the central vertical plane (see Fig. 1, *a*); the data were obtained from different models: DNS [23] (black curve), RSM (blue curve), k-ε RNG (red curve); approximations by the functions $Ev \sim f^{-5/4}$ (dashed line) and f^{-6} (dot-dashed line)

Spectral characteristics. Fig. 4 shows the energy spectra for the fluctuations of the axial velocity component at a point located at $x' = 0.35$ at the intersection of the $x'0y'$ plane and the central vertical plane. The spectra obtained in computations on a refined grid (C2, 3.7 million cells) for the RSM and k-ε RNG models are compared with the spectrum from [23], computed by the DNS method on a grid containing about 15 million cells. Notice that the spectrum calculated by the k-ω SST model practically coincides with the spectrum obtained using the Reynolds stress model (not shown in Fig. 4).

The spectrum obtained for the RSM model (as well as for k-ω SST) indicates that turbulent fluctuations are numerically resolved in a noticeable part of the quasi-inertial ramge, more pronounced in the case of DNS computations and suggesting a decrease in the spectral density proportionally to $f^{-5/4}$; this decrease rate is close to the classical law $Ev \sim f^{-5/3}$ (Ev is the spectral energy density, non-dimensionalized by its maximum value, f is the dimensionless frequency) for the inertial range in the case of developed isotropic turbulence. Accordingly, the transition to a pronounced 'dissipative' region characterized by rapid decrease, approximately proportional to f^{-6}, occurs earlier compared to DNS. Conversely, the k-ε RNG model predicts unsteady convection with quasi-periodic oscillations covering the region of intermediate frequencies. The difference in the results obtained by the k-ω SST and k-ε RNG models is primarily due to the fact that the latter generates a significantly higher level of turbulent viscosity compared to the k-ω SST model.

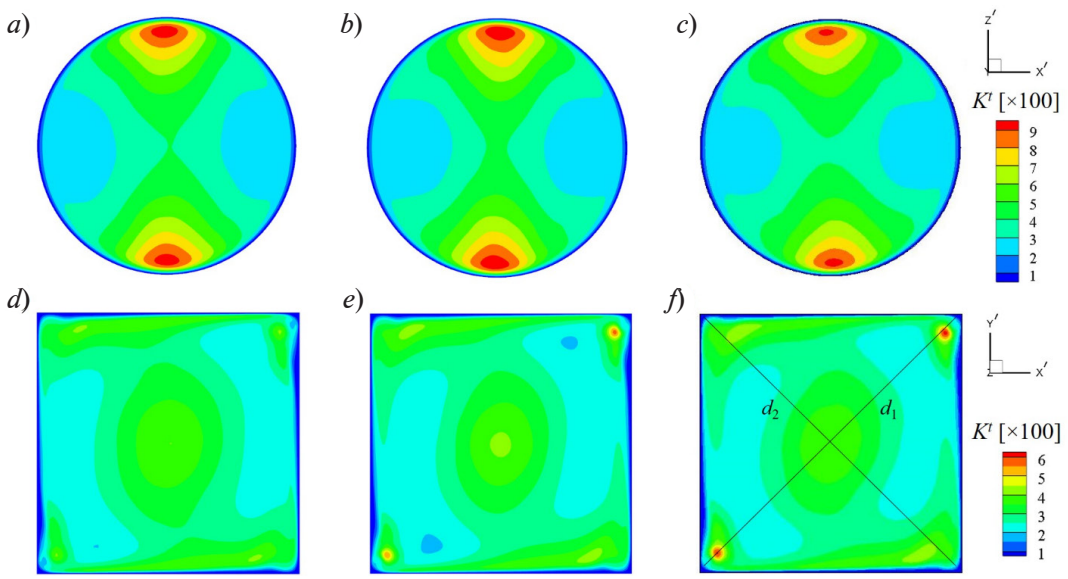

Fig. 5. Distributions of turbulent kinetic energy in two central planes of the cylinder obtained by RSM (*a*, *b*, *d*, *e*) and DNS [23] (*c*, *f*) models, as well as using C1 (*a*, *d*) and C2 (*b*, *e*) grids

Turbulent stresses and turbulent heat flux. Next, we consider the results obtained by the RANS models for second-order moments.

Fig. 5 illustrates the effect that the dimension of the computational grid has on the predictive capability of the RSM model for the characteristic features observed in the field of turbulent kinetic energy, compared with the DNS data.

These features are as follows:

1) the most intense level of fluctuations (red and yellow zones in Fig. 5, *a*–*c*) is observed in the mixing layers formed upon interaction of upward and downward flows in LSC;

2) extremely weak oscillatory motion is observed in the zones of strong upward and downward flows, while kinetic energy takes minimum values in these areas;

3) small zones with elevated kinetic energies are observed in the corners (red and yellow 'spots' in Fig. 5, *e*, *f*), where the corner vortices formed are, on average, stationary (this was established in [23]) and, accordingly, the mixing layers with a global vortex in the form of LSC. The first two features are well reproduced in the computations by the RSM model on both grids, while the third one cannot be predicted using a coarse grid (see Fig. 5,*d*). The same applies to the turbulent stress fields in the corners, which are analyzed below.

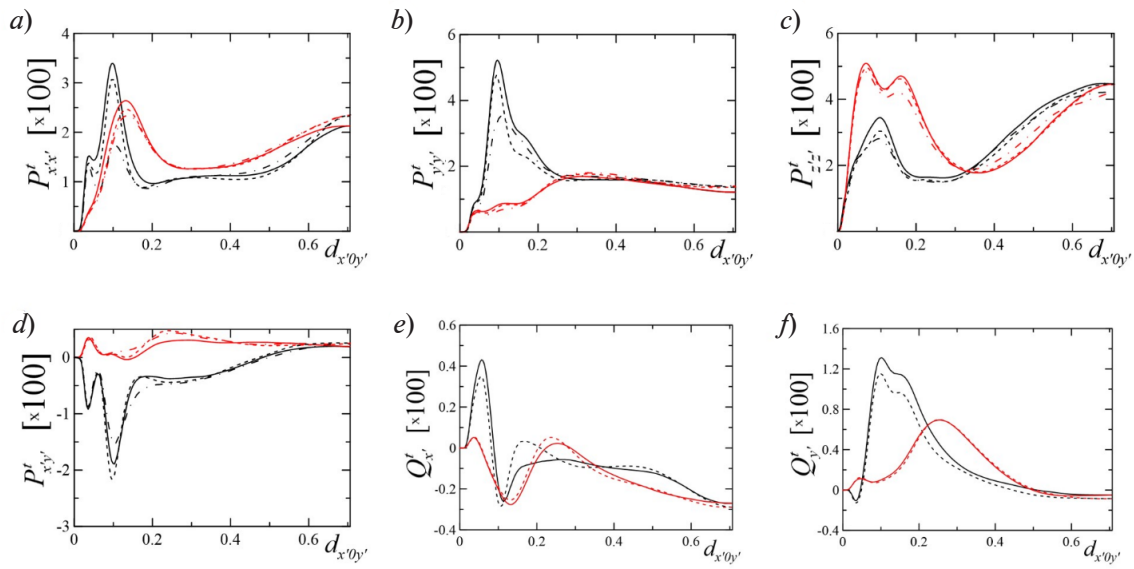

Fig. 6. Component distributions for turbulent stress tensor (*a*–*d*) and turbulent heat flux vector (*e*, *f*) along the diagonals d_1 (black curves) and d_2 (red curves) (see Fig. 5, *f*). Data were obtained from different models: DNS [23] (solid curves), URANS simulations by the RSM model (remaining curves), C1 (dash-dots) and C2 (dashes) grids

Fig. 6 shows the computational distributions for the distributions of the total turbulent stress tensor and the turbulent heat flux vector along the diagonals of the central longitudinal section of the container (see Fig. 5,*f*). The analysis of factors determining the form of the curves presented is carried out in our earlier study [23]. The curves for URANS computations by the RSM model reflect the total contribution from two components of the values considered: numerically resolvable and simulated. It can be seen that the results of URANS computations on the C2 grid are in very good agreement with the DNS data. As noted above, the coarse C1 grid does not reproduce the features of second-order statistics in the mixing layers formed by the interaction of corner vortices and LSC: this drawback is clearly traced from the computational results in Fig. 6, *a*, *b*. In view of this, the results of URANS computations of the turbulent heat flux vector (see Fig. 6, *e*, *f*) are shown only for the refined grid. Generally good agreement with the DNS data is also observed here.

Fig. 7 compares the axial component profiles of turbulent heat flux, obtained from different turbulence models for the line coinciding with the cylinder axis, with the DNS data; contributions from numerically resolved and simulated components of the flux, as well as their total contribution are given in the figure. Pronounced differences can be observed between the computational

results from different RANS models. The Reynolds stress model gives comparable values for both components of the total flux for the region $|y_r| < 0.2$ with large mean temperature gradients (see Fig. 2, *d*); however, the resolved component is clearly predominant.

Conversely, the simulated component is predominant for the case of the *k*-ω SST model (Fig. 7, *b*), while the contribution of the resolved component is practically absent for the *k*-ε RNG model. The latter circumstance is obviously due to an elevated level of turbulent viscosity in the case of the *k*-ε RNG model and the relatively low intensity of the predicted quasi-periodic flow. Accordingly, the *k*-ε RNG model gives the worst predictions for the profile of the total turbulent heat flux.

As evident from Fig. 7, the results obtained from the Reynolds stress model are in excellent agreement with the DNS data, even though a simplified approach adopting the gradient hypothesis was used to estimate the simulated component. Therefore, we can conclude that there is no need to solve differential equations for transport of turbulent heat flux components in the case of URANS simulations of Rayleigh–Bénard convection with three-dimensional LSC, carried out by the Reynolds stress model on sufficiently refined grids.

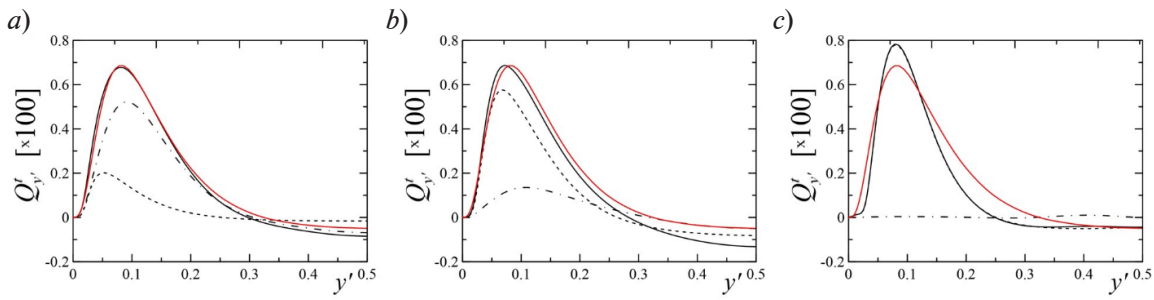

Fig. 7. Distributions for axial component of turbulent heat flux along the cylinder axis; comparison between the computational data from different RANS-models (black curves) and DNS data [23] (red curves), as well as between the contributions from components of turbulent heat flux: simulated (dashes), numerically resolved (dot-dashes) and the total of two components (solid lines). RANS models: RSM (*a*), *k*-ω SST (*b*), *k*-ε RNG (*c*)

Conclusion

The paper assesses the predictive capabilities of three different turbulence RANS models (*k*-ω SST, *k*-ε RNG and one of the well-known differential RSM-models) for local and integral characteristics of statistically three-dimensional Rayleigh–Bénard convection of liquid metal with the decisive role played by large-scale circulation (LSC). The conclusions are based on the computational results for unsteady convection (Unsteady RANS) in a slightly tilted cylindrical container with the Rayleigh number $Ra = 10^6$ and the Prandtl number $Pr = 0.025$, compared with the data for the same conditions obtained earlier by direct numerical simulation (DNS).

The test computations indicate it was found that the grid size of about half a million cells is sufficient to predict time-averaged fields of velocity, temperature, local and integral heat transfer if we use a software tool implementing second-order numerical schemes. This conclusion can be extended to the case of problems on three-dimensional Rayleigh-Bénard convection of liquid metal with similar geometry. Grids whose number of cells is higher by an order of magnitude are necessary to accurately predict second-order statistics (total turbulent stresses and components of the turbulent heat flux vector),

All RANS models of turbulence used predict time-averaged velocity and temperature fields, as well as local heat transfer at the end walls, which are in good agreement with the DNS data. The integral values of the Nusselt number obtained for different RNS models differ from the DNS data by no more than 3.6%; a deviation towards lower values is observed for the *k*-ε RNG model, and towards higher values for the other two models. The Reynolds stress model gives the result closest to the one obtained by the DNS method.

The numerical solution obtained via the k-ω SST and RSM models on a grid of 3.7 million cells has a turbulent character, with a continuous spectrum of resolved fluctuations making a large contribution to statistical second-order characteristics. In contrast, the k-ε RNG model predicts unsteady convection flow with quasi-periodic fluctuations of low intensity, where the simulated component comprises nearly the entire contribution to second-order moments. The best agreement with the DNS data for total second-order moments was obtained by the Reynolds stress model.

In view of the above, the experience outlined in our paper for applying this approach to solving the model problem can be useful in numerical studies on a wide range of industrial and geophysical problems associated with Rayleigh–Bénard convection where a statistically significant or even decisive role is played by three-dimensional large-scale circulation.

REFERENCES

1. **Ahlers G., Grossmann S., Lohse D.,** Heat transfer and large scale dynamics in turbulent Rayleigh – Bénard convection, Rev. Mod. Phys. 81 (2) (2009) 503–538.
2. **Chilla F., Schumacher J.,** New perspectives in turbulent Rayleigh – Bénard convection, Eur. Phys. J. E. 35 (7) (2012) 58.
3. **Castaing B., Gunaratne G., Heslot F., et al.,** Scaling of hard thermal turbulence in Rayleigh – Bénard convection, J. Fluid Mech. 204 (July) (1989) 1–30.
4. **Ahlers G., Xu X.,** Prandtl-number dependence of heat transport in turbulent Rayleigh – Bénard convection, Phys. Rev. Lett. 86 (15) (2001) 3320–3323.
5. **Shishkina O., Thess A.,** Mean temperature profiles in turbulent Rayleigh –Bénard convection of water, J. Fluid Mech. 633 (25 August) (2009) 449–460.
6. **Li Y.-R., Ouyang Y.-Q., Peng L., Wu S.-Y.,** Direct numerical simulation of Rayleigh – Bénard convection in a cylindrical container of aspect ratio 1 for moderate Prandtl number fluid, Phys. Fluids. 24 (7) (2012) 074103.
7. **Lakkaraju R., Stevens R. J. A. M., Verzicco R., et al.,** Spatial distribution of heat flux and fluctuations in turbulent Rayleigh – Bénard convection, Phys. Rev. E. 86 (5) (2012) 056315.
8. **Cioni S., Ciliberto S., Sommeria J.,** Experimental study of high-Rayleigh-number convection in mercury and water, // Dyn. Atmos. Oceans. 24 (1) (1996) 117–127.
9. **Qui X.-L., Tong P.,** Large-scale velocity structures in turbulent thermal convection, Phys. Rev. E. 64 (3) (2001) 036304.
10. **Sreenivasan K. R., Bershadskii A., Niemela J. J.,** Mean wind and its reversal in thermal convection, Phys. Rev. E. 65 (5) (2002) 056306.
11. **Zürner T., Schindler F., Vogt T., et al.,** Combined measurement of velocity and temperature in liquid metal convection, J. Fluid Mech. 876 (10 October) (2019) 1108–1128.
12. **Abramov A. G., Ivanov N. G., Smirnov E. M.,** Numerical study of high-Ra Rayleigh – Bénard mercury and water convection in confined enclosures using a hybrid RANS/LES technique, Proc. Eurotherm Seminar 74 “Heat Transfer in Unsteady and Transitional Flows”, March 23–26, 2003, Eindhoven, the Netherlands; Ed. by H. C. de Lange, A. A. van Steenhoven, TUE (2003) 33–38.
13. **Stevens R. J. A. M., Clercx H. J. H., Lohse D.,** Effect of plumes on measuring the large scale circulation in turbulent Rayleigh – Benard convection, Phys. Fluids. 23 (9) (2011) 095110.
14. **Mishra P. K., De A. K., Verma M. K., Eswaran V.,** Dynamics of reorientations and reversals of large-scale flow in Rayleigh – Bénard convection, J. Fluid Mech. 668 (10 February) (2011) 480–499.
15. **Schumacher J., Bandaru V., Pandey A., Scheel J. D.,** Transitional boundary layers in low-Prandtl-number convection, Phys. Rev. Fluids. 1 (8) (2016) 084402.
16. **Chilla F., Rastello M., Chaumat S., Castaing B.,** Long relaxation times and tilt sensitivity in Rayleigh – Bénard turbulence, Eur. Phys. J. B. 40 (2) (2004) 223–227.
17. **Brown E., Ahlers G.,** Rotations and cessations of the large-scale circulation in turbulent Rayleigh–Bénard convection, J. Fluid Mech. 568 (10 December) (2006) 351–386.
18. **Xi H.-D., Xia K.-Q.,** Azimuthal motion, reorientation, cessation, and reversal of the large-scale circulation in turbulent thermal convection: A comparative study in aspect ratio one and one-half geometries, Phys. Rev. E. 78 (3) (2008) 036326.
19. **Ji D., Bai K., Brown E.,** Effects of tilt on the orientation dynamics of the large-scale circulation in turbulent Rayleigh – Bénard convection, Phys. Fluids. 32 (7) (2020) 075118.

20. **Zwirner L., Khalilov R., Kolesnichenko I., et al.,** The influence of the cell inclination on the heat transport and large-scale circulation in liquid metal convection, J. Fluid Mech. 884 (10 February) (2020) A18.

21. **Shishkina O., Horn S.,** Thermal convection in inclined cylindrical containers // Journal of Fluid Mechanics. 790 (10 March) (2016) R3.

22. **Smirnov S. I., Abramov A. G., Smirnov E. M.,** Numerical simulation of turbulent Rayleigh – Bénard mercury convection in a circular cylinder with introducing small deviations from the axisymmetric formulation, J. Phys. Conf. Ser. 1359 (1) (2019) 012077.

23. **Smirnov S. I., Smirnov E. M.,** Direct numerical simulation of the turbulent Rayleigh – Bénard convection in a slightly tilted cylindrical contain, St. Petersburg State Polytechnical University Journal. Physics and Mathematics. 13 (1) (2020) 14–25 (in Russian).

24. **Smirnov S., Smirnovsky A., Bogdanov S.,** The emergence and identification of large-scale coherent structures in free convective flows of the Rayleigh – Bénard type, Fluids. 6 (12) (2021) 431–450.

25. **Van der Poel E. P., Stevens R. J. A. M., Lohse D.,** Comparison between two- and three-dimensional Rayleigh – Bénard convection, J. Fluid Mech. 736 (10 December) (2013) 177–194.

26. **Horn S., Shishkina O.,** Toroidal and poloidal energy in rotating Rayleigh – Bénard convection, J. Fluid Mech. 762 (10 January) (2015) 232–255.

27. **Scheel J. D., Schumacher J.,** Global and local statistics in turbulent convection at low Prandtl numbers, J. Fluid Mech. 802 (10 September) (2016) 147–173.

28. **Sakievich P. J., Peet Y. T., Adrian R. J.,** Large-scale thermal motions of turbulent Rayleigh–Bénard convection in a wide aspect-ratio cylindrical domain, Int. J. Heat Fluid Flow. 61 (2) (2016) 193–196.

29. **Kooij G. L., Botchev M. A., Frederix E. M. A., et al.,** Comparison of computational codes for direct numerical simulations of turbulent Rayleigh – Bénard convection, Comp. & Fluids. 166 (30 April) (2018) 1–8.

30. **Wan Z.-H., Wei P., Verzicco R., et al.,** Effect of sidewall on heat transfer and □ow structure in Rayleigh – Bénard convection, J. Fluid Mech. 881 (25 December) (2019) 218–243.

31. **Smirnov S. I., Smirnov E. M., Smirnovskiy A. A.,** Endwall heat transfer effects on the turbulent mercury convection in a rotating cylinder, St. Petersburg State Polytechnical University Journal. Physics and Mathematics. 10 (1) (2017) 31–46 (in Russian).

32. **Smirnov S. I., Smirnovskiy A. A.,** Numerical simulation of turbulent mercury natural convection in a heated-from-below cylinder with zero and non-zero thickness of the horizontal walls, Teplovyye Protsessy v Tekhnike [Thermal Processes in Technology]. 10 (3–4) (2018) 94–100 (in Russian).

33. **Borisov D. V., Kalaev V. V.,** ILES of melt turbulent convection with conjugated heat transfer in the crucible and gas flow for Czochralski silicon crystal growth system, J. Cryst. Growth. 573 (3) (2021) 126305.

34. **Kenjereš S., Hanjalić K.** Transient analysis of Rayleigh – Bénard convection with a RANS model, Int. J. Heat Fluid Flow. 20 (3) (1999) 329–340.

35. **Hanjalić K., Kenjereš S.,** Reorganization of turbulence structure in magnetic Rayleigh – Bénard convection: a T-RANS study, J. Turbul. 1 (8) (2000) 1–22.

36. **Kenjereš S., Hanjalić K.,** LES, T-RANS and hybrid simulations of thermal convection at high Ra numbers, Int. J. Heat Fluid Flow. 27 (5) (2006) 800–810.

37. **Choi S.-K., Han J.-W., Choi H.-K.,** Performance of second-moment differential stress and flux models for natural convection in an enclosure, Int. Commun. Heat Mass Transf. 99 (December) (2018) 54–61.

38. **Clifford C. E., Kimber M. L.,** Assessment of RANS and LES turbulence models for natural convection in a differentially heated square cavity, Numer. Heat Transf. Part A. 78 (10) (2020) 560–594.

39. **Levchenya A. M., Trunova S. N., Kolesnik E. V.,** Assessment of RANS turbulence models capabilities based on computational results for free convection developing near a suddenly heated vertical plate, St. Petersburg State Polytechnical University Journal. Physics and Mathematics. 13 (2) (2020) 27–40 (in Russian).

40. **Katsamis C., Craft T., Iacovides H., Uribe J. C.,** Use of 2-D and 3-D unsteady RANS in the computation of wall bounded buoyant flows, Int. J. Heat Fluid Flow. 93 (February) (2022) 108914.

41. **Levchenya A. M., Smirnov E. M., Trunova S. N.** Vliyaniye periodicheskoy makrosherokhovatosti na razvitiye turbulentnoy svobodnoy konvektsii u vnezapno nagrevayemoy vertikalnoy plastiny [The influence of periodical macroroughness on the development of free turbulent convection near a suddenly heated vertical plate], Pisma v Zhurnal Tekhnicheskoy Fiziki. 48 (3) (2022) 47–50 (in Russian).

42. **Orszag S. A., Yakhot V., Flannery W. S., et al.,** Renormalization group modeling and turbulence simulations, Proc. Int. Conf. Near-Wall Turbulent Flows, Tempe, Arizona, USA, 15–17 March (1993) 1031.

43. **Menter F. R.,** Two-equation eddy-viscosity turbulence models for engineering applications, AIAA J. 32 (8) (1994) 1598–1605.

44. **Menter F. R., Kuntz M., Langtry R.,** Ten 2022s of industrial experience with the SST turbulence model, In Book: Turbulence, Heat and Mass Transfer. Vol. 4. Proc. Fourth Int. Symp. Turbulence, Heat & Mass Transfer. Antalya, Turkey, 12–17 October (2003) 625–632.

45. **Launder B. E., Reece G. J., Rodi W.,** Progress in the development of a Reynolds-stress turbulence closure, J. Fluid Mech. 68 (3) (1975) 537–566.

46. **Gibson M. M., Launder B. E.,** Ground effects on pressure fluctuations in the atmospheric boundary layer, J. Fluid Mech. 86 (3) (1978) 491–511.

47. **Wilcox D. C.,** Turbulence modeling for CFD. 2nd edition, DCW Industries, La Canada, California, 1998.

СПИСОК ЛИТЕРАТУРЫ

1. **Ahlers G., Grossmann S., Lohse D.** Heat transfer and large scale dynamics in turbulent Rayleigh – Bénard convection // Reviews of Modern Physics. 2009. Vol. 81. No. 2. Pp. 503–538.

2. **Chilla F., Schumacher J.** New perspectives in turbulent Rayleigh – Bénard convection // The European Physical Journal. E. 2012. Vol. 35. No. 7. P. 58.

3. **Castaing B., Gunaratne G., Heslot F., Kadanoff L., Libchaber A., Thomae S., Wu X.-Z., Zaleski S., Zanetti G.** Scaling of hard thermal turbulence in Rayleigh – Bénard convection // Journal of Fluid Mechanics. 1989. Vol. 204. July. Pp. 1–30.

4. **Ahlers G., Xu X.** Prandtl-number dependence of heat transport in turbulent Rayleigh – Bénard convection // Physical Review Letters. 2001. Vol. 86. No. 15. Pp. 3320–3323.

5. **Shishkina O., Thess A.** Mean temperature profiles in turbulent Rayleigh –Bénard convection of water // Journal of Fluid Mechanics. 2009. Vol. 633. 25 August. Pp. 449–460.

6. **Li Y.-R., Ouyang Y.-Q., Peng L., Wu S.-Y.** Direct numerical simulation of Rayleigh – Bénard convection in a cylindrical container of aspect ratio 1 for moderate Prandtl number fluid // Physics of Fluids. 2012. Vol. 24. No. 7. P. 074103.

7. **Lakkaraju R., Stevens R. J. A. M., Verzicco R., Grossmann S., Prosperetti A., Sun C., Lohse D.** Spatial distribution of heat flux and fluctuations in turbulent Rayleigh – Bénard convection // Physical Review. E. 2012. Vol. 86. No. 5. P. 056315.

8. **Cioni S., Ciliberto S., Sommeria J.** Experimental study of high-Rayleigh-number convection in mercury and water // Dynamics of Atmospheres and Oceans. 1996. Vol. 24. No. 1. Pp. 117–127.

9. **Qui X.-L., Tong P.** Large-scale velocity structures in turbulent thermal convection // Physical Review. E. 2001. Vol. 64. No. 3. P. 036304.

10. **Sreenivasan K. R., Bershadskii A., Niemela J. J.** Mean wind and its reversal in thermal convection // Physical Review. E. 2002. Vol. 65. No. 5. P. 056306.

11. **Zürner T., Schindler F., Vogt T., Eckert S., Schumacher J.** Combined measurement of velocity and temperature in liquid metal convection // Journal of Fluid Mechanics. 2019. Vol. 876. 10 October. Pp. 1108–1128.

12. **Abramov A. G., Ivanov N. G., Smirnov E. M.** Numerical study of high-Ra Rayleigh – Bénard mercury and water convection in confined enclosures using a hybrid RANS/LES technique // Proceedings of the Eurotherm Seminar 74 “Heat Transfer in Unsteady and Transitional Flows”. March 23–26, 2003; Eindhoven, the Netherlands. Ed. by H. C. de Lange, A. A. van Steenhoven, TUE, 2003. Pp. 33–38.

13. **Stevens R. J. A. M., Clercx H. J. H., Lohse D.** Effect of plumes on measuring the large scale circulation in turbulent Rayleigh – Benard convection // Physics of Fluids. 2011. Vol. 23. No. 9. P. 095110.

14. **Mishra P. K., De A. K., Verma M. K., Eswaran V.** Dynamics of reorientations and reversals of large-scale flow in Rayleigh – Bénard convection // Journal of Fluid Mechanics. 2011. Vol. 668. 10 February. Pp. 480–499.

15. **Schumacher J., Bandaru V., Pandey A., Scheel J. D.** Transitional boundary layers in low-Prandtl-number convection // Physical Review Fluids. 2016. Vol. 1. No. 8. P. 084402.

16. **Chilla F., Rastello M., Chaumat S., Castaing B.** Long relaxation times and tilt sensitivity in Rayleigh – Bénard turbulence // The European Physical Journal. B. 2004. Vol. 40. No. 2. Pp. 223–227.

17. **Brown E., Ahlers G.** Rotations and cessations of the large-scale circulation in turbulent Rayleigh–Bénard convection // Journal of Fluid Mechanics. 2006. Vol. 568. 10 December. Pp. 351–386.

18. **Xi H.-D., Xia K.-Q.** Azimuthal motion, reorientation, cessation, and reversal of the large-scale circulation in turbulent thermal convection: A comparative study in aspect ratio one and one-half geometries // Physical Review. E. 2008. Vol. 78. No. 3. P. 036326.

19. **Ji D., Bai K., Brown E.** Effects of tilt on the orientation dynamics of the large-scale circulation in turbulent Rayleigh – Bénard convection // Physics of Fluids. 2020. Vol. 32. No. 7. P. 075118.

20. **Zwirner L., Khalilov R., Kolesnichenko I., Mamykin A., Mandrykin S., Pavlinov A., Shestakov A., Teimurazov A., Frick P., Shishkina O.** The influence of the cell inclination on the heat transport and large-scale circulation in liquid metal convection // Journal of Fluid Mechanics. 2020. Vol. 884. 10 February. P. A18.

21. **Shishkina O., Horn S.** Thermal convection in inclined cylindrical containers // Journal of Fluid Mechanics. 2016. Vol. 790. 10 March. P. R3.

22. **Smirnov S. I., Abramov A. G., Smirnov E. M.** Numerical simulation of turbulent Rayleigh – Bénard mercury convection in a circular cylinder with introducing small deviations from the axisymmetric formulation // Journal of Physics: Conference Series. 2019. Vol. 1359. No. 1. P. 012077.

23. Смирнов С. И., Смирнов Е. М. Прямое численное моделирование турбулентной конвекции Рэлея – Бенара в слегка наклоненном цилиндрическом контейнере // Научно-технические ведомости СПбГПУ. Физико-математические науки. 2020. Т. 13. № 1. С. 14–25.

24. **Smirnov S., Smirnovsky A., Bogdanov S.** The emergence and identification of large-scale coherent structures in free convective flows of the Rayleigh – Bénard type // Fluids. 2021. Vol. 6. No. 12. Pp. 431–450.

25. **Van der Poel E. P., Stevens R. J. A. M., Lohse D.** Comparison between two- and three-dimensional Rayleigh – Bénard convection // Journal of Fluid Mechanics. 2013. Vol. 736. 10 December. Pp. 177–194.

26. **Horn S., Shishkina O.** Toroidal and poloidal energy in rotating Rayleigh – Bénard convection // Journal of Fluid Mechanics. 2015. Vol. 762. 10 January. Pp. 232–255.

27. **Scheel J. D., Schumacher J.** Global and local statistics in turbulent convection at low Prandtl numbers // Journal of Fluid Mechanics. 2016. Vol. 802. 10 September. Pp. 147–173.

28. **Sakievich P. J., Peet Y. T., Adrian R. J.** Large-scale thermal motions of turbulent Rayleigh–Bénard convection in a wide aspect-ratio cylindrical domain // International Journal of Heat and Fluid Flow. 2016. Vol. 61. No. 2. Pp. 193–196.

29. **Kooij G. L., Botchev M. A., Frederix E. M. A., Geurts B. J., Horn S., Lohse D., van der Poel E. P., Shishkina O., Stevens R. J. A. M., Verzicco R.** Comparison of computational codes for direct numerical simulations of turbulent Rayleigh – Bénard convection // Computers & Fluids. 2018. Vol. 166. 30 April. Pp. 1–8.

30. **Wan Z.-H., Wei P., Verzicco R., Lohse D., Ahlers G., Stevens R. J. A. M.** Effect of sidewall on heat transfer and flow structure in Rayleigh – Bénard convection // Journal of Fluid Mechanics. 2019. Vol. 881. 25 December. Pp. 218–243.

31. **Смирнов С. И., Смирнов Е. М., Смирновский А. А.** Влияние теплопереноса в торцевых стенках на турбулентную конвекцию ртути во вращающемся цилиндре // Научно-технические ведомости СПбПУ. Физико-математические науки. 2017. Т. 10. № 1. С. 31–46.

32. **Смирнов С. И., Смирновский А. А.** Численное моделирование турбулентной свободной конвекции ртути в подогреваемом снизу цилиндре при нулевой и конечной толщине горизонтальных стенок // Тепловые процессы в технике. 2018. Т. 10. № 3–4. С. 94–100.

33. **Borisov D. V., Kalaev V. V.** ILES of melt turbulent convection with conjugated heat transfer in the crucible and gas flow for Czochralski silicon crystal growth system // Journal of Crystal Growth. 2021. Vol. 573. No. 3. P. 126305.

34. **Kenjereš S., Hanjalić K.** Transient analysis of Rayleigh – Bénard convection with a RANS model // International Journal of Heat and Fluid Flow. 1999. Vol. 20. No. 3. Pp. 329–340.

35. **Hanjalić K., Kenjereš S.** Reorganization of turbulence structure in magnetic Rayleigh – Bénard convection: a T-RANS study // Journal of Turbulence. 2000. Vol. 1. No. 8. Pp. 1–22.

36. **Kenjereš S., Hanjalić K.** LES, T-RANS and hybrid simulations of thermal convection at high Ra numbers // International Journal of Heat and Fluid Flow. 2006. Vol. 27. No. 5. Pp. 800–810.

37. **Choi S.-K., Han J.-W., Choi H.-K.** Performance of second-moment differential stress and flux models for natural convection in an enclosure // International Communications in Heat and Mass Transfer. 2018. Vol. 99. December. Pp. 54–61.

38. **Clifford C. E., Kimber M. L.** Assessment of RANS and LES turbulence models for natural convection in a differentially heated square cavity // Numerical Heat Transfer. Part A. 2020. Vol. 78. No. 10. Pp. 560–594.

39. Левченя **А. М.,** Трунова **С. Н., Колесник Е. В.** Оценка возможностей RANS-моделей турбулентности по результатам расчетов свободной конвекции, развивающейся вблизи внезапно нагретой вертикальной пластины // Научно-технические ведомости СПбГПУ. Физико-математические науки. 2020. Т. 13. № 2. С. 27–40.

40. **Katsamis C., Craft T., Iacovides H., Uribe J. C.** Use of 2-D and 3-D unsteady RANS in the computation of wall bounded buoyant flows // International Journal of Heat and Fluid Flow. 2022. Vol. 93. February. P. 108914.

41. **Левченя А. М., Смирнов Е. М.,** Трунова **С. Н.** Влияние периодической макрошероховатости на развитие турбулентной свободной конвекции у внезапно нагреваемой вертикальной пластины // Письма в Журнал технической физики. 2022. Т. 48. № 3. С. 47–50.

42. **Orszag S. A., Yakhot V., Flannery W. S., Boysan F., Choudhury D., Maruzewski J., Patel B.** Renormalization group modeling and turbulence simulations // Proceedings of the International Conference on Near-Wall Turbulent Flows, Tempe, Arizona, USA, 15–17 March 1993. P. 1031.

43. **Menter F. R.** Two-equation eddy-viscosity turbulence models for engineering applications // AIAA Journal (Journal of the American Institute of Aeronautics and Astronautics). 1994. Vol. 32. No. 8. Pp. 1598–1605.

44. **Menter F. R., Kuntz M., Langtry R.** Ten 2022s of industrial experience with the SST turbulence model // Turbulence, Heat and Mass Transfer. Vol. 4. Proceedings of the Fourth International Symposium on Turbulence, Heat and Mass Transfer. Antalya, Turkey, 12–17 October, 2003. Pp. 625–632.

45. **Launder B. E., Reece G. J., Rodi W.** Progress in the development of a Reynolds-stress turbulence closure // Journal of Fluid Mechanics. 1975. Vol. 68. No. 3. Pp. 537–566.

46. **Gibson M. M., Launder B. E.** Ground effects on pressure fluctuations in the atmospheric boundary layer // Journal of Fluid Mechanics. 1978. Vol. 86. No. 3. Pp. 491–511.

47. **Wilcox D. C.** Turbulence modeling for CFD. 2nd edition. La Canada, California: DCW Industries, 1998. 457 p.

THE AUTHORS

SMIRNOV Sergei I.
Peter the Great St. Petersburg Polytechnic University
29 Politechnicheskaya St., St. Petersburg, 195251, Russia
sergeysmirnov92@mail.ru
ORCID: 0000-0002-3972-9259

SMIRNOV Evgeny M.
Peter the Great St. Petersburg Polytechnic University
29 Politechnicheskaya St., St. Petersburg, 195251, Russia
smirnov_em@spbstu.ru
ORCID: 0000-0002-7218-6372

СВЕДЕНИЯ ОБ АВТОРАХ

СМИРНОВ Сергей Игоревич – *кандидат физико-математических наук, инженер научно-образовательного центра «Компьютерные технологии в аэродинамике и теплотехнике» Санкт-Петербургского политехнического университета Петра Великого.*

195251, Россия, г. Санкт-Петербург, Политехническая ул., 29
sergeysmirnov92@mail.ru
ORCID: 0000-0002-3972-9259

СМИРНОВ Евгений Михайлович – *доктор физико-математических наук, профессор Высшей школы прикладной математики и вычислительной физики Санкт-Петербургского политехнического университета Петра Великого.*

195251, Россия, г. Санкт-Петербург, Политехническая ул., 29
smirnov_em@spbstu.ru
ORCID: 0000-0002-7218-6372

Received 01.04.2022. Approved after reviewing 06.06.2022. Accepted 06.06.2022.

Статья поступила в редакцию 01.04.2022. Одобрена после рецензирования 06.06.2022. Принята 06.06.2022.

Original article
DOI: https://doi.org/10.18721/JPM.15305

SIMULATION OF AN UNSTEADY FLOW AND MIXING OF FINE GAS SUSPENSION IN A CLOSED VOLUME BY THE HYBRID METHOD OF LARGE PARTICLES

E. N. Shirokova✉

Military Space Academy named after A. F. Mozhaysky, St. Petersburg, Russia

✉ shirokhelen-78@mail.ru

Abstract. Hydrodynamic effects of convective transport and mixing of dispersed reagents determine the efficiency of chemical reactions in some cases. The paper sets and numerically solves the problem of a pulsed outflow and mixing of gas suspension in a volume limited by walls. The initial dispersed-phase concentration at which an anomalous subsonic regime (with the shock-wave structure formation) is replaced by supersonic one (as to the velocity of the carrier gas phase) has been found. It was established that phenomena of instability development and eddying dominate for a long-time interval. The resolution of the hybrid large-particles method was demonstrated for this class of problems.

Keywords: gas suspension, shock-wave structure, convective transport, mixing, hybrid large-particle method

Citation: Shirokova E. N., Simulation of an unsteady flow and mixing of fine gas suspension in a closed volume by the hybrid method of large particles, St. Petersburg Polytechnical State University Journal. Physics and Mathematics. 15 (3) (2022) 61–70. DOI: https://doi.org/10.18721/JPM.15305

Научная статья
УДК 532/529
DOI: https://doi.org/10.18721/JPM.15305

МОДЕЛИРОВАНИЕ НЕСТАЦИОНАРНОГО ТЕЧЕНИЯ И ПЕРЕМЕШИВАНИЯ МЕЛКОДИСПЕРСНОЙ ГАЗОВЗВЕСИ В ЗАМКНУТОМ ОБЪЕМЕ ГИБРИДНЫМ МЕТОДОМ КРУПНЫХ ЧАСТИЦ

Е. Н. Широкова✉

Военно-космическая академия имени А. Ф. Можайского, Санкт-Петербург, Россия

✉ shirokhelen-78@mail.ru

Аннотация. Гидродинамические эффекты конвективного переноса и перемешивания диспергированных реагентов в ряде случаев определяют результативность протекания химических реакций. В работе поставлена и численно решена задача импульсного истечения и перемешивания газовзвеси в объеме, ограниченном стенками. Определена начальная концентрация дисперсной фазы, при которой происходит смена аномального дозвукового режима течения (с образованием ударно-волновой структуры) сверхзвуковым режимом (по скорости несущей газовой фазы). Установлено, что при длительном временном интервале доминируют явления развития неустойчивости и образования вихрей. Продемонстрирована разрешающая способность гибридного метода крупных частиц для данного класса задач.

Ключевые слова: газовзвесь, ударно-волновая структура, конвективный перенос, перемешивание, гибридный метод крупных частиц

Ссылка для цитирования: Широкова Е. Н. Моделирование нестационарного течения и перемешивания мелкодисперсной газовзвеси в замкнутом объеме гибридным методом крупных частиц // Научно-технические ведомости СПбГПУ. Физико-математические науки. 2022. Т. 15. № 3. С. 61–70. DOI: https://doi.org/10.18721/JPM.15305

Introduction

Chemical technologies are based on complex interrelated hydromechanical phenomena (fluidization, precipitation, mixing), chemical processes (synthesis, catalysis, oxidation) and those related to heat and mass transfer (evaporation, condensation, crystallization) [1–4]. Methods of mathematical modeling are now widely used in the chemical industry. The effects of wave and convective transfer as well as mixing of dispersed chemicals play a major role in different technological processes.

Numerical methods for studying hydrodynamic phenomena are associated with mesh-based reconstruction of shock-wave processes, which are satisfactorily resolved within the framework of Euler equations. Simulation of various types of instabilities, mixing and turbulence generally requires more complex approaches, which are traditionally divided into methods of direct numerical simulation (DNS), large eddy simulation (LES) and Reynolds averaged Navier–Stokes equations (RANS), or their hybrid combinations [5, 6].

The conservation laws generally include the convective and diffusive (viscous) terms of equations in differential or integral form and the right-hand sides depending on the solution (sources). The resolution of a numerical method is largely determined by the level of numerical dissipation provided for approximating the convective terms of equations. For example, the accuracy of second and third-order convective schemes CFX and FLUENT packages was analyzed in [7]. Modern methods for mathematical modeling of hydrodynamic instabilities and turbulent mixing were reviewed in [8], focusing on approximation of convective flows in various numerical schemes.

The performance and dissipative properties of numerical methods approximating the flux terms are typically estimated by solving test problems in an inviscid formulation, for example, simulating the Rayleigh–Taylor [9], Kelvin–Helmholtz [10] and Richtmyer–Meshkov instabilities [11]. The discontinuities are smoothed, and the eddies are reconstructed to some degree, depending on the dissipative properties of the numerical schemes.

Simulation of two-phase flows encounters a number of additional fundamental problems [12]. One of them is rigidity of the problems including fast and slow components of the solution. This problem was apparently first formulated and solved for dispersed-gas systems in [13]. The problems of free and impact two-phase jet flows and cylindrical expansion of gas suspensions were numerically and experimentally considered in [14–16].

Our study considers a new formulation of the problem on the gas dynamics of wave and convective transfer and mixing of ideal carrier gas and suspended solid particles in pulsed outflow into a closed volume.

Constitutive equations

We write the conservation laws for dispersed gas in the formulation for interpenetrating continua [17]:

$$\begin{gathered}\frac{\partial \rho_i}{\partial t}+\nabla\cdot\left(\rho_i \mathbf{v}_i\right)=0,\ \frac{\partial}{\partial t}\left(\rho_1\mathbf{v}_1\right)+\nabla\left(\rho_1\mathbf{v}_1\mathbf{v}_1\right)+\alpha_1\nabla p=-\mathbf{F}_\mu,\\ \frac{\partial}{\partial t}\left(\rho_2\mathbf{v}_2\right)+\nabla\left(\rho_2\mathbf{v}_2\mathbf{v}_2\right)+\alpha_2\nabla p=\mathbf{F}_\mu,\frac{\partial}{\partial t}\left(\rho_2 e_2\right)+\nabla\cdot\left(\rho_2 e_2\mathbf{v}_2\right)=Q,\\ \frac{\partial}{\partial t}\left(\rho_1E_1+\rho_2E_2\right)+\nabla\cdot\left(\rho_1E_1\mathbf{v}_1+\rho_2E_2\mathbf{v}_2\right)+\nabla\cdot\left[p\left(\alpha_1\mathbf{v}_1+\alpha_2\mathbf{v}_2\right)\right]=0,\\ \rho_i=\rho_i^\circ\alpha_i,\ (i=1,\ 2),\ \alpha_1+\alpha_2=1,\ \rho=\rho_1+\rho_2,\ E_i=e_i+\mathbf{v}_i^2/2,\end{gathered}\tag{1}$$

where α_i, ρ_i, $\mathbf{v}_i$, E_i, e_i, p are the volume fraction, the reduced density (kg/m^3), the velocity vector (m/s), the total and internal energy (J/kg) of the ith component of the continuum (i = 1 for gas or i = 2 for dispersed phase), the gas pressure (Pa), respectively; $\mathbf{F}_\mu$, Q are the frictional force (N/m^3) and the heat transfer rate (W/m^3) between gas and particles; t, s, is the time; the superscript $^\circ$ indicates the true densities of gas and particle material.

System of equations (1) is closed by the equation of state for calorically perfect ideal gas and incompressible solid particles:

$$p = (\gamma_1 - 1)\rho_1^\circ e_1,\ e_1 = c_v T_1,\ e_2 = c_2 T_2,\ \{\gamma_1, c_v, c_2, \rho_2^\circ\} \equiv \text{const},$$

where T_1, T_2, K, are the temperatures of the carrier phase and particles; γ_1, c_v, J/(kg·K), are the adiabatic index and specific heat capacity of the gas at constant volume; c_2, J/(kg·K), is the specific heat capacity of the particles.

Interfacial friction and heat transfer $\mathbf{F}_\mu$, Q_T are determined from empirical dependences [18]:

$$\mathbf{F}_\mu = (3/8)(\alpha_2/r)C_\mu\left(\mathrm{Re}_{12}\right)\rho_1\left(\mathbf{v}_1 - \mathbf{v}_2\right)\left|\mathbf{v}_1 - \mathbf{v}_2\right|,$$

$$C_\mu = \begin{cases} C_\mu^{(1)} = \dfrac{24}{\mathrm{Re}_{12}} + \dfrac{4.4}{\mathrm{Re}_{12}^{1/2}} + 0,42,\ \alpha_2 \le 0.08, \\ C_\mu^{(2)} = \dfrac{4}{3\alpha_1}\left(1.75 + \dfrac{150\alpha_2}{\alpha_1 \mathrm{Re}_{12}}\right),\ \alpha_2 \ge 0.45, \\ \dfrac{(\alpha_2 - 0.08)C_\mu^{(2)} + (0.45 - \alpha_2)C_\mu^{(1)}}{0.37},\ 0.08 < \alpha_2 < 0.45, \end{cases}$$

$$Q_T = (3/2)(\alpha_2/r^2)\lambda_1 \mathrm{Nu}_1 (T_1 - T_2),$$

$$\mathrm{Nu}_1 = \begin{cases} 2 + 0.106\mathrm{Re}_{12}\mathrm{Pr}_1^{1/3}\ (\mathrm{Re}_{12} \le 200), \\ 2.274 + 0.6\mathrm{Re}_{12}^{0,67}\mathrm{Pr}_1^{1/3}\ (\mathrm{Re}_{12} > 200), \end{cases}$$

$$\mathrm{Re}_{12} = 2r\rho_1^\circ\left|\mathbf{v}_1 - \mathbf{v}_2\right|/\mu_1,\ \mathrm{Pr}_1 = c_v\gamma_1\mu_1/\lambda_1,$$

where Re_{12}, Nu_1, Pr_1 are the Reynolds, Nusselt and Prandtl numbers, respectively; C_μ, μ_1, r, are the coefficient of interfacial friction, dynamic viscosity (Pa·s) and particle radius (m).

Problem statement and computational procedure

Consider the axisymmetric problem on pulsed outflow of gas suspension from cylindrical channel *1* with the length L = 0.1 m and the radius R = 0.01 m into closed volume *2* (Fig. 1). At the initial moment of time, The channel is filled with a static mixture of high-pressure air ($p^{(1)} = 10^6$ Pa) and solid particles with a diameter of d = 1 μm, a density of ρ°_2 = 2500 kg/m^3 at thermodynamic equilibrium of $T^{(1)}_1 = T^{(1)}_2$ = 293 K. The disperse phase occupies a volume fraction of $\alpha^{(1)}_2$ = 0.1. Pure air with the parameters $p^{(2)} = 10^5$ Pa, $T^{(2)}_1$ = 293 K fills closed volume *2* outside the channel. No-slip conditions are imposed at the boundaries (the normal components of the phases are equal to zero).

Numerical simulation was based on a hybrid large-particle method [19] with centered hybrid reconstruction of phase flows in the form given in [20], suitable for solving stiff problems. The calculations are performed in a cylindrical coordinate system on a uniform mesh with the spacing of $h = L/400$ m. The time step was determined by the Courant number CFL =0.4.

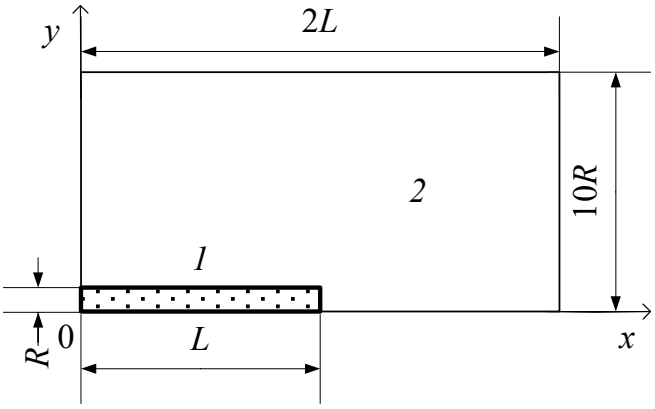

Fig. 1. Computational scheme of the problem (up to the symmetry axis 0*x*): Channel *1* of length *L* and radius *R*; closed volume *2*

Computational results

For convenience, the computational results are given in dimensionless form. Channel length L is selected as the linear scale. The phase pressures and densities are taken relative to the corresponding initial parameters in the channel, $p^{(1)}$ and $p^{(1)}_i$. The phase velocities are normalized by two values: the local speed of sound in the carrier gas $a_1 = \left(\gamma_1 p / \rho_1^{\circ}\right)^{1/2}$ or the local effective velocity of the mixture $a_e = \left[\gamma_e p / \left(\rho\alpha_1\right)\right]^{1/2}$. The effective polytropic index of the two-phase medium in the formula for a_e is found from the expression [19]:

$$\gamma_e = \left(x_1 c_v + x_2 c_2 + x_1 R_1\right) / \left(x_1 c_v + x_2 c_2\right),$$

where $x_i = \rho_i/\rho$ are the mass fractions of the phases, R_1, J/(kg·K), is the gas constant.

Time was counted in dimensionless form (Strouhal numbers) Sh = $a_e t/L$. For example, the time instant Sh =1 corresponds to the arrival of an equilibrium rarefaction wave after the initial discontinuity decays to the bottom of the channel.

The initial stage of outflow at Sh = 0.5 is shown in Fig. 2,*a* as a distribution of Mach numbers M = u_2/a_1 over a continuous grayscale. The bottom panel of the figure (Fig. 2,*b*) shows numerical schlieren images for the relative density gradient of the dispersed phase $S(\rho_2/\rho_2^{(1)})$, calculated by the technique described in [21].

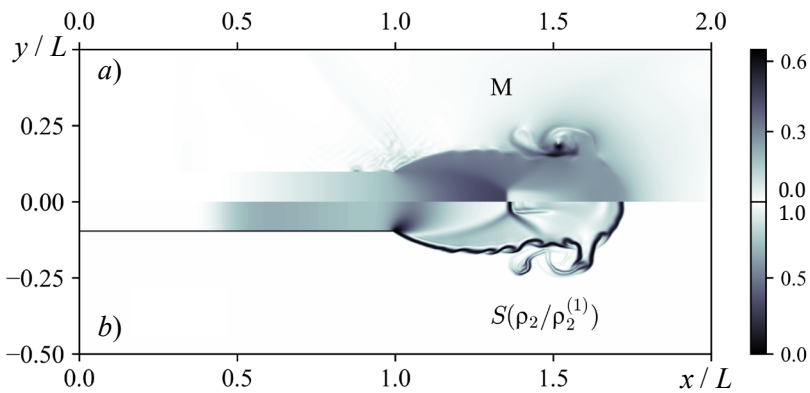

Fig. 2. Distribution of Mach numbers M in a continuous gray scale (*a*); numerical schlieren images $S(\rho_2/\rho_2^{(1)})$ as functions of the relative density gradient of the dispersed phase (*b*) (both graphs are given for the time instant Sh = 0.5)

The rarefaction wave front inside the channel reached the relative coordinate $x/L = 0.5$ at the considered instant Sh = 0.5. The first barrel shock with the Mach disk, located in the section $x/L = 1.3$, formed in the outflowing gas suspension. Primary and secondary vortex rings evolved in the head of the jet. A Kelvin–Helmholtz vortex instability develops on the side surface of the jet, visualized on the schlieren image in Fig. 2. As seen from the distribution of the Mach number, the shock-wave structure is anomalously formed in subsonic flow of carrier gas. This phenomenon was previously detected, as well as confirmed numerically and experimentally in a number of works, for example, in [14].

Bow shocks in pure gas typically form in supersonic flow. In view of this, it seems interesting to determine the concentrations of particles for which the flow regime of the gas suspension changes. For this purpose, we carried out a series of computations with above the initial data but changing the initial concentrations of the dispersed phase: $\alpha_2^{(1)} = 0.01$; 0.02; 0.10. Results are given in Fig. 3,*a* as axial distributions of Mach numbers, calculated from the local velocity of the carrier gas. The two-phase medium inside the channel in the region $0.5 < x/L < 1$ is accelerated in a one-dimensional rarefaction wave. Phase velocities in the outlet section of the tube with $x/L = 1$ are subsonic for the given particle concentrations. Their analytical values, calculated by Eqs. (19), are marked by symbols in Fig. 3,*a*.

The gas suspension subsequently accelerates after the nozzle exit to the Mach disk $1 < x/L < 1.3$ as an underexpanded two-dimensional jet. The two-phase medium at initial particle concentrations is accelerated to supersonic speeds of the carrier gas at a certain distance from the exit section. Conversely, the flow of the mixture along the symmetry axis is subsonic everywhere at $\alpha_2^{(1)} > 0.02$.

The reason for the anomaly is that a gas-dispersed medium with sufficiently fine particles acts as a 'heavy gas' whose equation of state and effective speed of sound are different from pure gas. Fig. 3,*b* shows the distributions of the Mach number normalized by the local effective speed of sound in a two-phase medium. Notably, the curves $M_e = u_2/a_e$ at the range of the rarefaction wave up to the Mach disk $0.5 < x/L < 1.3$ almost coincide for different particle concentrations in this representation. The flow velocity in the throat section, at $x/L = 1$, is equal to the local speed of sound $M_e = 1$. The gas suspension flow past the nozzle exit accelerates to supersonic velocities in a scale of a_e, up to the bow shock.

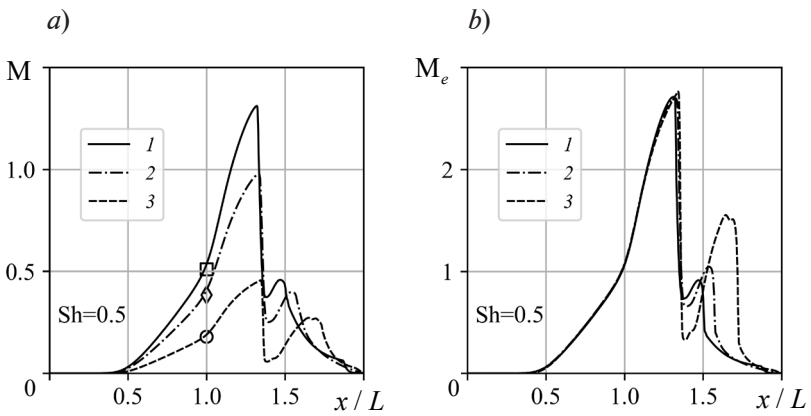

Fig. 3. Axial distributions of Mach numbers at time Sh = 0.5, computed from the local speed of sound in the carrier gas phase (*a*) and the local effective velocity of the mixture (*b*), for the initial concentrations of the dispersed phase $\alpha_2^{(1)}$: 0.001 (*1*); 0.02 (*2*); 0.10 (*3*). The symbols correspond to the analytical values of Mach numbers in the critical section for the given concentrations

Table

Maximum volume fractions of particles at dimensionless times

Sh	1	2	3	4	5	6
α_{max}	0.093	0.158	0.147	0.090	0.075	0.049

The time evolution of the gas suspension is shown as numerical schlieren images for the relative density gradient of dispersed phase $S(\rho_2/\rho_2^{(1)})$ in Fig. 4. The head of the two-phase jet reaches the wall at dimensionless time Sh = 0.72 with x/L = 2. After that, its radial expansion begins (Fig. 4,*a*). The lateral structure of two-phase flow along the symmetry axis persists until approximately Sh ≈ 2. It subsequently decays, with predominantly vortical flow observed (Fig. 4, *c*–*f*). The closed volume is largely filled by the time Sh ≈ 6, with gas suspension mixing within it.

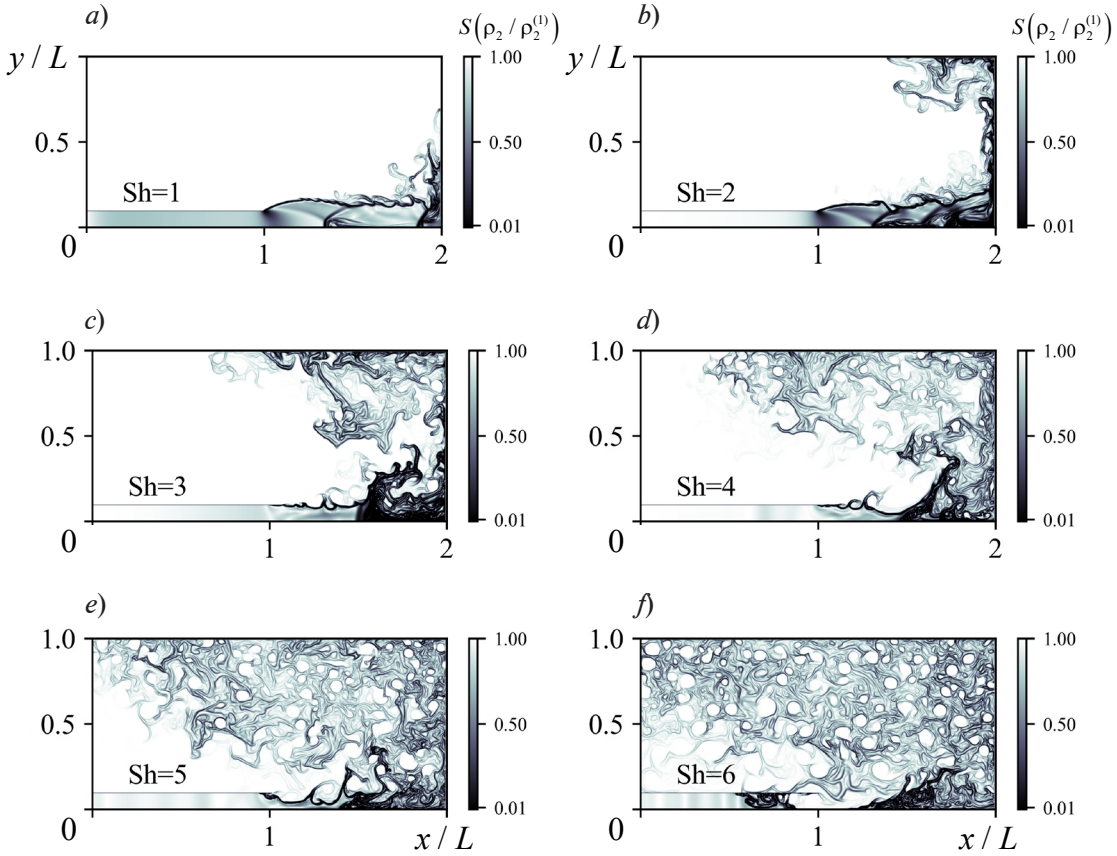

Fig. 4. Numerical schlieren images for relative density gradient of dispersed phase at successive points in time (Sh = 1– 6)

The volume fraction of particles does not reach the state of dense packaging during the process. The table gives the maximum values for the volume fractions of particles α_{max} in the entire flow field for successive dimensionless times Sh.

The pressure in the dispersed phase p_d was estimated by a more generalized model of the gas suspension [14]. The quantity p_d was estimated assuming equilibrium for the competing processes of chaotic particle motion generated by the Magnus forces and vortex flow of particles, as well as dissipation of chaotic rotation, translational motion and collisions of dispersed particles. Considering sufficiently fine chemical particles with a diameter of d = 1 μm in the range of relative motion of the mixture components $0 < |\mathbf{v}_1 - \mathbf{v}_2| < 100$ m/s, the pressure in the dispersed phase p_d is two orders of magnitude smaller than the gas dynamic pressure p in the carrier phase. The obtained estimate suggests that the collisionless model (1) is well applicable.

Correct simulation of this stage in the process, determining the turbulent characteristics, involves DNS, LES, RANS turbulence models or their combinations. At the same time, the qualitative picture of the flow is reconstructed satisfactorily. In addition, studies of instabilities developing in heterogeneous media established quantitative agreement between the data for the deformation and averaged dynamics of the interfaces obtained experimentally and computationally by various methods, for example, in simulations of the Richtmyer–Meshkov instability [22].

The hybrid large particle method provided high resolution and low dissipation for approximating the convective terms in the conservation laws on a moderately refined mesh for the problem considered.

Conclusion

A hybrid large-particle method was applied within the framework of interpenetrating continua to numerically solve the problem on pulsed outflow of the gas suspension into a volume limited by solid walls. Two characteristic time ranges of the process have been established. The wave effects on the flow of two-phase mixture with a shock-wave structure evolving are predominant at the initial stage. A series of computations yielded an initial concentration of the dispersed phase at which the flow mode is converted from anomalous subsonic to supersonic along the carrier gas phase. Developing instabilities and eddying prevail during the second time range. The capabilities of the hybrid large-particle method have been demonstrated for this class of problems. The method has low numerical viscosity in approximating the convective part of the equations and can serve as a basis for constucting numerical schemes to simulate turbulent flows of gas suspensions. We plan to make this problem the subject of our future studies.

REFERENCES

1. **Huilin L., Gidaspow D., Bouillard J., Wentie L.,** Hydrodynamic simulation of gas-solid flow in a riser using kinetic theory of granular flow, Chem. Eng. J. 95 (1–3) (2003) 1– 13.

2. **Zi C., Sun J., Yang Y., et al.,** CFD simulation and hydrodynamics characterization of solids oscillation behavior in a circulating fluidized bed with sweeping bend return, Chem. Eng. J. 307 (1 January) (2017) 604– 620.

3. **Gao X., Li T., Rogers W. A., et al.,** Validation and application of a multiphase CFD model for hydrodynamics, temperature field and RTD simulation in a pilot-scale biomass pyrolysis vapor phase upgrading reactor, Chem. Eng. J. 388 (15 May) (2020) 124279.

4. **Luge I. A., Bentzon J. R., Klingaa C. G., et al.,** Scale attachment and detachment: The role of hydrodynamics and surface morphology, Chem. Eng. J. 430, P. 2 (15 February) (2022) 132583.

5. **Volkov K. N., Emelyanov V. N.,** Modelirovaniye krupnykh vikhrey v raschetakh turbulentnykh techeniy [Large-eddy simulation of turbulent flows], Publishing House of Phys. & Math. Literature, Moscow, 2008 (in Russian).

6. **Garbaruk A. V.,** Sovremennyye podkhody k modelirovaniyu turbulentnosti [Modern approaches to turbulence simulation], Publishing House of Polytechnical Univ., St. Petersburg, 2016 (in Russian).

7. **Isaev S.A., Lysenko D.A.,** Testing of numerical methods, convective schemes, algorithms for approximation of flows, and grid structures by the example of a supersonic flow in a step-shaped channel with the use of the CFX and fluent packages, J. Eng. Phys. Thermophys. 82 (2) (2009) 321–326.

8. **Tishkin V. F., Gasilov V. A., Zmitrenko N. V., et al.,** Modern methods of mathematical modeling of the development of hydrodynamic instabilities and turbulent mixing, Matem. Mod. 32 (8) (2020) 57–90 (in Russian).

9. **Shi J., Zhang Y.-T., Shu C.-W.,** Resolution of high order WENO schemes for complicated flow structures, J. Comput. Phys. 186 (2) (2003) 690–696.

10. **Li J., Shu C.-W., Qiu J.,** Multi-resolution HWENO schemes for hyperbolic conservation laws, J. Comput. Phys. 2021. Vol. 446 (1 December) (2021) 110653.

11. **Wang B., Xiang G., Hu X. Y.,** An incremental-stencil WENO reconstruction for simulation of compressible two-phase flows, Int. J. Multiphase Flow. 104 (July) (2018) 20–31.

12. **Sadin D. V., Golikov I. O., Davidchuk V. A.,** Simulation of a shock wave interaction with a bounded inhomogeneous gas-particle layer using the hybrid large-particle method, Numerical Methods and Programming. 22 (1) (2021) 1–13 (in Russian).

13. **Sadin D. V.,** A modified large-particle method for calculating unsteady gas flows in a porous medium, Comput. Math. Math. Phys. 36 (10) (1996) 1453–1458.

14. **Sadin D. V., Lyubarskii S. D., Gravchenko Y. A.,** Features of an underexpanded pulsed impact gas-dispersed jet with a high particle concentration, Technical Physics. 62 (1) (2017) 18–23.

15. **Sadin D. V.,** Simulation of the pulsed outflow of air and fine powder mixture, partially filling the discharge channel, Scientific and Technical Journal of Information Technologies, Mechanics and Optics. 22 (1) (2022) 187–192 (in Russian).

16. **Shirokova E. N.,** A numerical study of the expansion of a gas-particles mixture with axial symmetry, Scientific and Technical Journal of Information Technologies, Mechanics and Optics. 21 (4) (2021) 606–612 (in Russian).

17. **Nigmatulin R. I.,** Dynamics of multiphase media, In 2 Vols. Hemisphere Publ. Corp., New York, USA, 1990.

18. **Ivandaev A. I., Kutushev A. G., Rudakov D. A.,** Numerical investigation of throwing a powder layer by a compressed gas, Combustion, Explosion and Shock Waves. 31 (4) (1995) 459–465.

19. **Sadin D. V.,** TVD scheme for stiff problems of wave dynamics of heterogeneous media of nonhyperbolic nonconservative type, Comput. Math. Math. Phys. 56 (12) (2016) 2068–2078.

20. **Sadin D. V.,** A modification of the large-particle method to a scheme having the second order of accuracy in space and time for shockwave flows in a gas suspension, Bulletin of the South Ural State University. Ser. Mathematical Modelling, Programming & Computer Software (Bulletin SUSU MMCS). 12 (2) (2019) 112–122 (in Russian).

21. **Quirk J. J., Karni S.,** On the dynamics of a shock-bubble interaction, J. Fluid Mech. 318 (10 July) (1996) 129–163.

22. **Wang M., Si T., Luo X.,** Experimental study on the interaction of planar shock wave with polygonal helium cylinders, Shock Waves. 25 (4) (2015) 347–355.

СПИСОК ЛИТЕРАТУРЫ

1. **Huilin L., Gidaspow D., Bouillard J., Wentie L.** Hydrodynamic simulation of gas-solid flow in a riser using kinetic theory of granular flow // Chemical Engineering Journal. 2003. Vol. 95, No. 1–3. Pp. 1– 13.

2. **Zi C., Sun J., Yang Y., Huang Z., Liao Z., Wang J., Yang Y., Han G.** CFD simulation and hydrodynamics characterization of solids oscillation behavior in a circulating fluidized bed with sweeping bend return // Chemical Engineering Journal. 2017. Vol. 307. 1 January. Pp. 604– 620.

3. **Gao X., Li T., Rogers W. A., Smith K., Gaston K., Wiggins G., Parks J. E.** Validation and application of a multiphase CFD model for hydrodynamics, temperature field and RTD simulation in a pilot-scale biomass pyrolysis vapor phase upgrading reactor // Chemical Engineering Journal. 2020. Vol. 388. 15 May. P. 124279.

4. **Lluge I. A., Bentzon J. R., Klingaa C. G., Walther J. H., Anabaraonye B. U., Fosbul P. L.** Scale attachment and detachment: The role of hydrodynamics and surface morphology // Chemical Engineering Journal. 2022. Vol. 430. Part 2. 15 February. P. 132583.

5. **Волков К. Н., Емельянов В. Н.** Моделирование крупных вихрей в расчетах турбулентных течений. М.: Физматлит, 2008. 368 с.

6. **Гарбарук А. В.** Современные подходы к моделированию турбулентности. СПб.: Изд-во Политехнического ун-та, 233 .2016 с.

7. **Исаев С. А., Лысенко Д. А.** Тестирование численных методов, конвективных схем, алгоритмов аппроксимации потоков и сеточных структур на примере сверхзвукового течения в ступенчатом канале с помощью пакетов CFX и FLUENT // Инженерно-физический журнал. 2009. Т. 2 № .82. С. 326 – 330.

8. **Тишкин В. Ф., Гасилов В. А., Змитренко Н. В., Кучугов П. А., Ладонкина М. Е., Повещенко Ю. А.** Современные методы математического моделирования развития гидродинамических неустойчивостей и турбулентного перемешивания // Математическое моделирование. 2020. Т. 32. № 8. С. 57–90.

9. **Shi J., Zhang Y.-T., Shu C.-W.** Resolution of high order WENO schemes for complicated flow structures // Journal of Computational Physics. 2003. Vol. 186. No. 2. Pp. 690–696.

10. **Li J., Shu C.-W., Qiu J.** Multi-resolution HWENO schemes for hyperbolic conservation laws // Journal of Computational Physics. 2021. Vol. 446. 1 December. P. 110653.

11. **Wang B., Xiang G., Hu X. Y.** An incremental-stencil WENO reconstruction for simulation of compressible two-phase flows // International Journal of Multiphase Flow. 2018. Vol. 104. July. Pp. 20–31.

12. **Садин Д. В., Голиков И. О., Давидчук В. А.** Моделирование взаимодействия ударной волны с ограниченным неоднородным слоем газовзвеси гибридным методом крупных частиц // Вычислительные методы и программирование. 2021. Т. 1 № .22. С. 1–13.

13. **Садин Д. В.** Модифицированный метод крупных частиц для расчета нестационарных течений газа в пористой среде // Журнал вычислительной математики и математической физики. 1996. Т. 10 № .36. С. 158–164.

14. **Садин Д. В., Любарский С. Д., Гравченко Ю. А.** Особенности недорасширенной импульсной импактной газодисперсной струи с высокой концентрацией частиц // Журнал технической физики. 2017. Т. 1 № .87. С. 22–26.

15. **Садин Д. В.** Моделирование импульсного истечения смеси воздуха и мелкодисперсного порошка, частично заполняющего выбросной канал // Научно-технический вестник информационных технологий, механики и оптики. 2022. Т. 1 № .22. С. 187–192.

16. **Широкова Е. Н.** Численное исследование разлета смеси газа и частиц с осевой симметрией // Научно-технический вестник информационных технологий, механики и оптики. 2021. Т. 4 № .21. С. 606–612.

17. **Нигматулин Р. И.** Динамика многофазных сред. Ч. 1. М.: Наука, 464 .1987 с.

18. **Ивандаев А. И., Кутушев А. Г., Рудаков Д. А.** Численное исследование метания слоя порошка сжатым газом // Физика горения и взрыва. 4 № .1995. С. 63–70.

19. **Садин Д. В.** TVD-схема для жестких задач волновой динамики гетерогенных сред негиперболического неконсервативного типа // Журнал вычислительной математики и математической физики. 2016. Т. 56. № 12. С. 2098–2109.

20. **Садин Д. В.** Модификация метода крупных частиц до схемы второго порядка точности по пространству и времени для ударно-волновых течений газовзвеси // Вестник Южно-Уральского государственного университета. Сер. Математическое моделирование и программирование. 2019. Т. 12. № 2. С. 112–122.

21. **Quirk J. J., Karni S.** On the dynamics of a shock-bubble interaction // Journal of the Fluid Mechanics. 1996. Vol. 318. 10 July. Pp. 129–163.

22. **Wang M., Si T., Luo X.** Experimental study on the interaction of planar shock wave with polygonal helium cylinders // Shock Waves. 2015. Vol. 25. No. 4. Pp. 347–355.

THE AUTHOR

SHIROKOVA Elena N.
Military Space Academy named after A.F. Mozhaysky
13 Zhdanovskaya St., St. Petersburg, 197198, Russia
shirokhelen-78@mail.ru
ORCID: 0000-0002-8188-2003

СВЕДЕНИЯ ОБ АВТОРЕ

ШИРОКОВА Елена Николаевна – *кандидат химических наук, преподаватель Военно-космической академии имени А. Ф. Можайского.*
197198, Россия, Санкт-Петербург, Ждановская ул., 13
shirokhelen-78@mail.ru
ORCID: 0000-0002-8188-2003

Received 17.04.2022. Approved after reviewing 17.05.2022. Accepted 17.05.2022.
Статья поступила в редакцию 17.04.2022. Одобрена после рецензирования 17.05.2022. Принята 17.05.2022.

Original article
DOI: https://doi.org/10.18721/JPM.15306

THE INFLUENCE OF THE TRAPPING MODEL CHOICE ON THE ADEQUATE DESCRIPTION OF HYDROGEN DIFFUSION INTO METALS FROM EXTERNAL ENVIRONMENT

P. M. Grigoreva✉

Institute for Problems of Mechanical Engineering RAS, St. Petersburg, Russia

✉ gpm@ipme.ru

Abstract: The paper considers the hydrogen diffusion into metals from their external environment. In order to properly describe a time-stable boundary layer (experimentally observed) with a hydrogen concentration being tens of times higher than that inside the body, the previously obtained hydrogen diffusion equation has been modified. This equation obtained from the first principles and taking into account the influence of the stress-strain state of solid on the transport process of the gas component, was supplemented with a stock term describing the diffusion with trapping modes. This modification was carried out in two ways: using the classical McNabb model and using the tensor of damageability. The boundary-value problem was solved for both approaches. The solution results were compared with published experimental data.

Keywords: hydrogen diffusion, trap model, solid, boundary layer, stress-strain state

Funding: The reported study was funded by Russian Science Foundation (grant 18-19-00160). The grant is entitled "Development of fundamental principles for computational and experimental hydrogen diagnostics of the propertied of structural materials in aggressive corrosive environments".

Citation: Grigoreva P. M., The influence of the trapping model choice on the adequate description of hydrogen diffusion into metals from external environment, St. Petersburg Polytechnical State University Journal. Physics and Mathematics. 15 (3) (2022) 71–82. DOI: https://doi.org/10.18721/JPM.15306

Научная статья
УДК 539.3
DOI: https://doi.org/10.18721/JPM.15306

ВЛИЯНИЕ ВЫБОРА ЛОВУШЕЧНОЙ МОДЕЛИ НА АДЕКВАТНОСТЬ ОПИСАНИЯ ДИФФУЗИИ ВОДОРОДА В МЕТАЛЛЫ ИЗ ВНЕШНЕЙ СРЕДЫ

П. М. Григорьева✉

Институт проблем машиноведения РАН, Санкт-Петербург, Россия

✉ gpm@ipme.ru

Аннотация. В работе рассматривается явление диффузии водорода в металлы из внешней среды. Для того чтобы наиболее корректно описать возникновение стабильного во времени пограничного слоя (наблюдается экспериментально), обладающего концентрацией водорода, в десятки раз превышающей его концентрацию внутри тела, модифицируется ранее полученное уравнение диффузии водорода. В это уравнение, учитывающее из первых принципов взаимовлияние между напряженно-деформированным состоянием твердого тела и процессом транспорта газового компонента, вводится стоковый член, который описывает диффузию по ловушечным модам. Указанная модификация выполняется двумя способами: с помощью классической модели МакНабба и с использованием тензора поврежденности. Для обоих подходов решается краевая задача, результаты решения сравниваются с опубликованными экспериментальными данными.

Ключевые слова: диффузия водорода, ловушечная модель, твердое тело, пограничный слой, напряженно-деформированное состояние

Финансирование: исследование выполнено при финансовой поддержке Российского научного фонда, грант № 18-19-00160 «Разработка фундаментальных основ для расчетно-экспериментальной водородной диагностики деградации свойств конструкционных материалов в агрессивных коррозионных средах».

Ссылка для цитирования: Григорьева П. М. Влияние выбора ловушечной модели на адекватность описания диффузии водорода в металлы из внешней среды // Научно-технические ведомости СПбГПУ. Физико-математические науки. 2022. Т. 15. № 3. С. 71–82. DOI: https://doi.org/10.18721/JPM.15306

Introduction

The effect of hydrogen degradation on the strength properties of metals has remained one of the most pressing problems in mechanics for over a century [1]. It is known that metals can absorb hydrogen from the external environment, consequently losing strength and fracture toughness [2], which is especially critical for industrial applications, where increasingly stringent requirements are imposed on the strength characteristics of steels. Experimental estimates and measurements of hydrogen concentration profiles in metals [3–6] suggest that hydrogen concentration in the boundary layer is dozens or even hundreds of times higher than in the entire volume of the metal. Recent experimental studies [7–9] suggest that this thin layer (its thickness is about one micrometer) has the strongest influence on the elastic properties, brittleness and viscosity of the metal. Thus, there is much theoretical and practical interest in simulation of a thin boundary layer produced by hydrogen diffusion from the environment into the metal, providing descriptions for the mutual influence between the diffusion process and the mechanical properties of the metal.

No consensus has been reached in the literature as to how to take into account the influence of mechanical stresses on diffusion. One of the first models still widely used is based on empirical

evaluation of experimental data [10]. The next generations of widespread models are based on the thermodynamics of irreversible processes, representing a generalization of Fourier-type equations that describe irreversible processes by linear differential equations with constant coefficients. This approach assumes that the diffusion rate is proportional to thermodynamic forces, which can be expressed in terms of gradients of the corresponding potentials, depending, in particular, on the stress-strain state (see, for example, [11– 13]). These additional thermodynamic forces are generally associated with a change in the volume or stiffness of the solid material or a change in gas concentration. Some studies formulate the thermodynamic force accounting for the influence of stresses in terms of the chemical potentials of materials, using Eshelby's tensor as the chemical potential of the deformable solid [14–17]. However, such models are rarely used, due to some difficulties in determining model constants. Moreover, experiments indicate that hydrogen not only diffuses through the crystalline substance of the metal, but also redistributes in trap sites [4, 18–20].

Therefore, hydrogen diffusion in metals cannot be characterized as conventional grain-boundary diffusion. Many papers on hydrogen diffusion in metals consider the trapping mechanism for this diffusion (see the fundamental studies [21, 22] and many others, e.g., [17, 23–26]). Such models are very peculiar, failing to adequately describe the entire range of diverse experimental data. Consequently, hydrogen diffusion coefficients are given in handbooks with an accuracy up to the order of magnitude (see, for example, [27]). Notably, most models for trapping and bulk diffusion have been verified for small gradients of hydrogen concentration in the material. This does not allow to account for the observed boundary layer and requires significant modification of these models.

The experimentally observed near-surface layer contains a high concentration of hydrogen, is relatively time-stable and does not expand into the bulk of the metal due to diffusion. To describe this layer more accurately, we introduced the sink term into the equation of hydrogen transport inside the metal in a stress-strain state (the equation was obtained earlier in several studies, see, for example, book [28] and references therein).

Two models introducing the sink term are considered in the study. The first is the classical McNabb model [21]. The second is an alternative model of two-channel diffusion, separately accounting for the flow through inhomogeneities inside the metal.

Hydrogen diffusion by the trapping mechanism accounting for the influence of the stress-strain state in metal

Our previous studies (see, for example, [28] and references therein) explored the approach of linear non-equilibrium thermodynamics. Assuming that the chemical potential of diffusing gas depends on Eshelby's energy-momentum tensor, a modified diffusion equation was obtained, accounting for the dependence of gas transport process inside the solid on its stress-strain state. This equation was written as follows for the case of ideal gas and linear elastic body:

$$\frac{\partial c}{\partial t} = \nabla \cdot \left(D_{eff} \nabla c + \mathbf{V} c \right). \tag{1}$$

The effective diffusion coefficient D_{eff} was defined as

$$D_{eff} = D_0 \left(1 + \frac{cM}{RT\rho} \frac{E}{1-2\nu} \left[-\alpha \mathrm{tr}\boldsymbol{\varepsilon} + 3\alpha^2 c \right] \right). \tag{2}$$

The proposed additional term taking the form $\mathbf{V}c$ expresses a drag force proportional to the concentration, where the proportionality factor follows the expression

$$\mathbf{V} = \frac{D_0 ME}{RT\rho} \left(\frac{\nu}{(1+\nu)(1-2\nu)} \mathrm{tr}\boldsymbol{\varepsilon} \nabla (\mathrm{tr}\boldsymbol{\varepsilon}) - \frac{1}{1-2\nu} \alpha c \nabla (\mathrm{tr}\boldsymbol{\varepsilon}) + \frac{1}{2(1+\nu)} \nabla (\boldsymbol{\varepsilon} \cdot\cdot \boldsymbol{\varepsilon}) \right). \tag{3}$$

The following notations are used in Eqs. (2) and (3): c is the concentration of hydrogen in diffusive motion; T is the temperature; R is the universal gas constant; M, ρ are the molar mass and density of the solid; D_0 is temperature-dependent principal values.

Additionally, this notation of the diffusion equation takes into account that the diffusing gas induces internal strains $\boldsymbol{\varepsilon}_{diff,}$ proportional to the concentration and exhibiting isotropic behavior: $\boldsymbol{\varepsilon}_{diff} = \alpha c\mathbf{E}$ ($\mathbf{E}$ is the unit tensor).

Evidently, the last term of expressions (2) and (3) can be discarded due to smallness in the case of linear theory, since the linear strain tensor is included. However, the diffusion equation also takes a non-classical form in this case; moreover, it contains additional terms aside from the widely used diffusion models, accounting for the stress-strain state by means of a pressure gradient (this is the factor $\nabla(\mathrm{tr}\varepsilon)$ for the proposed model).

The obtained diffusion equation does indeed yield high gradients of gas concentration inside the solid for solutions of specific boundary-value problems, while its concentration profile is equalized more slowly as the sample under consideration is saturated with the gas component. These results suggest that the proposed diffusion equation can be used to describe the transport of hydrogen into the metal from the external environment. However, no internal stresses can cause almost a hundred-fold difference in gas concentrations at the interface and in the bulk of the solid within this approach, which means that an additional diffusion channel needs to be taken into account.

As mentioned above, many studies into the processes associated with hydrogen degradation of metals assume that diffusion of hydrogen in the metal is governed by the trapping mechanism. The trapping mechanisms can differ in nature and depend on both the mechanical and thermodynamic characteristics of the metal-hydrogen system. Classical models accounting for trapping diffusion are the McNabb model of hydrogen interchange [21] or its simplified version, excluding the dependence of the interchange rate on time, proposed by Oriani [22].

We intend to use the McNabb model along with the modified diffusion equation (1) to more accurately describe the experimentally observed near-surface layer with a high concentration of hydrogen, which is relatively stable over time and is not diffused into the bulk of the metal over time. Although this trapping model is most commonly used to solve problems related to hydrogen diffusion, it has never been used this far to solve boundary-value problems accounting for the influence of the stress-strain state of the metal on the diffusion process from first principles.

The processes of bulk diffusion and trapping diffusion are believed to proceed independently from each other. Therefore, we can decompose the total hydrogen concentration into a sum of two concentrations:

$$c = c_{vd} + c_{trap}, \tag{4}$$

where c_{vd} is the concentration of hydrogen diffused by the bulk mechanism; c_{trap} is the concentration of hydrogen diffused by the trapping sites.

Hydrogen concentration in the traps is calculated by introducing two additional quantities: θ_{trap} is the degree of trap occupancy and N_{trap} is the density of trap distribution.

Accordingly, the hydrogen concentration in the traps is then expressed as

$$c_{trap} = \theta_{trap} N_{trap}. \tag{5}$$

The trap density N_{trap} is assumed to be known (from the experiment or additional constitutive equations). For consistency with the data published in the literature, we assume that the N_{trap} is a time-independent quantity.

To find the trap occupancy, we introduce an additional constitutive equation incorporating two more quantities, similarly to the approach for c_{trap} in Eq. (5): θ_{vd} is the occupancy of grain boundaries; N_{vd} is the density of grain boundaries into which mobile hydrogen can diffuse.

According to the data given in [21], the constitutive equation for θ_{trap} is as follows:

$$\frac{\partial \theta_{trap}}{\partial t} = p\theta_{vd}\left(1 - \theta_{trap}\right) - k\theta_{trap}, \tag{6}$$

where p, k are the parameters of the material (metal) determined experimentally.

To account for the dependences of the diffusion process and the concentration c_{vd} on the stress-strain state of the solid, we use Eq. (1). Only terms of first-order smallness are taken in expressions (2) and (3) The system of equations for finding the concentration profile of the gas component in the solid, taking into account diffusion by the trapping mechanism, is then written as follows:

$$\begin{cases} \dfrac{\partial c_{vd}}{\partial t} + N_{trap}\dfrac{\partial \theta_{trap}}{\partial t} = \nabla\cdot\left(D_{eff}\nabla c_{vd} + \mathbf{V}c_{vd}\right) \\ \dfrac{\partial \theta_{vd}}{\partial t} = p\theta_{vd}\left(1-\theta_{trap}\right) - k\theta_{trap} \\ D_{eff} = D_0\left(1 - \dfrac{cM}{RT\rho}\dfrac{E}{1-2\nu}\alpha \mathrm{tr}\boldsymbol{\varepsilon}\right) \\ \mathbf{V} = \dfrac{D_0 ME}{RT\rho}\left(\dfrac{\nu}{(1+\nu)(1-2\nu)}\mathrm{tr}\boldsymbol{\varepsilon} - \dfrac{1}{1-2\nu}\alpha c\right)\nabla(\mathrm{tr}\boldsymbol{\varepsilon}) \\ c = c_{vd} + N_{trap}\theta_{trap} \\ \nabla\cdot\left[\dfrac{\nu}{1-2\nu}\left(\mathrm{tr}\boldsymbol{\varepsilon} - 3\alpha c\right)\mathbf{E} + \left(\boldsymbol{\varepsilon} - \alpha c\mathbf{E}\right)\right] = 0. \end{cases} \tag{7}$$

The last equation in system (7) is the elasticity equation, accounting for the deformations induced by diffused hydrogen.

It is assumed in the available literature (see, for example, [29–31]) that trapping sites are associated with inhomogeneities within the metal (nanopores, dislocations, microcracks, etc.) where diffusing hydrogen accumulates. Recent experimental studies [32, 33] considering damage in metals provide data for distribution of damage over the bulk of metals. In particular, the concept of scalar damage is extended in [33] to proposes a damage tensor **D**, defined as

$$\left(\mathbf{E}-\mathbf{D}\right)\cdot\mathbf{n}\delta S = \bar{\mathbf{n}}\left(\delta S - \delta S_T\right), \tag{8}$$

where δS is the area of some site; δS_T is the area of damage in this site; $\bar{\mathbf{n}}$ is the normal defining the given flow; $\underline{\mathbf{n}}$ is the normal to the site.

Since trapping diffusion is in fact an additional flow through the defects in the solid (microcracks, pores, dislocations, etc.), multichannel diffusion can be suggested as an alternative to the McNabb approach, assuming flow of hydrogen through the metal defects in addition to the standard diffusion flow in the system; the gas component is deposited on these defects. Since the diffusive flow of gas **j** is expressed as

$$\mathbf{j} = \rho\mathbf{V}S,$$

where **V** is the flow velocity vector of the diffusing gas; ρ is the gas density; S is the area of the site through which this gas flows, we obtain that the additional flow through trapping sites $\mathbf{j}_{trap}$ is

$$\mathbf{j}_{trap} = \mathbf{D}\cdot\mathbf{j}, \tag{9}$$

and thus the diffusion equation in this case takes the form

$$\frac{\partial c}{\partial t} = \nabla\cdot\left[\left(\mathbf{E}-\mathbf{D}\right)\cdot\left(D_{eff}\nabla c + \mathbf{V}c\right)\right]. \tag{10}$$

The equivalent of the sink term here is

$$-\nabla\cdot\left[\mathbf{D}\cdot\left(D_{eff}\nabla c+\mathbf{V}c\right)\right]. \tag{11}$$

The system of equations for finding the concentration profile of the gas component in the solid, taking into account diffusion by the trapping mechanism, is then written as follows:

$$\begin{cases} \dfrac{\partial c}{\partial t}=\nabla\cdot\left[\left(\mathbf{E}-\mathbf{D}\right)\cdot\left(D_{eff}\nabla c+\mathbf{V}c\right)\right] \\ D_{eff}=D_0\left(1-\dfrac{cM}{RT\rho}\dfrac{E}{1-2\nu}\alpha\,\mathrm{tr}\boldsymbol{\varepsilon}\right) \\ \mathbf{V}=\dfrac{D_0ME}{RT\rho}\left(\dfrac{\nu}{(1+\nu)(1-2\nu)}\mathrm{tr}\boldsymbol{\varepsilon}-\dfrac{1}{1-2\nu}\alpha c\right)\nabla(\mathrm{tr}\boldsymbol{\varepsilon}) \\ \nabla\cdot\left[\dfrac{\nu}{1-2\nu}\left(\mathrm{tr}\boldsymbol{\varepsilon}-3\alpha c\right)\mathbf{E}+\left(\boldsymbol{\varepsilon}-\alpha c\mathbf{E}\right)\right]=0. \end{cases} \tag{12}$$

Since most experiments are carried out with cylindrical specimens, where the tensile stresses are applied along their symmetry axes, we verify the model by considering a cylinder under uniaxial tension as a boundary-value problem (Fig. 1). It is assumed that the length of the cylinder along the z axis significantly exceeds its radius r_{out}, and hydrogen penetrates only from the lateral surface. Therefore, the deformations that occur in the cylinder and the concentration of hydrogen inside it depend only on the coordinate r, by virtue of symmetry.

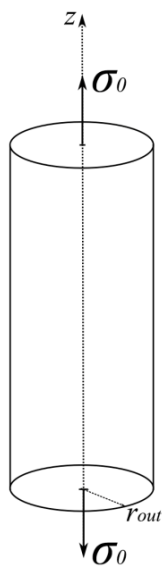

Fig. 1. Scheme for the formulation of the boundary-value problem: a cylindrical specimen with the radius r_{out} is exposed to axial tensile stresses σ_0 and gas flow from the lateral surface

The boundary conditions for finding the stress-strain state are given by the uniaxial tensile stress σ_0 and the stress-free lateral surface, and by the concentration of the gas component given on the lateral surface for the diffusion problem.

Notably, the elasticity equation contains components that depend on the concentration, and the diffusion equation contains coefficients that depend on deformations (both in r and in z directions). Thus, we obtain a conjugate problem, and these two equations cannot be solved separately. The boundary-value problem (both the elasticity problem and the diffusion equation) is solved numerically using an explicit finite difference scheme that corresponds to the finite volume method. To examine the surface effects in more detail, we constructed a mesh clustered to the surface of the specimen (i.e., with the coordinate r close to r_{out}). Discrete formulations of the corresponding integral balance equations were considered in the scheme instead of the differential equations for local balances. Displacements and concentration were given in the nodes of the mesh, and strains, stresses and diffusivities were given in the cells. The scheme itself is verified and analyzed for convergence for a particular case of a one-dimensional diffusion problem in a cylindrical coordinate system with a constant diffusivity in the absence of a stress-strain state.

Experimental data for the calculations are taken from [34] for T24 steel. The parameter α, corresponding to expansion due to hydrogen diffusion, is tailored so that all deformations of the solid remain within the linear-elastic range. The selected parameters are given in the table. The distribution of traps and vacancies for diffusively mobile hydrogen and the parameters *p* and *k* for the McNabb model are taken from [35, 36]; the values of damage depending on the coordinate and necessary for calculating the radial component of the tensor are taken from [32].

Table

Parameters of the simulated solid and gas component

Parameter	Notation	Unit	Value
Diffusion coefficient	D_0	mm/s^2	$3.5\cdot10^{-9}$
Temperature	T	K	293
Young's modulus	E	GPa	182
Poisson's ratio	ν	–	0.295
Steel density ratio to molar mass	ρ/M	mol/m^3	$1.45\cdot10^4$
External radius of cylinder	r_{out}	mm	1.1
Coefficient of thermal expansion	α	–	0.03

Fig. 2 shows the solutions to the diffusion problem accounting for the diffusion of hydrogen by the trapping mechanism. The concentration profile obtained by the McNabb model (Fig. 2,*a*) practically does not penetrate into the bulk of the metal over time, exhibiting the same locking effect and near-surface layer formation that was observed experimentally. Notably, however, this result was obtained using the phenomenological dependence N_{trap} on the coordinate [35], constructed assuming a highly uneven distribution of hydrogen throughout the sample as a result of its transport from the external environment. Varying the parameter N_{vd} does not produce a significant change in the concentration profiles and redistribution of hydrogen during diffusion.

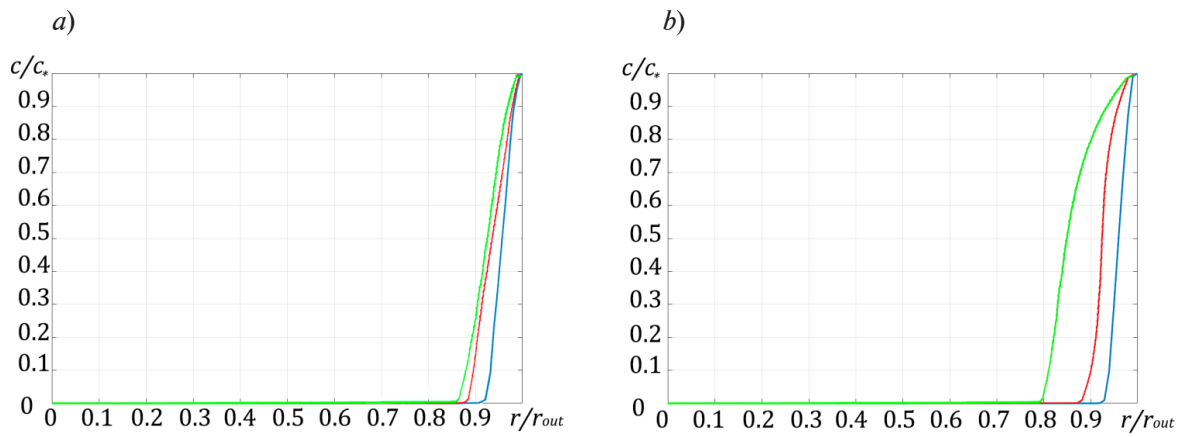

Fig. 2. Dependences of normalized hydrogen concentration in the solid on normalized radius at different times with a step of 600 minutes); the computational data are obtained using the McNabb trap model, provided that the distribution of N_{trap} is non-uniform (*a*), and a modified model accounting for flow through trapping sites by a damage tensor (*b*)

Accounting for hydrogen diffusion through traps based on the damage tensor (Fig. 2, *b*) eliminates a pronounced locking effect, while the concentration gradient tends to smooth out, and the hydrogen itself moves deep into the metal specimen. Apparently, the result obtained suggests that the components of the damage tensor are time-independent, so it is impossible to take into account the degree of occupancy of these traps, as well as the redistribution of hydrogen from the traps to the grain boundaries (and vice versa). However, this approach also remains attractive for further research, since the values of damage tensor components and their dependence on the coordinate can be calculated independently.

Conclusion

The paper theoretically investigates the diffusion of hydrogen into a solid in a stress-strain state, considering the mutual influence between the deformations inside the body and hydrogen transport from the external environment surrounding the solid. A modification of an earlier model is proposed to more accurately describe the experimentally observed near-surface layer with a high concentration of hydrogen, which is relatively time-stable and does not expand into the bulk of the metal due to diffusion. The diffusion equation obtained this way, taking into account the influence of the stress-strain state on the diffusion process, contains a sink term reflecting hydrogen flow by the trapping mechanism as the second diffusion channel. This modification was carried out in two ways: using the classical McNabb model and within the concept of damage.

A boundary-value problem was solved for the modified diffusion equation with the new sink term, the results were analyzed and compared. We have found that the results differ slightly, but movement of the diffusion front and ‘smearing’ of the near-surface hydrogen layer are slower for the McNabb model, which is more consistent with the experimental data.

Notably, the concept of damage allows to avoid some of the physical contradictions that inevitably arise within the McNabb model. These contradictions are removed if the flow of hydrogen is considered by the trapping mechanism within the concept of damage. However, because this model cannot account for the occupancy of traps and does not include a mechanism for redistribution of hydrogen within the solid (from trapping sites to grain boundaries and vice versa), the computational results are less consistent with the experimental data. We can thus conclude that the modification of the model is insufficient and requires further elaboration.

REFERENCES

1. **Cailletet M. L.,** First report of H embrittlement of metals, Compt. Rend. 58 (23) (1864) 327–328.
2. **Khrustalev Yu. A., Simakov Yu. S., Glazunov M. P., Gubin V. V.,** Obrazovaniye vodoroda pri sukhom trenii metallov [Hydrogen formation at dry friction of the metals] Zhurnal Fizicheskoy Khimii [Russian Journal of Physical Chemistry] 63 (5) (1989) 1355–1357 (in Russian).
3. **Frolova K., Vilchevskaya E., Polyanskiy V., Alekseeva E.,** Modelling of a hydrogen saturated layer within the micropolar approach, In Book: "New Achievements in Continuum Mechanics and Thermodynamics", Edited by Abali B., et al., Book Series: Advanced Structured Materials. Vol. 108. Springer, Cham (2019) 117–128.
4. **López-Suárez A., Valencia C. E., López-Patico J., et al.,** Improvement of titanium hydrogenation by low energy ion irradiation, Int. J. Hydrog. Energy. 40 (11) (2015) 4194–4199.
5. **Wu T.-I., Wu J.-Ch.,** Effects of cathodic charging and subsequent solution treating parameters on the hydrogen redistribution and surface hardening of Ti–6Al–4V alloy, J. Alloys Compd. 466 (1–2) (2008) 153–159.
6. **Martinsson E., Sandström R.,** Hydrogen depth profile in phosphorus-doped, oxygen-free copper after cathodic charging, J. Mater. Sci. 47 (19) (2012) 6768–6776.
7. **Arseniev D. G., Belyaev A. K., Polyanskiy A. M., et al.,** Benchmark study of measurements of hydrogen diffusion in metals, In book: 'Dynamical Processes in Generalized Continua and Structures", Ed. by Altenbach H., et al., Book Ser. "Advanced Structured Materials" Springer Cham, Switzerland (2019) 37–61.
8. **Polyanskiy V. A., Belyaev A. K., Alekseeva E. L., et al.,** Phenomenon of skin effect in metals due to hydrogen absorption, Contin. Mech. Thermodyn. 31 (6) (2019) 1961–1975.
9. **Andronov D. Y., Arseniev D. G., Polyanskiy A. M., et al.,** Application of multichannel diffusion model to analysis of hydrogen measurements in solid, Int. J. Hydrog. Energy. 42 (1) (2017) 699–710.
10. **Sutardja P., Oldham W. G.,** Modeling of stress effects in silicon oxidation, IEEE Trans. Electron Devices. 36 (11) (1989) 2415–2421.
11. **Birnbaum H. K., Sofronis P.,** Hydrogen-enhanced localized plasticity – a mechanism for hydrogen-related fracture, Mater. Sci. Eng. A. 176 (1–2) (1994) 191–202.
12. **Stashchuk M., Dorosh M.,** Analytical evaluation of hydrogen induced stress in metal, Int. J. Hydrog. Energy. 42 (9) (2017) 6394–6400.
13. **Drexler A, Bergmann C., Manke G., et al.,** On the local evaluation of the hydrogen susceptibility of cold-formed and heat treated advanced high strength steel (AHSS) sheets, Mater. Sci. Eng. A. 800 (7 January) (2021) 140276.
14. **Larcht'e F. C., Cahn J. L.,** The effect of self-stress on diffusion in solids, Acta Metallurg. 30 (10) (1982) 1835–1845.
15. **Wu Ch. H.** The role of Eshelby stress in composition-generated and stress-assisted diffusion, J. Mech. Phys. Solids. 49 (8) (2001) 1771–1794.
16. **Knyazeva A. G.,** Cross effects in solid media with diffusion, J. Appl. Mech. Techn. Phys. 44 (3) (2003) 373–384.
17. **Toribio J., Kharin V., Lorenzo M., Vergara D.,** Role of drawing-induced residual stresses and strains in the hydrogen embrittlement susceptibility of prestressing steels, Corr. Sci. 53 (10) (2011) 3346–3355.
18. **Hadam U., Zakroczymski T.,** Absorption of hydrogen in tensile strained iron and high-carbon steel studied by electrochemical permeation and desorption techniques, Int. J. Hydrog. Energy. 34 (5) (2009) 2449–2459.
19. **Turnbull A.** Perspectives on hydrogen uptake, diffusion and trapping, Int. J. Hydrog. Energy. 40 (47) (2015) 16961–16970.
20. **Liu Q., Venezuela J., Zhang M., et al.,** Hydrogen trapping in some advanced high strength steels, Corr. Sci. 111 (October) (2016) 770–785.
21. **McNabb A., Foster P. K.,** A new analysis of diffusion of hydrogen in iron and ferritic steels, Trans. Metallurg. Soc. AIME. 227 (3) (1963) 618–627.
22. **Oriani R. A.,** The diffusion and trapping of hydrogen in steel, Acta Metallurg. 18 (1) (1970) 147–157.
23. **Oudriss A., Creus J., Bouhattate J., et al.,** Grain size and grain-boundary effects on diffusion and trapping of hydrogen in pure nickel, Acta Mater. 60 (19) (2012) 6814–6828.

24. **Takahashi J., Kawakami K., Kobayashi Y.,** Origin of hydrogen trapping site in vanadium carbide precipitation strengthening steel, Acta Mater. 153 (July) (2018) 193–204.

25. **Depover T., Van den Eeckhout E., Verbeken K.,** Hydrogen induced mechanical degradation in tungsten alloyed steels, Mater. Charact. 136 (February) (2018) 84–93.

26. **Zhang Zh., Moore K. L., McMahon G., et al.,** On the role of precipitates in hydrogen trapping and hydrogen embrittlement of a nickel-based superalloy, Corr. Sci. 146 (January) (2019) 58–69.

27. Handbook of physical quantities, 1st edition, Ed. by Grigoriev I. S., Meilikhov E. Z., CRC Press, Florida, USA, 1997.

28. **Grigoreva P. M., Vilchevskaya E. N., Polyanskiy V. A.,** Influence of linear elastic stresses on hydrogen diffusion into metals, In book: Advances in Hydrogen Embrittlement Study., Ed. by V. A. Polyanskiy and A. K. Belyaev. Springer, Cham, Switzerland (2021) 143–157.

29. **Hu J., Liu J., Lozano-Perez S., et al.,** Hydrogen pickup during oxidation in aqueous environments: The role of nano-pores and nano-pipes in zirconium oxide films, Acta Mater. 180 (November) (2019) 105–115.

30. **Pressouyre G. M., Bernstein I. M.,** An example of the effect of hydrogen trapping on hydrogen embrittlement, Metallurg. Trans. A. 12 (5) (1981) 835–844.

31. **Chen L., Xiong X., Tao X., et al.,** Effect of dislocation cell walls on hydrogen adsorption, hydrogen trapping and hydrogen embrittlement resistance, Corr. Sci. 166 (15 April) (2020) 108428.

32. **Semenov A. S., Polyanskiy V. A., Shtukin L. V., Tretyakov, D. A.** Effect of surface layer damage on acoustic anisotropy, Journal of Applied Mechanics & Technical Physics. 59 (6) (2018) 1136–1134.

33. **Belyayev A. K., Polyanskiy V. A., Tretyakov D. A.,** Estimating of mechanical stresses, plastic deformations and damage by means of acoustic anisotropy, PNRPU Mechanics Bulletin. (4) (2020) 130–151 (in Russian).

34. **Rhode M., Mente T., Steppan E., et al.,** Hydrogen trapping in T24 Cr-Mo-V steel weld joints – microstructure effect vs. experimental influence on activation energy for diffusion, Weld. World. 2018. Vol. 62 (2) (2018) 277–287.

35. **Taha A., Sofronis P.,** A micromechanics approach to the study of hydrogen transport and embrittlement, Eng. Fract. Mech. 68 (6) (2001) 803–837.

36. **Sofronis P., Lufrano J.,** Interaction of local elastoplasticity with hydrogen: embrittlement effects, Mater. Sci. Eng. A. 260 (1–2) (1999) 41–47.

СПИСОК ЛИТЕРАТУРЫ

1. **Cailletet M. L.** First report of H embrittlement of metals // Comptes Rendus Chemie. 1864. Vol. 58. No. 23. Pp. 327–328.

2. Хрусталев Ю. А., Симаков Ю. С., Глазунов М. П., Губин В. В. Образование водорода при сухом трении металлов // Журнал физической химии. 1989. Т. 63. № 5. С. 1355–1357.

3. **Frolova K., Vilchevskaya E., Polyanskiy V., Alekseeva E.** Modelling of a hydrogen saturated layer within the micropolar approach // New Achievements in Continuum Mechanics and Thermodynamics. Edited by Abali B., et al. Book Series: Advanced Structured Materials. Vol. 108. Springer, Cham, 2019. Pp. 117–128.

4. **López-Suárez A., Valencia C. E., López-Patico J., Vargas M. C., Fuentes B. E.** Improvement of titanium hydrogenation by low energy ion irradiation // International Journal of Hydrogen Energy. 2015. Vol. 40. No. 11. Pp. 4194–4199.

5. **Wu T.-I., Wu J.-Ch.** Effects of cathodic charging and subsequent solution treating parameters on the hydrogen redistribution and surface hardening of Ti–6Al–4V alloy // Journal of Alloys and Compounds. 2008. Vol. 466. No. 1–2. Pp. 153–159.

6. **Martinsson E., Sandström R.** Hydrogen depth profile in phosphorus-doped, oxygen-free copper after cathodic charging // Journal of Materials Science. 2012. Vol. 47. No. 19. Pp. 6768–6776.

7. **Arseniev D. G., Belyaev A. K., Polyanskiy A. M., Polyanskiy V. A., Yakovlev Yu. A.** Benchmark study of measurements of hydrogen diffusion in metals // Dynamical Processes in Generalized Continua and Structures. Ed. by Altenbach H., et al. Book Series “Advanced Structured Materials” Switzerland: Springer, Cham, 2019. Pp. 37–61.

8. **Polyanskiy V. A., Belyaev A. K., Alekseeva E. L., Polyanskiy A. M., Tretyakov D. A., Yakovlev Yu. A.** Phenomenon of skin effect in metals due to hydrogen absorption // Continuum Mechanics and Thermodynamics. 2019. Vol. 31. No. 6. Pp. 1961–1975.

9. **Andronov D. Y., Arseniev D. G., Polyanskiy A. M., Polyanskiy V. A., Yakovlev Y. A.** Application of multichannel diffusion model to analysis of hydrogen measurements in solid // International Journal of Hydrogen Energy. 2017. Vol. 42. No. 1. Pp. 699–710.

10. **Sutardja P., Oldham W. G.** Modeling of stress effects in silicon oxidation // IEEE Transactions on Electron Devices. 1989. Vol. 36. No. 11. Pp. 2415–2421.

11. **Birnbaum H. K., Sofronis P.** Hydrogen-enhanced localized plasticity – a mechanism for hydrogen-related fracture // Materials Science and Engineering A. 1994. Vol. 176. No. 1–2. Pp. 191–202.

12. **Stashchuk M., Dorosh M.** Analytical evaluation of hydrogen induced stress in metal // International Journal of Hydrogen Energy. 2017. Vol. 42. No. 9. Pp. 6394–6400.

13. **Drexler A, Bergmann C., Manke G., Kokotin V., Mraczek K., Pohl M., Ecker W.** On the local evaluation of the hydrogen susceptibility of cold-formed and heat treated advanced high strength steel (AHSS) sheets // Materials Science & Engineering. A. 2021. Vol. 800. 7 January. P. 140276.

14. **Larcht'e F. C., Cahn J. L.** The effect of self-stress on diffusion in solids // Acta Metallurgica. 1982. Vol. 30. No. 10. Pp. 1835–1845.

15. **Wu Ch. H.** The role of Eshelby stress in composition-generated and stress-assisted diffusion // Journal of the Mechanics and Physics of Solids. 2001. Vol. 49. No. 8. Pp. 1771–1794.

16. **Knyazeva A. G.** Cross effects in solid media with diffusion // Journal of Applied Mechanics and Technical Physics. 2003. Vol. 44. No. 3. Pp. 373–384.

17. **Toribio J., Kharin V., Lorenzo M., Vergara D.** Role of drawing-induced residual stresses and strains in the hydrogen embrittlement susceptibility of prestressing steels // Corrosion Science. 2011. Vol. 53. Vol. 10. Pp. 3346–3355.

18. **Hadam U., Zakroczymski T.** Absorption of hydrogen in tensile strained iron and high-carbon steel studied by electrochemical permeation and desorption techniques // International Journal of Hydrogen Energy. 2009. Vol. 34. No. 5. Pp. 2449–2459.

19. **Turnbull A.** Perspectives on hydrogen uptake, diffusion and trapping // International Journal of Hydrogen Energy. 2015. Vol. 40. No. 47. Pp. 16961–16970.

20. **Liu Q., Venezuela J., Zhang M., Zhou Q., Atrens A.** Hydrogen trapping in some advanced high strength steels // Corrosion Science. 2016. Vol. 111. October. Pp. 770–785.

21. **McNabb A., Foster P. K.** A new analysis of diffusion of hydrogen in iron and ferritic steels // Transactions of the Metallurgical Society of AIME. 1963. Vol. 227. No. 3. Pp. 618–627.

22. **Oriani R. A.** The diffusion and trapping of hydrogen in steel // Acta Metallurgica. 1970. Vol. 18. No. 1. Pp. 147–157.

23. **Oudriss A., Creus J., Bouhattate J., Conforto E., Berziou C., Savall C., Feaugas X.** Grain size and grain-boundary effects on diffusion and trapping of hydrogen in pure nickel // Acta Materialia. 2012. Vol. 60. No. 19. Pp. 6814–6828.

24. **Takahashi J., Kawakami K., Kobayashi Y.** Origin of hydrogen trapping site in vanadium carbide precipitation strengthening steel // Acta Materialia. 2018. Vol. 153. July. Pp. 193–204.

25. **Depover T., Van den Eeckhout E., Verbeken K.** Hydrogen induced mechanical degradation in tungsten alloyed steels // Materials Characterization. 2018. Vol. 136. February. Pp. 84–93.

26. **Zhang Zh., Moore K. L., McMahon G., Morana R., Preuss M.** On the role of precipitates in hydrogen trapping and hydrogen embrittlement of a nickel-based superalloy // Corrosion Science. 2019. Vol. 146. January. Pp. 58–69.

27. Физические величины. Справочник. Ред. И. С. Григорьев, Е. З. Мейлихов. М.: Энергоатомиздат, 1991. 1232 с.

28. **Grigoreva P. M., Vilchevskaya E. N., Polyanskiy V. A.** Influence of linear elastic stresses on hydrogen diffusion into metals // Advances in Hydrogen Embrittlement Study. Ed. by V. A. Polyanskiy and A. K. Belyaev. Switzerland: Springer, Cham, 2021. Pp. 143–157.

29. **Hu J., Liu J., Lozano-Perez S., Grovenor C. R. M., Christensen M., Wolf W., Wimmer E., Mader E. V.** Hydrogen pickup during oxidation in aqueous environments: The role of nano-pores and nano-pipes in zirconium oxide films // Acta Materialia. 2019. Vol. 180. November. Pp. 105–115.

30. **Pressouyre G. M., Bernstein I. M.** An example of the effect of hydrogen trapping on hydrogen embrittlement // Metallurgical Transactions A. 1981. Vol. 12. No. 5. Pp. 835–844.

31. **Chen L., Xiong X., Tao X., Su Y., Qiao L.** Effect of dislocation cell walls on hydrogen adsorption, hydrogen trapping and hydrogen embrittlement resistance. // Corrosion Science. 2020. Vol. 166. 15 April. P. 108428.

32. **Семенов А. С., Полянский В. А., Штукин Л. В., Третьяков Д. А.** Влияние поврежденности поверхностного слоя на акустическую анизотропию // Прикладная механика и техническая физика. 2018. Т. 59. № 6. С. 201–210.

33. **Беляев А. К., Полянский В. А., Третьяков Д. А.** Оценка механических напряжений, пластических деформаций и поврежденности посредством акустической анизотропии // Вестник Пермского национального исследовательского политехнического университета. Механика. 2020. № 4. С. 130–151.

34. **Rhode M., Mente T., Steppan E., Steger J., Kannengiesser T.** Hydrogen trapping in T24 Cr-Mo-V steel weld joints – microstructure effect vs. experimental influence on activation energy for diffusion // Welding in the World. 2018. Vol. 62. No. 2. Pp. 277–287.

35. **Taha A., Sofronis P.** A micromechanics approach to the study of hydrogen transport and embrittlement // Engineering Fracture Mechanics. 2001. Vol. 68. No. 6. Pp. 803–837.

36. **Sofronis P., Lufrano J.** Interaction of local elastoplasticity with hydrogen: embrittlement effects // Materials Science & Engineering. A. 1999. Vol. 260. No. 1–2. Pp. 41–47.

THE AUTHOR

GRIGOREVA Polina M.
Institute for Problems of Mechanical Engineering RAS
61 Bolshoi Ave., V. Isl., St. Petersburg, 199178, Russia
gpm@ipme.ru
ORCID: 0000-0001-9846-7888

СВЕДЕНИЯ ОБ АВТОРЕ

ГРИГОРЬЕВА Полина Михайловна – *стажер-исследователь Института проблем машиноведения РАН.*
199178, Россия, г. Санкт-Петербург, Большой проспект В.О., 61.
gpm@ipme.ru
ORCID: 0000-0001-9846-7888

Received 01.04.2022. Approved after reviewing 24.05.2022. Accepted 24.05.2022.
Статья поступила в редакцию 01.04.2022. Одобрена после рецензирования 24.05.2022. Принята 24.05.2022.

Original article
DOI: https://doi.org/10.18721/JPM.15307

RECONSTRUCTING THE THERMAL PROCESS MODEL USING THE TIME-SPACE DISTRIBUTIONS OF TEMPERATURE

N. Yu. Bykov[1, 2]✉

[1] ITMO University, St. Petersburg, Russia

[2] Peter the Great St. Petersburg Polytechnic University, St. Petersburg, Russia

✉ nbykov2006@yandex.ru

Abstract. The method of generative model design (GMD) has been applied to reconstruct the structure and coefficients of a partial differential equation describing the target's heating and its evaporation by laser radiation. The initial synthetic data includes heating scenarios corresponding to surface energy absorption or to volume one. It was shown that reconstructing the model correctly required the use of a preprocessing technique providing the exclusion of a part of the initial data if the volume absorption took place. A modification of the method that made it possible to take into account the temperature dependence of the coefficients of the reconstructed equation was put forward. The influence of various statistical criteria used in selecting the optimal subset of elements on the accuracy of reconstructing the equation structure was discussed. The efficiency of the GMD was demonstrated for a wide range of target heating parameters and different options for setting the energy input. The possibility of model generating by noisy data was shown.

Keywords: method of generative model design, data-driven model, heat transfer equation, laser heating and evaporation

Funding: The reported study was funded by Russian Science Foundation (Grant 21-11-00296).

Citation: Bykov N. Yu., Reconstructing the thermal process model using the time-space distributions of temperature, St. Petersburg Polytechnical State University Journal. Physics and Mathematics. 15 (3) (2022) 83–99. DOI: https://doi.org/10.18721/JPM.15307

Научная статья
УДК 519.6
DOI: https://doi.org/10.18721/JPM.15307

ВОССТАНОВЛЕНИЕ МОДЕЛИ ТЕПЛОВОГО ПРОЦЕССА ПО ПРОСТРАНСТВЕННО-ВРЕМЕННЫМ РАСПРЕДЕЛЕНИЯМ ТЕМПЕРАТУРЫ

Н. Ю. Быков[1, 2]✉

[1] Национальный исследовательский университет ИТМО, Санкт-Петербург, Россия

[2] Санкт-Петербургский политехнический университет Петра Великого, Санкт-Петербург, Россия

✉ nbykov2006@yandex.ru

Аннотация. Метод генеративного дизайна модели (ГДМ) применен для восстановления структуры и коэффициентов дифференциального уравнения в частных производных, описывающего процесс нагрева и испарения мишени лазерным излучением. Исходные синтетические данные включают сценарии нагрева, соответствующие поверхностному или объемному поглощению энергии. Показано, что в случае объемного поглощения для корректного восстановления модели требуется применение процедуры препроцессинга, предусматривающей исключение части исходных данных. Предложена модификация метода, позволяющая учитывать зависимость коэффициентов восстанавливаемого уравнения от температуры. Обсуждается влияние различных статистических критериев, применяемых при селекции оптимального подмножества элементов, на точность восстановления структуры уравнения. Эффективность применения метода ГДМ продемонстрирована для широкого диапазона параметров нагрева мишени и разных вариантов задания энергоподвода. Показана возможность генерации модели по зашумленным данным.

Ключевые слова: метод генеративного дизайна, управляемая данными модель, уравнение теплопроводности, лазерный нагрев

Финансирование: Исследование выполнено при финансовой поддержке Российского научного фонда (грант № 00296-11-21, https://rscf.ru/project/21-11-00296/)

Ссылка для цитирования: Быков Н. Ю. Восстановление модели теплового процесса по пространственно-временным распределениям температуры // Научно-технические ведомости СПбГПУ. Физико-математические науки. 2022. Т. 15. № 3. С. 83–99. DOI: https://doi.org/10.18721/JPM.15307

Introduction

Data-driven models are widely used for predicting the parameters of social, political or physical processes and subsequently controlling them [1, 2]. The requirements imposed on such models generally include accuracy of the predictions and interpretability of the models themselves. If the object is characterized by quantitative predictors, then the model is typically a linear or nonlinear regression function [3]. Alternative models are formulated as ordinary differential equations (ODE) or partial differential equations (PDE), reconstructed from the available data. The data-driven models based on differential equations are expected to provide both good interpretability and accuracy of the predictions they yield [2].

Different methods for reconstructing the model of a process as a PDE based on the available data are widespread in studies of heat and mass transfer. The form of the ODE describing the majority of the thermal processes is well known: in the simplest case, it is a classical equation

of thermal conductivity. However, the equation may include a second derivative of temperature with respect to time in the general case [4, 5], and a corresponding convective term for a moving medium. If energy is released inside the object, one or more additional terms appear in the equation determining the power of internal heat sources [5]. A tool for selecting the significant terms of the equation from a large array of 'building blocks' should allow to detect the processes that occur within the internal volume of the object and cannot therefore be visualized during the experiment. Examples of such processes are phase transitions and chemical reactions. Reconstructing the convective term with the corresponding weight in the energy equation allows to assess the presence of convective processes in the object considered. What is more, data can be obtained for the qualitative changes in the thermal process (for example, transition from predominantly thermal conductivity to well-developed convection with the liquid heated non-uniformly [6]).

Problems on reconstructing the structure of PDE and determining the coefficients of the equation with respect to thermal processes can be solved by the method of generative model design (GMD) proposed in [7]. The method comprises several stages.

I. The most complete possible structure of the reconstructed equation is determined.

II. PDE elements are discretized.

III. Values are calculated for the vector elements of discretized templates based on available data on spatial-temporal temperature distributions.

IV. Statistical methods are applied to determine the optimal structure and the PDE coefficients.

Even though the core of the method has been formulated, some questions are yet to be addressed.

First of all, the effectiveness of the method clearly depends on the quality of the initial data. In addition to the above stages of the GMD algorithm, we should consider the stage when the available synthetic or experimental data are preprocessed. The quality of such data should be analyzed at this stage in order to make a decision as to whether they can be used fully or partially.

Secondly, the algorithm for constructing discretized stencils for the case of temperature-dependent parameters of the model is not discussed in detail in the literature.

Thirdly, different statistical criteria can be adopted at the stage when the optimal structure of the equation is chosen (Mallow's criterion, information criteria, etc.). The statistical criterion selected should be assessed for adequacy to determine the optimal structure of the model.

Fourthly, an important question yet to be answered definitively is whether the GMD algorithm is applicable to noisy data.

In general, the potential offered by the GMD method should explored further to accumulate experience with its practical applications.

This study concentrated on developing the GMD method proposed in [7]. Our intention was to further expand the scope of the method, trying to answer the above questions.

Generation of initial synthetic data

To better illustrate the capabilities of the GMD method, the initial data for reconstructing the thermal process model include information about the spatio-temporal evolution of temperature in the material, accounting for both the presence/absence of physical processes accompanying heating, and the temperature dependence of the thermophysical parameters of the medium.

The process of heating a metal target with laser radiation is a convenient object to consider. Firstly, this process depends on the radiation parameters and can be accompanied by phase transitions (melting of the material and evaporation of its surface); secondly, the temperature range of the material is very wide and requires taking into account the temperature dependence of the medium parameters. Thirdly, the data can be obtained synthetically by numerical modeling [8–10].

As an example, we consider a niobium target heated by moderate-intensity laser pulses. This unsteady process can be assumed to be one-dimensional for the case when the depth to which the target is heated is much smaller depth than the diameter of the laser spot.

Data on the spatio-temporal distribution of temperature $T(x,t)$ in the target are generated to subsequently use the GMD method by numerically solving the thermal conductivity equation [5, 9, 10] taking the form

$$c\rho\left(\frac{\partial T}{\partial t}-\omega\frac{\partial T}{\partial x}\right)=\frac{\partial}{\partial x}\lambda\frac{\partial T}{\partial x}+q_V, \quad (1)$$

where x, m, is the spatial coordinate; t, s, is the time; ρ, kg/m^3, c, J/(kg·K), $\lambda(T)$, W/(m·K), are the density, heat capacity, and thermal conductivity of the material, respectively; q_v, W/m^3, is the volumetric heat source; ω, m/s, is the speed of the evaporating surface.

The velocity ω depends on the surface temperature T_S ($T_S \equiv T(x = 0)$) and is the function of time only: $\omega = \omega(t)$. Eq. (1) is written in the moving coordinate system X, with the origin corresponding to the target surface. Surface evaporation does not occur for surface temperatures significantly lower than T_b ($T_b = 5033$ K is the boiling point of niobium at normal pressure p_b [11]), and the surface velocity is $\omega = 0$. Surface evaporation is observed at temperatures exceeding or close to T_b. The velocity ω starts to differ from zero. The coefficient $\omega \neq 0$ can serve as an indicator pointing to the presence of an evaporation process. Melting of niobium is not taken into account in the given formulation (melting point of niobium $T_L = 2750$ K [11]).

The boundary condition on the surface is imposed as

$$-\lambda \left.\frac{\partial T}{\partial x}\right|_{x=0} = q_S - L\rho\omega, \tag{2}$$

where q_s, W/m^2, is the energy flux of laser radiation over the target surface; L, J/kg, is the latent heat of evaporation.

The initial temperature at the remote boundary $T(\infty,t) = T_0$ corresponds to $T(x,0) = T_0$ ($T_0 = 300$ K).

Two scenarios of laser energy absorption are considered in this paper:

(*i*) the energy flux of laser radiation through the target surface per unit time (surface flux) is given by the expression

$$q_S = (1 - R_f)W_0, \tag{3}$$

where W_0, W/m^2, is the density of the radiation flux incident on the target surface; R_f is the reflectance of the material surface. Volume absorption is absent in this case ($q_V = 0$).

(*ii*) it is assumed that the volumetric absorption $q_V \neq 0$, $q_s = 0$.

In the latter case, the heat input at a distance x from the surface is determined by the expression

$$q_V(x,t) = \alpha_a I(x,t), \tag{4}$$

$$I(x,t) = I_0(t)\exp(-\alpha_a x), \tag{5}$$

where $I(x,t)$, W/m^2, is the radiation intensity in the material at a distance x from the surface; $I_0(t)$, W/m^2, is the density of the radiant flux penetrating the material, $I_0(t) = (1 - R_f)W_0$; α_a, m^{-1}, is the absorptance.

Eq. (5) expresses the Beer–Lambert–Bouguer absorption law.

It is assumed that the radiation power does not change, i.e.,

$$W_0 = const,\ t \le t_0;\ W_0 = 0,\ t > t_0. \tag{6}$$

The required values of the optical parameters are taken from [12, 13]: $\alpha_a = 5\cdot10^7$ m^{-1} (for lasing wavelength of the order of 1 μm), $R_f = 0.77$. Laser pulse duration $t_0 = 0.1$ μs.

The generated data correspond to two temperature ranges:

I. Target temperature is substantially below the boiling point T_b (and the melting point T_L);

II. Surface temperature is above T_b.

The experimental data [14] on the thermal conductivity of niobium in the range $300 < T < 2200$ K are approximated by a third degree polynomial for temperature range I:

$$\lambda = \lambda_0 + 6.687\cdot10^{-3}T + 6.652\cdot10^{-6}T^2 - 2.256\cdot10^{-9}T^3, \tag{7}$$

where $\lambda_0 = 51.49$ W/(m·K).

The density and heat capacity of niobium are assumed to be constant in this formulation, amounting to $\rho = 8570$ kg/m^3, $c_0 = 263$ J/(kg·K).

The temperature dependences given in the literature for the parameters of liquid niobium differ considerably near its melting point for Range II [14]. In this case, we assume the thermal conductivity and the heat capacity to be constant over the entire temperature range. In this case, the thermophysical parameters correspond to the parameters of liquid niobium [11, 14]:

$$\rho_L = 7580 \text{ kg/m}^3, c_{0L} = 449.9 \text{ J/(kg·K)}, \lambda_{0L} = 65 \text{ W/(m·K)}.$$

The surface moves with a velocity corresponding to Hertz's law and the assumption that 18% of the evaporated atoms are dispersed back to the surface due to collisions in the gas phase [15]. The density of saturated vapor follows the Clausius–Clapeiron law [15, 8]:

$$\omega(t) = 0.82\frac{p_b}{\rho}\left(\frac{m}{2\pi k_B T_S}\right)^{1/2} \exp\left[\frac{Lm}{k_B}\left(\frac{1}{T_b} - \frac{1}{T_S}\right)\right], \tag{8}$$

where k_B, J/K, is the Boltzmann constant; m, kg, is the atomic mass.

The Crank-Nicolson scheme of the finite difference method is used to numerically solve Eq. (1), providing a second-order approximation with respect to both the spatial and the temporal coordinate [5]. Thermal conductivity at the point between grid nodes j and j+1 was determined by the mean temperature in the nodes:

$$\lambda_{j+1/2} = \lambda\left((T_{j+1} + T_j)/2\right).$$

The thermal conductivities were tailored during the iterative process for each subsequent time step (n + 1), accounting for the relationship between thermal conductivity and temperature.

The computational scheme of the problem with volume absorption assumes that the volume where the absorption occurs is present around each grid node. The volume boundaries for node j with the coordinate x_j are defined for this one-dimensional case as

$$x_j - \Delta x/2 \le x < x_j + \Delta x/2.$$

Taking into account the Booger–Lambert–Beer law (see Eq. (5)), the power density of the heat source in the volume is expressed as

$$q_V(x_j, t) = \frac{I_0(t)}{\Delta x}\left\{\exp[-\alpha_a(x_j - \Delta x/2)] - \exp[-\alpha_a(x_j + \Delta x/2)]\right\}. \tag{9}$$

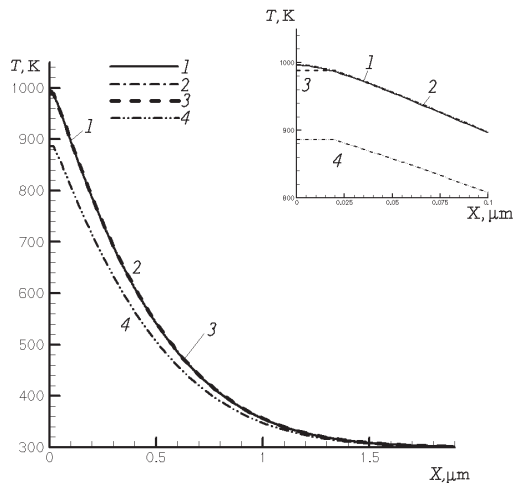

Fig. 1. Distributions of temperature T over the target depth X at time t = 10 ns, with volume absorption of laser radiation (computational case 6). The inset shows the initial region X.
Analytical solution [16] (curve *1*) is compared with the results of different computational cases:
taking into account Eq. (9), with steps of 2 nm (curve *2*) and 40 nm (curve *3*);
taking into account Eqs. (4), (5) and with steps of 40 nm (curve *4*)

Provided that $\Delta x \to 0$, expression (9) corresponds to expressions (4), (5). Taking into account the final value of the step Δx, the main numerical algorithm incorporates expression (9). The first node inside the body has the coordinate $x_0 = \Delta x/2$ for the problem statement with volume absorption (the target surface corresponds to the coordinate value $x = 0$). In addition to volume absorption, the boundary condition should be taken into account in form (2) at $q_s = 0$. A fictitious boundary node with the coordinate $x_{-1} = -\Delta x/2$ was included into the scheme to satisfy this boundary condition. There is no absorption of laser energy in this node,

$$T(x_{-1}, t) = T(x_0, t) = T_S(t).$$

The heating process in the target was observed for a total time of 2 μs.

The numerical algorithm intended for extracting data by GMD was verified by comparison with the analytical solutions available in monograph [16], obtained in the absence of surface evaporation ($\omega = 0$) both for the case of volume absorption (see expression (4)) and for the energy flux through the surface given by Eq. (3).

The data obtained by numerically solving the thermal conductivity equation (1) are in good agreement with the analytical solutions (Figs. 1 and 2). Using Eq. (9) and the described algorithm for volume absorption of radiation energy significantly increases the computational accuracy compared with the results obtained using expressions (4) and (5) for a large spatial step (see Fig. 1). If the surface flux is given (Fig. 2), the solution is similar to the case of volume absorption. The solutions differ only in the region of the target located directly near the surface.

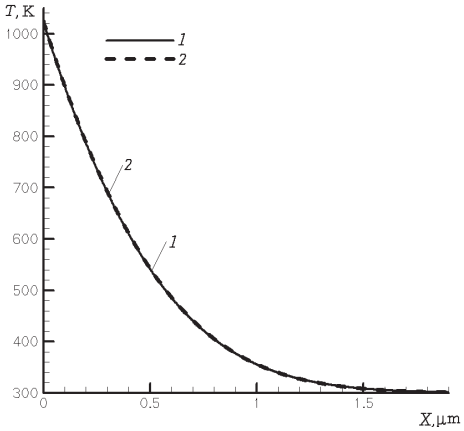

Fig. 2. Distributions of temperature T over the target depth X at time $t = 10$ ns, with radiation flux through the surface (computational case 1).
Analytical solution [16] (curve *1*) is compared with the computational result (curve *2*)

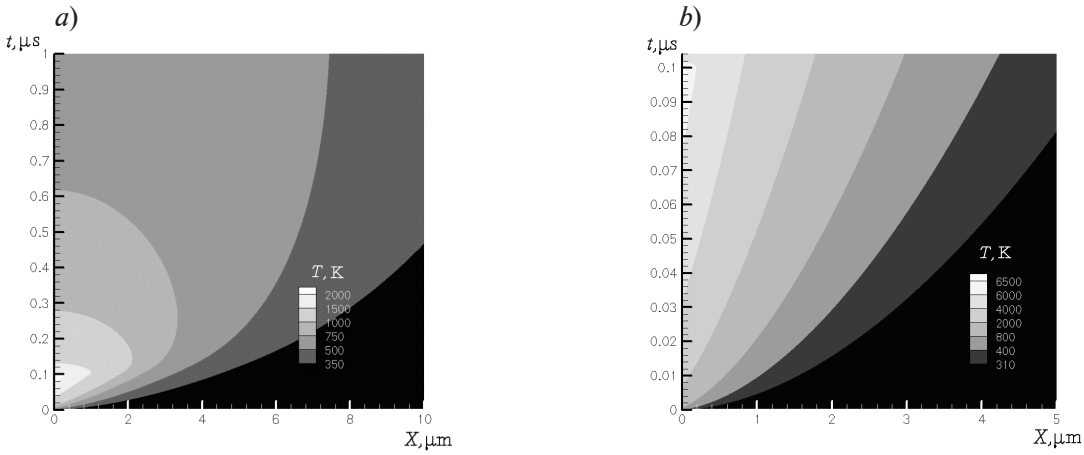

Fig. 3. Spatio-temporal temperature distributions for Cases 4 (*a*) and 11 (*b*) (see Table 1)

The cases corresponding to the generated data are given in Table 1, and example data for the temperature distributions are shown in Fig. 3.

The computational results for the second temperature range correspond to Case 11 (see Table 1 and Fig. 3,*b*). For radiation intensity of 1.2 TW/m^2 and a pulse duration of 100 ns, the surface temperature exceeds the boiling point by the time the laser pulse stops, and surface evaporation is observed. The velocity of the evaporation front is approximately 0.3 m/s by the end of the radiation time interval.

Table 1

Computational cases for generating the input data

Case	Energy input	Time sample, μs	λ	Δx, nm	N_d
1	$q_V = 0$	0.01	λ_0	2.0	973
2		1.00	λ_0		11333
3		0.01	(7)		998
4		1.00	(7)		11704
5		2.00	(7)		15962
6	$q_s = 0$	0.01	λ_0		775
7		1.00	λ_0		11333
8		0.01	(7)		801
9		1.00	(7)		11704
10		1.00	(7)	100	228
Case 11: $q_V = 0$, time sample is 0.0975 μs, $I_0(t) = 1.2$ TW/m^2, $c = c_{0L}$, $\lambda = \lambda_{0L}$, $\Delta x = 2$ nm, $N_d = 3355$					

Note. $I_0(t) = 0.3$ TW/m^2, $c = c_0$ for cases 1–10.

Notations: q_V is the bulk absorption of laser radiation; q_s is the energy flux through the target surface; $I_0(t)$ is the density of the radiant flux penetrating the material; c is the heat capacity, $c_0 = 263$ J/(kg·K), $c_{0L} = 449.9$ J/(kg·K); λ is the coefficient of thermal conductivity, $\lambda_0 = 51.49$ W/(m·K), $\lambda_{0L} = 65$ W/(m·K), (7) is the number of the polynomial formula; N_d is the number of degrees of freedom.

Method of generative design

The first stage of the GMD algorithm consists of determining the total number of possible elements in the reconstructed equation (depending on the type of problem). The full stencil of the PDE for the problem considered includes a convective term and is written as follows:

$$-\frac{\partial T}{\partial t} + \frac{1}{c\rho}\frac{\partial}{\partial x}\lambda\frac{\partial T}{\partial x} + \omega\frac{\partial T}{\partial x} + \frac{q_v}{c\rho} = 0, \tag{10}$$

where the coefficients λ and ω are assumed to be unknown, while the coefficients ρ, s and the heat source power q_v are known.

The temperature dependence of thermal conductivity λ is assumed to be known:

$$\lambda = \beta_0 + \beta_1 T + \beta_2 T^2 + \beta_3 T^3, \tag{11}$$

where β_p are the unknown coefficients.

The second stage of the GMD algorithm involves discretization of the equation elements by finite difference (FD) [7] or finite element (FE) methods [17] and calculating the values of discretized stencils based on the available data. We applied an FD method in this study.

The difference template of the second derivative in space for the regular mesh takes the form

$$\frac{\partial}{\partial x}\left(\lambda\,\frac{\partial T}{\partial x}\right)\approx\frac{1}{\Delta x^2}\left[\lambda_{j+1/2}T_{j+1}-(\lambda_{j+1/2}+\lambda_{j-1/2})T_j+\lambda_{j-1/2}T_j\right]\ . \tag{12}$$

In view of dependence (11), expression (12) takes the form

$$\frac{\partial}{\partial x}\left(\lambda\,\frac{\partial T}{\partial x}\right)\approx\sum_{s=0}^{3}K_s^{i,l}\beta_s, \tag{13}$$

$$K_s^{i,l}=0.5K_s^{i,n}+0.5K_s^{i,n+1}, \tag{14}$$

$$K_s^{i,n}=\frac{1}{\Delta x^2}\left[\left(\frac{T_{j+1}^n+T_j^n}{2}\right)^s(T_{j+1}^n-T_j^n)+\left(\frac{T_{j-1}^n+T_j^n}{2}\right)^s(T_{j-1}^n-T_j^n)\right]. \tag{15}$$

The superscript index i in Eqs. (13)–(15) and below corresponds to a spatial slice comprising three nodes: $j-1$, j and $j+1$; the superscript l corresponds to a time slice comprising two time layers: n and $n+1$. The coefficients $K_s^{i,n+1}$ are determined by Eqs. (15) substituting the index n by the index $n+1$.

The discretized equation (10) for the spatial slice i and the time slice l takes the form

$$\sum_{p=1}^{P_t}a_p^{il}\alpha_p=0, \tag{16}$$

where $P_t = 7$ for near-surface nodes during the pulse with volume absorption, and $P_t = 6$ in other cases; $\alpha_1 = -1$, $\alpha_p = \beta_{p-2}/(c\rho)$ for $2 \le p \le 5$; $\alpha_6 = \omega$, $\alpha_7 = q_V/(c\rho)$. Parameters α_2–α_6 are unknown and should be determined.

The coefficients a_p^{il} can be found from the available synthetic (or experimental) data:

$$a_1^{il}=\frac{T_j^{n+1}-T_j^n}{\Delta t}, \tag{17}$$

$$a_s^{il}=K_{s-2}^{i,l}\ \ for\ 2\le s\le 5, \tag{18}$$

$$a_6^{il}=0.5\frac{T_{j+1}^{n+1}-T_{j-1}^{n+1}}{2\Delta x}+0.5\frac{T_{j+1}^n-T_{j-1}^n}{2\Delta x}, \tag{19}$$

$$a_7^{il}=1. \tag{20}$$

In vector form, expression (16) can be represented as

$$\sum_{p=1}^{P_t}\mathbf{V}_p\alpha_p=\mathbf{Z}_0, \tag{21}$$

where $\mathbf{Z}_0$ is a zero vector; the vector $\mathbf{V}_p$ consists of elements a_p^{il}, where the superscript i varies from 2 to $N-1$ (the spatial index j varies from 1 to N (N is the number of spatial nodes)); the superscript l varies from 1 to L (L is the number of time slices) $L < n$ (n is the number of time steps):

$$\begin{aligned}\mathbf{V}_p^T&=(v^{p1}\ v^{p2}\ v^{p3}\ \ldots v^{p\ (N-2)\times L})=\\&=(a_p^{21}\ a_p^{31}\ a_p^{41}\ \ldots a_p^{N-1\ 1}\ a_p^{22}\ a_p^{32}\ a_p^{42}\ \ldots a_p^{N-1\ 2}\ \ldots a_p^{2L}\ a_p^{3L}\ a_p^{4L}\ \ldots a_p^{N-1\ L}).\end{aligned} \tag{22}$$

Expression (21) can be represented as

$$\mathbf{Y} = \alpha_0 + \sum_{p=2}^{P_t} \mathbf{V}_p \alpha_p, \tag{23}$$

where $\mathbf{Y} = -\alpha_1 \mathbf{V_1}$, $\alpha_1 = -1$, $\alpha_0 = 0$.

Estimates of coefficients α_p can be obtained by the ordinary least squares (OLS) method.

The presence of the initial data allows us to calculate the component values of the vectors $\mathbf{V}_p$.

The third stage of the GMD algorithm involves applying statistical learning methods to expression (23). These methods rely on algorithms for selecting the optimal subset of elements and statistical criteria for selecting a single 'correct' combination of elements [3, 18]. The Bayesian information criterior (BIC) or C_p (Mallow's criterion) can be used for this purpose [3, 19, 20]. The respective criteria are calculated as

$$\mathrm{BIC} = n \ln \frac{\mathrm{RSS}}{n} + k \ln n, \tag{24}$$

where $n = (N - 2)\ L$ is the number of observations; RSS is the residual square sum; $k = p_e + 2$, p_e – is the number of elements included in the sum in the right-hand side of expression (23) (the maximum possible number of elements: $P = P_t - 1$),

$$\tilde{N}_p = \frac{\mathrm{RSS}}{S^2} - n + 2(p_e + 1), \tag{25}$$

where S^2 is mean squared residual after regression over the entire set of predictors.

Illustration of GMD method

In general, the reconstruction accuracy for a model in the form of a PDE with derivative coefficients depending on the solution is determined by a quantitative parameter that is the number of degrees of freedom (DoF), as well as by the quality of the data. The number of DoF in the given problem is the number of nodes (points) with a known temperature value. This number depends on the grid spacing and the instant in time that the data correspond to. Heat penetrates deep into the material over time, with an increase in the heated area and, accordingly, the number of nodes for the case of a uniform grid. Data quality refers to several factors: the temperature range covered by the data; possible correlation of the data, as well as the presence and type of energy supply.

If the heat flux through the surface is given as condition (2) and expression (3), the thermal balance of a unit volume associated with the grid node j is determined only by the process of thermal conductivity. It is expected that data in all nodes of the area under consideration can be used to generate a model.

In the case of volume absorption, this process occurs in the near-surface layer of the target with a characteristic scale of about $\delta \approx 1/\alpha_a = 0.2 \cdot 10^{-7}$ m (20 nm). The contribution of the term q_V to equation (1) for near-surface nodes is significant with respect to the thermal process. The quantity Os_L, which is the ratio of the energy supplied to the unit volume corresponding to the node j with the boundaries

$$x_j - \Delta x / 2 \le x < x_j + \Delta x / 2$$

for absorption of radiation to the energy supplied/discharged from the unit volume due to thermal conductivity, can be defined as

$$\mathrm{Os}_L = \left| \frac{q_V(x_j, t)\Delta x}{q_{-\Delta x/2} - q_{\Delta x/2}} \right|, \tag{26}$$

$$q_{-\Delta x/2} = -\lambda \frac{\partial T}{\partial x}\bigg|_{x_j - \Delta x/2}, \quad q_{\Delta x/2} = -\lambda \frac{\partial T}{\partial x}\bigg|_{x_j + \Delta x/2}.$$

The boundary of 'influence' of energy absorption on the heat balance depends on the distribution of the modulus of the local Ostrogradsky number $|Os_L|$. Fig. 4 shows an example for the variation in $|Os_L|$ for the case of volume absorption and the time $t = 0.1$ μs. $|Os_L| >> 1$ for points in the near-surface layer around the coordinate $x = 7 \cdot 10^{-8}$ and the thermal conductivity process also plays a secondary role. The latter circumstance affects the reconstruction accuracy for the thermophysical parameters and the quality of generation for the equation model.

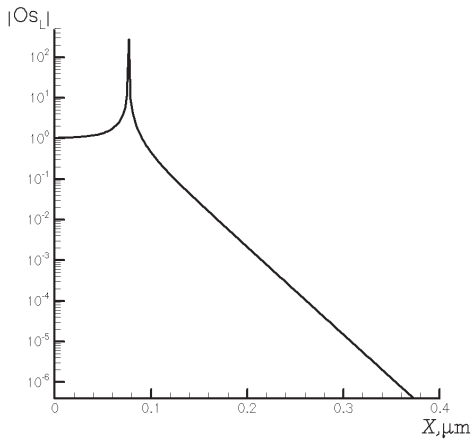

Fig. 4. Modulus distribution of the local Ostrogradsky number along the coordinate X

A total of 200 near-surface nodes were excluded from the data intended for generative design for the irradiation stage and the case of volume absorption, while the sum in expression (23) included the total number of predictors $P = P_t - 1 = 5$ ($P_t = 6$). The reconstruction error of the coefficients exceeded 50% accounting for either the near-surface nodes in the initial data or only the near-surface nodes for which expression (23) also included the term associated with volume energy release ($P = 6$, $P_t = 7$), while the reconstructed model included an 'extra' convective term for the first range of temperatures below the melting point T_L. One near-boundary node was excluded from the data for the heat diffusion stage after the pulse stopped to account for the specifics of how finite-difference stencils are set.

Cases with the energy flux through the surface were not sensitive to the presence of information about near-surface nodes in the data under consideration. If the surface energy flux was set regardless of the process stage, one node immediately adjacent to the target surface was excluded from the data.

The target temperature varies in a wide range during heating: $T_0 = 300 \leq T < 2200$ K for the first temperature range and $T_0 = 300 \leq T < 7000$ K for the second one. Internal tests indicate that it is ineffective to use data for points deep within the target with a temperature below $1.003 T_0 = 301$ K. These nodes were also excluded from consideration.

Data generated for different time slices correlate with each other [3]. The model of the equation is reconstructed from the data corresponding to a single time slice consisting of two time layers. We considered the data corresponding to the time slices at both the irradiation stage ($t = 10$ and 100 ns) and after the laser pulse stopped (1 and 2 μs).

The number of DoF used to generate the model ranged from 220,000 to 16,000 and depended on the case (see Table 1).

In the first stage of the study, the GMD method was applied to the data corresponding to Cases 1, 2, 6 and 7, assuming constant thermal conductivity λ_0 and a temperature range not exceeding the melting point (see Table 1). The results of the algorithm for selecting the optimal subset of elements for Case 1 are summarized in Table 2. The number in the first column corresponds to the number of elements p_e included under the summation sign in Eq. (23). According to the results obtained, the minimum values of the BIC and C_p criteria correspond to an equation with one term with the coefficient α_2 (aside from the term with the coefficient $\alpha_1 = -1$) for Case 1. The statistical procedure of the package *R* [18] for all cases determines the value of the coefficient α_2 as equal to $2.2845 \cdot 10^{-5}$ (Table 3), which corresponds to the value of thermal conductivity

$$\alpha_2 = \lambda_0 / (\rho c_0) = 2.2845 \cdot 10^{-5} \text{ m}^2/\text{s}$$

(see expression (7)), which is used to generate data.

Notably, in addition to exact reconstruction of the coefficient, the structure of the equation, which should not include the convective term with the coefficient α_6, is also reconstructed correctly. Thus, the results obtained for generating an equation with constant coefficients can be assumed to be satisfactory.

Similarly, the GMD method was applied to reconstructing the equation from the data implying a temperature dependence for the thermal conductivity of the parameters in the form (7). Table 2 presents an example of applying the procedure for selecting the optimal subset of elements for Case 3 (surface energy flux and the time t = 10 ns) corresponding to the irradiation mode. The procedure correctly reproduces the stencil for the equation without the convective term corresponding to the coefficient α_6 for this case. Cases 4 and 5 (see Table 1) correspond to later times of the process: t = 1 and 2 μs, respectively. The temperature of the target decreases, and its variation range is 300–550 K by the time of 2 μs. The number of DoF increases to 16,000. The reconstruction quality of the model structure remains virtually unchanged for later times, and the convective term is not reproduced. The structure of the required equation is also reconstructed correctly for the cases with volume absorption (Cases 8 and 9). Varying the computational parameters, i.e., increasing the spatial step by 50 times and decreasing the number of DoF in Case 10 proportionally (relative to Case 9) does not affect the reconstruction quality of the structure.

The results obtained by running the GMD algorithm for Cases 1 – 10 are given in Table 3. The normalized coefficients corresponding to expression (7) (in bold) and the coefficient α_6 associated with the surface evaporation rate are given here. The rest of the rows show the values of the reconstructed coefficients for the given cases, the values of the normalized coefficients in the dependence $\lambda(T)$ are reproduced with good accuracy. The reconstruction error of the coefficients only weakly depends on the time slice corresponding to the data and on the type of energy input, provided that some of the data for the near-surface layer are excluded for the case of volume energy absorption.

The maximum reconstruction error for the coefficients of polynomial dependence of thermal conductivity is 0.01%. The error is determined as

$$\varepsilon = \left|\alpha_m / \alpha_t - 1\right| \cdot 100\%,$$

where α_m is the coefficient for which the maximum discrepancy with the theoretical value α_t is observed.

The error for the total thermal conductivity is even less and does not exceed 0.002%. The error is the same for Case 9 and 10, even though the number of DoF differs by 50 times.

The initial data for Case 11 assumes an evaporation process on the target surface, since the surface temperature for the corresponding high radiation intensity (see Table 1) and the pulse time exceeds the boiling point of niobium. The GMD method allows to correctly reconstruct the structure of the model, which includes a convective term for this case (see Table 3). The reconstructed coefficient value α_6 for Case 11 is different from 0.

Table 2 shows the values of criteria C_p and BIC for two cases: 1 and 3. The minimum criteria correspond to the same set of elements for these cases. However, unlike BIC, the criterion C_p predicts an incorrect structure of the model for several cases. Moreover, using BIC produces a sparser model with fewer elements.

We can therefore conclude that the BIC criterion is preferable for the given class of problems.

It is extremely important for real-life applications that the GMD method can work with noisy data. Below, we consider an additional computational case to illustrate this capability, corresponding to the time slice t = 0.0975 ms; its initial parameters are similar to Cases 1 and 2 from Table 1. The same as above (Cases 1 and 2), the synthetic data are generated on a grid with a step Δx = 2 nm. The effect of noise was achieved by simulating the temperature values by the law

$$T_\delta(x,t) = T(x,t)\left(1 + \theta\delta_r\right), \tag{27}$$

where $T(x,t)$ is the temperature found from numerical solution (1); θ is a random variable with a uniform distribution from the interval [–1, 1], δ_r is the relative error.

Table 2

Procedure for selecting the optimal element subset for Cases 1 and 3

Number of elements p_e	α_2	α_3	α_4	α_5	α_6	BIC	C_p
Case 1							
1	*	–	–	–	–	**–29,196.57**	**2.59**
2	*	–	–	–	*	– 29,190.57	3.71
3	*	*	–	–	*	– 29,183.85	5.54
4	*	*	*	*	–	– 29,178.95	5.56
5	*	*	*	*	*	– 29,173.63	6.00
Case 3							
1	*	–	–	–	–	– 3,628.85	$2.44\cdot10^{14}$
2	*	–	–	–	*	– 1,098.50	$1.60\cdot10^{11}$
3	*	*	–	–	*	– 12,940.78	$2.26\cdot10^{10}$
4	*	*	*	*	–	**– 29,934.64**	**4.53**
5	*	*	*	*	*	– 29,928.26	6.00

Notations: α_2–α_6 are the coefficients from Eq. (23); BIC, C_p are statistical criteria. Notes. 1. The number of elements p_e included under the summation sign in Eq. (23) is given in the left column. 2. The selected results are highlighted in bold.

Table 3

Illustration of GMD method

Case	α_0	α_2 ($\times10^5$)	α_3 ($\times10^9$)	α_4 ($\times10^{12}$)	α_5 ($\times10^{15}$)	α_6
Comparison of theoretical and reconstructed values						
1, 2, 6, 7	**0**	**2.2845**	**0**			**0**
1	$-7.1669\cdot10^{-5}$	2.2845	0			0
2	$1.0482\cdot10^{-7}$		0			
6	$-3.6375\cdot10^{-5}$		0			
7	$-8.8505\cdot10^{-8}$		0			
Comparison of theoretical and reconstructed values						
3–5, 8–10	**0**	**2.2845**	**2.9668**	**2.9513**	**–1.0009**	**0**
3	$2.2415\cdot10^{-5}$	2.2845	2.9669	2.9513	–1.0009	0
4	$1.2132\cdot10^{-7}$		2.9668			
5	$-3.1960\cdot10^{-8}$			2.9514		
8	$8.7904\cdot10^{-6}$		2.9669	2.9511	–1.0008	
9	$4.1593\cdot10^{-8}$		2.9668	2.9513	–1.0010	
10	$-3.8343\cdot10^{-7}$			2.9515		
Comparison of theoretical and reconstructed values						
11	**0**	**1.9060**	**0**			**–**
11	$1.4656\cdot10^{-5}$	1.9060	0			0,3

Notes. 1. The values of normalized coefficients corresponding to expression (7) (theoretical) are highlighted in bold. 2. For all cases, $\alpha_1 = -1$.

Noisy data were generated with the value of δ_r varying from 10^{-5} to 10^{-2} (see Table 4).

The GMD method does not allow to correctly reconstruct both the structure of the PDE and the coefficients for the derivatives for the given noise level. For this reason, an additional regularization procedure had to be applied for noisy data, accounting for the function assignment error generated when the grid step is selected [21].

As noted above, synthetic data are generated with a small step with respect to the spatial coordinate, allowing to tailor a larger step, a multiple of Δx. Using the procedure for determining the step (described in [21]) for the relative errors of the initial data given in Table 4, we obtained the value of $\Delta x_{reg} = 0.1$ μm. With the given step value, the GMD correctly reproduces the structure of the equation without the convective term ($\alpha_6 = 0$) for all values of δ_r considered, and the reconstruction error of the thermal conductivity coefficient

$$\varepsilon = \left|\alpha_2 / \alpha_t - 1\right| \cdot 100\%$$

($\alpha_t = 2.2845 \cdot 10^{-5}$ m²/s is the theoretical value of the coefficient) varies from 0.04% for the relative error of the initial data amounting to 10^{-5} to 47% for $\delta_r = 10^{-2}$ (see Table 4). The relative error $\delta_r = 10^{-2}$ corresponds to the absolute error of determining the temperature determination at about 25 K near the target surface and 3 K near the remote boundary.

If the step with respect to the spatial coordinate cannot be varied for synthetic or experimental data, an alternative regularization procedure can be used, based on temperature interpolation with spline functions [21].

Table 4

Application of GMD method to noisy data

Case	δ_r	α_2	ε, %
s1	10^{-5}	$2.2854 \cdot 10^{-5}$	0.04
s2	10^{-4}	$2.2912 \cdot 10^{-5}$	0.29
s3	10^{-3}	$2.5112 \cdot 10^{-5}$	9.92
s4	10^{-2}	$3.3634 \cdot 10^{-5}$	47.22

Note. $\alpha_6 = 0$ for cases s1–s4.
Notations: δ_r is the variable relative error; α_2, α_6 are the coefficients from Eq. (23); ε is the error, $\varepsilon = |\alpha_2/\alpha_t - 1| \cdot 100\%$ (α_t is the theoretical value).

Conclusions

The GMD method holds much promise for reconstructing the PDE describing thermal processes. GMD can be used both to directly construct a mathematical model of a complex phenomenon from the available data and to visualize the accompanying processes, such as chemical reactions or phase transformations, as well as to refine the thermophysical parameters of materials. However, little experience has been accumulated so far with applying the GMD in practice, so the method itself needs to be developed further.

This paper continues the efforts on optimizing the algorithm for generative model design as applied to reconstructing a model of a thermal process, which may generally include a convective term, with the material parameters assumed to depend on temperature.

We report on the reconstruction of a partial differential equation describing heating and evaporation of a metal target by a laser pulse.

The initial data for subsequent application of the GMD method were generated by numerically solving the thermal conductivity equation an unsteady process for different approaches to describing the laser energy. We propose a method for improving the computational accuracy for the case of volume absorption and limited computational resources, which require a large step with respect to the spatial coordinate. The computational algorithm is verified by comparison with existing analytical solutions.

Our findings indicate that the GMD method is sensitive to the type of data used. The proportion of data that can be used to generate the model has to be additionally estimated for the case where the initial data for reconstructing the model correspond to volume absorption of the material and the stage when the target is irradiated. Excluding the data on temperature in near-surface nodes allows to reconstruct the model structure with better quality and minimum error in finding the temperature-dependent coefficients of the PDE generated. On the other hand, there is no problem with excluding near-surface nodes and pre-processing of the data if the data corresponds to the stage of heat diffusion after the laser pulse stops for volume absorption or any stage of the process with the heat flux through the target surface.

If the model is generated as a PDE with variable coefficients, a significantly larger number of predictors have to be taken into account to apply statistical learning methods in the search for the optimal structure and coefficients of the equation. Despite this circumstance, we have confirmed that applying generative model design to the available data yields good results in reconstructing the structure of the model. The structure of the equation does not include a convective term at temperatures substantially lower than the boiling point of the material. If the surface temperature of the target exceeds the boiling point, the convective term associated with the surface evaporation process is reconstructed. The reconstruction error for the temperature-dependent coefficient of thermal conductivity is less than 0.002% for the given number of degrees of freedom (more than 200).

We have established that the GMD method can be used to reconstruct a model from noisy data. In this case, additional regularization procedures are to be introduced to obtain the correct structure of the equation and the coefficient values of the derivatives.

As a direction for future research, we intend to validate the method of generative design with real experimental data.

REFERENCES

1. **Hutter F., Kotthoff L., Vanschoren J.** (Eds.), Automated machine learning. Methods, systems, challenges, (The Springer Series on Challenges in Machine Learning), Springer Nature, Cham, Switzerland, 2019.

2. **Maslyaev M., Hvatov A., Kalyuzhnaya A. V.,** Partial differential equations discovery with EPDE framework: Application for real and synthetic data, J. Comp. Sci. 53 (July) (2021) 101345.

3. **James G., Witten D., Hastie T., Tibshirani R.,** An introduction to statistical learning: with applications in R, Springer, New York, 2013.

4. **Lykov A. V.**, **Mikhailov Y. A.,** Theory of heat and mass transfer, Institute for the Promotion of Teaching Science and Technology (IPST), Thailand, 1963.

5. **Samarskii A. A., Vabishchevich P. N.,** Computational heat transfer, in 2 Vols., Willey, Chichester, 1995.

6. **Manukhin B. G., Kucher D. A., Chivilikhin S. A., et al.,** Optical diagnostics of the process of free liquid convection, Optics and Spectroscopy. 119 (3) (2015) 392–397.

7. **Bykov N. Yu., Khvatov A. A., Kalyuzhnaya A. V., Bukhanovskiy A. V.,** A method for reconstructing models of heat and mass transfer from the spatio-temporal distribution of parameters, Technical Physics Letters. 47 (24) (2021) 9–12 (in Russian).

8. **Bulgakov A. V., Bulgakova N. M., Burakov I. M., Bykov N. Y., et al.,** Nanosized material synthesis by action of high-power energy fluxes on matter, Institute of Thermophysics SB RAS, Novosibirsk, 2009 (in Russian).

9. **Bykov N. Y., Bulgakova N. M., Bulgakov A. V., Loukianov G. A.,** Pulsed laser ablation of metals in vacuum: DSMC study versus experiment, Appl. Phys. A. 79 (4–6) (2004) 1097–1100.

10. **Bykov N. Y., Lukyanov G. A.,** The direct simulation Monte Carlo of cluster formation processes in laser plume, Proc. 25-th Int. Symp. Rarefied Gas Dynamics, Publishing House of SB RAS, Novosibirsk (2007) 645–650.

11. Niobiy [Niobium], In Book: Khimicheskaya entsiklopediya, T. 3. Pod red. N. S. Zefirova i dr. [Encyclopedia of chemistry, Vol. 3, Edited by N. S. Zefirov et al.], Soviet Encyclopedia Publishing, Moscow, 1992. P. 249 (in Russian).

12. **Zolotarev V. M., Morozov V. N., Smirnova E. V.,** Opticheskiye postoyannyye prirodnykh i tekhnicheskikh sred [Handbook of optical constants of natural and technical media], Khimiya Publishing, Leningrad, 1984 (in Russian).

13. **Grigoriev I.S., Melikhov E. Z.** (Eds.), Handbook of physical quantities, CRC Press, Boca Raton, Florida, USA, 1997.

14. **Zinoviev V. E.,** Teplofizicheskiye svoystva metallov pri vysokikh temperaturakh [Thermal properties of metals at high temperatures], Handbook, Metallurgia, Moscow, 1989 (in Russian).

15. **Anisimov S. I., Imas Ya. I., Romanov G. S., Khodyko Yu. V.,** Deystviye izlucheniya bolshoy moshchnosti na metally [Effect of high-power radiation on metals], Nauka Publishing, Moscow, 1970 (in Russian).

16. **Carslaw H. S., Jaeger J. C.,** Conduction of heat in solids, 2-nd ed., Oxford University Press, Oxford, UK, 1959.

17. **Bykov N., Hvatov A., Kalyuzhnaya A., Boukhanovsky A.,** A method of generative model design based on irregular data in application to heat transfer problems, J. Phys. Conf. Ser. 1959 (2021) 012012.

18. R Core Team. R: A language and environment for statistical computing, R Foundation for Statistical Computing, Vienna, Austria, 2020. Available online at https://www.R-project.org/.

19. **Priestley M. B.,** Spectral analysis and time series (Probability and Mathematical Statistics), Academic Press, Cambridge, UK (1981).

20. **Mallows C. L.,** Some comments on C_p, Technometrics. 15 (4) (1973) 661–675.

21. **Vatulyan A. O.,** Koeffitsiyentnyye obratnyye zadachi mekhaniki [Inverse coefficient problems in mechanics], Fizmatlit, Moscow, 2019 (in Russian).

СПИСОК ЛИТЕРАТУРЫ

1. **Hutter F., Kotthoff L., Vanschoren J.** (Eds.) Automated machine learning. Methods, systems, challenges. (The Springer Series on Challenges in Machine Learning). Cham, Switzerland: Springer Nature, 2019. 220 p.

2. **Maslyaev M., Hvatov A., Kalyuzhnaya A. V.** Partial differential equations discovery with EPDE framework: Application for real and synthetic data // Journal of Computer Science. 2021. Vol. 53. July. P. 101345.

3. **Гарет Д., Уиттон Д., Хасти Т., Тибширани Р.** Введение в статистическое обучение с примерами на языке R. Пер. с англ. С. Э. Мастицкого. Изд. 2-е, испр. М.: ДМК Пресс, 2017. 456 с.

4. **Лыков А. В. Теория теплопроводности.** М.: Высшая школа, 1967. 600 с.

5. **Самарский А. А., Вабищевич П. Н.** Вычислительная теплопередача. М.: Едиториал УРСС, 2003. 784 с.

6. **Манухин Б. Г., Гусев М. Е., Кучер Д. А., Чивилихин С. А., Андреева О. В.** Оптическая диагностика процесса свободной конвекции жидкости // Оптика и спектроскопия. 2015. Т. 3 № .119. С. 423–418.

7. **Быков Н. Ю., Хватов А. А., Калюжная А. В., Бухановский А. В.** Метод восстановления моделей тепломассопереноса по пространственно-временным распределениям параметров // Письма в Журнал технической физики. 2021. Т. 47. № 24. С. 9–12.

8. **Булгаков А. В., Булгакова Н. М., Бураков И. М., Быков Н. Ю. и др.** Синтез наноразмерных материалов при воздействии мощных потоков энергии на вещество. Новосибирск: Институт теплофизики СО РАН, 2009. 462 с.

9. **Bykov N. Y., Bulgakova N. M., Bulgakov A. V., Loukianov G. A.** Pulsed laser ablation of metals in vacuum: DSMC study versus experiment // Applied Physics A. 2004. Vol. 79. No. 4–6. Pp. 1097–1100.

10. **Bykov N. Y., Lukyanov G. A.** The direct simulation Monte Carlo of cluster formation processes in laser plume // Proceedings of the 25-th International Symposium on Rarefied Gas Dynamics. Novosibirsk: Publishing House of SB RAS, 2007. Pp. 645–650.

11. Ниобий // Химическая энциклопедия. В 5 тт. (1998–1988). Т. 3. Мед–Пол. Под ред. Н. С. Зефирова, И. Л. Кнунянца, Н. Н. Кулова. М.: Советская энциклопедия, 1992. С. 249.

12. **Золотарев В. М., Морозов В. Н., Смирнова Е. В.** Оптические постоянные природных и технических сред. Ленинград: Химия, 1984. 216 с.

13. Физические величины. Справочник. Под ред. И. С. Григорьева и Е. З. Мелихова. М.: Энергоатомиздат, 1991. 1230 с.

14. Зиновьев В. Е. Теплофизические свойства металлов при высоких температурах. М.: Металлургия, 384 .1989 с.

15. Анисимов С. И., Имас **Я. И., Романов Г. С.,** Ходыко **Ю. В.** Действие излучения большой мощности на металлы. М.: Наука, 272 .1970 с.

16. **Карслоу Г., Егер Д.** Теплопроводность твердых тел. Пер. с англ. М.: Наука, 1964. 488 с.

17. **Bykov N., Hvatov A., Kalyuzhnaya A., Boukhanovsky A.** A method of generative model design based on irregular data in application to heat transfer problems // Journal of Physics: Conference Series. 2021. Vol. 1959. P. 012012.

18. R Core Team. R: A language and environment for statistical computing. R Foundation for Statistical Computing, Vienna, Austria, 2020. Available online at https://www.R-project.org/.

19. **Priestley M. B.** Spectral analysis and time series (Probability and Mathematical Statistics). Cambridge, UK: Academic Press, 1981. 706 p.

20. **Mallows C. L.** Some comments on C_p // Technometrics. 1973. Vol. 15. No. 4. Pp. 661–675.

21. **Ватульян А. О.** Коэффициентные обратные задачи механики. М.: Физматлит, 2019. 272 с.

THE AUTHOR

BYKOV Nikolay Yu.
ITMO University, St. Petersburg,
Peter the Great St. Petersburg Polytechnic University
49A, Kronverksky Ave., St. Petersburg, 197101, Russia
nbykov2006@yandex.ru
ORCID: 0000-0003-0041-9971

СВЕДЕНИЯ ОБ АВТОРЕ

БЫКОВ Николай Юрьевич – *доктор физико-математических наук, старший научный сотрудник факультета цифровых трансформаций Научно-исследовательского университета ИТМО; ведущий научный сотрудник, профессор кафедры физики Санкт-Петербургского политехнического университета Петра Великого.*
195251, Россия, г. Санкт-Петербург, Кронверкский пр., 49А
nbykov2006@yandex.ru
ORCID: 0000-0003-0041-9971

Received 08.04.2022. Approved after reviewing 06.06.2022. Accepted 06.06.2022.
Статья поступила в редакцию 08.04.2022. Одобрена после рецензирования 06.06.2022. Принята 06.06.2022.

Original article
DOI: https://doi.org/10.18721/JPM.15308

THE THERMOELASTIC STRESSES DURING LASER ANNEALING OF TITANIUM DIOXIDE ON A SAPPHIRE SUBSTRATE

Yu. V. Klunnikova[1]✉, *M. V. Anikeev*[2], *A. V. Filimonov*[3]

[1] Southern Federal University, Rostov-on-Don, Russia;

[2] Fraunhofer SIT | ATHENE, Darmstadt, Germany;

[3] Peter the Great St. Petersburg Polytechnic University, St. Petersburg, Russia

✉ yvklunnikova@sfedu.ru

Abstract. In order to analyze the technique of laser annealing of titanium dioxide films on sapphire substrates and to optimize the film properties, a thermomechanical model of this technique has been considered. The model allowed us to monitor and vary the values of thermoelastic stresses in the film-substrate structures caused by changes of film annealing technological parameters such as the laser power, the film thickness, the pulse duration, the speed of laser emission, etc. The temperature field under the laser beam was simulated and then the stresses were analyzed using the thermomechanical finite element model. The simulation results showed an important role of the TiO_2 film-to-substrate thickness ratio. The optimal combination of technological parameters was selected to prevent formation of cracks and other defects in the films.

Keywords: film, thermoelastic property, laser annealing, substrate, numerical method, sapphire substrate

Funding: The research was funded by the Ministry of Science and Higher Education of the Russian Federation and the German Academic Exchange Service (DAAD) within the framework of the joint program “Mikhail Lomonosov” (project no. 2293-21), the Ministry of Science and Higher Education of the Russian Federation (project no. 0784-2020-0025)

Citation: Klunnikova Yu. V., Anikeev M. V., Filimonov A. V., The thermoelastic stresses during laser annealing of titanium dioxide on a sapphire substrate, St. Petersburg Polytechnical State University Journal. Physics and Mathematics. 15 (3) (2022) 100–110. DOI: https://doi.org/10.18721/JPM.15308

Научная статья
УДК 621.382
DOI: https://doi.org/10.18721/JPM.15308

ТЕРМОУПРУГИЕ НАПРЯЖЕНИЯ ПРИ ЛАЗЕРНОМ ОТЖИГЕ ДИОКСИДА ТИТАНА НА САПФИРОВОЙ ПОДЛОЖКЕ

Ю. В. Клунникова[1]✉, *М. В. Аникеев*[2], *А. В. Филимонов*[3]

[1] Южный федеральный университет, г. Ростов-на-Дону, Россия;

[2] Институт информационной безопасности общества Фраунгофера, г. Дармштадт, Германия;

[3] Санкт-Петербургский политехнический университет Петра Великого, Санкт-Петербург, Россия

✉ yvklunnikova@sfedu.ru

Аннотация. С целью анализа технологии лазерного отжига пленок оксида титана на сапфировых подложках и оптимизации свойств пленок рассмотрена термомеханическая модель этого отжига. Она позволяет контролировать и варьировать значения термоупругих напряжений в структурах пленка-подложка, вызванных изменением технологических параметров отжига пленок, таких как мощность лазера, толщина пленки, длительность импульса, скорость лазерного излучения и др. Температурное поле под лазерным лучом моделировали с последующим анализом напряжений с помощью термомеханической модели конечных элементов. Результаты моделирования показали важную роль соотношения между значениями толщины пленки и подложки. Подобрано оптимальное сочетание технологических параметров, позволяющее предотвратить образование в пленках трещин и других дефектов.

Ключевые слова: пленка, термоупругие свойства, лазерный отжиг, подложка, численный метод

Финансирование: Исследование выполнено при финансовой поддержке Министерства науки и высшего образования Российской Федерации и Германской службы академических обменов (DAAD) в рамках совместной программы «Михаил Ломоносов» (проект № 2293-21), а также проекта № 0784-2020-0025 Министерства науки и высшего образования Российской Федерации.

Ссылка для цитировании: Клунникова Ю. В., Аникеев М. В., Филимонов А. В. Термоупругие напряжения при лазерном отжиге диоксида титана на сапфировой подложке // Научно-технические ведомости СПбГПУ. Физико-математические науки. 2022. Т. 15. № 3. С. 100–110. DOI: https://doi.org/10.18721/ JPM.15308

Introduction

The possibility of obtaining thin films on substrates is important for the design of functional devices such as photoelectric converters or sensitive elements of gas sensors. Modern semiconductor gas sensors use thin films of metal oxides (TiO_2, Fe_2O_3, V_2O_5, SnO_2, WO_3, ZnO) as sensing elements. These materials are popular because of their workability, low cost, high chemical stability, mechanical strength, and high adhesion to sapphire. As the result, semiconductor gas sensors are characterized by small sizes, high sensitivity, and reliability [1, 2].

Traditional technologies of microelectronics, such as vacuum deposition and photolithography, can be used for creating thin films. Application of more sophisticated technologies increases the performance of gas sensor and decreases its cost and power consumption [3].

Laser radiation (LR) for obtaining thin films on sapphire substrates increases the performance of gas element production, provides stability of film parameters and higher oxide quality. Decreased duration of film laser annealing (LA) on sapphire surface excludes the necessity to provide vacuum conditions or special inert atmosphere to prevent uncontrolled surface impurities [4–8]. The main benefits of gas sensor development on a sapphire substrate with titanium oxide (TiO_2) film are high selectivity to detectable gases, reduced operating temperature, and increased stability over time.

The mismatch of the lattice parameters and the thermal expansion properties between thin film layers and substrate materials is the main cause of the cross-layer defect development and stress generation. Thermoelastic stresses in a thin film often hamper its performance. Therefore, it is important to be able to control the stress formation in thin film.

The Stoney formula [9] is commonly used for estimation of stresses in the thin film systems. This formula has been extended to calculate stresses in multi-layered thin films deposited on a substrate exposed to non-uniform misfit strains, which provides a way to experimentally determine stresses in such systems [10]. Analytical and experimental methods, including the substrate curvature and X-ray methods, are also useful but they cannot provide the stress distribution in thin film systems when manufacturing and across individual film layers.

The numerical simulation is an efficient technique for studying complex systems, including studies in thermoelastic stress analysis of the thin film-substrate system. Multiphysics package as ANSYS is very suitable for such investigations. It allows to perform the thermomechanical analysis for both temperature and stress estimation. The simulation gives the opportunity to analyze the generation and evolution of stresses in thin film structures and processing conditions on the stress distribution. A more comprehensive investigation was carried out by Pramanik and Zhang [11]; they used anisotropic material properties and a three-dimensional finite element (FE) model to investigate the residual stresses in the thin film and substrate. Citirik et al. [12] used the FE analysis to simulate the residual stresses developed in density modulated silicon (Si) thin films, which incorporate alternating low- and high-density layers. Tinoko et al. [13] showed a methodology to estimate mechanical parameters of thin films by means of a bulge test and a numerical approach. Although many studies in stress evolution during thin film production have been carried out, some questions related to underlying mechanisms remain unanswered, and it remains unknown how the stresses are stipulated by specific material structures and manufacturing conditions, influence of material nonlinearity properties in temperature range, etc.

The goal of our research was to investigate the thermoelastic stresses in the thin TiO_2 films on substrates obtained by LA and to analyze occurrence and evolution of thermoelastic stresses and defects in the film-substrate structure and to determine the conditions that prevent cracks formation.

It is necessary to find optimal conditions for manufacturing TiO_2 films on sapphire substrates for microelectronics application and to improve not only substrate quality but also films characteristics (i.e., reduce defects, improve oxide quality as well as reproducibility and stability of film parameters over time). The influence of the technological process on thermoelastic stresses in TiO_2 films has been studied experimentally and with simulation. We have investigated the effects of material properties, thin film structure and processing conditions on the distribution of stresses.

Computational approach

The localization of the thermal effect during TiO_2 films LA on a sapphire substrate leads to a large temperature gradient in the zone of the laser beam influence, which results in thermomechanical stresses and possible defects. The scheme of LR of a TiO_2 film 10 μm thick on the sapphire surface 430 μm thick is presented in Fig. 1.

Numerical methods allow to carry out simulations and determine the optimal parameters of films LA. Two sequential steps have to be performed for the thermomechanical stress analysis: (1) a pure thermal analysis which provides temperature and heat flux distributions in space and time, (2) a thermoelastic analysis to compute the mechanical stresses due to the temperature gradients.

To calculate the temperature fields, we use a three-dimensional heat equation:

$$C\rho\frac{\partial T}{\partial t}-\left(\frac{\partial}{\partial x}k\frac{\partial}{\partial x}T+\frac{\partial}{\partial y}k\frac{\partial}{\partial y}T+\frac{\partial}{\partial z}k\frac{\partial}{\partial z}T\right)=q, \quad (1)$$

where C is the heat capacity; ρ is the mass density; T is the temperature; t is the time; k is the thermal conductivity coefficient and q is the power density of the heat source.

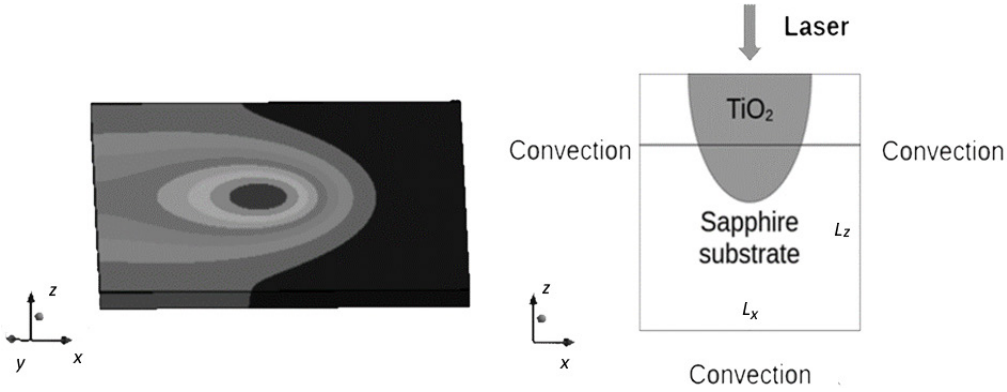

Fig. 1. Scheme of laser annealing of the titanium oxide – sapphire system (*b*) and the temperature distribution in the system's cross-section at time instant *t* (*a*);
L_x, L_z are the width and height of the sample, the laser moved from left to right

Laser energy absorbed by the structure is described by the Bouguer–Lambert–Beer expression

$$q = a(1-R)I_0(t)e^{-az}, \tag{2}$$

where *R*, *a* are the reflection coefficient and the absorption one, respectively, and
$I_0(t)$ is the laser power (LP) density.

The spatial distribution of the laser power density while pulse duration follows a Gaussian distribution, which was approximated using the equation:

$$I_0(t) = I_0 e^{\frac{-(x^2+y^2)}{r}}, \tag{3}$$

where *r* is the radius of laser beam and *x*, *y* are the spatial coordinates.

The initial condition for the heat Eq. (1) is $T(x, y, z, t = 0) = T_0$.

The boundary conditions are set to simulate convection on all boundaries:

$$-k\frac{\partial T}{\partial n} = \beta(T - T_0),$$

where β is the convection heat transfer coefficient.

The Neumann boundary conditions (flux-type) were used on the top surface for the calculation of heat transfer from the film to the substrate. The boundary condition on the top layer can be described as

$$-k\frac{\partial T}{\partial z}\Big|L_z = q_{i,j,k},$$

where $q_{i,j,k}$ is the part of flux in the nodal point *i*, *j*, *k*.

The boundary condition between the layers (with the film thickness L_1 and substrate thickness L_2) defines the equivalent temperatures in both layers:

$$T_1(z = L_1 - 0, t) = T_2(z = L_1 + 0, t).$$

After laser annealing, the cooling takes place in the air. The laser scan speed was varied for the simulation. Due to large temperature gradients, thermal stresses appear during the heating-up and the cooling-down processes. The material strains can be described as [14]:

$$\varepsilon_{tot} = \varepsilon_{el} + \varepsilon_{th}, \tag{4}$$

where ε_{tot} is the total strain, ε_{el} is the elastic strain, ε_{th} is the thermal strain.

The thermal strain is described by linear temperature dependence:

$$\varepsilon_{th} = \alpha(\Delta T). \tag{5}$$

The elastic stress is determined by the Hooke's law [14]:

$$\sigma = [D]\{\varepsilon_{th}\}. \tag{6}$$

As consequence of Eqs. (4)–(6), the strain-stress relationship for isotropic material can be described as

$$\begin{aligned}
\varepsilon_{xx} &= \frac{1}{E}\left(\sigma_{xx} + \nu(\sigma_{yy} + \sigma_{zz})\right) + \alpha(\Delta T),\\
\varepsilon_{yy} &= \frac{1}{E}\left(\sigma_{yy} + \nu(\sigma_{xx} + \sigma_{zz})\right) + \alpha(\Delta T),\\
\varepsilon_{zz} &= \frac{1}{E}\left(\sigma_{zz} + \nu(\sigma_{xx} + \sigma_{yy})\right) + \alpha(\Delta T),\\
\varepsilon_{yz} &= \frac{2(1+\nu)\sigma_{yz}}{E},\\
\varepsilon_{zx} &= \frac{2(1+\nu)\sigma_{zx}}{E},
\end{aligned} \tag{7}$$

where E is Young's modulus, ν is Poisson's ratio, α is the coefficient of linear thermal expansion, ΔT is the local rise of temperature.

The support on the three adjacent faces is assumed frictionless.

The thermophysical properties adopted for both, substrate and film are displayed in Table [2].

Three different thicknesses of the substrates whose sizes are assumed to be 10 × 10 × 0.43 mm, 10 × 10 ×1 mm, 10 × 10 × 1.5 mm have been investigated. The film thickness is varied from 1 to 30 μm.

The simulation parameters are the following: the laser power is 30–90 W; the scan speed is 1–25 mm/s; the laser scan length is 8 mm; the laser beam radius is 1.25 mm.

The FE package ANSYS was used to perform the thermophysical analysis. The temperature history calculation was used as an input for structural analysis. The transient thermal analysis was performed for the temperature distribution in the TiO_2 film on the sapphire substrate.

Table

Thermophysical properties of the titanium dioxide and sapphire substrate

Parameter	Parameter value	
	Titanium dioxide	Sapphire
Mass density, $kg \cdot m^{-3}$	4260	4000
Heat capacity, $J \cdot kg^{-1} \cdot K^{-1}$	690	1430
Thermal conductivity, $W \cdot m^{-1} \cdot K^{-1}$	85	5
Coefficient of thermal expansion, K^{-1}	$9.19 \cdot 10^{-6}$	$8.8 \cdot 10^{-6}$
Young's modulus, GPa	282	350
Poisson's ratio	0.27	0.27

A challenge arises from meshing the thin layers in order of good element quality. The number of elements used in our ANSYS simulation for the case with substrate thickness 1 mm is 5720 in which 44.5 % are the 10-node SOLID291 elements, 3.93% is the 20-node SOLID279 element, 18.69 % 8-node contact elements CONTA174 and 32.88 % are thermal surface elements SURF152. The minimum orthogonal quality is 0.04 (more than 0.01), which is the evidence of adequate meshing. The average element surface area is $3.6683 \cdot 10^{-5}$ m^2. The mesh density is finer in the laser path trajectory which gives us the opportunity to concentrate the elements in regions with large temperature gradients, obtaining increased computational efficiency.

Materials and methods

For the experiments a thin film of tetraethoxytitanium $Ti(OC_2H_5)_4$ was brought up onto a sapphire substrate with a thickness of 430 μm by centrifugation (centrifuge SPIN NXG-P1, rotor rotation speed of 2000–3000 rpm, application time of 30 s). Sapphire supports to promote high adhesion strength to the gas sensitive material and has a high melting point, high chemical and radiation resistance, high hardness and transparency, which leads to the quality and stability improvement of the gas sensitive material [15, 16].

After pre-drying in the oven at 100–120 °C for 15–20 min (the solvent and hydrolysis products have been removed from the film before) LA is carried out using the radiation of a pulsed solid-state Nd:YAG laser with a wavelength of 1064 nm (film temperature of 500–600 °C, laser beam scanning rate of 1–20 mm/s, laser power of 30–90 W). With that treatment the crystalline structure is modified and defects are reduced in order to improve the quality and stability of the gas sensitive material. The use of LA makes it possible to shorten the processing time to obtain the gas sensitive material in comparison with traditional methods (annealing in a muffle furnace) [4–8].

a)

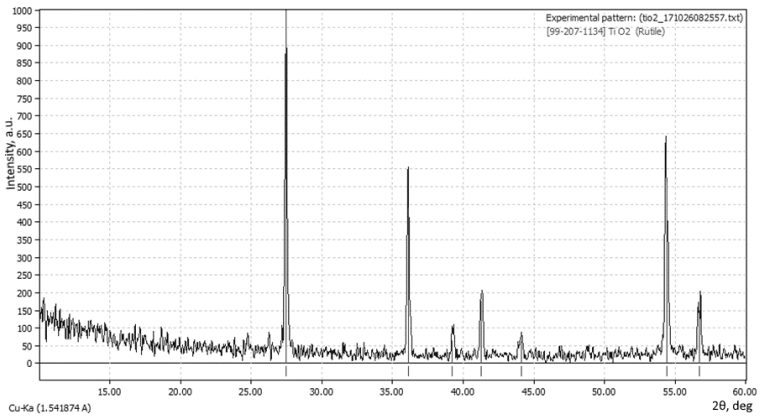

b)

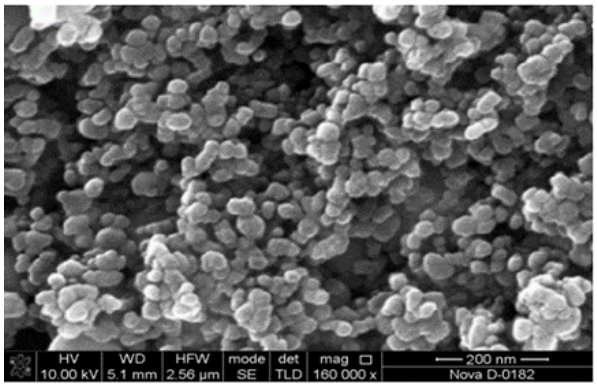

Fig. 2. The X-ray roentgenogram of the TiO_2 film obtained by laser annealing (*a*) and the SEM image of the surface morphology of the film on sapphire substrate (*b*); laser wavelength is 1.064 μm

The phase composition of the thin film structure was investigated by powder X-ray diffractometry [17]. The diffractometer ARLX'TRA, Thermo ARL was used to perform X-ray phase analysis of obtained thin films. A qualitative analysis of the phase composition was performed using an open database (card index) COD (Crystallography Open Database) and the Match program. The X-ray roentgenogram of the obtained film, reflexes of the standardized roentgenogram and Miller indices are shown in Fig. 2,*a*. We have chosen the X-ray roentgenogram for titanium oxide with the structure of rutile (card No. 99-207-1134) for reference. It can be seen from the obtained data that the reflexes of the standard sample coincide with the reflexes of the resulting film. Therefore, the material has a phase composition like the rutile modification of titanium oxide. Fig. 2,*b* shows SEM image of the surface morphology of the titanium dioxide film.

We carried out experimental studies to measure thermal stresses in thin TiO_2 films on the Tencor FLX-2320 (Japan) in the laboratories of "Piezopribor" Research Center (Rostov-on-Don, Russia).

Results and discussions

Different calculation scenarios for TiO_2 film laser annealing on sapphire substrate were considered. The experimental results showed that the temperature for TiO_2 film structure formation was about 500 °C [18]. Thermal analyses showed a temperature peak on the film surface.

We calculated the stress distribution in the TiO_2 film – sapphire structure caused from LR. The general purpose FE code ANSYS was used to simulate TiO_2 film–sapphire LA with variation of laser parameters such as the its speed and power. We investigated the scenarios with different substrate thicknesses (0.43, 1.00, and 1.50 mm). The influence of laser power, substrate thickness and laser beam speed on maximum temperature for TiO_2 laser annealing on sapphire substrate is presented in Fig. 3. Increasing the speed of the laser leads to a decrease in maximum temperature on the sample surface. This decrease can be explained by the fact that the heating and cooling require less time and the material gets less energy. The cooling rate significantly influenced the formation of TiO_2 film on sapphire substrate.

It can be seen from Fig. 3 and 4 that the large temperature gradients are the source of thermal stresses on the film surface. The heated part of material expands but the rest material restrains the movement of heated one. So, we have the compressive region in the under irradiated zone. During the cooling, compressive stresses appeared in irradiated zone, but the rest is in tensile state.

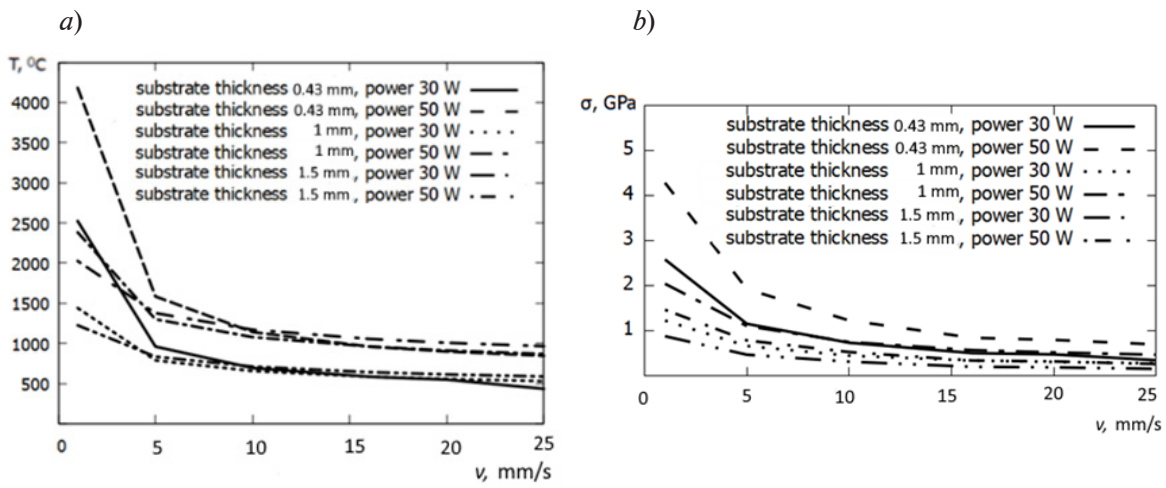

Fig. 3. The dependences of the sapphire substrates' temperature *T* (*a*) and its stress σ (*b*) on the laser beam speed at different laser power values and the thicknesses of sapphire substrates; the thickness of a TiO_2 film is 5 μm

Fig. 4 illustrates the equivalent (von-Mises) stresses during TiO_2 film LA on sapphire substrate. The maximum temperature for that case was about 530 °C at a laser scan speed of 25 mm/s, suba strate thickness was 1 mm and laser power was 30 W. When the laser beam begins to scan a path (Fig. 4, *a*–*c*), the stresses increase, but the low temperature of the surrounding material restricts the heated zone expansion causing the formation of compressive stresses (equivalent (von-Mises) stress is 1.3 GPa at 0.08 s of LA). When cooling, the temperature decreases and the material is exposed to lower stresses (equivalent (von-Mises) stress is 8.42 MPa at 8 s, the laser treatment time is 0.32 s).

The behavior of stresses in the processed material strongly depends on the temperature gradients. The maximum principal stress (see Figs. 3, 4) indicates the overall stress state of material. When the largest principal stress exceeds the uniaxial tensile strength 30, a crack might be initiated. The tensile strength limit of TiO_2 film on sapphire substrate is 333 MPa. If the maximum principal stress is less than the tensile strength limit for titanium dioxide, no cracks formation is expected.

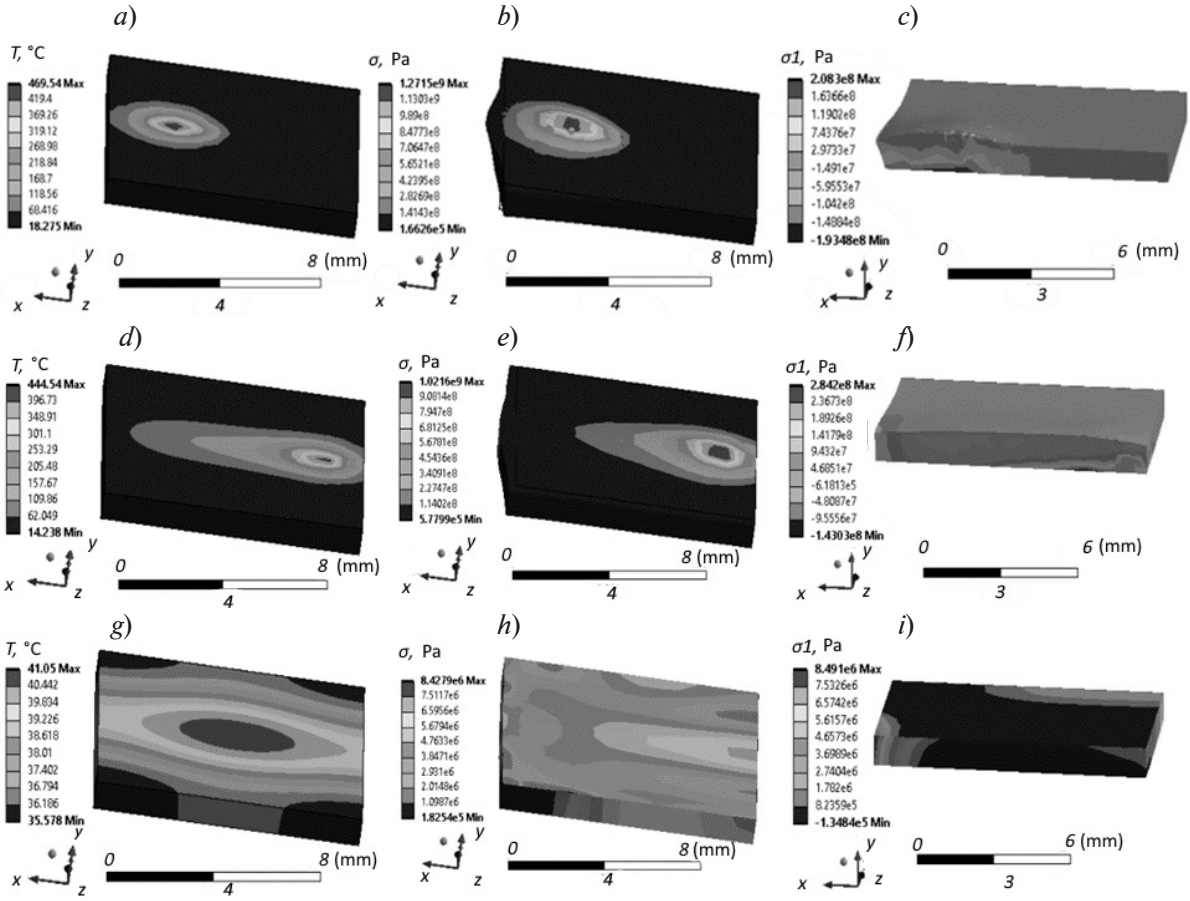

Fig. 4. The calculated distributions of maximum temperature (*a*, *d*, *g*), of equivalent von Mises stresses (*b*, *e*, *h*), and of maximum principle stresses (*c*, *f*, *i*) over a vertical cross-section of the body at different time points in the laser processing, s: 0.08 (*a*, *b*, *c*), 0.32 (*d*, *e*, *f*) and 8.0 (*g*, *h*, *i*). These are criteria for crack initiation during TiO_2 film LA, under the following conditions: a laser scan speed is 25 mm/s; LP is 30 W; the film thickness is 5 μm, the substrate one is 1 mm; the duration of laser treatment is 0.32 s

The simulation results indicate that the thickness ratio between the TiO_2 film and the sapphire substrate plays an important role in the LA. The capability of the substrate to diffuse the heating from the film enables a proper temperature distribution inside the film, avoiding the overheating of the surface. It has significant influence on defects like cracks formation.

The increase of film thickness from 5 to 30 μm decreases the maximum principal stresses. The stress variation induced by an annealing is as much higher as film thickness is low. We can see in Fig. 3 that the thicker substrate (1 mm) and the higher laser speed (more than 2 cm/s at laser

power of 30 W) allow to obtain a film without cracking risk. It is possible to control and vary the value of thermoelastic stresses in the film-substrate structures due to changes of film annealing processing parameters: substrate temperature, laser radiation power, film and substrate thicknesses, pulse duration, sample movement velocity, etc. Thereby one can optimize film properties for the task and device design.

Conclusion

We have simulated TiO_2 thin films processing on sapphire substrates and conducted related experiments. We developed a three-dimensional model for the analysis of the stress distribution in film-substrate structure. The films properties were investigated with atomic force microscopy method, scanning electron microscopy, and X-ray phase analysis.

The thermomechanical model for TiO_2 LA on sapphire substrate was implemented in ANSYS software. We investigated that the temperature on TiO_2 film (thickness of 5 μm) surface is about 500 – 600 °C at an average LR power of 30 W, which is a prerequisite for the growth of films on the substrate surface. It corresponds to the level of thermoelastic stresses (much less than the material elastic limit) such that the cracks formation is not expected. The morphology of the film structure can be varied by changing the laser power and temperature, which allows to reallocate defects in the structure and to improve the films quality for their usage in microelectronics and thin film optics.

Higher scan speed leads to lower temperatures and larger temperature gradient during the material heating and cooling. The film and substrate thickness play a key role in the formation of cracks and defects in film. The studies showed that cracks on the surface can be formed in thicker films. The thicker substrate (1 mm), the bigger laser scan speed (more than 20 mm/s), and the smaller laser power (30 W) allow to obtain the film without cracking risk. Thus, the TiO_2 film-to-substrate thickness ratio, LP, laser scan speed are the most important parameters to process a uniform film for their application in microelectronics.

REFERENCES

1. **Krylov O. V.,** Geterogennyi karaliz [Heterogeneous catalysis], Academkniga, Moscow, 2004 (in Russian).

2. **Gas'kov A. M., Rumyantseva M. N.,** Materials for solid-state gas sensors, Inorg. Mater. 36 (3) (2000) 293–301.

3. **Ugai Ya. A.,** Introduction to semiconductor chemistry, 2nd edition, Vysshaya Shkola, Moscow, 1975 (in Russian).

4. **Malyukov S. P., Kulikova I. V., Sayenko A. V., Klunnikova Yu. V.,** Optimization of the structure nanoporous TiO_2 film in a dye-sensitized solar cell, J. Phys. Conf. Ser. 541 (2014) 012060.

5. **Malyukov S. P., Sayenko A. V., Klunnikova Yu. V.,** Research of influence of laser annealing parameters on structural and morphological properties of TiO_2 thin films, IOP Conf. Series: Mater. Sci. & Eng. Vol. 475 (VII and VIII Int. Conf. Phys. & Technol. Nanoheterostruct. Microwave Electr., Russian Federation, Moscow (2019) 012008.

6. **Klunnikova Yu. V., Malyukov S. P., Sayenko A. V., Tolstunov M. I.,** Investigation of titanium oxide film on sapphire substrate for gas sensor, J. Phys. Conf. Ser. 1124 (2) (2018) 022003.

7. **Klunnikova Yu. V., Malyukov S. P., Sayenko A. V., Biyatenko Yu. N.,** Investigation of internal thermoelastic stresses in TiO_2 film on sapphire substrate, Int. J. Civil Eng. & Technol. 10 (1) (2019) 227–232.

8. **Malyukov S. P., Klunnikova Yu. V. Sayenko A. V.,** Laser annealing of oxide films on the sapphire surface, J. Russ. Laser Res. 36 (3) (2015) 276–280.

9. **Stoney G. G.,** The tension of metallic films deposited by electrolysis, Proc. Royal Soc. London A. 82 (553) (1909) 172–175.

10. **Brown M. A., Rosakis A. J., Feng X., et al.,** Thin film/substrate systems featuring arbitrary film thickness and misfit strain distributions, P. II: Experimental validation of the non-local stress/curvature relations, Int. J. Solids & Struct. 44 (6) (2007) 1755–1767.

11. **Pramanik A., Zhang L. C.,** Residual stresses in silicon-on-sapphire thin film systems, Int. J. Solids & Struct. 48 (9) (2011) 1290–1300.

12. **Citirik E., Demirkan M. T., Karabacak T.,** Stress modeling of density modulated silicon thin films using finite element, J. Vacuum Sci. & Technol. A. 33 (2) (2015) 021503.

13. **Tinoco H. A., Holzer J., Pikálek T., et al.,** Estimation of mechanical parameters of thin films using finite element analysis, Proc. 20-th Int. Conf. Appl. Mech. 20 (April) (2018) 157–162.

14. **Rubino F., Astarita A., Carlone P.,** Thermo-mechanical finite element modeling of the laser treatment of titanium cold-sprayed coatings, Coatings. 8 (6) (2018) 219.

15. **Dobrovinskaya E. R., Lytvynov L. A., Pishchik V.,** Sapphire: material, manufacturing, applications, Springer, New York, 2009.

16. **Akselrod M. S., Bruni F. J.,** Modern trends in crystal growth and new applications of sapphire, J. Cryst. Growth. 360 (1 December) (2012) 134–145.

17. **Kovba L. M., Trunov V. K.,** Rentgenofazovyi analiz [X-ray phase analysis], Moscow State University Publishing, Moscow, 1976 (in Russian).

18. **Welsch G., Boyer R., Collings E.** (Eds.), Materials properties handbook: Titanium alloys, ASM International, Materials Park OH, USA,1994.

19. **Wang Y., Wang Q., Chen H., et al.,** Comparative study on crack initiation and propagation of glass under thermal loading, Mater. 9 (10) (2016) 794.

СПИСОК ЛИТЕРАТУРЫ

1. **Крылов О. В.** Гетерогенный катализ. М.: Академкнига, 2004. 679 с.

2. **Гаськов А. М., Румянцева А. М.** Выбор материалов для твердотельных газовых сенсоров // Неорганические материалы. 2000. Т. 3 № .36. С. 378–369.

3. **Угай Я. А.** Введение в химию полупроводников. -2е изд. М.: Высшая школа, 1975. 302 с.

4. **Malyukov S. P., Kulikova I. V., Sayenko A. V., Klunnikova Yu. V.,** Optimization of the structure nanoporous TiO_2 film in a dye-sensitized solar cell // Journal of Physics: Conference Series. 2014. Vol. 541. P. 012060.

5. **Malyukov S. P., Sayenko A. V., Klunnikova Yu. V.** Research of influence of laser annealing parameters on structural and morphological properties of TiO_2 thin films // IOP Conf. Series: Materials Science and Engineering. 2019. Vol. 475. VII and VIII International Conf. on Physics and Technologies of Nanoheterostructure Microwave Electronics. Moscow, Russian Federation. P. 012008.

6. **Klunnikova Yu. V., Malyukov S. P., Sayenko A. V., Tolstunov M. I.** Investigation of titanium oxide film on sapphire substrate for gas sensor // Journal of Physics: Conference Series. 2018. Vol. 1124. No. 2. P. 022003.

7. **Klunnikova Yu. V., Malyukov S. P., Sayenko A. V., Biyatenko Yu. N.** Investigation of internal thermoelastic stresses in TiO_2 film on sapphire substrate // International Journal of Civil Engineering and Technology. 2019. Vol. 10. No. 1. Pp. 227–232.

8. **Malyukov S. P., Klunnikova Yu. V. Sayenko A. V.** Laser annealing of oxide films on the sapphire surface // Journal of Russian Laser Research. 2015. Vol. 36. No. 3. Pp. 276–280.

9. **Stoney G. G.** The tension of metallic films deposited by electrolysis // Proceedings of the Royal Society of London A. 1909. Vol. 82. No. 553. Pp. 172–175.

10. **Brown M. A., Rosakis A. J., Feng X., Huang Y., Üstündag E.** Thin film/substrate systems featuring arbitrary film thickness and misfit strain distributions. Part II: Experimental validation of the non-local stress/curvature relations // International Journal of Solids and Structures. 2007. Vol. 44. No. 6. Pp. 1755–1767.

11. **Pramanik A., Zhang L. C.** Residual stresses in silicon-on-sapphire thin film systems, // International Journal of Solids and Structures. 2011. Vol. 48. No. 9. 1290–1300.

12. **Citirik E., Demirkan M. T., Karabacak T.** Stress modeling of density modulated silicon thin films using finite element // Journal of Vacuum Science and Technology A. 2015. Vol. 33. No. 2. P. 021503.

13. **Tinoco H. A., Holzer J., Pikálek T., Buchta Z., Lazar J., Chlupová A., Kruml T., Hutař P.** Estimation of mechanical parameters of thin films using finite element analysis // 20-th International Conference of Applied Mechanics. 2018. Vol. 20. April. Pp. 157–162.

14. **Rubino F., Astarita A., Carlone P.** Thermo-mechanical finite element modeling of the laser treatment of titanium cold-sprayed coatings // Coatings. 2018. Vol. 8. No. 6. P. 219.

15. **Добровинская Е., Литвинов Л., Пищик В.** Энциклопедия сапфира. Харьков: НТК «Институт материалов», 2004. 503 с.

16. **Akselrod M. S., Bruni F. J.** Modern trends in crystal growth and new applications of sapphire // Journal of Crystal Growth. 2012. Vol. 360. 1 December. Pp. 134–145.

17. **Ковба Л. М., Трунов В. К.** Рентгенофазовый анализ. 2-е изд. М.: Изд-во МГУ, 1976. 232 с.

18. **Welsch G., Boyer R., Collings E.** (Eds.). Materials properties handbook: Titanium Alloys. USA: ASM International, Materials Park OH, 1994. 517 p.

19. **Wang Y., Wang Q., Chen H., Sun J., He L.** Comparative study on crack initiation and propagation of glass under thermal loading // Materials. 2016. Vol. 9. No. 10. P. 794.

THE AUTHORS

KLUNNIKOVA Yulia V.
Southern Federal University
105 Bolshaya Sadovaya St., Rostov-on-Don, 344006, Russia
yvklunnikova@sfedu.ru
ORCID: 0000-0002-2015-3739

ANIKEEV Maxim V.
Fraunhofer SIT | ATHENE
75 Rheinstr., Darmstadt, 64295, Germany
maxim.anikeev@sit.fraunhofer.de
ORCID: 0000-0002-4959-2663

FILIMONOV Alexey V.
Peter the Great St. Petersburg Polytechnic University
29 Politechnicheskaya St., St. Petersburg, 195251, Russia
filimonov@rphf.spbstu.ru
ORCID: 0000-0002-2793-5717

СВЕДЕНИЯ ОБ АВТОРАХ

КЛУННИКОВА Юлия Владимировна – *кандидат технических наук, доцент кафедры конструирования электронных средств Института нанотехнологий, электроники и приборостроения Южного Федерального университета.*
344006, Россия, г. Ростов-на-Дону, Большая Садовая ул., 105.
vklunnikova@sfedu.ru
ORCID: 0000-0002-2015-3739

АНИКЕЕВ Максим Владимирович – *кандидат технических наук, доцент Института безопасных информационных технологий Общества Фраунгофера (члена научно-исследовательского центра «Афина»).*
Рейнштрассе, 75, г. Дармштадт, 64295, Германия
maxim.anikeev@sit.fraunhofer.de
ORCID: 0000-0002-4959-2663

ФИЛИМОНОВ Алексей Владимирович – *доктор физико-математических наук, профессор Высшей инженерно-физической школы, соруководитель Научно-образовательного центра «Физика нанокомпозитных материалов электронной техники» Санкт-Петербургского политехнического университета Петра Великого.*
195251, Россия, г. Санкт-Петербург, Политехническая ул., 29
filimonov@rphf.spbstu.ru
ORCID: 0000-0002-2793-5717

Received 14.04.2022. Approved after reviewing 27.05.2022. Accepted 27.05.2022.
Статья поступила в редакцию 14.04.2022. Одобрена после рецензирования 27.05.2022. Принята 27.05.2022.

Original article
DOI: https://doi.org/10.18721/JPM.15309

NUMERICAL SIMULATION OF TURBULENT AIRFLOW AND HEAT TRANSFER AROUND A SEATED THERMAL MANIKIN IN THE ROOM WITH MIXING VENTILATION

M. A. Zasimova, A. A. Marinova, N. G. Ivanov✉*, A. D. Podmarkova*

Peter the Great St. Petersburg Polytechnic University, St. Petersburg, Russia

✉ ivanov_ng@spbstu.ru

Abstract. The numerical simulation of turbulent flow and heat transfer, when air moves around a thermal manikin sitting in a model room with mixing ventilation, has been carried out. The calculations were performed on the basis of the RANS approach using the standard k-ε turbulence model. The buoyancy effects were described in the Boussinesq approximation. The obtained calculated data were close to the experimental ones, although there were local differences in the temperature distribution near the surface of the room walls. The impossibility of correct determination of the integral heat removal from the surface of the body without taking into account the radiation heat transfer was established. Along with studies in the ventilation regime with predominant forced convection, corresponding to the experiment, the characteristics of the flow and heat transfer in the free convection regime were analyzed, where the flow structure being caused by an intensive thermal plume forming above the manikin, and the temperature field being stratified in height.

Keywords: ventilation, thermal mannequin, turbulent airflow, heat transfer, natural and forced convection

Funding: The research work was supported by a grant from the President of the Russian Federation (No. MK-1762.2022.1.1).

Citation: Zasimova M. A., Marinova A. A., Ivanov N. G., Podmarkova A. D., Numerical simulation of turbulent airflow and heat transfer around a seated thermal manikin in the room with mixing ventilation, St. Petersburg Polytechnical State University Journal. Physics and Mathematics. 15 (3) (2022) 111–131. DOI: https://doi.org/10.18721/JPM.15309

Научная статья
УДК 532.517
DOI: https://doi.org/10.18721/JPM.15309

ЧИСЛЕННОЕ МОДЕЛИРОВАНИЕ ВОЗДУШНЫХ ПОТОКОВ ПРИ ОБТЕКАНИИ СИДЯЩЕГО ТЕПЛОВОГО МАНЕКЕНА В ПОМЕЩЕНИИ С ПЕРЕМЕШИВАЮЩЕЙ ВЕНТИЛЯЦИЕЙ

М. А. Засимова, А. А. Маринова, Н. Г. Иванов✉*, А. Д. Подмаркова*

Санкт-Петербургский политехнический университет Петра Великого,

Санкт-Петербург, Россия

✉ ivanov_ng@spbstu.ru

Аннотация. Выполнено численное моделирование турбулентного течения и теплообмена при обтекании воздушным потоком сидящего теплового манекена, размещенного в модельном помещении с перемешивающей вентиляцией. Расчеты проведены на основе RANS-подхода с использованием стандартной k-ε модели турбулентности. Эффекты плавучести описаны в приближении Буссинеска. Полученные расчетные данные близки к экспериментальным, хотя имеются локальные отличия по распределению температуры вблизи поверхности стенок помещения. Установлено, что без учета лучистого теплообмена невозможно правильно определить интегральный теплосъем с поверхности тела. Наряду с исследованиями режима вентиляции с преобладанием вынужденной конвекции, соответствующим эксперименту, были изучены характеристики течения и теплообмена в свободноконвективном режиме, где структура течения определяется интенсивным тепловым факелом, формирующимся над манекеном, а поле температуры стратифицировано по высоте.

Ключевые слова: вентиляция, тепловой манекен, турбулентное течение, теплообмен, естественная и вынужденная конвекция

Финансирование: Работа выполнена при финансовой поддержке гранта президента Российской Федерации МК1762.2022.1.1-.

Ссылка для цитирования: Засимова М. А., Маринова А. А., Иванов Н. Г., Подмаркова А. Д. Численное моделирование воздушных потоков при обтекании сидящего теплового манекена в помещении с перемешивающей вентиляцией // Научно-технические ведомости СПбГПУ. Физико-математические науки. 2022. Т. 15. № 3. С. 111–131. DOI: https://doi.org/10.18721/JPM.15309

Introduction

Heating, ventilation, and air conditioning systems (HVAC) are aimed at ensuring thermal comfort for humans in residential structures, providing environments with controlled parameters [1, 2]. In real-life conditions, rooms are almost always occupied by people, as well as blocked by furniture or other interior objects. Computations of ventilation systems are often performed for empty rooms free of obstructions [3, 4] in order to minimize geometric uncertainties. The temperature field of a person or a group of people in the room plays the major role in assessments of thermal comfort and air quality. The thermal characteristics, as well as the general structure of the flow can vary substantially in this case. Experimental studies typically use models reproducing the human body parameters to some extent, rather than living people (whose individual characteristics are nearly impossible to reproduce).

The model of the human body can be greatly simplified; for example, lamps with heat emission corresponding to the human body were used in [5], experimentally studying the air distribution

in the room for various ventilation scenarios. However, most studies describe human-like thermal manikins (one or several) with controlled parameters, including thermal conditions on the body surface [6]. Accordingly, virtual thermal manikins that fully or partially reproduce these parameters are used for numerical simulations. One or more realistic thermal manikins were used in computations of air distribution and estimation of thermal comfort parameters in [7–9].

However, uncertainties associated with setting a large number of a priori unknown parameters appear even in applied ventilation problems formulated and solved with controlled thermal manikins; these parameters include the number of people in the room, all kinds of movements they make, the exact location of a person in space in the operating conditions, the geometric configuration (exact shape) of the body, the thermal insulation properties of clothing, etc. If all of these parameters are based on some approximate estimates, it is virtually impossible to solve the problem fully accounting for all of the given conditions, so the influence of the parameters complicating the problem is generally considered separately.

One of the parameters examined in a number of studies is the influence of the thermal manikin's shape on the characteristics of flow and heat transfer. Clearly, the shape of a physical or virtual thermal manikin can be greatly simplified. For example, simplified geometric shapes of the manikin can be used to account for obstructions in the room [10, 11]. However, it is established in [12–14], the shape of the manikin can significantly affect the local characteristics of the flow near the manikin. Four manikin shapes were considered in the experimental study in [12]: one approximating the human shape and three simplified shapes (a cylinder, a parallelepiped and a combination of these figures). Airflow computations were carried out in [13] near six manikin shapes with different details. Numerical simulation was performed in [14] for the problem with three manikin shapes (the one approximating the shape of the human body, as well as partially and completely simplified shapes composed of parallelepipeds). Studies indicate that the shape of the manikin close to the human body should be used to predict local characteristics.

Computations in unsteady conditions were carried out in [15, 16] with the position of the manikin spatially varied over time. A full-scale experiment and computer simulation (Large Eddy Simulation) were carried out in [15] to study the flow evolving for a manikin moved between rooms with different concentrations of polluted air. The door between the rooms was opened during the experiment, and the manikin was moved through the doorway, but the variations in the positions of manikin's individual parts were not taken into account. The influence of the thermal manikin's movement on stratification of the temperature field was experimentally investigated in [16]. The variables were the velocity of the manikin, the movement duration, the intensity of heat generation from the surface and the air change rate (airflow per unit time).

Generally, a clothed manikin and the specific characteristics of its clothing can significantly affect the heat transfer from its surface (see, for example, [12, 17, 18]). For example, the thermal insulation characteristics of clothing, the presence of hair on the surface of the head and the design of the chair on which the manikin was seated were varied in [12]. The effect of clothing on heat transfer was considered in [17]. The main parameter in the experimental study [18] was the type of clothing; the mannequin was dressed in light summer clothes, in warm winter clothes and in a business suit.

The respiration process of a thermal manikin was considered in [19, 20]: the periodic propagation of an air jet produced during exhalation can modify the structure of the flow near the manikin and affect the characteristics of heat and mass transfer. The unsteady processes of inhalation and exhalation through the nostrils and mouth were modeled in [19] for a sitting and standing manikin under transient conditions. The air flow was also simulated inside the manikin. The RANS-approach was applied in [20] in a steady-state formulation to simulate three phases of breathing (inhalation, exhalation and the pause between them) for a standing manikin. The review [21] considers studies that performed numerical simulation of breathing in a manikin, giving the boundary conditions (periodic breathing cycles) set in the corresponding computations on the surface of the manikin's mouth. Several recent publications are aimed at solving the crucial problem of predicting the dispersion of saliva droplets released during breathing or coughing (sneezing) [22–24].

Numerous experimental and computational studies described the structure of the flow and the characteristics of heat and mass transfer in ventilated rooms occupied by people. Efforts are also underway to validate the computational techniques, generally considering rooms unoccupied rooms (see, for example, [25–27]). Computational validations require data from well-documented

experimental tests; however, such tests are scarce for rooms with thermal manikins. Experiments at the Danish Technical University (Lyngby, Denmark) were carried out in 2003 and 2007 for the conditions of displacement [28] and mixing [28–31] ventilation (the results are compiled into a database at http://www.cfdbenchmarks.com/). Data from the test with displacement ventilation were used earlier to validate numerical simulation techniques in [14, 32, 33]. Data from the test with mixing ventilation were used earlier in [34–36]. The conditions of this test are reproduced in this paper.

The goal of our study consists in numerical analysis of the structure of turbulent flow and the characteristics of heat transfer for airflow around a sitting thermal manikin in a model room.

Computations were performed for conditions close to experimental ones [30, 31], and the results of numerical simulation are compared with the experimental data. Aside from validating the computational technique, we analyzed the influence of thermal conditions on the surface of the manikin (constant temperature or constant specific heat flux). Furthermore, the role of various heat transfer mechanisms was considered as part of the parametric study.

Problem statement

Geometric model. The model of the ventilated room corresponds to the data of experimental studies [30, 31] and is a parallelepiped with the length $L = 2.44$ m (along the axis x), height $H = 2.46$ m (along the axis y) and the width $W = 1.20$ m (along the axis z). One of the side walls of the room is open (marked as Inlet in Fig. 1,*a*); air enters the room through this interface, assumed to be an inlet opening for the computational domain. Two circular exhaust opening with the same diameter equal to $d_{out} = 0.25$ m are located on the opposite side wall (marked as Outlet in Fig. 1,*a*). The outlet openings are centered relative to the axis z, the centers of the lower and upper openings are located 0.6 m away from the floor and ceiling of the room, respectively.

A seated thermal manikin (see Fig. 1) was placed in the room 0.5 m from the open boundary (0.7 m to the manikin's knees). The distances from the manikin surface to the side walls of the room are the same in the transverse direction (axis z), amounting to 0.325 m; there is a gap 0.002 m high between the floor of the room and the manikin's feet. The geometry of the manikin is taken from the database at www.cfd-benchmarks.com, with the description of the conditions and results of the experiment. The characteristic (maximum) size of the manikin is $l_m = 0.76$ m in the longitudinal direction (along the axis x), $h_m = 1.36$ m in the vertical direction (along the axis y) and $w_m = 0.55$ m in the transverse direction (along the axis z) . The surface area of the manikin is $S_m = 1.60$ m^2.

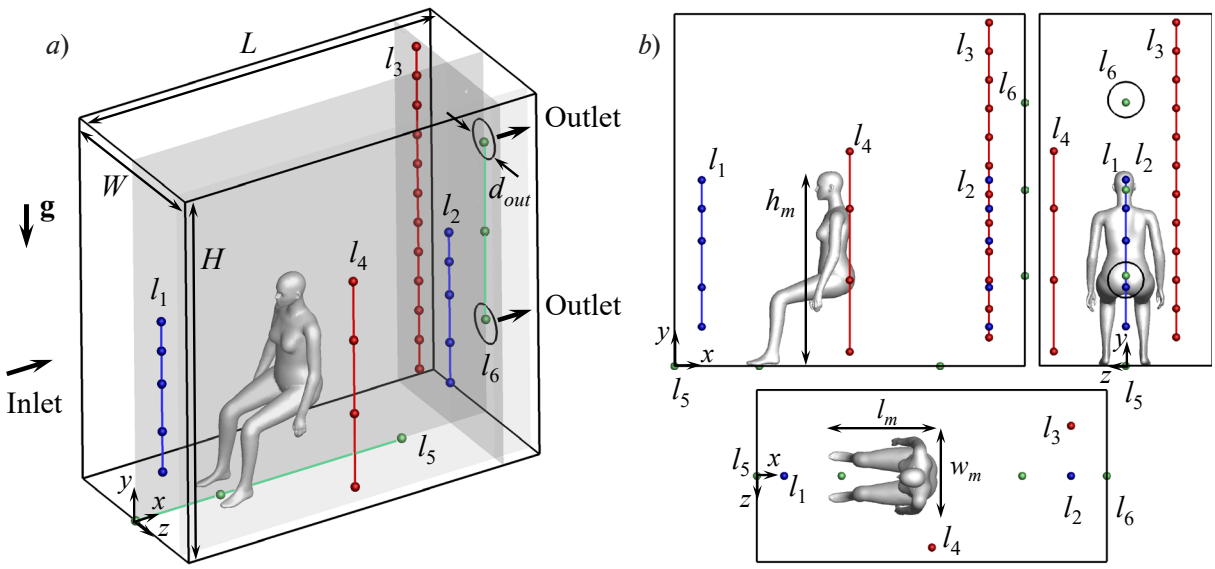

Fig. 1. Images of computational model of the room with a seated manikin in isometric projection (*a*) and in planes (*b*).
Lines l_1–l_6 show the points where the velocity (blue) and temperature (red and green) were measured (see [30, 31])

No modifications were introduced in the present study to the geometric model of the manikin provided in the database. However, as evident from the illustrations both for the experiments described in [30, 31] and for subsequent studies dedicated to numerical simulation [34, 35], the manikin was tilted by some angle relative to the vertical axis. We can therefore assume that the positions of the individual parts of the manikin in the experimental setup were different from those available in the database, although no information about this is given in either the studies or the documentation. Thus, the position of the manikin in the room is somewhat unclear, so it cannot be accounted for in the statement to the computational problem.

The positions of lines l_1–l_6 along which the measurements were carried out [30, 31] are shown in Fig. 1. The points highlighted are the ones for which experimental values are given in the database. The velocity magnitudes were measured along the lines l_1 and l_2 using a spherical thermal anemometer; the lines are located in the central section of room $z = 0$ 0.19 m and 2.19 m away from its open boundary, respectively. The temperature was measured with thermocouples along the lines l_3 and l_4 placed near the walls of the room ($x = 2.19$ m, $z = -0.35$ m and $x = 1.22$ m, $z = 0.50$, respectively), and along the lines l_5 and l_6 on the surface of the room ($y = 0$, $z = 0$ and $x = L$, $z = 0$).

Physical parameters of the environment and boundary conditions. We considered the flow of air whose properties were assumed to be constant at a temperature of 20 °C. The Prandtl number was equal to $\mathrm{Pr} = \mu C_p/\lambda = 0.7$, where μ is the dynamic viscosity equal to $1.81 \cdot 10^{-5}$ kg/(m·s); C_p is the specific heat of air at a constant pressure of 1.005 kJ/(kg·K); λ is the thermal conductivity equal to 25.9 mW/(m·K).

The computational cases with different inlet boundary conditions, thermal conditions on the manikin surface, and parameters of the physical model are given in Tables 1 and 2.

Two values of airflow rate were considered: 0.7970 m^3/s (the corresponds to the experimental value in [30, 31]) and 0.0295 m^3/s. The air in the experiment was sucked through the outlet openings, and the conditions for air inflow through the open endwall of the room ensured a uniform profile. A uniform distribution of the inlet velocity was adopted in the computations, also with two values: $V_{in} = 0.27$ and 0.01 m/s (respectively). In accordance with the experimental conditions in [30, 31], constant air temperature was maintained at the inlet boundary, equal to $T_{in} = 20.4$ °C. The Reynolds number constructed from the inlet air velocity and the width of the manikin, i.e.,

$$\mathrm{Re} = \rho w_m V_{in}/\mu,$$

where ρ is the air density equal to 1.205 kg/m^3, was Re = 366 and 9886 at $V_{in} = 0.01$ and 0.27 m/s, respectively.

With the room height used as a linear scale, the Reynolds number $\mathrm{Re}_H = \rho H V_{in}/\mu$ amounted to $\mathrm{Re}_H = 1.638$ and 44.218, respectively.

The no-slip condition was imposed at the solid boundaries of the room, the walls were assumed to be adiabatic (setting zero heat flux q_w including the conductive and the convective component). Constant pressure was imposed at the outlet boundaries.

Table 1

Boundary conditions for different computational cases

Parameter	Value for case						
	1	2	3	4	5	6	7
V_{in}, m/s	0.27				0.01		
T_w, °C	34.0	–					
q_w, W/m^2	–		139.3	80.5	139.3	66.1	139.3

Notations: V_{in} is the air velocity at the entrance to the room, T_w is the temperature at the surface of the thermal manikin, q_w is the total specific heat flux including three components (conductive, convective and radiative).

Either constant temperature T_w or constant total specific heat flux q_w including all three components (conductive, convective and radiative) were set on the surface of the manikin for different computational cases. In accordance with the experimental conditions given in [30, 31], a constant temperature equal to T_w = 34 °C was maintained on the manikin surface. The computational case best reproducing the experimental conditions is Case 1 in Table 1. The Grashof number, constructed from the height of the manikin,

$$\mathrm{Gr} = \rho^2 g\beta(T_w - T_{in})h_m{}^3/\mu^2,$$

was equal to Gr = $5.06 \cdot 10^9$ (g is the gravity acceleration, β is the thermal expansion coefficient equal to 0.0034 K^{-1}).

Notably, part of the manikin surface around the knees was thermally insulated in [30, 31]; this was not taken into account in our computations because there is no accurate data about the location of this area.

Table 2

Parameters of the physical model for computational cases

Case	1	2	3	4	5	6	7
Radiation model	+	–	+	–	+	–	+
Gravity	+						–

The computational software allowed to comprehensively analyze the contributions from various heat transfer mechanisms to integral heat removal from the manikin surface. Evidently, forced convection is predominant in Cases 1–4 and free convection in Cases 5–7; Cases 1, 3, 5, 7 accounted for the contribution from radiative heat transfer to heat removal, while radiative heat transfer was not simulated in Cases 2, 4, 6. Additional computations were carried out for low flow rate of air under zero gravity conditions (see Tables 1 and 2, Case 7): radiative heat transfer is predominant, the contribution from free convection is absent. These conditions correspond, for example, to those at the International Space Station under ventilation shutdown [37, 38].

The air in the room was assumed to be transparent for simulation of thermal radiation, the emissivity (degree of blackness) was taken equal to 0.93 for the thermal manikin and 0.83 for the solid surfaces of the room model.

Mathematical and computational model. Turbulent airflow was simulated by the RANS approach (solving the Reynolds-averaged Navier–Stokes equations); see monograph [39] for more details. The Reynolds stress tensor was calculated from the Bussinesq approximation, while the turbulent viscosity was determined by the standard k-ε turbulence model. The Enhanced Wall Treatment option was used near the solid walls. The following turbulence characteristics were set at the inlet boundary in accordance with the selected model: turbulence intensity I = 6% and the ratio of turbulent to molecular viscosity μ_t/μ = 10.

The system of governing equations for motion includes the equation for heat balance, while the buoyancy force is described in the Bussinesq approximation. The direction of the gravitational acceleration vector is marked by the arrow in Fig. 1,*a*.

Radiative energy transfer was accounted for using the surface-to-surface (S2S) model available in ANSYS Fluent. The model allows to determine the transfer of energy between differently heated solid surfaces, while the transmissivity of the body is taken equal to zero.

The computational mesh was constructed in the ICEM CFD package; the resulting mesh consisted of tetrahedral elements away from solid surfaces and prismatic layers near them. The mesh was clustered near the surface of the manikin. Five prismatic layers were set near each wall of the room without clustering, the height of the first near-wall layer was y_p = 5 mm; eleven prismatic layers with a clustering coefficient of 1.1 were set near the surface of the manikin, with y_p = 1 mm. ANSYS Fluent tools were used to convert the tetrahedral elements of the mesh to polyhedra, the total size of the transformed mesh was 590,000 cells. This mesh was used in all computations (Fig. 2,*a*).

The distribution of the dimensionless distance y^+ from the center of the first near-wall cell to the wall is shown in Fig. 2, *b*, *c*. The value of the quantity y^+ averaged 1.37 over the manikin surface, its maximum value of 3.81 was detected on the surface of the manikin's hands. The average value of y^+ on the walls perpendicular to the axes *y* and *z* was 3.34, the maximum values of y^+ lay near the outlet opening, reaching 80 locally.

The computations were performed using the ANSYS Fluent CFD package. The equations were discretized with second-order accuracy. The Coupled scheme was used to relate the fields of pressure and velocity components. The residuals in the presented computations converge in the steady-state formulation.

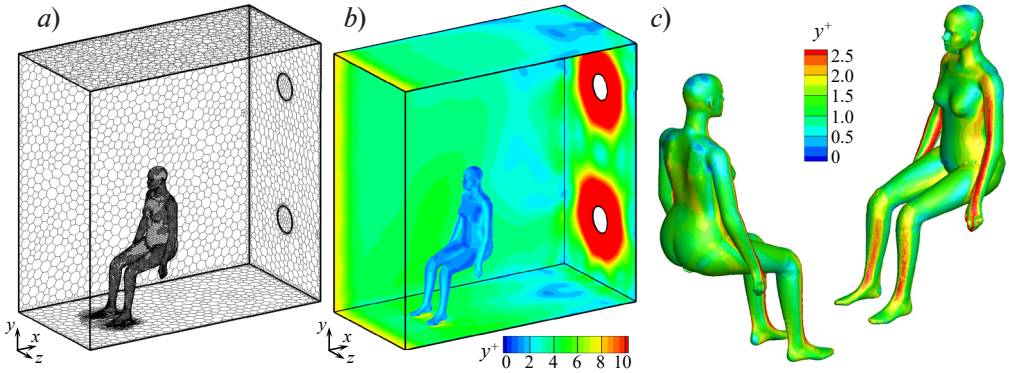

Fig. 2. Illustration of computational aspects: general view of computational mesh (*a*), distribution of quantity y^+ over the surfaces of room walls (*b*) and manikin (*c*)

Computational results

Description of the flow structure and parameters of heat transfer from the manikin surface. The general structure of the flow is illustrated based on the data obtained for Case 1, approximated to the conditions of the experiments in [30, 31]. Fig. 3 shows the streamlines colored in accordance with the velocity magnitude, as well as the velocity and temperature fields in several sections of the room. As the airflow reaches an obstacle (in this case, the manikin), it decelerates to the left and to the right around the manikin's torso; regions of accelerated flow evolve in the vicinity of the floor, where the velocities reach 0.4 m/s (see Fig. 3, *a*, *b*). An extensive separation region (with rarefied flow) appears behind the manikin. Circulation regions with slow flow are also observed near the floor and ceiling of the room, at the end wall opposite to the entrance. As the flow approaches the outlet openings, it accelerates, with the velocity level reaching 10 m/s. Notice that outflow separation is uniform: the airflow rate through the upper and lower openings is almost the same.

The temperature fields (see Fig. 3, *c*) illustrate the heating of air in the separated region behind the manikin, where the temperatures range from 34 °C at the surface to 21 °C away from the manikin. No thermal plume is observed above the manikin: it is carried away by strong incident airflow. Because the walls were assumed to be adiabatic, they are apparently heated by thermal radiation. This can be seen in Fig. 3,*c*, where the temperature field on the bottom wall is shown as an example. The mean temperatures over the surface are as follows:

21.2 °C for the ceiling,
21.6 °C for the side walls,
22.0 °C for the floor,
21.2 °C for the end wall.

As seen from Fig. 3,*c*, heating of the walls produces a slight increase in the temperature of air in their vicinity.

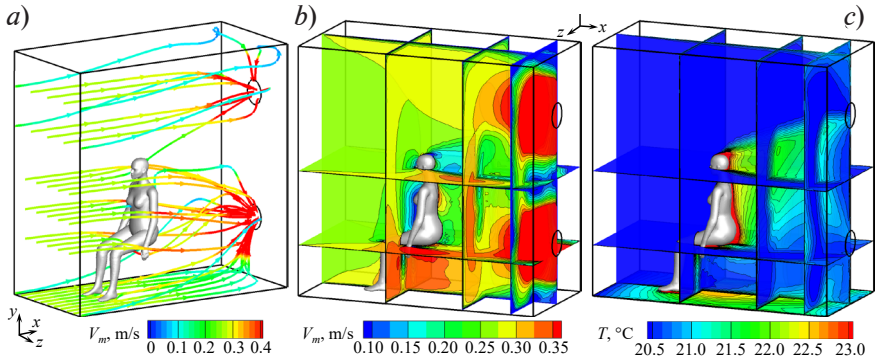

Fig. 3. Computational structure of airflow in the room, shown for Case 1 (see Table 1) by the streamlines colorized in accordance with the velocity magnitudes (*a*), fields of velocity magnitude (*b*) and temperature (*c*) in several sections of the room

Fig. 4,*a* shows the distribution of the total specific heat flux q_w over the manikin surface; the flux includes all three components of heat transfer: thermal conductivity, convection, and radiative heat flux. The distribution of the quantity q_{w_rad} reflecting the radiative component of the heat flux is shown in Fig. 4,*b*, and the distribution of the quantity q_{w_conv} including the conductive and convective components is shown in Fig. 4,*c*. These distributions are characterized by strong spatial non-uniformity due to geometry of the manikin and the characteristics of airflow. In particular, the convective heat flux on the front surface of the manikin is significantly higher than on the back surface for incoming flow of cold air.

Table 3 gives the heat fluxes averaged over the elements of the manikin surface (the positions of the elements numbered from I to VI are shown in Fig. 4,*a*; the elements taken for processing the computational data approximately correspond to the experimental setup). The averaging was performed separately for the elements located symmetrically on the left and right sides of the manikin; thus, the total number of elements is 11. Some heat flux asymmetry was observed both in the computations and (to a greater extent) in the experiment. The asymmetry of the computational results can be attributed to some degree of dissymmetry in the geometry and computational mesh.

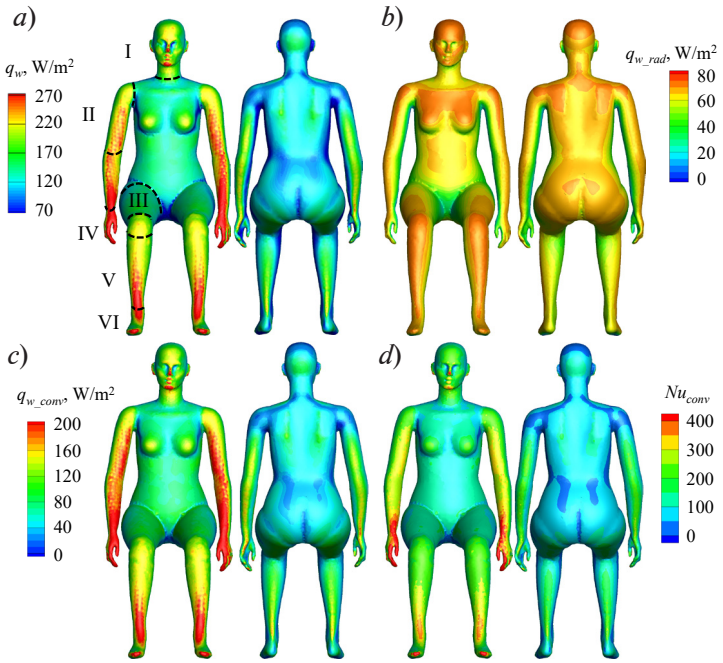

Fig. 4. Distributions of heat fluxes over the manikin surface (Case 1): total (*a*), radiative (*b*), convective (*c*); corresponding distributions of the Nusselt number (*d*); The positions of the elements are numbered from I to VI (see Table 3)

Table 3

Heat fluxes on the surface of the manikin (see Fig. 4)

#	Computed value						Experiment	
	q_w, W/m^2		q_{w_conv}, W/m^2		q_{w_rad}, W/m^2		q_w, W/m^2	
	left	right	left	right	left	right	left	right
I	134.7		68.7		66.0		–	
II	156.0	156.2	98.7	98.9	57.3	57.3	129.6	122.0
III	124.4	123.9	68.2	68.5	56.2	55.4	104.5	100.0
IV	195.8	198.4	145.6	149.5	50.2	48.9	185.2	163.0
V	160.1	160.3	98.3	98.4	61.8	61.9	144.6	142.7
VI	146.0	143.8	88.1	86.7	57.9	58.1	159.7	153.4
∑	139.3		80.5		58.8		122.3	

Notations: q_w, q_{w_conv}, q_{w_rad} are the total, convective and radiative heat fluxes, respectively; the positions on the manikin are numbered from I to VI, ∑ is the sum of fluxes I–VI.

Fig. 4,*d* shows the distribution of dimensionless heat transfer (Nusselt number)

$$\mathrm{Nu}_{conv} = q_{w\_conv} w_m / \lambda (T_w - T_{in}).$$

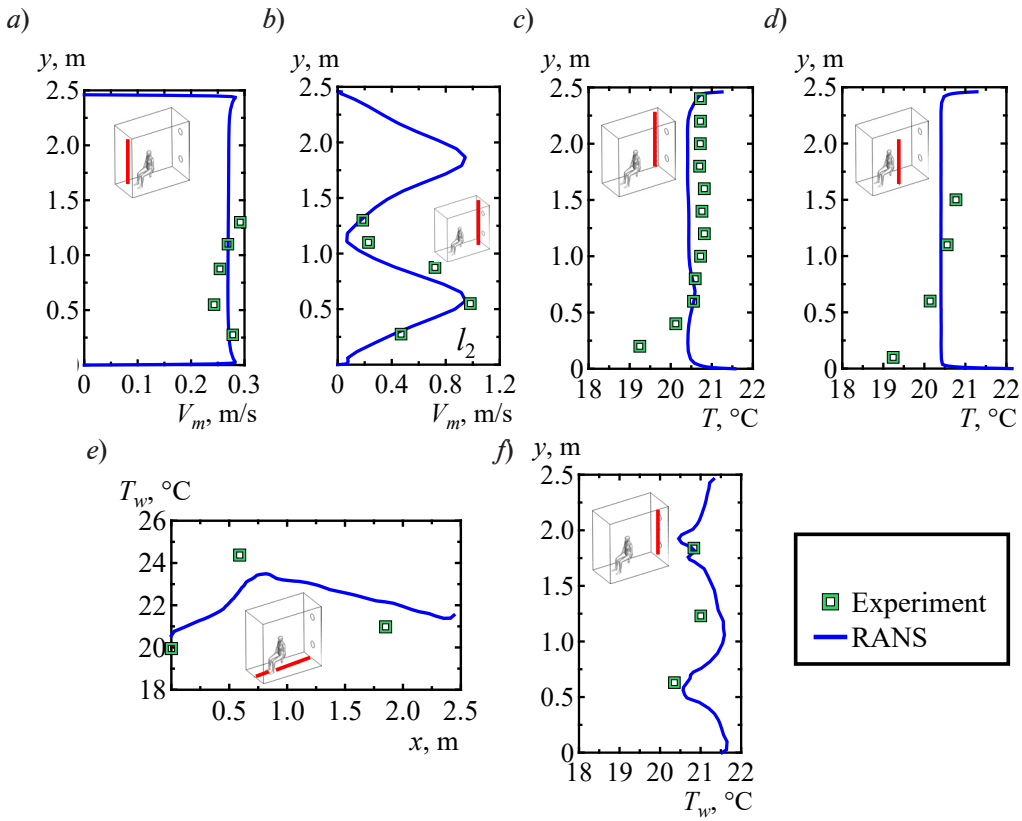

Fig. 5. Computational and experimental velocity profiles in sections l_1 (*a*) and l_2 (*b*); temperature profiles in sections l_3 (*c*) and l_4 (*d*); temperature distribution on the surface of the walls in sections l_5 (*e*) and l_6 (*f*) (see Fig. 1)

We can observe from this distribution that the contribution of the conductive term of heat flux to the total heat transfer is insignificant for the given problem: the Nusselt number averaged over the manikin surface $<Nu_{conv}> = 125$. The local maximum of convective heat transfer is located at the front of the manikin on the hands: the average heat transfer in this region is about 150 W/m^2 (see Table 3), which corresponds to $<Nu_{conv}> = 234$.

Radiative heat flux only slightly varies both over the height of the manikin and locally in its different elements (see Fig. 4,*b* and Table 3), the average value of the radiative term over the manikin surface was 58.8 W/m^2. The total integral heat transfer from the manikin surface is 139.3 W/m^{2}and the integral heat removal from the manikin surface is 223 W. As it turned out for the computational case considered, the contribution from the radiative term of heat flux to the total heat removal was 42%, the contribution from the convective term was 58% (the contribution from the conductive term was less than 1%).

Comparison of computational results with experimental data. We can directly compare the computational results for Case 1 with the experimental data in [30, 31] for the conditions close to experimental ones. Fig. 5, *a*, *b* shows the graphs for the velocity magnitude in the central section of the room, constructed along the vertical lines l_1 and l_2 (see Fig. 1 for the positions of the lines).

The graph in Fig. 5,*a* shows the velocity distribution near the inlet boundary, at a distance of 0.19 m from it. A somewhat non-uniform velocity was detected during the experiment in this section (measurements were carried out only in the lower half of the room). The velocity distribution obtained in the computations based on the boundary condition imposed is almost uniform, with only a small local increase in velocity recorded near the solid walls. The computational and experimental data are generally in good agreement. The velocity distribution shown along the line l_2, located 0.25 m away from the outlet boundary, has two local maxima (the velocity is about 1 m/s), appearing because outlet openings are nearby; the computational and experimental data almost coincide here.

The temperature profiles are shown along two vertical lines: l_3, located in one of the corners of the room near the exits (Fig. 5,*c*), and l_4, located near the manikin (Fig. 5,*d*). The computational temperature profiles are almost uniform, with an increase in the temperature by about 1 degree observed near the walls because they are heated by the radiative heat flux. The experimental data indicate that the temperature profiles are considerably non-uniform, with a pronounced minimum near the floor, while the values at points below 0.5 m turned out to be lower than the inlet temperature $T_{in} = 20.4$ °C, recommended in the documentation for the experimental data and adopted in the computations. The nature of the experimental temperature profiles near the floor may point to some undocumented experimental conditions that cannot be reproduced in computational problems. The computational and experimental temperatures are in good agreement at a height over 0.5 m.

Fig. 5, *e*, *f* compares the computational and experimental data for the surface temperature on the line l_5, passing along the floor, and line l_6, passing along the end wall (crossing the outlet openings). As can be seen from Fig. 5,*e*, a local increase in wall temperature can be observed near the manikin's legs. The local temperature minima in Fig. 5,*f* are due to the presence of the outlet openings. Even though experimental data are scarce, we can conclude from the comparison that the computational and experimental values are in good agreement, including for heating of the walls with external thermal insulation.

The experimental database contains information about the average heat transfer from different elements on the surface of the thermal manikin (see Table 3, two right columns). Documentation does not provide the exact positions for the boundaries of these surfaces, so the experimental data given in Table 3 for the eleven elements only approximately correspond to the processing results of the corresponding computational data. Furthermore, discussing the experimental data presented in [30, 31], the studies do not address the considerable asymmetry of the mean heat flux, with the differences in the values obtained for the left and right elements of the manikin reaching 12%. Nevertheless, qualitative agreement is observed for the spatial inhomogeneities of the heat flux recorded in the computations and in the experiments: the maximum heat transfer in both cases is observed on the hands, and the minimum around the hips. The value of specific heat removal averaged over the entire surface of the manikin obtained computationally was 139.3 W/m^2, exceeding the experimental value of 122.3 W/m^2 by 14%.

Influence of thermal conditions on the manikin surface. One of the reasons for the uncertainty arising in simulations of the human body with a thermal manikin is the type of thermal boundary conditions imposed on the surface. The sensitivity of the flow field and the heat transfer

characteristics to this parameter was estimated in this study based on the computations setting a constant temperature on the surface of the manikin (the conditions corresponding to the experimental setup) and a constant heat flux. In addition, parametric computations were carried for both types of boundary conditions to investigate the radiative contribution to heat transfer.

Case 2 (see Tables 1 and 2) is fully identical with the statement of Case 1, but does not account for the radiative heat transfer. Second-kind boundary conditions were imposed in Cases 3 and 4, the radiative model was activated in Case 3, while radiation was not taken into account in Case 4. Imposing boundary conditions in Case 3, we adopted that q_w = 139.3 W/m^2, which corresponds to the total heat flux obtained in Case 1, and q_w = 80.5 W/m^2 in Case 1, which corresponds to the convective term of the heat flux obtained in Case 1. The heat transfer parameters for the four cases are as follows (based on the data in Tables 1 and 2):

Case	Parameter	Mean value over manikin surface
1	q_w, W/m^2	139.3
2	q_w, W/m^2	80.6
3	T_w, °C	34.2
4	T_w, °C	34.8

Analyzing the computational data, we can conclude that varying the thermal boundary conditions has little effect on the overall structure of the flow: the velocity fields are nearly identical in all four cases (and generally correspond to the illustrations for Case 1 in Figs. 3, *a*, *b* and 5, *a*, *b*). Notably, if the radiative model is deactivated, there is slight rearrangement of the flow in the vicinity of solid boundaries: the mechanism for heating the walls and the near-wall layers of air is switched off in the absence of radiation. Accordingly, the contribution of free convection changes in these layers, and the velocities turn out to be slightly lower.

Fig. 6,*a* shows the distribution of specific convective heat flux over the manikin surface for Case 2. Comparing these data with those in Fig. 4,*c*, we can see that they nearly coincide, which is consistent with the coincidence of the flow structures mentioned above. Evidently, the integral heat removal from the body surface cannot be determined correctly without accounting for radiative heat transfer, since the mean values of the specific total heat flux obtained in Cases 1 and 2 differ significantly.

Temperature distributions obtained in the cases when a constant heat flux (total or convective) was set on the surface are shown in Fig. 6, *b*, *c*. The temperature fields are consistent with the heat flux distributions obtained in the cases with constant surface temperature (compare Fig. 4,*a* with Fig. 6,*b*, and Fig. 6,*a* with 6,*c*). Local heat flux minima correspond to local temperature maxima, and vice versa. We should note that if a heat flux is set at the surface of the manikin, accounting for radiative heat transfer considerably affects the temperature distribution (compare

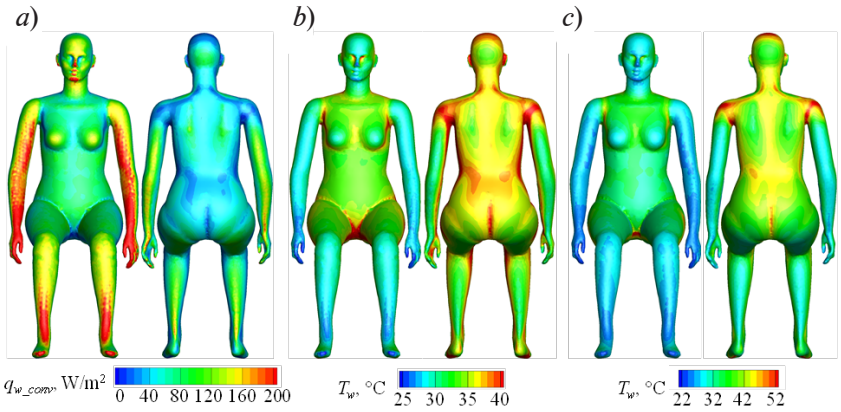

Fig. 6. Distribution of total heat flux over the manikin surface for Case 2 (*a*); distribution of temperature over the manikin surface for Cases 3 (*b*) and 4 (*c*)

Figs. 6,*b* and 6,*c*). A similar spatial structure of the temperature field is observed in both cases, but the temperatures vary in a wider range in the case without accounting for radiative heat transfer, and are higher by 0.6 °C on average.

Characteristics of flow and heat transfer in free-convection flow. The airflow rate set in the experiment provided that forced convection made a significant contribution to determining the flow structure and the heat transfer characteristics. Free-convective heat transfer mechanisms play a major role in problems on ventilation with flow around a heated human body. The contribution from free convection to the evolving processes was analyzed by formulating an additional problem where the inlet air velocity was reduced by 27 times, amounting to V_{in} = 0.01 m/s (see Table 1, Case 5). The statement otherwise coincided with Case 3, where the radiative heat transfer was simulated (see Table 2), and the total heat flux was set on the surface of the manikin.

Fig. 7 shows a comparison of the flow structures and temperature fields for flows with predominantly forced and free convection. As the inlet velocity decreases, the flow structure and, accordingly, the heat transfer characteristics vary significantly. The air in free-convection flow rises slowly along the heated surface of the manikin and moves vertically upward towards the ceiling: a strong thermal plume appears above the manikin. The maximum velocity in this plume reaches 0.34 m/s (see Fig. 7,*e*), which is approximately 40% of the characteristic buoyancy velocity of 0.79 m/s. Buoyant flow impinges on the ceiling and reverses so that regions with recirculation flow appear in front of the manikin and behind it.

Recirculation flow in front of the manikin has a higher intensity because the problem is for-

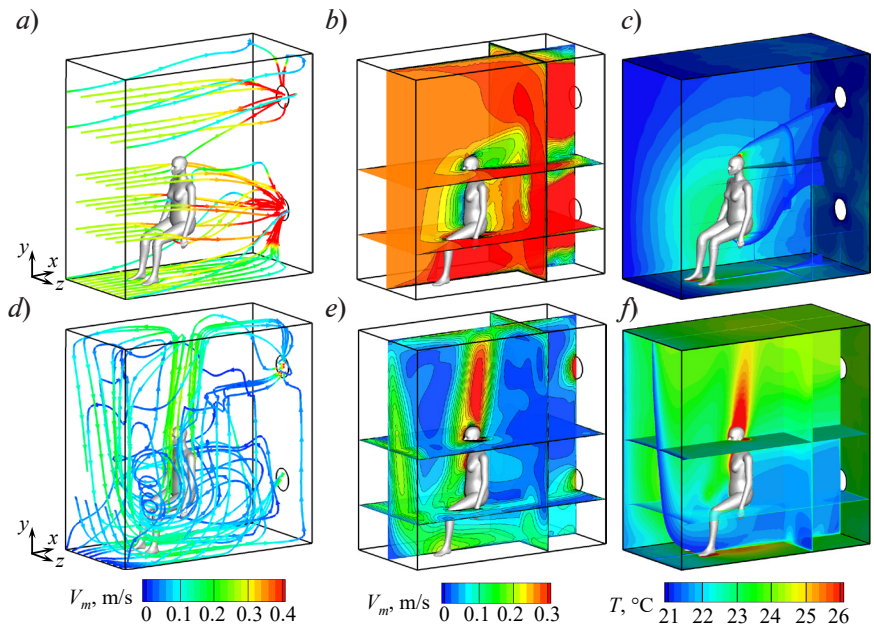

Fig. 7. Structure of airflow in the room for Cases 3 (*a*–*c*) and 5 (*d*–*f*), marked by streamlines colored in accordance with the velocity magnitude (*a*, *d*), as well as the fields of velocity magnitude (*b*, *e*) and temperature (*c*, *f*) in several sections of the room (*b*, *e*, *f*)

mulated in an asymmetric statement (air flows slowly across the open boundary and is blown out through two opening on the opposite wall): the maximum velocity in the descending jet reaches 0.19 m/s. The flow along the floor is characterized by velocities up to 0.15 m/s, partly drawn into a vertical buoyant jet and partly moving along the floor past the manikin, where it is carried towards the exits.

The free-convection mode is characterized by a stratification of temperature over the height (see Fig. 7, *f*): the flow is heated from the manikin in the upper part of the room, and the temperatures are close to the inlet value in the lower part. Local temperature maxima are observed in the thermal boundary layers near the manikin surface as well as in the thermal plume. In general, the air temperature is higher in Case 5 than in Case 3.

Fig. 8 compares the distributions of temperature and heat flux over the manikin surface for flow with predominantly forced and free convection. As expected, the low intensity of free-convection flow produces a decrease in heat transfer, compared to the flow around the manikin in forced-convection flow (see Fig. 8, *c* and *f*). Accordingly, the surface temperatures of the manikin (Figs. 8, *a* and *d*) increase appreciably (by an average of 4.3 °C): the averaged temperatures over the surface are T_w = 34.2 °C for Case 3 and T_w = 38.5 °C for Case 5. The positions of the local temperature extrema, i.e., the maxima around the torso and forearm, and the minima around the hands and feet, are the same. The increase in surface temperature is accompanied by more intense radiative heat transfer. Provided that the same value of the total heat flux is set in both cases, its components are redistributed: the share of the radiative term was 42.5% in Case 3, the share of the convective term 57.5%, while the shares of radiative and convective terms in Case 5 amounted to 52.5 and 47.5%, respectively (Table 4).

Along with Case 5, two other cases were considered for low flow rate conditions (V_{in} = 0.01 m/s):

Case 6 without accounting for radiation, setting the heat flux equal to the convective component of the heat flux obtained in Case 5 (q_w = 66.1 W/m²) on the surface of the manikin;

Case 7 for weightlessness (the formulation corresponds to Case 5, but the gravitational acceleration is taken to equal zero).

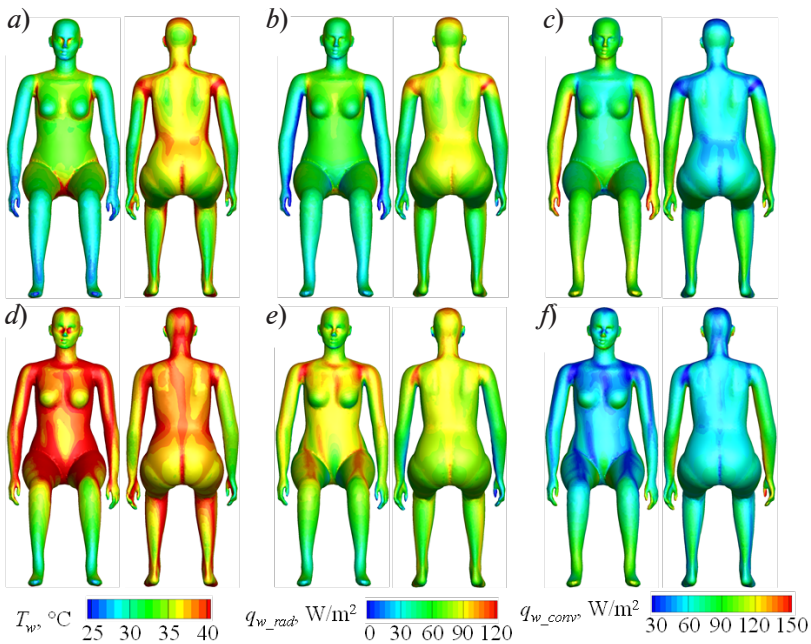

Fig. 8. Fields of temperature (*a, d*), radiative (*b*, *e*) and convective (*c*, *f*) heat fluxes on the surface of the manikin; computational results for cases 3 (*a*–*c*) and 5 (*d* – *f*) are given

Table 4

Parameters of heat transfer from the manikin surface

Case	T_w	q_{w_rad}	q_{w_conv}	q_{w_rad}/q_w	q_{w_conv}/q_w
	°C	W/m²		%	
3	34.2	59.2	80.1	42.5	57.5
5	38.5	73.2	66.1	52.5	47.5
6	38.6	–	66.1	–	100
7	50.2	114.5	24.8	82.2	17.8

The velocity and temperature fields for these cases are shown in Fig. 9 and the temperature distributions over the manikin surface are shown in Fig. 10; the integral heat transfer parameters are summarized in Table 4. Evidently, the results obtained for Case 6 are somewhat different from the data for Case 5: the same as with forced-convection flow (discussed earlier), excluding radiation from analysis does not allow to describe the increase in the wall temperature and the heating of the near-wall regions. In the case of free convection, the absence of heated near-wall layers of air modifies the structure of the flow to a greater extent, decreasing the velocities near the floor; this is accompanied by more intense temperature stratification (see Fig. 9, *c*). The mean temperature over the surface of the manikin is practically the same, about 38.5 °C (see Table 4).

Flow is virtually absent for Case 7 (see Fig. 9, *b*) and the total share of conductive and convective mechanisms of heat transfer was 17.8%. The main contribution to heat transfer is from radiative heat transfer whose share is equal to 82.2%. The walls of the rooms are heated considerably: the temperature averaged over the wall surface was 27.7 °C in Case 7 and 23.8 °C in the baseline Case 5. The surface-averaged temperature of the manikin was 50.2 °C (local values lie in the range from 35.4 to 151.4 °C). Such a high temperature corresponds to a critical value for emergency shutdown of forced ventilation in a spacecraft cabin during an orbital flight (for example, at the International Space Station), without accounting for human thermoregulation mechanisms.

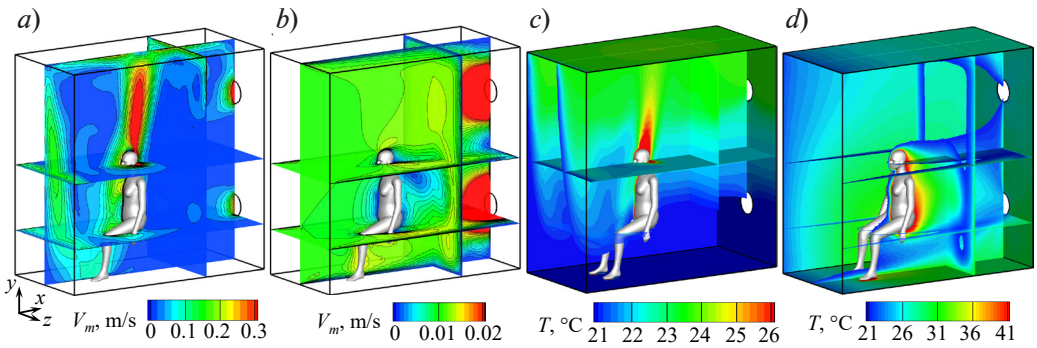

Fig. 9. Fields of velocity magnitude (*a*, *b*) and temperature (*c*, *d*), obtained in computations for Cases 6 (*a*, *c*) and 7 (*b*, *d*) in several sections of the room

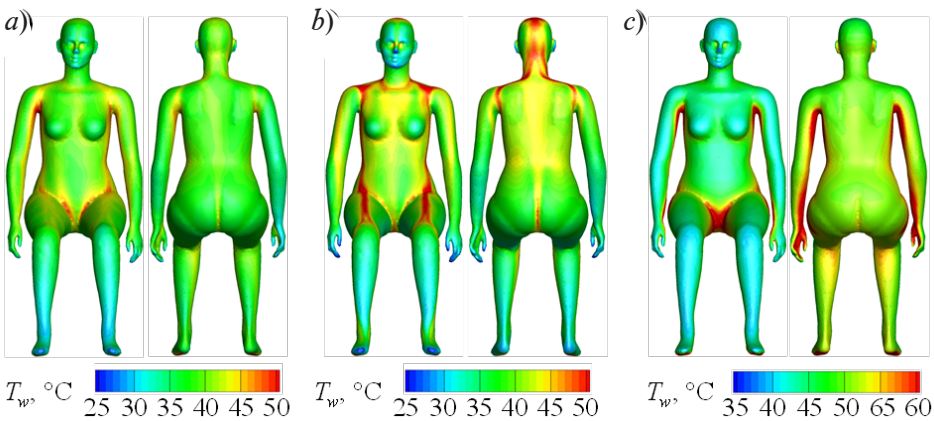

Fig. 10. Temperature distributions over manikin surface obtained in computations for Cases 5 (*a*), 6 (*b*) and 7 (*c*)

Conclusion

The paper presents the results of numerical simulation of three-dimensional turbulent flow and heat transfer in the case of airflow around a seated thermal manikin placed in a model room with mixing ventilation. The computations were carried out in a steady-state formulation based on solving the Reynolds equations closed by the standard k-ε turbulence model; the buoyancy effects were described in the Boussinesq approximation; the radiative energy transfer was taken into account using the Surface-to-surface model. The distributions of velocity and temperature of air in the room, obtained by numerical simulations, are qualitatively and quantitatively consistent with the experimental data presented in the literature. The computational values of specific heat removal from the surface of the manikin were slightly higher than the experimental ones.

Computations were performed in the course of parametric studies both with a constant temperature on the surface of the manikin (which corresponds to the experimental conditions) and with a constant heat flux. We have established that varying the thermal boundary conditions has virtually no effect on the overall structure of the flow, while the general heat release remains consistent. The influence of the radiative contribution to heat transfer was investigated for both types of boundary conditions. It is confirmed that integral heat removal from the surface of a body cannot be determined correctly without accounting for radiative heat transfer: the share of radiative heat flux exceeded 40%. In addition, accounting for radiation affects the computed temperature of room walls and the airflow in the near-wall layers.

Along with studies of ventilation with predominantly forced convection (corresponding to the experiment), we also considered the characteristics of flow and heat transfer for free convection. We have observed that the structure of the flow under predominantly free convection is determined by a strong thermal plume evolving above the manikin and the temperature field is stratified by height. The free-convection conditions with low-velocity airflow is characterized by lower values of heat transfer compared to the flow around a manikin under forced convection, which is accompanied by an increase in the surface temperature and more intense radiative heat transfer.

REFERENCES

1. **Grimitlin M. I.,** Raspredelenie vozdukha v pomeshcheniyakh [Air distribution in the rooms], 3rd Ed., AVOK Severo-Zapad, St. Petersburg, 2004 (in Russian).

2. **Awbi H. S.,** Ventilation of buildings, Taylor & Francis Group (Spon Press), London, 2005.

3. **Hurnik M., Blaszczok M., Popiolek Z.,** Air distribution measurement in a room with a sidewall jet: A 3D benchmark test for CFD validation, Build. Environ. 2015. Vol. 93-2 (November) (2015) 319–330.

4. **Markov D., Ivanov N., Pichurov G., et al.,** On the procedure of draught rate assessment in indoor spaces, Appl. Sci. 10 (15) (2020) 5036.

5. **Yamasawa H., Kobayashi T., Yamanaka T., et al.,** Experimental investigation of difference in indoor environment using impinging jet ventilation and displacement ventilation systems, Int. J. Vent., Publ, 27 Jan. 2021 (18 p.) https://doi.org/10.1080/ 14733315. 2020. 1864572.

6. **Nilsson H. O., Comfort** climate evaluation with thermal manikin methods and computer simulation models. Ph. D thesis, Royal Inst. Technol., Depart. of Civil and Architect. Eng., Sweden, 2004.

7. **Kilic M., Sevilgen G.,** Evaluation of heat transfer characteristics in an automobile cabin with a virtual manikin during heating period, Numer. Heat Transf. A. 56 (6) (2009) 515–539.

8. **Yang C., Zhang X., Yao Z., He F.,** The Large Eddy Simulation and stability analysis of flow field in a generic cabin, Proc. Eng. 121 (2015) 1749–1756.

9. **Croitoru C., Nastase I., Bode F., Cojocaru G.,** Assessment of virtual thermal manikins for thermal comfort numerical studies. Verification and validation, E3S Web Conf. 111 (CLIMA 2019 Congress) (2019) 02018.

10. **Kabanshi A., Wigö H., Sandberg M.,** Experimental evaluation of an intermittent air supply system. P. 1: Thermal comfort and ventilation efficiency measurements, Build. Environ. 95 (January) (2016) 240–250.

11. **Villi G., De Carli M.,** Detailing the effects of geometry approximation and grid simplification on the capability of a CFD model to address the benchmark test case for flow around a computer simulated person, Build. Simul. 7 (1) (2014) 35–55.

12. **Zukowska D., Melikov A., Popiolek Z.,** Thermal plume above a simulated sitting person with different complexity of body geometry, Proc. Roomvent 2007 (Conf. at Helsinki, 13–15 June, 2007). 3 (2007) 191–198.

13. **Yan Y., Li X., Yang L., Tu J.,** Evaluation of manikin simplification methods for CFD simulations in occupied indoor environments, Energy Build. 127 (1 September) (2016) 611–626.

14. **Stepasheva E. D., Zasimova M. A., Ivanov N. G.,** Thermal manikin shape influence on airflow and heat transfer in the model room with displacement ventilation, St. Petersburg State Polytechnical University Journal. Physics and Mathematics. 14 (3) (2021) 90–106.

15. **Saarinen P. E., Kalliomäki P., Tang J. W., Koskela H.,** Large Eddy Simulation of air escape through a hospital isolation room single hinged doorway – validation by using tracer gases and simulated smoke videos, PLoS ONE. 10 (7) (2015) e0130667.

16. **Feng L., Zeng F., Li R., Ju R., Gao N.,** Influence of manikin movement on temperature stratification in a displacement ventilated room, Energy Build. 234 (1 March) (2021) 110700.

17. **Oguro M., Arens E., de Dear R.J., et al.,** Convective heat transfer coefficients and clothing insulations for parts of the clothed human body under airflow conditions, J. Archit. Plan. (Trans. AIJ). 67 (561) (2002) 21–29.

18. **Oliveira A. V. M., Branco V. J., Gaspar A. R., Quintela D. A.,** Measuring thermal insulation of clothing with different manikin control methods. Comparative analysis of the calculation methods, Proc. 7th Int. Thermal Manikin and Model. Meeting (at Univ. of Coimbra, Portugal), September, 2008.

19. **Wang C., Yoo S.-J., Tanabe S., Ito K.,** Investigation of transient and heterogeneous microclimate around a human body in an enclosed personalized work environment, Energy Built Environ. 1 (4) (2020) 423–431.

20. **Ivanov M., Mijorski S.,** CFD modelling of flow interaction in the breathing zone of a virtual thermal manikin, Energy Proc. 112 (March) (2017) 240–251.

21. **Gao N. P., Niu J. L.,** CFD Study of the thermal environment around a human body: A review, Indoor Built Environ. 14 (1) (2005) 5–16.

22. **Yan Y., Li X., Tu J.,** Thermal effect of human body on cough droplets evaporation and dispersion in an enclosed space, Build. Environ. 148 (15 January) (2019) 96–106.

23. **Gao N., Niu J., Morawska L.,** Distribution of respiratory droplets in enclosed environments under different air distribution methods, Build. Simul. 1 (4) (2008) 326–335.

24. **Xu C., Wei X., Liu L., et al.,** Effects of personalized ventilation interventions on airborne infection risk and transmission between occupants, Build. Environ. 180 (August) (2020) 107008.

25. **Van Hooff T., Blocken B., Tominaga Y.,** On the accuracy of CFD simulations of cross-ventilation flows for a generic isolated building: comparison of RANS, LES and experiments, Build. Environ. 114 (March) (2017) 148–165.

26. **Zasimova M. A., Ivanov N. G., Markov D.,** Numerical modeling of air distribution in a test room with 2D sidewall jet. I. Foundations for eddy resolving approach application based on periodical formulation, St. Petersburg State Polytechnical University Journal. Physics and Mathematics. 13 (3) (2020) 56–74.

27. **Zasimova M. A., Ivanov N. G., Markov D.,** Numerical modeling of air distribution in a test room with 2D sidewall jet. II. LES-computations for the room with finite width, St. Petersburg State Polytechnical University Journal. Physics and Mathematics. 13 (3) (2020) 75–92.

28. **Nielsen P. V., Murakami S., Kato S., et al.,** Benchmark tests for a computer simulated person, Indoor Environmental Engineering, Aalborg University, Denmark, 2003.

29. **Topp C., Hesselholt P., Trier M. R., Nielsen P. V.,** Influence of geometry of thermal manikins on room airflow, Proc. ISIAQ 7th Int. Conf. "Healthy Buildings 2003", Singapore, December 7–22, 2003.

30. **Nilsson H., Brohus H., Nielsen P.,** Benchmark test for a computer simulated person – manikin heat loss for thermal comfort evaluation, Indoor Environmental Engineering, Aalborg University, Denmark, 2007.

31. **Nilsson H., Brohus H., Nielsen P.,** CFD modeling of thermal manikin heat loss in a comfort evaluation benchmark test, Proc. Roomvent 2007 (Conf. at Helsinki, 13–15 June, 2007), 2007.

32. **Taghinia J. H., Rahman M. M., Lu X.,** Effects of different CFD modeling approaches and simplification of shape on prediction of flow field around manikin, Energy Build. 170 (1 July) (2018) 47–60.

33. **Deevy M., Sinai Y., Everitt P., et al.,** Modelling the effect of an occupant on displacement ventilation with computational fluid dynamics, Energy Build. 40 (3) (2008) 255–264.

34. **Martinho N., Lopes A., Silva M.,** CFD modelling of benchmark tests for flow around a detailed computer simulated person, Proc. 7th Int. Thermal Manikin and Model. Meeting (at Univ. of Coimbra, Portugal). September, 2008.

35. **Martinho N., Lopes A., da Silva M. G.,** Evaluation of errors on the CFD computation of air flow and heat transfer around the human body, Build. Environ. 58 (December) (2012) 58–69.

36. **Siodlaczek M., Gaedtke M., Simonis S., et al.,** Numerical evaluation of thermal comfort using a large eddy lattice Boltzmann method, Build. Environ. 192 (April) (2021) 107618.

37. **Smirnov E. M., Ivanov N. G., Telnov D. S., Son C. H.,** CFD modeling of cabin air ventilation in the International Space Station: A comparison of RANS and LES data with test measurements for the Columbus Module, Int. J. Vent. 5 (2) (2006) 219–228.

38. **Ivanov N. G., Telnov D. S., Smirnov E. M., Son C. H.,** Propagation of CO_2 field after fire extinguisher discharge: A numerical study, Proc. 41st Int. Conf. Environ. Syst. (AIAA); Portland, Oregon, July 2011. Rep. AIAA 2011-5078.

39. **Wilcox D. C.,** Turbulence modeling for CFD, 3-th Ed., DCW Industries, Inc., California, La Cacada, 2006.

СПИСОК ЛИТЕРАТУРЫ

1. **Гримитлин М. И.** Распределение воздуха в помещениях. СПб.: Изд-во «АВОК Северо-Запад», 2004. 320 с.

2. Awbi H. S. Ventilation of buildings. London: Taylor & Francis Group (Spon Press), 2005. 522 p.

3. **Hurnik M., Blaszczok M., Popiolek Z.** Air distribution measurement in a room with a sidewall jet: a 3D benchmark test for CFD validation // Building and Environment. 2015. Vol. 93. Part 2. November. Pp. 319–330.

4. **Markov D., Ivanov N., Pichurov G., Zasimova M., Stankov P., Smirnov E., Simova I., Ris V., Angelova R., Velichkova R.** On the procedure of draught rate assessment in indoor spaces // Applied Sciences. 2020. Vol. 10. No. 15. P. 5036.

5. **Yamasawa H., Kobayashi T., Yamanaka T., Choi N, Matsuzaki M.** Experimental investigation of difference in indoor environment using impinging jet ventilation and displacement ventilation systems // International Journal of Ventilation. Published 27 Jan. 2021 (18 p.) https://doi.org/10.1080/14733315. 2020. 1864572.

6. **Nilsson H. O.** Comfort climate evaluation with thermal manikin methods and computer simulation models. Ph. D thesis. Royal Institute of Technology. Department of Civil and Architectural Engineering. Sweden, 2004. 202 p.

7. **Kilic M., Sevilgen G.** Evaluation of heat transfer characteristics in an automobile cabin with a virtual manikin during heating period // Numerical Heat Transfer. Part A. 2009. Vol. 56. No. 6. Pp. 515–539.

8. **Yang C., Zhang X., Yao Z., He F.** The Large Eddy Simulation and stability analysis of flow field in a generic cabin // Procedia Engineering. 2015. Vol. 121. Pp. 1749–1756.

9. **Croitoru C., Nastase I., Bode F., Cojocaru G.** Assessment of virtual thermal manikins for thermal comfort numerical studies. Verification and validation // E3S Web of Conferences. 2019. Vol. 111. CLIMA 2019 Congress. P. 02018.

10. **Kabanshi A., Wigö H., Sandberg M.** Experimental evaluation of an intermittent air supply system e Part 1: Thermal comfort and ventilation efficiency measurements // Building and Environment. 2016. Vol. 95. January. Pp. 240–250.

11. **Villi G., De Carli M.** Detailing the effects of geometry approximation and grid simplification on the capability of a CFD model to address the benchmark test case for flow around a computer simulated person // Building Simulation. 2014. Vol. 7. No. 1. Pp. 35–55.

12. **Zukowska D., Melikov A., Popiolek Z.** Thermal plume above a simulated sitting person with different complexity of body geometry // Proceedings of Roomvent 2007 (Conference at Helsinki, 13–15 June, 2007). Finland, 2007. Vol. 3. Pp. 191–198.

13. **Yan Y., Li X., Yang L., Tu J.** Evaluation of manikin simplification methods for CFD simulations in occupied indoor environments // Energy and Buildings. 2016. Vol. 127. 1 September. Pp. 611–626.

14. **Степашева Е. Д., Засимова М. А., Иванов Н. Г.** Влияние формы теплового манекена на течение и теплообмен в модельном помещении с вытесняющей вентиляцией // Научно-технические ведомости СПбГПУ. Физико-математические науки. 2021. Т. 14. № 3. С. 94–111.

15. **Saarinen P. E., Kalliomäki P., Tang J. W., Koskela H.** Large Eddy Simulation of air escape through a hospital isolation room single hinged doorway – validation by using tracer gases and simulated smoke videos // PLoS ONE. 2015. Vol. 10. No. 7. P. e0130667.

16. **Feng L., Zeng F., Li R., Ju R., Gao N.** Influence of manikin movement on temperature stratification in a displacement ventilated room // Energy and Buildings. 2021. Vol. 234. 1 March. P. 110700.

17. **Oguro M., Arens E., de Dear R.J., Zhang H., Katayama,** T. Convective heat transfer coefficients and clothing insulations for parts of the clothed human body under airflow conditions // Journal of Architecture and Planning (Transactions of AIJ). 2002. Vol. 67. No. 561. Pp. 21–29.

18. **Oliveira A. V. M., Branco V. J., Gaspar A. R., Quintela D. A.** Measuring thermal insulation of clothing with different manikin control methods. Comparative analysis of the calculation methods // Proceedings of the 7th International Thermal Manikin and Modelling Meeting (at University of Coimbra, Portugal). September, 2008. 7 p.

19. **Wang C., Yoo S.-J., Tanabe S., Ito K.** Investigation of transient and heterogeneous microclimate around a human body in an enclosed personalized work environment // Energy and Built Environment. 2020. Vol. 1. No. 4. Pp. 423–431.

20. **Ivanov M., Mijorski S.** CFD modelling of flow interaction in the breathing zone of a virtual thermal manikin // Energy Procedia. 2017. Vol. 112. March. Pp. 240–251.

21. **Gao N. P., Niu J. L.** CFD Study of the thermal environment around a human body: A review // Indoor and Built Environment. 2005. Vol. 14. No. 1. Pp. 5–16.

22. **Yan Y., Li X., Tu J.** Thermal effect of human body on cough droplets evaporation and dispersion in an enclosed space // Building and Environment. 2019. Vol. 148. 15 January. Pp. 96–106.

23. **Gao N., Niu J., Morawska L.** Distribution of respiratory droplets in enclosed environments under different air distribution methods // Building Simulation. 2008. Vol. 1. No. 4. Pp. 326–335.

24. **Xu C., Wei X., Liu L., Su L., Liu W., Wang Y., Nielsen P. V.** Effects of personalized ventilation interventions on airborne infection risk and transmission between occupants // Building and Environment. 2020. Vol. 180. August. P. 107008.

25. **Van Hooff T., Blocken B., Tominaga Y.** On the accuracy of CFD simulations of cross-ventilation flows for a generic isolated building: comparison of RANS, LES and experiments // Building and Environment. 2017. Vol. 114. March. Pp. 148–165.

26. **Засимова М. А., Иванов Н. Г., Марков Д.** Численное моделирование циркуляции воздуха в помещении при подаче из плоской щели. Часть 1: отработка применения вихреразрешающего подхода с использованием периодической постановки // Научно-технические ведомости СПбГПУ. Физико-математические науки. 2020. Т. 13. № 3. С. 56–74.

27. **Засимова М. А., Иванов Н. Г., Марков Д.** Численное моделирование циркуляции воздуха в помещении при подаче из плоской щели. Часть 2: LES-расчеты для помещения конечной ширины // Научно-технические ведомости СПбГПУ. Физико-математические науки. 2020. Т. 13. № 3. С. 75–92.

28. **Nielsen P. V., Murakami S., Kato S., Topp C., Yang J.-H.** Benchmark tests for a computer simulated person. Aalborg University, Denmark: Indoor Environmental Engineering, 2003. October. 7 p. ISSN 1395-7953 R0307.

29. **Topp C., Hesselholt P., Trier M. R., Nielsen P. V.** Influence of geometry of thermal manikins on room airflow // Proceedings of ISIAQ 7th International Conference "Healthy Buildings 2003". Singapore, December 7–22, 2003. 6 p.

30. **Nilsson H., Brohus H., Nielsen P.** Benchmark test for a computer simulated person – manikin heat loss for thermal comfort evaluation. Aalborg University, Denmark: Indoor Environmental Engineering, Aalborg University, 2007. 7 p.

31. **Nilsson H., Brohus H., Nielsen P.** CFD modeling of thermal manikin heat loss in a comfort evaluation benchmark test // Proceedings of Roomvent 2007 (Conference at Helsinki, 13 – 15 June, 2007). Finland, 2007. (7 p.)

32. **Taghinia J. H., Rahman M. M., Lu X.** Effects of different CFD modeling approaches and simplification of shape on prediction of flow field around manikin // Energy and Buildings. 2018. Vol. 170. 1 July. Pp. 47–60.

33. **Deevy M., Sinai Y., Everitt P., Voigt L., Gobeau N.** Modelling the effect of an occupant on displacement ventilation with computational fluid dynamics // Energy and Buildings. 2008. Vol. 40. No. 3. Pp. 255–264.

34. **Martinho N., Lopes A., Silva M.** CFD modelling of benchmark tests for flow around a detailed computer simulated person // Proceedings of the 7th International Thermal Manikin and Modelling Meeting (at University of Coimbra, Portugal). September, 2008. 6 p.

35. **Martinho N., Lopes A., da Silva M. G.** Evaluation of errors on the CFD computation of air flow and heat transfer around the human body // Building and Environment. 2012. Vol. 58. December. Pp. 58–69.

36. **Siodlaczek M., Gaedtke M., Simonis S., Schweiker M., Homma N., Krause M. J.** Numerical evaluation of thermal comfort using a large eddy lattice Boltzmann method // Building and Environment. 2021. Vol. 192. April. P. 107618.

37. **Smirnov E. M., Ivanov N. G., Telnov D. S., Son C. H.** CFD modeling of cabin air ventilation in the International Space Station: a comparison of RANS and LES data with test measurements for the Columbus Module // International Journal of Ventilation. 2006. Vol. 5. No. 2. Pp. 219–228.

38. **Ivanov N. G., Telnov D. S., Smirnov E. M., Son C. H.** Propagation of CO_2 field after fire extinguisher discharge: A numerical study // Proceedings of the 41st International Conference on Environmental Systems. American Institute of Aeronautics and Astronautics (AIAA); Portland, Oregon, July 2011. Report No. AIAA 2011-5078 (8 p.).

39. **Wilcox D. C.** Turbulence modeling for CFD. 3-th Ed. La Cacada, California: DCW Industries, Inc., 2006. 515 p.

THE AUTHORS

ZASIMOVA Marina A.
Peter the Great St. Petersburg Polytechnic University
29 Politechnicheskaya St., St. Petersburg, 195251, Russia
zasimova_ma@spbstu.ru
ORCID: 0000-0002-4103-6574

MARINOVA Alexandra A.
Peter the Great St. Petersburg Polytechnic University
29 Politechnicheskaya St., St. Petersburg, 195251, Russia
sanmarinova@gmail.com
ORCID: 0000-0002-9612-5814

IVANOV Nikolay G.
Peter the Great St. Petersburg Polytechnic University
29 Politechnicheskaya St., St. Petersburg, 195251, Russia
ivanov_ng@spbstu.ru
ORCID: 0000-0001-9897-5401

PODMARKOVA Anna D.
Peter the Great St. Petersburg Polytechnic University
29 Politechnicheskaya St., St. Petersburg, 195251, Russia
ann.podmarkova@mail.ru
ORCID: 0000-0002-8329-7094

СВЕДЕНИЯ ОБ АВТОРАХ

ЗАСИМОВА Марина Александровна – *кандидат физико-математических наук, доцент Высшей школы прикладной математики и вычислительной физики Санкт-Петербургского политехнического университета Петра Великого.*
195251, Россия, г. Санкт-Петербург, Политехническая ул., 29
zasimova_ma@spbstu.ru
ORCID: 0000-0002-4103-6574

МАРИНОВА Александра Андреевна – *студентка Высшей школы прикладной математики и вычислительной физики Санкт-Петербургского политехнического университета Петра Великого.*
195251, Россия, г. Санкт-Петербург, Политехническая ул., 29
sanmarinova@gmail.com
ORCID: 0000-0002-9612-5814

ИВАНОВ Николай Георгиевич – *кандидат физико-математических наук, доцент Высшей школы прикладной математики и вычислительной физики, заведующий научно-исследовательской лабораторией гидроаэродинамики Санкт-Петербургского политехнического университета Петра Великого.*
195251, Россия, г. Санкт-Петербург, Политехническая ул., 29
ivanov_ng@spbstu.ru
ORCID: 0000-0001-9897-5401

ПОДМАРКОВА Анна Дмитриевна – *аспирантка Высшей школы прикладной математики и вычислительной физики Санкт-Петербургского политехнического университета Петра Великого.*
195251, Россия, г. Санкт-Петербург, Политехническая ул., 29
ann.podmarkova@mail.ru
ORCID: 0000-0002-8329-7094

Received 16.06.2022. Approved after reviewing 28.06.2022. Accepted 28.06.2022.
Статья поступила в редакцию 16.06.2022. Одобрена после рецензирования 28.06.2022. Принята 28.06.2022.

PHYSICAL ELECTRONICS

Original article
DOI: https://doi.org/10.18721/JPM.15310

SIMULATION OF AN ELECTRON BEAM IN A GYROTRON TAKING INTO ACCOUNT THE CATHODE SURFACE ROUGHNESS AND THERMAL EFFECTS IN THE ELECTRON GUN

O. I. Louksha✉, *P. A. Trofimov*, *A. G. Malkin*

Peter the Great St. Petersburg Polytechnic University, St. Petersburg, Russia

✉ louksha@rphf.spbstu.ru

Abstract. In the paper, a 3D trajectory analysis taking into account the surface roughness of the thermionic cathode and thermal effects caused by its heating has been performed in the electron-optical system of a gyrotron with a frequency of 74,2 GHz and an output power of approximately 100 kW. A new approach based on the use of standard settings available in the 3D simulation software when the model parameters of thermionic emission being given, was used for consideration of the micron-sized cathode surface roughness. A comparison between the calculated and experimental data made it possible to clarify the regularities of the influence of the initial velocity spread and the change of geometry of the cathode assembly caused by its heating on the parameters of the electron beam formed in the electron-optical gyrotron system.

Keywords: microwave electronics, gyrotron, helical electron beam, cathode, surface roughness, heating

Funding: The reported study was funded by Russian Science Foundation (Grant No. 22-29-00136). The results were obtained using the computing resources of the Supercomputer Center of the Peter the Great St. Petersburg Polytechnic University (http://www.scc.spbstu.ru).

Citation: Louksha O. I., Trofimov P. A., Malkin A. G., Simulation of an electron beam in a gyrotron taking into account the cathode surface roughness and thermal effects in the electron gun, St. Petersburg State Polytechnical University Journal. Physics and Mathematics. 15 (3) (2022) 132–142. DOI: https://doi.org/10.18721/JPM.15310

Научная статья
УДК 621.385.6
DOI: https://doi.org/10.18721/JPM.15310

МОДЕЛИРОВАНИЕ ЭЛЕКТРОННОГО ПОТОКА В ГИРОТРОНЕ С УЧЕТОМ ШЕРОХОВАТОСТИ ПОВЕРХНОСТИ КАТОДА И ТЕПЛОВЫХ ЭФФЕКТОВ В ЭЛЕКТРОННОЙ ПУШКЕ

О. И. Лукша✉, *П. А. Трофимов*, *А. Г. Малкин*

[1] Санкт-Петербургский политехнический университет Петра Великого,

Санкт-Петербург, Россия

✉ louksha@rphf.spbstu.ru

Аннотация. Выполнен трехмерный траекторный анализ в электронно-оптической системе гиротрона с частотой 74,2 ГГц и выходной мощностью примерно 100 кВт, с учетом шероховатости поверхности термоэмиссионного катода и тепловых эффектов, вызванных его нагревом. Для учета шероховатостей поверхности катода микронного размера использован новый подход, основанный на использовании стандартных инструментов, доступных в программе трехмерного моделирования при задании параметров термоэлектронной эмиссии. Сопоставление расчетных данных с экспериментальными позволили уточнить закономерности влияния разброса начальных скоростей и изменения геометрии катодного узла при его нагреве на параметры электронного потока, формируемого в электронно-оптической системе гиротрона.

Ключевые слова: СВЧ электроника, гиротрон, винтовой электронный поток, катод, шероховатость поверхности, нагрев

Финансирование: Исследование выполнено при финансовой поддержке гранта Российского научного фонда (проект № 00136-29-22). Часть результатов была получена с использованием вычислительных ресурсов суперкомпьютерного центра СПбПУ (http://www.scc.spbstu.ru).

Ссылка для цитирования: Лукша О. И., Трофимов П. А., Малкин А. Г. Моделирование электронного потока в гиротроне с учетом шероховатости поверхности катода и тепловых эффектов в электронной пушке // Научно-технические ведомости СПбГПУ. Физико-математические науки. 2022. Т. 15. № 3. С. 132–142. DOI: https://doi.org/10.18721/JPM.15310

Introduction

Gyrotrons have become the predominant source of powerful microwave radiation in the millimeter and submillimeter wavelength ranges. In particular, they are used for heating high-temperature plasma and current drive in controlled thermonuclear fusion devices, requring gyrotrons with megawatt levels of output power, operating in continuous and long-pulse modes [1 – 3]. The efficiency of these devices and their maximum achievable parameters depend on the quality of helical electron beam (HEB) entering the resonator. HEB parameters are determined during the design stage through numerical trajectory analysis in the electron-optical system (EOS). The most common type is an adiabatic system including a magnetron injection gun (MIG) with a thermionic cathode and a magnetic compression region [3, 4].

A high-quality HEB is characterized by high mean pitch $\alpha = v_\perp / v_\parallel$ ($v_\perp$, $v_\parallel$ are the transverse and longitudinal velocities of electrons), low velocity ($\delta v_\perp$) and energy ($\delta\varepsilon$) spreads, a specific spatial structure, no parasitic oscillations of the space charge (see, for example, monograph [4]). A major

factors leading to degradation in the quality of HEB is associated with roughness of the cathode surface where the typical sizes of inhomogeneities range from units to tens of microns [4 – 11]. Three-dimensional trajectory analysis can be complicated in a system whose cathode surface has inhomogeneities of similar size. As gyrotron EOSs are typically hundreds of millimeters long, a mesh accounting for such a cathode has a large number of cells, which is unacceptable for modern computational systems. Different algorithms have been developed to implicitly take into account the roughness of the emitting surface in the EOS model with a smooth cathode by setting the initial velocity of each particle emitted from the cathode [10, 11]. These algorithms rely on data from preliminary computations, performed separately for each specific gyrotron.

In practice, disagreement is often observed between the theoretical and experimental values of HEB parameters; to avoid this, trajectory analysis should take into account the possible variations in MIG geometry due to heating of the thermionic cathode. Accounting for thermal effects in an electron gun is also a problem specific to each particular device with its characteristic dimensions of EOS elements.

The method we adopt in this paper to account for the cathod roughness during computations of electron trajectories in gyrotron EOS is simpler compared to the approaches in [10, 11]. We used tools from the CST Studio Suite [12] available for setting the parameters of thermionic emission. The suite was used for all computations described in the paper. The computations yielded the HEB characteristics in the EOS of the gyrotron at Peter the Great St. Petersburg Polytechnic University with an operating frequency of 74.2 GHz and an output power of ~100 kW [13 – 16], helping establish the influence of the emitter's surface roughness and heating on these characteristics.

Cathode model with rough surface and effect of roughness on HEB parameters

The electrons emitted from the MIG cathode acquire an initial transverse velocity under the action of crossed electric and magnetic fields. Following the adiabatic theory of MIG (see, for example, [4, 5]), we assume that the transverse electron velocity near the cathode is expressed as

$$v_{\perp c} = \overline{v_{\perp c}} \pm v_{\theta}, \tag{1}$$

where $\underline{v}_{\perp c} = E_{\perp c}/B_c$ is the mean transverse velocity in the cathode; $E_{\perp c}$ is the component of the electric field near the cathode, perpendicular to the magnetic field; B_c is the induction of the magnetic field near the cathode; v_{θ} is the initial velocity magnitude in the direction perpendicular to the magnetic field (coincides with the azimuthal direction for the axially symmetric gyrotron EOS).

If the cathode has a rough surface, the electrons acquire initial velocities under the action of microfields near local inhomogeneities on this surface. As a result, a spread of the initial transverse velocities of electrons is observed in the cathode:

$$\delta v_{\perp c} = \frac{\Delta v_{\theta}}{\overline{v_{\perp c}}}, \tag{2}$$

where Δv_{θ} is the absolute spread of the initial velocities.

In addition to roughness, another factor leading to an increase in $\delta v_{\perp c}$ is the spread in the initial thermal velocities of electrons emitted from the surface of the cathode. Importantly, the magnitude of the relative spread in transverse velocities accounting for all factors of this spread remains unchanged as HEB moves in an adiabatically increasing magnetic field, which is used for pumping the transverse electron velocity in the gyrotron EOS.

The velocity distributions of electrons in a model of a planar diode without a magnetic field are compared in [17] with two types of cathodes: the first one has a rough surface with regularly spaced hemispheres of radius r_0, and the second one has a smooth surface.

The electron distribution $f(v_x)$ (x is the coordinate along its surface) for the first type of cathode practically does not change with increasing distance z from the cathode, if it exceeds a value equal to approximately $2r_0$. It was established that the initial velocity spectra of cathodes with the rough surface are in satisfactory agreement with those of the cathode with the smooth surface, if a Maxwell distribution of the emitted particle velocities is given for the former, namely

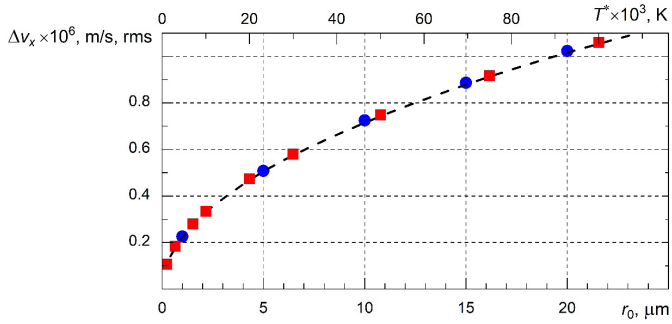

Fig. 1. Dependences of the spread in velocities of electrons emitted from the cathode on the radius r_0 in the model with the rough cathode (—●—) and on the effective temperature T^* in the model with a smooth cathode (—■—) with a macroscopic field strength of 30 kV/cm in the cathode-anode gap

$$f(v)dv = 4\pi v^2 \left(\frac{m}{2\pi kT}\right)^{3/2} \exp\left(-\frac{mv^2}{2kT}\right) dv, \tag{3}$$

with the temperature T^* appreciably higher than the actual cathode temperature T_c, if the azimuth angles $\Delta\theta$ are set between the normal to the cathode surface and the direction of the initial velocity vector equal to ±90°. Fig. 1 shows the dependences for the spread in initial velocities Δv_x on the effective temperature T^* for the model with a smooth cathode and on the radius r_0 for the model with a rough cathode. The spread in electron velocities here and below is defined as the root-mean-square (rms) deviation from the mean velocity. The values of Δv_x for the rough cathode model were obtained after averaging the initial velocity spectra calculated for different distances between the hemispheres at a given radius r_0. If we assume that r_0 = 10 μm corresponds to $T^* = 46 \cdot 10^3$ K, then the dependences $\Delta v_x(r_0)$ and $\Delta v_x(T^*)$ almost coincide (see Fig. 1).

Notably,the cathode in an axially symmetric EOS is cone-shaped and there is a magnetic field near it [4]. As noted above, the velocity v_x changes at a short distance from the cathode, not exceeding several radii r_0. At this distance, the electron motion has little difference with the motion in a planar diode. Moreover, the influence of the magnetic field on this motion is insignificant [4]. Therefore, the calculated velocity spread Δv_x can be regarded as the spread in the initial transverse velocity $\Delta v_{\perp c}$. Since the temperature $T^* >> T_c$ for typical values of r_0, the spread in the initial velocities Δv_x, calculated from the temperature T^*, can be attribued to the total effect induced by the surface roughness of the cathode and the spread of thermal velocities.

Table 1

Main geometric parameters and characteristics of computational operating mode in SPbPU gyrotron

Parameter	Value
Accelerating voltage U_0, kV	30
Beam current I_b, A	10
Magnetic field induction in the cavity B_0, T	2.75
Magnetic field induction near cathode B_c, T	0.152
Operating mode	$TE_{12.3}$
Mean radius of emissive strip in the cathode R_c, mm	35
Distance between cathode and anode D_{ca}, mm	10.4
Slant angle of conical emissive strip to device axis, ψ_c, deg	35
Slant angle of magnetic field line to cathode surface ϕ_c, deg	19.2

The approach to accounting for cathode roughness proposed in [17], based on an EOS model with a smooth cathode and setting the distribution of initial velocities (3) with the given values of the parameters T^* and $\Delta\theta$, was also used in our study to perform trajectory analysis for the gyrotron at SPbPu during operation [13 – 16]. The main parameters of this gyrotron are presented in Table 1. The image of gun region in this gyrotron is shown below in Figs. 3 and 4. If we select the velocity spread $\Delta v_{\perp c} = 7.25 \bullet 10^5$ m/s, which corresponds to $r_0 = 10$ μm (see Fig. 1), then, according to (1) and (2), the spread in the initial transverse velocities in the cathode $\delta v_{\perp c}$ for the values of U_0, B_c, D_{ca}, ψ_c, φ_c given in Table 1 is equal to 3.63% due to the cathode's roughness.

Two configuration of the magnetron injection gun were used in the calculations [18]. The slant angle of the conical part of the cathode, equal to 35°, was the same along the entire generatrix in the standard gun configuration. The gyrotron operates with the mean pitch α equal to approximately 1.3 for the gun with the parameters given in Table 1. The values of the pitch α and the velocity spread $\delta v_\perp$ discussed in this paper were determined in the central plane of the resonator for the peak of the magnetic field distribution along the longitudinal coordinate. A control electrode was installed Ii the modified version of the gun, with the inclination angle of the conical part increased to 50°. Earlier studies [19] indicate that controlling the voltage between the cathode and the control electrode U_{cont} can help optimize the distribution of the electric field in the near-cathode region of the MIG, consequently reducing the velocity spread in the beam. This allows increasing the working pitch and the efficiency of the gyrotron [20].

Trajectory analysis was carried out with the model of the SPbPU gyrotron, described in detail in [18]. The number of emission centers was increased to about $3 \cdot 10^4$, producing smoother velocity distributions of electrons at higher temperatures of the cathode. Tracking Solver was used to calculate the trajectories. The dependences of the mean pitch α and the velocity spread $\delta v_\perp$ on the effective temperature T^* for two configurations of the MIG are shown in Fig. 2. An increase in $\delta v_\perp$ is observed with the increase in temperature T^*. Provided that $T^* \approx 0$, the velocity spread is due to the difference in the values of external electrical and magnetic fields, as well as the intrinsic field of the HEB space charge for electrons starting from different points of the emitter. This spread in positions is smaller for the modified MIG for the optimal value $U_{cont} = -9$ kV compared to the standard MIG. It is then self-evident why introducing an additional spread of initial velocities produces a more noticeable increase in the total velocity spread for a gyrotron with a modified MIG.

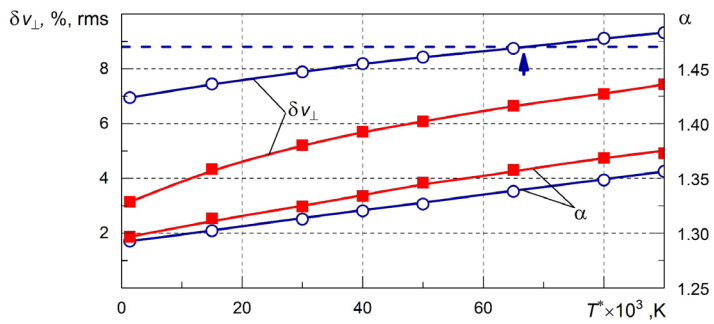

Fig. 2. Dependences of transverse velocity spread $\delta v_\perp$ and the mean pitch α on the effective temperature T^* for standard (–○–) and modified (–■–) magnetron injection gun; $U_{cont} = -9$ kV

Experimental data obtained earlier at the SPbPU gyrotron with a standard MIG [21] suggest that the velocity spread $\delta v_\perp$ is approximately 8.8% for a cathode with uniform emission. This spread value was recorded in particular in experiments with a cathode made of lanthanum hexaboride (LaB_6), whose active substance has typical particle sizes of about 10 μm. The active substance can escape from the surface of the emitter as the cathode operates. This partially exposes a sponge whose grain size may be noticeably larger than the particle size in the lanthanum hexaboride powder. An additional consideration is that the area of the emitting surface is also rather large, about 10 cm². This surface may be inhomogeneous, which is due to uneven heating and non-uniform beams of the particles bombarding the cathode surface. In view of these factors,

we can assume that the size of the roughnesses appearing on the cathode during measurements (determining the magnitude of the spread in the initial velocities $\delta v_{\perp c}$) is different from that of the particles in the active substance of the emitter. As evident from Fig. 2, the spread $\delta v_{\perp} = 8.8\%$ is achieved for a standard MIG at $T^* \approx 67 \cdot 10^3$ K. We can therefore conclude from the dependences in Fig. 1 that the LaB6 cathode for which a velocity spread of 8.8% was recorded in the experiments was characterized by a mean roughness with a radius $r_0 \approx 14$ μm.

Simulation of thermal effects associated with cathode heating

The model of the SPbPU gyrotron used in the calculations of the temperature distribution is shown in Fig. 3. Cathode *1* of the device can be disassembled, allowing to easily replace component *2* with the emitting strip. The cathode is heated with tungsten heating coil *3*. Filament current I_h of the heater flows along central core *4* of the cathode. Thermal shields and special gaps between the components provide thermal insulation of the heating coil and the emitting strip from the remaining elements of the cathode assembly. More than ten emitters of two types were used in the SPbPU gyrotron at different stages of the study: porous tungsten-barium (operating temperature $T_c \approx 1100$ °C) and lanthanum hexaboride ($T_c \approx 1600$ °C) [22].

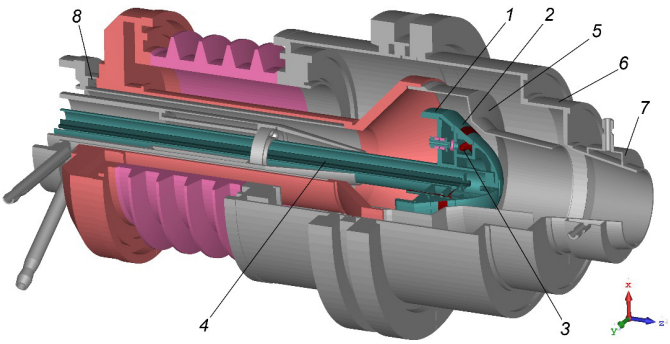

Fig. 3. 3D image of SPbPU gyrotron gun:
cathode assembly *1*; component with emitting strip *2*;
coil *3*; central core *4*; anode *5*; vessel *6*; water cavities *7*, *8*

The problem on determining the deformation of MIG elements due to heating of the thermionic cathode was solved in three stages. During the first stage, we calculated the current density in the heater circuit using the Stationary Current Solver accounting for the conductive properties of the materials and the geometry of the elements in the cathode assembly. The data obtained were used to calculate the amount of heat released during ohmic heating of conductive components with the current I_h flowing through them.

During the second stage, we calculated the steady-state temperature distribution with the Thermal Static Solver. In addition to ohmic heating considered in the first stage, we acconted for the radiation of heated bodies which are secondary sources of heat in the vacuum system. We determined the losses of heated bodies assumed to be additional heat sources for bodies absorbing thermal radiation. Fig. 4 shows the temperature distribution in the cathode assembly of the gyrotron at a current $I_h = 30$ A, corresponding to heating of the cathode made of lanthanum hexaboride. Evidently, the most heated elements are the ones in the cathode assembly. The thermal deformation associated with their heating can modify the geometry of the MIG and, as a result, lead to changes in the parameters of the electron beam generated.

At the third stage, the thermal strains were calculated with the Linear Structural Mechanics Solver allowing to find the parameters characterizing the linear and volumetric expansion of solids. The cathode stem used for attaching the cathode is connected to the gyrotron vessel through the insulator in the end area of the gyrotron (see Fig. 3). Therefore, the cathode is shifted towards the resonator due to linear expansion of the elements of the cathode assembly in the longitudinal direction. Volumetric expansion is accompanied by an increase in the mean radius of the emitting strip. The values of the corresponding parameters Δz and Δr, which were calculated at filament currents I_h, required for heating LaB_6 and W-Ba cathodes, are given in Table 2.

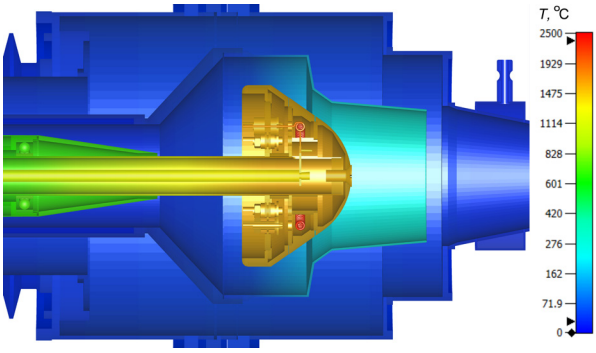

Fig. 4. Simulated temperature distribution across gyrotron elements with lanthanum hexaboride cathode

Table 2

Deformation of MIG elements for two types of thermal cathode

Operating characteristics of MIG			Variation in MIG geometry	
Material of cathode	I_h	T_c	Δz	Δr
	A	°C	mm	
LaB_6	30	1616	1.41	0.29
W-Ba	25	1100	0.98	0.21

Notations: I_h is the filament current, T_c is the cathode temperature, Δz is the longitudinal displacement of the cathode, Δr is the radial expansion of the emissive strip, MIG is the magnetron injection gun.

The electron trajectories were computed depending on the values of the parameters Δz and Δr for the modified MIG, since its geometry was optimized to obtain a minimum velocity spread. Initially, the cathode temperature was set equal to T_c, that is, only the spread in the initial thermal velocities of electrons exclusive of cathode roughness was taken into account. The dependences of the mean pitch α and the velocity spread $\delta v_\perp$ on the parameters Δz and Δr are shown in Fig. 5. Only the change in the sizes of the cathode assembly component with the emitting strip was taken into account for varying Δr, (see Fig. 3).

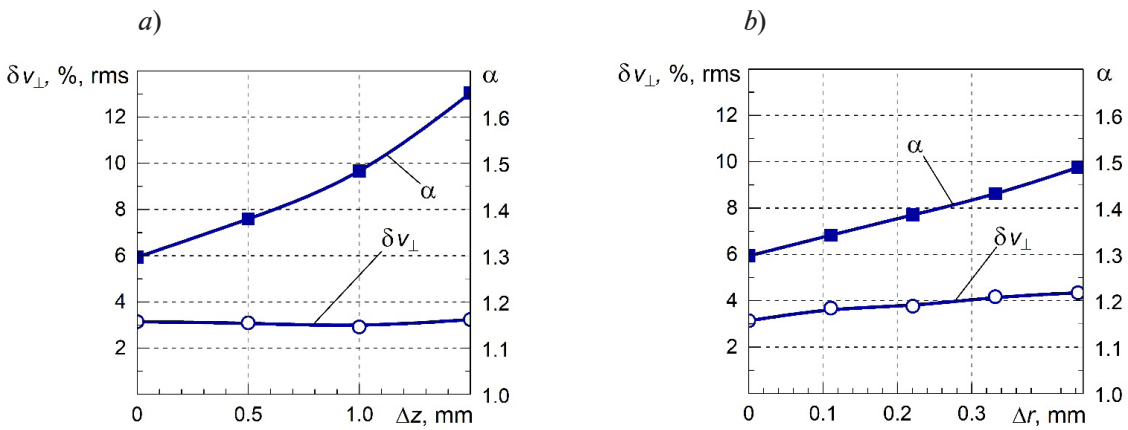

Fig. 5. Dependences of the spread in transverse velocities $\delta v_\perp$ and the mean pitch α on the longitudinal displacement Δz (*a*) of the cathode and on the radial expansion Δr (*b*) of the emitting strip for the modified MIG; $U_{cont} = -9$ kV

Elongation of the cathode stem leads to a reduction in the distance between the cathode and the anode, consequently increasing the amplitude of the electrical field in this region. As a result, the initial transverse velocity in the cathode and the mean pitch increase. The distribution of the electric field (the form of equipotentials) remains virtually invariable with varying Δz. Since the magnitude of the velocity spread depends mainly on this distribution , it also varies insignificantly with varying Δz. The increase in α with growing Δr can also be explained by a reduction in the distance between the cathode and the anode. The radial expansion of the component with the emitting strip is accompanied by some change in the distribution of the electric field. Since this distribution was optimized in the initial state ($\Delta r = 0$) to obtain a minimum velocity spread, any variation in this distribution is accompanied by an increase in the value of $\delta v_\perp$ (Fig. 5, *b*).

As the final stage of the study, we carried out trajectory analysis for the SPbPU gyrotron with a modified MIG accounting for both cathode roughness and the thermal effects due to its heating. We considered a temperature regime corresponding to the cathode made of lanthanum hexaboride. Given that $\Delta z = 1.41$ mm, $\Delta r = 0.29$ mm, $T^* = 67 \cdot 10^3$ K and $\Delta\theta = \pm 90°$, we obtained the following values of the mean pitch factor and velocity spread: $\alpha = 2.25$ and $\delta v_\perp = 5.89\%$. A marked increase in the pitch compared to the initial value $\alpha \approx 1.3$ (see Fig. 2) occurred due to simultaneous elongation of the cathode stem and expansion of the emitting strip. At large values of α and $\delta v_\perp$, a part of electrons with largeand transverse velocities is reflected from the magnetic plug in the region before entering the resonator (see, for example, articles [18, 21]). The reflected particles can accumulate in the trap between the cathode and the magnetic mirror, which is accompanied by excitation of parasitic low-frequency oscillations (LFO) negatively affecting the quality of the HEB generated. In the above-described configuration, 364 particles out of 30,120 starting from the cathode were reflected from the magnetic mirror. This corresponds to the reflection coefficient $K_{refl} = 1.2 \cdot 10^{-2}$. Parasitic LFO with a considerable amplitude can be excited with such a reflection coefficient [21].

The values of α and K_{refl} can be decreased by increasing the magnetic field induction B_c near the cathode and, accordingly, reducing the magnetic compression coefficient B_0/B_c. The values of the main parameters U_0, B_0 and I_b primarily determining the generated power and radiation frequency remain unchanged. The magnetic field near the cathode of the SPbPU gyrotron can be increased by increasing the number of turns of the cathode coil [22]. The results described above for the modified MIG were obtained for $B_0/B_c = 19.20$, which corresponds to 22 turns of the cathode coil. Adopting the configuration with 24 turns is accompanied by a decrease in B_0/B_c to 18.02. The values of the pitch and the velocity spread calculated with this B_0/B_c amounted to $\alpha = 1.44$ and $\delta v_\perp = 6.59\%$. These values indicate that HEB has high quality, with no electron reflection from the magnetic mirror, and improved performance of the gyrotron with a large value of electronic efficiency [20].

Conclusion

The new technique proposed in this paper can be used to account for the spread of the initial electron velocities due to roughness of the cathode surface during 3D simulations of electron trajectories in the electron-optical system of the gyrotron. We have determined the effect of cathode roughness on the velocity spread and the mean pitch of electrons in the EOS of a medium-power 4 mm gyrotron. Comparing the data obtained in the experiment with the results of trajectory analysis, we have determined the average size of inhomogeneities on the surface of the cathode used in this gyrotron.

We have acquired data characterizing the heating of various EOS elements at operating temperatures of thermionic cathodes used in the gyrotron. The effects of cathode stem elongation and radial expansion of the emitting strip on HEB parameters have been determined. It was confirmed that the gyrotron can generate high-quality HEBs in an operational mode accounting the relationship of its parameters with cathode roughness and thermal effects in the electron gun.

REFERENCES

1. **Litvak A. G., Denisov G. G., Myasnikov V. E., et al.,** Development in Russia of megawatt power gyrotrons for fusion, J. Infrared Millim. Terahertz Waves. 32 (3) (2011) 337–342.

2. **Thumm M.,** State-of-the-art of high-power gyro-devices and free electron masers, J. Infrared Millim. Terahertz Waves. 41 (1) (2020) 1–140.

3. **Nusinovich G. S.,** Introduction to physics of gyrotrons, Johns Hopkins University Press, Baltimore, USA, 2004.

4. **Tsimring Sh. E.,** Electron beams and microwave vacuum electronics, John Wiley & Sons, Hoboken, 2007.

5. **Tsimring Sh. E.,** On the spread of velocities in helical electron beams, Radiophys. Quant. El. 15 (8) (1972) 952–961.

6. **Avdoshin E. G., Nikolaev L. V., Platonov I. N., Tsimring Sh. E.,** Experimental investigation of the velocity spread in helical electron beams, Radiophys. Quant. El. 16 (4) (1973) 461–466.

7. **Lau Y. Y.,** Effects of cathode surface roughness on the quality of electron beams, J. Appl. Phys. 61 (1) (1987) 36–44.

8. **Lygin V. K.,** Numerical simulation of intense helical electron beams with the calculation of the velocity distribution functions, Int. J. Infrared Millim. Waves. 16 (2) (1995) 363–376.

9. **Zapevalov V. E., Kornishin S. Yu., Kotov A. V., et al.**, System for the formation of an electron beam in a 258 GHz gyrotron designed for experiments on dynamic polarization of nuclei, Radiophys. Quant. El. 53 (4) (2010) 229–236.

10. **Leshcheva K. A., Manuilov V. N.,** Numerical simulation of 3-D systems of formation of helical electron beams of gyro-devices with azimutally inhomogeneous distribution of emission current, Advances in Applied Physics. 7 (3) (2019) 298–308 (in Russian).

11. **Zhang J., Illy S., Pagonakis I., Avramidis K., et al.,** Influence of emitter surface roughness on high power fusion gyrotron operation, Nucl. Fusion. 56 (2) (2016) 026002.

12. CST Studio Suite, URL: https://www.3ds.com/products-services/simulia/ products/cst-studio-suite/. Accessed July 06, 2022.

13. **Kas'yanenko D. V., Louksha O. I., Sominsky G. G., et al.,** Low-frequency parasitic space-charge oscillations in the helical electron beam of a gyrotron, Radiophys. Quant. El. 47 (5–6) (2004) 414–420.

14. **Louksha O. I., Piosczyk B., Sominski G. G., et al.,** Suppression of parasitic space-charge oscillations in a gyrotron, Radiophys. Quant. El. 49 (10) (2006) 793–798.

15. **Louksha O. I.,** Simulation of low-frequency collective processes in gyrotron electron beams, Radiophys. Quant. El. 52 (5–6) (2009) 386–397.

16. **Louksha O. I., Sominski G. G., Arkhipov A. V., et al.,** Gyrotron research at SPbPU: Diagnostics and quality improvement of electron beam, IEEE Trans. Plasma Sci. 44 (8) (2016) 1310–1319.

17. **Louksha O. I., Trofimov P. A., Malkin A. G.,** Vliyaniye sherokhovatosti poverkhnosti katoda na kharakteristiki elektronnogo potoka v elektronno-opticheskoy sisteme girotrona [Effect of cathode surface roughness on the characteristics of the electron beam in the electron optical system of a gyrotron], In book: XI Vserossiyskaya nauchno-tekhnicheskaya konferentsiya "Elektronika i mikroelektronika SVCH". Sbornik dokladov [Transactions of XI All-Russian Scientific and Technical Conference "Electronics and Microelectronics of Microwaves", May 31 – June 3, 2022, St. Petersburg, Russia. The collection of reports, ETU "LETI", St. Petersburg (2022) 562–566 (in Russian).

18. **Louksha O. I., Trofimov P. A.,** Simulation of non-uniform electron beams in the gyrotron electron-optical system, Tech. Phys. 63 (4) (2018) 598–604.

19. **Louksha O. I., Samsonov D. B., Sominskii G. G., Tsapov A. A.,** Improvement of the helical electron beam quality and the gyrotron efficiency by controlling the electric field distribution near a magnetron injection gun, Tech. Phys. 57 (6) (2012) 835–839.

20. **Louksha O. I., Trofimov P. A.,** Highly efficient gyrotron with multi-stage recuperation of residual electron energy, Tech. Phys. 64 (12) (2019) 1889–1897.

21. **Louksha O. I., Samsonov D. B., Sominskii G. G., Semin S. V.,** Dynamic processes in helical electron beams in gyrotrons, Tech. Phys. 58 (5) (2013) 751–759.

22. **Louksha O. I., V**intovye elektronnye potoki girotronov: dinamika prostranstvennogo zaryda i metody povysheniya kachestva [Gyrotron helical electron beams: Space charge dynamics and methods for quality improvement], Thesis for a Doctor's degree (phys.-math. sci.), St. Petersburg, SPbPU, 2011.

СПИСОК ЛИТЕРАТУРЫ

1. **Litvak A. G., Denisov G. G., Myasnikov V. E., Tai E. M., Azizov E. A., Ilin V. I.** Development in Russia of megawatt power gyrotrons for fusion // Journal of Infrared, Millimeter, and Terahertz Waves. 2011. Vol. 32. No. 3. Pp. 337–342.

2. **Thumm M.** State-of-the-art of high-power gyro-devices and free electron masers // Journal of Infrared, Millimeter, and Terahertz Waves. 2020. Vol. 41. No. 1. Pp. 1–140.

3. **Nusinovich G. S.** Introduction to physics of gyrotrons. Baltimore, USA: Johns Hopkins University Press, 2004. 335 p.

4. **Цимринг Ш. Е.** Введение в высокочастотную вакуумную электронику и физику электронных пучков. Пер. с англ. Нижний Новгород: Ин-т прикладной физики РАН, 2012. 575 с.

5. **Цимринг Ш. Е.** О разбросе скоростей в винтовых электронных пучках // Известия вузов. Радиофизика. 1972. Т. 15. № 8. С. 1247–1259.

6. **Авдошин Е. Г., Николаев Л. В., Платонов И. М., Цимринг Ш. Е.** Экспериментальное исследование скоростного разброса в винтовых электронных пучках // Известия вузов. Радиофизика. 1973. Т. 16. № 4. С. 605–612.

7. **Lau Y. Y.** Effects of cathode surface roughness on the quality of electron beams // Journal of Applied Physics. 1987. Vol. 61. No. 1. Pp. 36–44.

8. **Lygin V. K.** Numerical simulation of intense helical electron beams with the calculation of the velocity distribution functions // International Journal of Infrared and Millimeter Waves. 1995. Vol. 16. No. 2. Pp. 363–376.

9. **Запевалов В. Е., Корнишин С. Ю., Котов А. В., Куфтин А. Н., Малыгин О. В., Мануилов В. Н., Седов А. С., Цалолихин В. И.** Система формирования электронного пучка для гиротрона с частотой 258 ГГц, предназначенного для экспериментов по динамической поляризации ядер // Известия вузов. Радиофизика. 2010. Т. 53. № 4. С. Р. 251–259.

10. **Лещева К. А., Мануилов В. Н.** Численное 3D-моделирование систем формирования винтовых электронных пучков гироприборов с азимутально неоднородным распределением тока эмиссии // Успехи прикладной физики. 2019. Т. 7. № 3. С. 298–308.

11. **Zhang J., Illy S., Pagonakis I., Avramidis K., Thumm M., Jelonnek J.** Influence of emitter surface roughness on high power fusion gyrotron operation // Nuclear Fusion. 2016. Vol. 56. No. 2. P. 026002.

12. CST Studio Suite. Режим доступа: https://www.3ds.com/products-services/simulia/products/cst-studio-suite/ (Дата обращения: 17.06.2022).

13. **Касьяненко Д. В., Лукша О. И., Пиосчик Б., Соминский Г. Г., Тумм М.** Низкочастотные паразитные колебания пространственного заряда в винтовом электронном пучке гиротрона // Известия вузов. Радиофизика. 2004. Т. 47. № 5–6. С. 463–470.

14. **Лукша О. И., Пиосчик Б., Соминский Г. Г., Тумм М., Самсонов Д. Б.** Подавление паразитных колебаний пространственного заряда в гиротроне // Известия вузов. Радиофизика. 2006. Т. 49. № 10. С. 880–886.

15. **Лукша О. И.** Моделирование низкочастотных коллективных процессов в электронных потоках гиротронов // Известия вузов. Радиофизика. 2009. Т. 52. № 5–6. С. 425–437.

16. **Louksha O. I., Sominski G. G., Arkhipov A. V., Dvoretskaya N. V., Kolmakova N. G., Samsonov D. B., Trofimov P. A.** Gyrotron research at SPbPU: Diagnostics and quality improvement of electron beam // IEEE Transactions on Plasma Science. 2016. Vol. 44. No. 8. Pp. 1310–1319.

17. **Лукша О. И., Трофимов П. А., Малкин А. Г.** Влияние шероховатости поверхности катода на характеристики электронного потока в электронно-оптической системе гиротрона // XI Всероссийская научно-техническая конференция «Электроника и микроэлектроника СВЧ». 31 мая – 3 июня 2022 г., г. Санкт-Петербург, Россия. Сборник докладов. СПб.: СПбГЭТУ «ЛЭТИ», 2022. С. 562–566.

18. **Лукша О. И., Трофимов П. А.** Моделирование неоднородных электронных потоков в электронно-оптической системе гиротрона // ЖТФ. 2018. Т. 88. № 4. С. 614–620.

19. **Лукша О. И., Самсонов Д. Б., Соминский Г. Г., Цапов А. А.** Повышение качества винтового электронного потока и КПД гиротрона при регулировании распределения электрического поля в области магнетронно-инжекторной пушки // ЖТФ. 2012. Т. 82. № 6. С. 101–105.

20. **Лукша О. И., Трофимов П. А.** Высокоэффективный гиротрон с многоступенчатой рекуперацией остаточной энергии электронов // ЖТФ. 2019. Т. 89. № 12. С. 1988–1996.

21. **Лукша О. И., Самсонов Д. Б., Соминский Г. Г., Семин С. В.** Динамические процессы в винтовых электронных потоках гиротронов // ЖТФ. 2013. Т. 83. № 5. С. 132–140.

22. **Лукша О. И.** Винтовые электронные потоки гиротронов: динамика пространственного заряда и методы повышения качества. Дисс. ... докт. физ.-мат. наук. 01.04.04. Защ. 01 декабря 2011 г.: утв. 01.12.2011. СПб.: СПбГПУ, 2011. 285 с.

THE AUTHORS

LOUKSHA Oleg I.
Peter the Great St. Petersburg Polytechnic University
29 Politechnicheskaya St., St. Petersburg, 195251, Russia
louksha@rphf.spbstu.ru
ORCID: 0000-0002-6402-8112

TROFIMOV Pavel A.
Peter the Great St. Petersburg Polytechnic University
29 Politechnicheskaya St., St. Petersburg, 195251, Russia
trofpa@yandex.ru
ORCID: 0000-0002-3585-1169

MALKIN Alexander G.
Peter the Great St. Petersburg Polytechnic University
29 Politechnicheskaya St., St. Petersburg, 195251, Russia
alexmalkin47@gmail.com
ORCID: 0000-0003-4047-3956

СВЕДЕНИЯ ОБ АВТОРАХ

ЛУКША Олег Игоревич – *доктор физико-математических наук, профессор Высшей инженерно-физической школы Санкт-Петербургского политехнического университета Петра Великого.*
195251, Россия, г. Санкт-Петербург, Политехническая ул., 29
louksha@rphf.spbstu.ru
ORCID: 0000-0002-6402-8112

ТРОФИМОВ Павел Анатольевич – *кандидат физико-математических наук, инженер Высшей инженерно-физической школы Санкт-Петербургского политехнического университета Петра Великого.*
195251, Россия, г. Санкт-Петербург, Политехническая ул., 29
trofpa@yandex.ru
ORCID: 0000-0002-3585-1169

МАЛКИН Александр Геннадьевич – *студент Высшей инженерно-физической школы Санкт-Петербургского политехнического университета Петра Великого.*
195251, Россия, г. Санкт-Петербург, Политехническая ул., 29
alexmalkin47@gmail.com
ORCID: 0000-0003-4047-3956

Received 31.05.2022. Approved after reviewing 06.07.2022. Accepted 06.07.2022.
Статья поступила в редакцию 31.05.2022. Одобрена после рецензирования 06.07.2022. Принята 06.07.2022.

PHYSICAL MATERIALS TECHNOLOGY

Original article
DOI: https://doi.org/10.18721/JPM.15311

INFLUENCE OF TEMPERATURE ON THERMOELECTRIC EFFECT IN THE COMPOSITE MATERIAL BASED ON CARBON NANOTUBES AND POLYANILINE

A. A. Tretyakov[1], *V. M. Kapralova*[1], *V. V. Loboda*[1], *I. Yu. Sapurina*[2], *N.T. Sudar*[1]✉

[1] Peter the Great St. Petersburg Polytechnic University, St. Petersburg, Russia;

[2] Institute of Macromolecular Compounds RAS, St. Petersburg, Russia

✉ sudar53@mail.ru

Abstract. In the paper, the effect of temperature (range 22–140 °C) on the power factor (PF) of composite material made of multi-walled carbon nanotubes with a 10 nm thick polyaniline coating applied to their surface has been studied. The conductivity value of the coating was varied by treating the composite with buffer solutions of different pH values. The nanotubes were randomly oriented relative to each other in the composite samples under study. It was found that the composite material where polyaniline was in an oxidized conductive form had the highest PF value. In that sample, the PF values were about 0.5 μW/(m·K^2) at room temperature and about 1 μW/(m·K^2) at 140 °C.

Keywords: thermoelectricity, polyaniline, nanotube, Seebeck coefficient, conductivity, buffer solution, pH value

Funding: The research is funded by the Ministry of Science and Higher Education of the Russian Federation, within the framework of the program “The World-Class Research Centre: Advanced Digital Technologies” (Contract No. 075-15-2022-311 dated April 20, 2022).

Citation: Tretyakov A. A., Kapralova V. M., Loboda V. V., Sapurina I. Yu., Sudar N. T., Influence of temperature on thermoelectric effect in the composite material based on carbon nanotubes and polyaniline, St. Petersburg State Polytechnical University Journal. Physics and Mathematics. 15 (3) (2022) 143–153. DOI: https://doi.org/10.18721/JPM.15311

Научная статья
УДК 53.043
DOI: https://doi.org/10.18721/JPM.15311

ВЛИЯНИЕ ТЕМПЕРАТУРЫ НА ТЕРМОЭЛЕКТРИЧЕСКИЙ ЭФФЕКТ В КОМПОЗИЦИОННОМ МАТЕРИАЛЕ НА ОСНОВЕ УГЛЕРОДНЫХ НАНОТРУБОК И ПОЛИАНИЛИНА

А. А. Третьяков[1], *В. М. Капралова*[1], *В. В. Лобода*[1], *И. Ю. Сапурина*[2], *Н. Т. Сударь*[1]✉

[1] Санкт-Петербургский политехнический университет Петра Великого, Санкт-Петербург, Россия;

[2] Институт высокомолекулярных соединений РАН, Санкт-Петербург, Россия

✉ sudar53@mail.ru

Аннотация. В работе исследовано влияние температуры (диапазон 140 – 22 °C) на коэффициент мощности (КМ) композиционного материала из многостенных углеродных нанотрубок с нанесенным на их поверхность полианилиновым покрытием (толщина около 10 нм). Величина проводимости покрытия варьировалась путем обработки композита буферными растворами с различными значениями pH. В исследуемых образцах композита нанотрубки были беспорядочно ориентированы друг относительно друга. Установлено, что наибольшим значением КМ обладает композиционный материал, в котором полианилин находится в окисленной проводящей форме. У этого образца при комнатной температуре значение КМ составило примерно 0,5 мкВт/(м·K^2), а при 140 °C – около 1 мкВт/(м·K^2).

Ключевые слова: термоэлектричество, полианилин, нанотрубка, коэффициент Зеебека, проводимость, буферный раствор, водородный показатель

Финансирование: Исследование финансируется Министерством науки и высшего образования Российской Федерации в рамках программы «Исследовательский центр мирового уровня: передовые цифровые технологии» (контракт № 311-2022-15-075 от 20.04.2022)

Ссылка для цитирования: Третьяков А. А., Капралова В. М., Лобода В. В., Сапурина И. Ю., Сударь Н. Т. Влияние температуры на термоэлектрический эффект в композиционном материале на основе углеродных нанотрубок и полианилина // Научно-технические ведомости СПбГПУ. Физико-математические науки. 2022. Т. .15 3 №. С. 143–153. DOI: https://doi.org/10.18721/JPM.15311

Introduction

Interest towards clean energy has grown over the recent years. Thermoelectric generators (TEG), capable of converting thermal energy directly into electrical energy, show promise as sources of such energy [1–4].

Inorganic semiconductor materials are commonly used to fabricate TEG. For example, highly doped lead chalcogenides PbTe, PbSe, PbS are the key materials for applications in thermoelectrics [4, 5]. The efficiency of energy conversion by thermoelectrics can be estimated by the power factor P, defined as $P = \alpha^2\sigma$ (α is the Seebeck coefficient, σ is the electrical conductivity). Power factor values amounting to about 400 μW/(m·K^2) have been achieved in the temperature range from 600 to 950 K for inorganic thermoelectrics. However, along with such an advantage as high energy conversion efficiency, inorganic semiconducting materials also have a number of

disadvantages: they are considerably expensive and difficult to produce, highly toxic, and therefore cannot be used in everyday life. The negative properties of such thermoelectrics significantly limit their potential applications as TEG.

Novel non-toxic materials can be proposed as an alternative to traditional inorganic thermoelectric materials, in particular, electroconductive polyconjugated polymers. They have a range of unique properties, namely: low specific gravity, low thermal conductivity, easy synthesis, small cost, as well as, importantly, potential for constructing flexible TEG [3]. Remarkably, organic TEG exhibit acceptable thermoelectric characteristics over the temperature range of 200–380 K, i.e., are capable of operating at much lower temperatures than their inorganic counterparts. Therefore, they can be installed in residential buildings and even included in the composition of electronic textiles for clothing [6].

On the other hand, despite these advantages, organic electrically conductive polymers have a relatively low conductivity and a low Seebeck coefficient, so they cannot compete on an equal footing with inorganic thermoelectric materials [7].

Composites with organic and inorganic components can offer far better thermoelectric properties; composite materials based on conductive polymers and carbon nanotubes (CNTs) have been the subject of particular attention [8–11]. The properties of such composites depend on a variety of factors, including the type (single or multilayer), chirality, purity, defect density, and size (length and diameter) of the nanotubes, dispersion state and alignment of the nanotubes in the polymer matrix, and interfacial adhesion between the nanotube and the polymer matrix. These factors should be taken into account when presenting, interpreting and comparing the results obtained for nanotube composites with polymers [12].

Another study [10] examined a sample of polyaniline composite (PANI) with multilayer (multi-walled) carbon nanotubes (MWCNTs), prepared using two methods in several stages. At the first stage, the CNT/PANI composite was synthesized by *in situ* polymerization of aniline in the presence of MWCNTs. Next, microfibers based on MWCNT / PANI composite were electrospun, where 1D MWCNT/PANI particles were aligned parallel to each other. This technique allowed to obtain a material with a highly ordered structure. The conductivity and Seebeck coefficient in this composite were 17.1 S/cm and 10 μV/K, respectively, and the power factor was0.171 $\mu W/(m \cdot K^2)$. A porous PANI layer was formed in [8] on the surface of the MWCNT, allowing to increase the Seebeck coefficient to 79.8 μV/K with a virtually unchanged conductivity of 14.1 S/cm, providing a significant increase in the power factor to about 9 $\mu W/(m \cdot K^2)$. The authors believe that the presence of pores 10–20 nm in size (comparable to the mean free path of phonons in PANI) leads to a significant increase in phonon scattering and, as a result, to a decrease in the thermal conductivity of the composite.

Composites based on single-walled carbon nanotubes (SWCNTs) and PANI exhibit considerably higher electrical conductivity and Seebeck coefficient [9–11] than MWCNT/ PANI composites. The power factor of SWCNT/ PANI composites was, according to the estimates in [11], 175 $\mu W/(m \cdot K^2)$, which is the current record for P among organic thermoelectric composites and is comparable to the value of the power factor in inorganic thermoelectric materials. It is hypothesized that the reason for the increase in the specific conductivity and the Seebeck coefficient in these composites is the strong interaction between (π–π)-conjugated bonds of carbon nanotubes and polyaniline molecules, serving to produce a more ordered structure of polymer chains along the nanotube.

The goal of this study is to monitor the variation in the thermoelectric parameters of the MWCNT/PANI composite in a wide temperature range, evaluating the effect of polyaniline doping on the thermoelectric characteristics of the experimental samples.

We expect that achieving this goal will allow to establish the optimal conditions for fabricating the composite with the highest value of the power factor.

Experimental samples and measurement procedure

We used multiwall carbon nanotubes obtained by catalytic pyrolysis of hydrocarbons, 17 ± 5 nm in diameter and 10 μm in length. MWSNTs were not aggregated; they entangled chaotically, forming a homogeneous material. The chemicals (aniline and ammonium persulfate from Fluka, USA) were used without prior purification. Fixed-pH solutions were prepared using 0.1 n of standard fixing agents and distilled water.

PANI was applied to the surface of MWCNTs by heterophase synthesis (*in-situ* polymerization), via oxidative polymerization of aniline in the presence of MWCNTs dispersed in the reaction medium. The reaction was carried out in a water/alcohol solution mixed with ammonium persulfate at 0 °C and stirred vigorously. After the synthesis was finished, the product was decanted into a filter and washed first with an acidified aqueous solution, and then with acetone. It was then dried under normal conditions until the weight of the product was stabilized. The PANI content in the composition of the material was found from the increase in the weight of the composite, which correlated well with the 100% yield of the polymer during synthesis. The reference material used was PANI synthesized under the synthetic conditions but in the absence of MWCNTs.

PANI was synthesized in an oxidized electrically conductive form. The decrease in conductivity was controlled by treating the MWCNT / PANI composite with buffer solutions with specific pH. The material was then filtered from the buffer solution and dried to constant weight.

The morphology of the materials was studied via of NANOSEM 450, a scanning electron microscope (SEM) from by Fei (USA), at an accelerating voltage of 5 kV and a pressure of 90 Pa.

The MWCNT/ PANI composites were compressed into pellets 16 mm in diameter and 1–3 mm in thickness under 392 MPa for thermoelectric measurements.

Conductivity and Seebeck coefficient were measured with the NETZSCH SBA 458 Nemesis setup (Netzsch, Germany). A four-point method was used to measure the specific conductivity of the sample. The temperature gradient for measuring the Seebeck coefficient was generated by means of two microheaters located at the edges of the sample. The quantities α and σ were measured automatically, alternately for each temperature point (with a constant step). The measurement accuracy was 7% for the Seebeck coefficient, and 6–7% for specific conductivity.

Experimental results and discussion

A typical morphology of PANI produced by template-free polymerization (particularly carbon nanotubes), serving as a reference material, is shown in Fig. 1, *a*. The polymer has a hierarchical structure. The first hierarchical level formed by self-assembly of insoluble aniline oligomers consisted of spherical particles about 10 nm in diameter. They assemble into quasi-spherical agglomerates of submicron sizes during synthesis (the agglomerates are clearly visible in the figure). These agglomerates then stick together to form shapeless micron-sized particles, which then precipitate into powdered polymer material [13].

If the template has a large specific surface area, which is the case with MWCNTs, rather than self-assemble into nanospheres, the oligomers are adsorbed onto the surface of the MWCNT, followed by heterophase growth of the polymer shell covering the surface of carbon tubes.

Fig. 1, *b*, *c* shows images of the original carbon nanotubes (MWCNT) and the MWCNT/ PANI composite. The initial carbon material is a homogeneous porous mat of chaotically entangled MWCNTs (Fig. 1,*b*). The overall structure of the material did not change when PANI was deposited, but the diameter of the composite tubes nearly doubled (Fig. 1, *c*), so the thickness of the PANI shell can be estimated at about 10 nm. Evidently, the structure is homogeneous and extended. The entire material has a nanocable-like morphology. The nanotubes are randomly oriented relative to each other.

Fig. 2 shows the temperature dependences for conductivity σ, Seebeck coefficient α and power factor of the MWCNT/ PANI composites treated with buffer solutions with different pH values. As evident from Fig. 2, *a*, the maximum conductivity is observed in the composite treated with the most acidic buffer solution with the pH value = 1.0. An increase in the hydrogen index of the buffer solution leads to an uneven decrease in the conductivity of the composite over the entire temperature range considered. For example, an increase in the pH of the buffer from 1.0 to 2.0 at a temperature of 296 K provides a decrease in specific conductivity from 32 to 22 S/cm, while an increase in the pH from 3.5 to 7 is accompanied with a decrease in the conductivity from 18.5 to 16.5 S/cm. It is known for buffer pH values of 1.5–2.0 that PANI films show a sharp transition from the basic emeraldine form (when it is a dielectric) to doped acidic emeraldine form, when its conductivity increases sharply [14]. However, it is noteworthy in this case that the treating the MWCNT / PANI composite in acidic (pH = 1.0) and neutral (pH = 7) buffers only produces a twofold change in its conductivity, while treating the powder or a sufficiently thick PANI film in solutions with the same acidity reduces its conductivity by several orders of magnitude [14, 15].

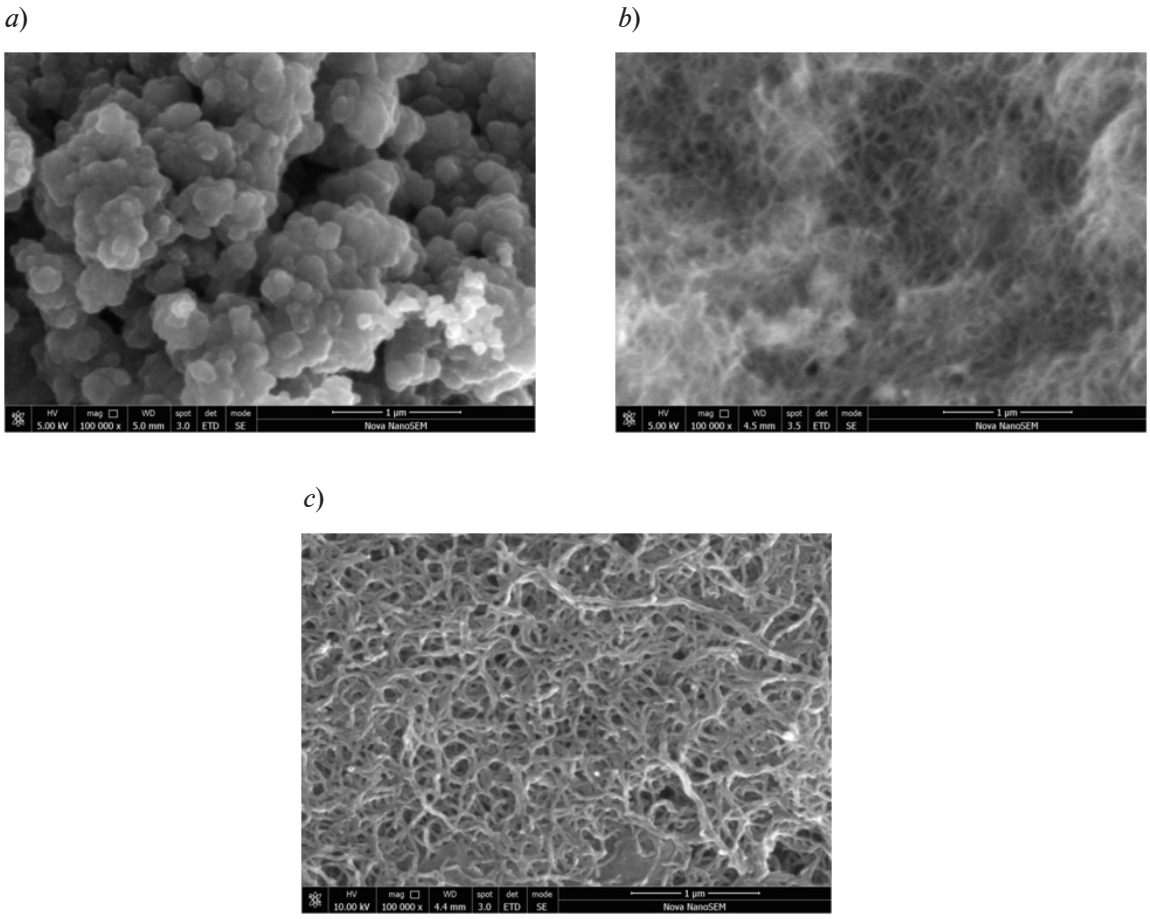

Fig. 1. SEM images of polyaniline (reference material) obtained in the absence of MWCNTs (*a*); initial carbon nanotubes (*b*) and the same nanotubes after PANI deposition (*c*).
All scale bars are equal to 1 μm

Studies of electrical conductivity of PANI established that the contact between aggregates at the last hierarchical level is limited to transport of charge carriers [16]. Such aggregates are shapeless unconsolidated particles of micron sizes, formed primarily during PANI sedimentation after the synthesis is completed. The highest electrical conductivity is observed in nanospheres, which are particles of the first hierarchical level where polymer chains are densely packed during synthesis. Dedoping the micron particles critically reduces the electrical conductivity of the material. On the other hand, dedoping of densely packed spheres only occurs at the edges of the particles and does not lead to a significant decrease in their conductivity. Apparently, the shell of the MWCNT/PANI composite is a densely packed layer of macromolecules, similar to particles of the first hierarchical level. It has increased electrical conductivity and is weakly dedoped, so the conductivity of MWCNT / PANI decreases slightly with an increase in pH.

The temperature dependences of conductivity exhibit different behaviors in composite samples treated with buffer solutions with different pH values. When the composite is treated with a buffer with pH = 7, the temperature only slightly affects the specific conductivity, which increases approximately linearly from 16.5 to 17.5 S/cm with an increase in temperature from 295 to 413 K. The linear nature of the σ (T) dependence is preserved at pH = 6.0, but the slope of the line increases markedly, i.e., heating of the sample produces a more significant increase in its conductivity. Starting from pH = 3.5, the $\sigma(T)$ dependence ceases to be linear, a peak starts to form on it (at $T \approx 370$ K), becoming pronounced for samples with high conductivity.

Repeating the heating cycle for a sample of highly conductive MWCNT / PANI composite to 413 K with subsequent cooling, we found that the $\sigma(T)$ dependences measured during heating and cooling do not coincide. Fig. 3 shows a graph of the $\sigma(T)$ dependence for the MWCNT/PANI

composite treated with a buffer solution with pH = 1.0, during heating and subsequent cooling. Evidently, the σ(*T*) curve characterizing cooling passes below the curve corresponding to heating. The difference in σ values is about 2 S/cm. We can hypothesize that water and dopant losses in the samples may be the reason why the conductivity of the composite decreases upon heating above 370 K. Such a process may occur in PANI exposed at elevated temperatures, as described in [17].

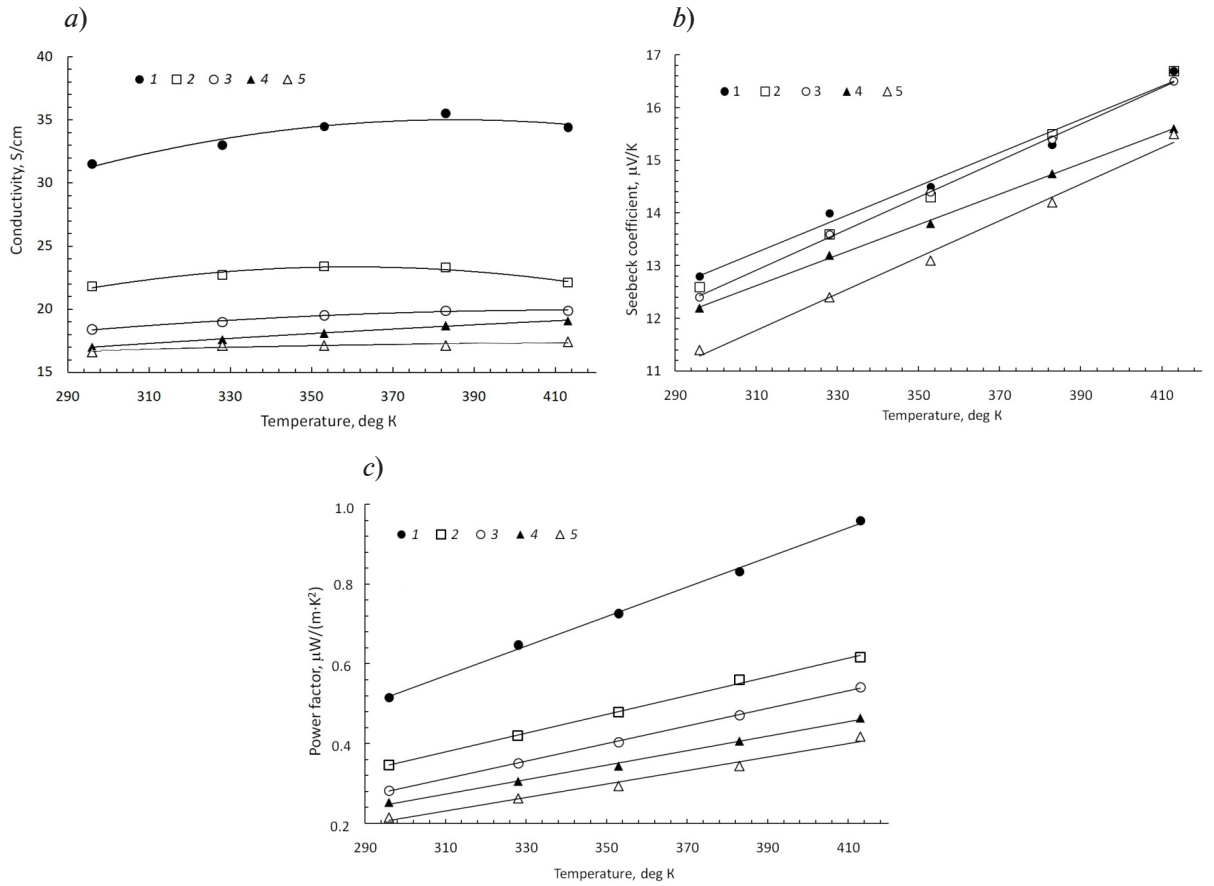

Fig. 2. Temperature dependences of conductivity (*a*), Seebeck coefficient (*b*) and power factor (*c*) for samples of MWCNT/PANI composite after treatment with solutions with different pH values: 1.0 (*1*), 2.0 (*2*), 3.5 (*3*); 6.0 (*4*) and 7.0 (*5*)

Fig. 2, *b* shows the temperature dependence for the Seebeck coefficient of the given samples treated with buffer solutions with different pH. The value of α exhibits linear growth over the entire temperature range considered for all pH values. The increase in the Seebeck coefficient relative to the initial value at $T = 413$ K amounted to approximately 30%. As seen from the graph, the highest Seebeck coefficient in the entire temperature range is observed in the sample with the highest conductivity, treated with a buffer solution with pH = 1.0. As the pH increases, the value of α decreases.

Based on the measurement results obtained for σ(*T*) and α(*T*), we calculated the temperature dependences of the power factor for all samples (see Fig. 2,*c*). Apparently, regardless of the doping degree, an increase in temperature leads to an increase in *P* by a law close to linear. The highest value of the power factor is characteristic for the composite material treated with a buffer solution with pH = 1.0. $P \approx 0.5$ μW/(m·K^2) for this sample at room temperature, while this coefficient increases to about 1 μW/(m·K^2) at 413 K. However, its thermoelectric characteristics gradually deteriorate over time at such a high temperature, due to loss of dopant from the sample. Therefore, despite a significant increase in the power factor, it seems impractical to use this composite at temperatures above 370 K.

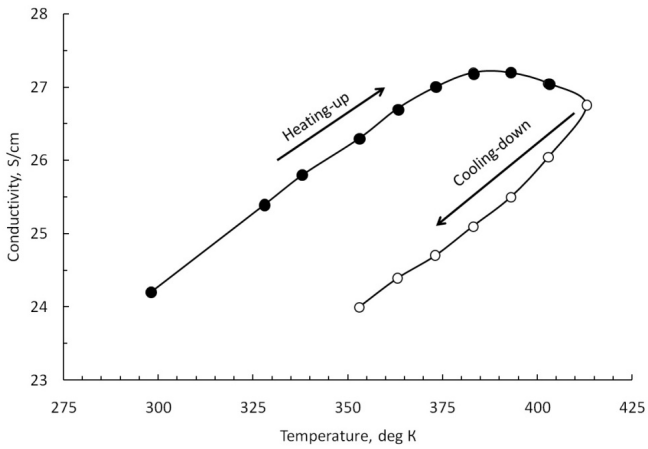

Fig. 3. Variation in specific conductivity of MWCNT/PANI composite sample treated with a buffer solution with pH = 1.0 during heating and subsequent cooling

Conclusion

Thus, considering the effect of temperature on the MWCNT/PANI composite material at varying doping concentrations of PANI, we found that the composite with the highest conductivity exhibited the greatest power factor equal to 0.5 μW/(m· K^2) at room temperature. Comparing the obtained results with the data available in the literature, we can conclude that the power factor of this sample, characterized by chaotic arrangement of nanotubes, substantially exceeds the value of P for the MWSNT/PANI composite, obtained in [10] via a far more complex technology, that is, electrospinning, which achieves ordering of MWSNTs relative to each other.

Even though the magnitude of P in the samples considered grows with increasing temperature ($P \approx 0.8$ W/(m·K^2) for $T = 370$ K), it seems ill-advised to use this composite at 370 K, since it can be assumed that the dopant gradually withdraws from the composite at high temperatures, and its conductivity decreases.

As the following step, aimed at improving the thermoelectric characteristics of the MWSNT/PANI composite, we plan to develop the technology for producing samples with increased porosity of PANI coating on MWSNT surface.

REFERENCES

1. **Bulat L. P., Sergiyenko O. I., Savoskula V. A.,** Thermoelectric energy converters: Environmental aspects, Semiconductors. 51 (7) (2017) 932–935.

2. **Korotkov A. S., Loboda V. V.,** Thermoelectricity: From history to modernity through the CASS activity, IEEE Circ. Syst. Mag. 21 (3) (2021) 57–65.

3. **Wang H., Yu C.,** Organic thermoelectrics: Materials preparation, performance optimization, and device integration, Joule. 3 (1) (2019) 53–80.

4. **Beretta D., Neophytou N., Hodges J. M., et al.,** Thermoelectrics: From history, a window to the future, Mater. Sci. Eng. R. 138 (October) (2019) 100501.

5. **Buslaev R., Galitskaya A, Loboda V.,** Simulation of flexible thermoelectric generators based on Bi_2Te_3/Sb_2Te_3 synthesized by electrochemical deposition method, Proc. 2019 IEEE Int. Conf. on Elect. Eng. Photonics (EExPolytech), Oct. 17–18, 2019. St. Petersburg. Peter the Great Polytechnical University, Institute of Electrical and Electronics Engineers (2019) 54–57.

6. **Chatterjee K., Ghosh T. K.,** Thermoelectric materials for textile applications, Molecules. 26 (11) (2021) 3154.

7. **Mateeva N., Niculescu H., Schlenoff J., Testardi L. R.,** Correlation of Seebeck coefficient and electric conductivity in polyaniline and polypyrrole, J. Appl. Phys. 83 (6) (1998) 3111–3117.

8. **Zhang K., Davis M., Qiu J., et al.,** Thermoelectric properties of porous multi-walled carbon nanotube/polyaniline core/shell nanocomposites, Nanotechnol. 23 (38) (2012) 385701.

9. **Yao Q., Chen L., Zhang W., et al.,** Enhanced thermoelectric performance of single-walled carbon nanotubes/polyaniline hybrid nanocomposites, ACS Nano. 4 (4) (2010) 2445–2451.

10. **Wang Q., Yao Q., Chang J., Chen L.,** Enhanced thermoelectric properties of CNT/PANI composite nanofibers by highly orienting the arrangement of polymer chains, J. Mater. Chem. 22 (34) (2012) 17612–17618.

11. **Yao Q., Wang Q., Wang L., Chen L.,** Abnormally enhanced thermoelectric transport properties of SWNT/PANI hybrid films by the strengthened PANI molecular ordering, Energy & Environ. Sci. 7 (11) (2014) 3801–3807.

12. **Moniruzzaman M., Winey K. I.,** Polymer nanocomposites containing carbon nanotubes, Macromol. 39 (16) (2006) 5194–5205.

13. **Shishov M., Moshnikov V., Sapurina I.,** Self-organization of polyaniline during oxidative polymerization: formation of granular structure, Chem. Papers. 67 (8) (2013) 909–918.

14. **Ivanov B. F., Gribkova O. L., Vannikov A. V.,** Wide-range regulation of polyaniline conduction by interphase doping of a polyaniline film, Russian Journal of Electrochemistry. 42 (3) (2006) 263–267.

15. **McManus P. M., Cushman R. J., Yang S. C.,** Influence of oxidation and protonation on the electrical conductivity of polyaniline, J. Phys. Chem. 91 (3) (1987) 744–747.

16. **Moučka R., Kazantseva N., Sapurina I.,** Electric properties of MnZn ferrite/polyaniline composites: the implication of polyaniline morphology, J. Mater. Sci. 53 (3) (2018) 1995–2004.

17. **Prokeš J., Stejskal J.,** Polyaniline prepared in the presence of various acids: 2. Thermal stability of conductivity, Polym. Degr. Stab. 86 (1) (2004) 187–195.

СПИСОК ЛИТЕРАТУРЫ

1. **Булат Л. П., Сергиенко О. И., Савоскула В. А.** Термоэлектрические преобразователи энергии: экологические аспекты //Физика и техника полупроводников. 2017. Т. 51. № 7. С. 970–974.

2. **Korotkov A. S., Loboda V. V.** Thermoelectricity: From history to modernity through the CASS activity // IEEE Circuits and Systems Magazine. 2021. Vol. 21. No. 3. Pp. 57–65.

3. **Wang H., Yu C.** Organic thermoelectrics: materials preparation, performance optimization, and device integration // Joule. 2019. Vol. 3. No. 1. Pp. 53–80.

4. **Beretta D., Neophytou N., Hodges J. M., et al.** Thermoelectrics: From history, a window to the future // Materials Science and Engineering: R: Reports. 2019. Vol. 138. October. P. 100501.

5. **Buslaev R., Galitskaya A, Loboda V.** Simulation of flexible thermoelectric generators based on Bi_2Te_3/Sb_2Te_3 synthesized by electrochemical deposition method // Proceedings of the 2019 IEEE International Conference on Electrical Engineering and Photonics (EExPolytech). October 17–18, 2019. St. Petersburg. Peter the Great Polytechnical University, Institute of Electrical and Electronics Engineers. Pp. 54–57.

6. **Chatterjee K., Ghosh T. K.** Thermoelectric materials for textile applications // Molecules. 2021. Vol. 26. No. 11. P. 3154.

7. **Mateeva N., Niculescu H., Schlenoff J., Testardi L. R.** Correlation of Seebeck coefficient and electric conductivity in polyaniline and polypyrrole // Journal of Applied Physics. 1998. Vol. 83. No. 6. Pp. 3111–3117.

8. **Zhang K., Davis M., Qiu J., Hope-Weeks L., Wang S.** Thermoelectric properties of porous multi-walled carbon nanotube/polyaniline core/shell nanocomposites // Nanotechnology. 2012. Vol. 23. No. 38. P. 385701.

9. **Yao Q., Chen L., Zhang W., Liufu S., Chen X.** Enhanced thermoelectric performance of single-walled carbon nanotubes/polyaniline hybrid nanocomposites // ACS (American Chemical Society) Nano. 2010. Vol. 4. No. 4. Pp. 2445–2451.

10. **Wang Q., Yao Q., Chang J., Chen L.** Enhanced thermoelectric properties of CNT/PANI composite nanofibers by highly orienting the arrangement of polymer chains // Journal of Materials Chemistry. 2012. Vol. 22. No. 34. Pp. 17612–17618.

11. **Yao Q., Wang Q., Wang L., Chen L.** Abnormally enhanced thermoelectric transport properties of SWNT/PANI hybrid films by the strengthened PANI molecular ordering // Energy & Environmental Science. 2014. Vol. 7. No. 11. Pp. 3801–3807.

12. **Moniruzzaman M., Winey K. I.** Polymer nanocomposites containing carbon nanotubes // Macromolecules. 2006. Vol. 39. No. 16. Pp. 5194–5205.

13. **Shishov M., Moshnikov V., Sapurina I.** Self-organization of polyaniline during oxidative polymerization: formation of granular structure // Chemical Papers. 2013. Vol. 67. No. 8. Pp. 909–918.

14. **Иванов В. Ф., Грибкова О. Л., Ванников А. В.** Регулирование в широких пределах проводимости полианилина при межфазном допировании полианилинового слоя // Электрохимия. 2006. Т. 42. № 3. С. 304–309.

15. **McManus P. M., Cushman R. J., Yang S. C.** Influence of oxidation and protonation on the electrical conductivity of polyaniline // Journal of Physical Chemistry. 1987. Vol. 91. No. 3. Pp. 744–747.

16. **Moučka R., Kazantseva N., Sapurina I.** Electric properties of MnZn ferrite/polyaniline composites: the implication of polyaniline morphology // Journal of Materials Science. 2018. Vol. 53. No. 3. Pp. 1995–2004.

17. **Prokeš J., Stejskal J.** Polyaniline prepared in the presence of various acids: 2. Thermal stability of conductivity // Polymer Degradation and Stability. 2004. Vol. 86. No. 1. Pp. 187–195.

THE AUTHORS

TRETYAKOV Artem A.
Peter the Great St. Petersburg Polytechnic University
29 Politechnicheskaya St., St. Petersburg, 195251, Russia
tretartem@gmail.com
ORCID: 0000-0003-1009-8016

KAPRALOVA Viktoria M.
Peter the Great St. Petersburg Polytechnic University
29 Politechnicheskaya St., St. Petersburg, 195251, Russia
kapralova2006@yandex.ru
ORCID: 0000-0001-9050-4453

LOBODA Vera V.
Peter the Great St. Petersburg Polytechnic University
29 Politechnicheskaya St., St. Petersburg, 195251, Russia
vera_loboda@mail.ru
ORCID: 0000-0003-3103-7060

SAPURINA Irina Yu.
Institute of Macromolecular Compounds RAS
31 Bolshoy Ave. V. Isl., St. Petersburg, 199004, Russia
sapurina@mail.ru
ORCID: 0000-0001-7579-7577

SUDAR Nikolay T.
Peter the Great St. Petersburg Polytechnic University
29 Politechnicheskaya St., St. Petersburg, 195251, Russia
sudar53@mail.ru
ORCID: 0000-0001-7380-7727

СВЕДЕНИЯ ОБ АВТОРАХ

ТРЕТЬЯКОВ Артем Александрович – *аспирант Высшей школы электроники и микросистемной техники Санкт-Петербургского политехнического университета Петра Великого.*
195251, Россия, г. Санкт-Петербург, Политехническая ул., 29
tretartem@gmail.com
ORCID: 0000-0003-1009-8016

КАПРАЛОВА Виктория Маратовна – *кандидат физико-математических наук, доцент Высшей школы электроники и микросистемной техники Санкт-Петербургского политехнического университета Петра Великого.*
195251, Россия, г. Санкт-Петербург, Политехническая ул., 29
kapralova2006@yandex.ru
ORCID: 0000-0001-9050-4453

ЛОБОДА Вера Владимировна – *кандидат физико-математических наук, директор Высшей школы электроники и микросистемной техники Санкт-Петербургского политехнического университета Петра Великого.*
195251, Россия, г. Санкт-Петербург, Политехническая ул., 29
vera_loboda@mail.ru
ORCID: 0000-0003-3103-7060

САПУРИНА Ирина Юрьевна – *доктор химических наук, ведущий научный сотрудник Института высокомолекулярных соединений РАН.*
199004, г. Санкт-Петербург, Большой пр. В. О., 31
sapurina@mail.ru
ORCID: 0000-0001-7579-7577

СУДАРЬ Николай Тобисович – *доктор физико-математических наук, профессор Высшей школы электроники и микросистемной техники Санкт-Петербургского политехнического университета Петра Великого.*
195251, Россия, г. Санкт-Петербург, Политехническая ул., 29
sudar53@mail.ru
ORCID: 0000-0001-7380-7727.

Received 31.05.2022. Approved after reviewing 19.06.2022. Accepted 19.06.2022.
Статья поступила в редакцию 31.05.2022. Одобрена после рецензирования 19.06.2022. Принята 19.06.2022.

Original article
DOI: https://doi.org/10.18721/JPM.15312

EFFECTIVE DIFFUSION PROPERTIES OF A POLYCRYSTAL

D. M. Pashkovsky[1]✉, *K.P. Frolova*[2], *E. N. Vilchevskaya*[2]

[1] Peter the Great St. Petersburg Polytechnic University, St. Petersburg, Russia;

[2] Institute for Problems in Mechanical Engineering RAS, St. Petersburg, Russia

✉ mr.vivivilka@icloud.com

Abstract. The paper deals with the calculation of polycrystalline material effective diffusion coefficients. The polycrystalline material has been simulated by two-phase composite consisting of matrix and spheroidal inhomogeneities. The Mori – Tanaka scheme was used to account interactions between inhomogeneities. The proposed simulation took into account the effect of segregation as well. The paper put forward two models to describe the polycrystalline material. The former considered grains to be inhomogeneities, and grain boundaries to be a material matrix. The latter, in contrast, did the grain boundaries to be inhomogeneities, and the grains to be a material matrix. The simulation results were compared with experimental data. The importance of taking into account the segregation parameter when calculating effective diffusion coefficients of polycrystalline material was shown.

Keywords: two-phase composite, polycrystalline material, Mori – Tanaka scheme, effective diffusion properties, segregation effect

Funding: The reported study was funded by Russian Science Foundation (Project No. 18–19–00160).

Citation: Pashkovsky D. M., Frolova K. P., Vilchevskaya E. N., Effective diffusion properties of a polycrystal, St. Petersburg Polytechnical State University Journal. Physics and Mathematics. 15 (3) (2022) 154–168. DOI: https://doi.org/10.18721/JPM.15312

Научная статья
УДК 536.2
DOI: https://doi.org/10.18721/JPM.15312

ЭФФЕКТИВНЫЕ ДИФФУЗИОННЫЕ СВОЙСТВА ПОЛИКРИСТАЛЛА

Д. М. Пашковский[1]✉, *К. П. Фролова*[2], *Е. Н. Вильчевская*[2]

[1] Санкт-Петербургский политехнический университет Петра Великого, Санкт-Петербург, Россия;

[2] Институт проблем машиноведения РАН, Санкт-Петербург, Россия

✉ mr.vivivilka@icloud.com

Аннотация. Работа посвящена определению эффективных коэффициентов диффузии поликристаллического материала, для описания которого используется модель двухфазного композита, состоящего из матрицы и сфероидальных неоднородностей. Для учета взаимодействия между неоднородностями используется схема Мори – Танаки. В модели также учтен эффект сегрегации. Предложены две модели описания поликристаллического материала. В первой зерна моделируются неоднородностями, а граница зерен матрицей; во второй модели, наоборот, граница зерен моделируется неоднородностями, а зерна – матрицей материала. Результаты моделирования сравниваются с экспериментальными данными. Показано, что важно учитывать параметр сегрегации при расчете эффективных коэффициентов диффузии поликристаллического материала.

Ключевые слова: двухфазный композит, поликристаллический материал, схема Мори – Танаки, эффективные диффузионные свойства, эффект сегрегации

Финансирование: работа выполнена при поддержке Российского научного фонда, проект № 00160–19–18.

Ссылка для цитирования: Пашковский Д. М., Фролова К. П., Вильчевская Е. Н. Эффективные диффузионные свойства поликристалла // Научно-технические ведомости СПбГПУ. Физико-математические науки. 2022. Т. 15. № 3. С. 154–168. DOI: https://doi.org/10.18721/JPM.15312

Introduction

Finding the effective diffusion coefficients of solids is a crucial problem in many areas of industry and construction. Gas diffusion in a solid may produce pores, cracks, or other micro-defects that may grow over time and lead to fracture of structural elements. For this reason, the concentrations of the diffusing substance should be taken into account in evaluations of strength properties of the material.

The main practical applications include measures for preventing hydrogen embrittlement in metals and alloys or fracture in thin films. Hydrogen embrittlement produces a decrease in the strength properties of the metal alloy due to hydrogen diffusion, subsequently leading to fracture of the material [1]. It is essential to account for this effect in structures engineered for hydrogen energy storage or fuel cells in hydrogen-powered vehicles. Thin films are understood here as thin layers of another material applied to structural elements. One of the most typical examples are anti-corrosion coatings. The presence of defects in such coatings can produce increased concentrations of the diffusing substance, breaching the insulation of metals from the aggressive environment.

This paper considers the problem on quantifying the diffusion coefficients of polycrystalline material, which is inhomogeneous and contains a large number of randomly oriented single crystals, each of which can have different chemical and physical properties.

The single crystal is also called a grain in the literature, and the space between single crystals is known as the grain boundary [2].

There are many different mathematical models for quantifying the diffusion coefficients of polycrystalline materials. For example, Hart [3] obtained volumetric bulk coefficients for the case when the material contains dislocations; an equation similar to the rule of mixtures was used. Another study by Barrer [4] relied on the similarities between the processes of thermal conductivity and diffusion to find the tensor of effective diffusion coefficients similar to the tensor of conductivity in the thermal conductivity problem. Additionally, a ratio between the effective characteristics and properties of the material components was obtained. Barrer's approach is also used in other studies [5, 6].

Zhang and Liu [7] found that the concentration in the diffusion problem is not a continuous function at the interface, in contrast to the temperature in the thermal conductivity problem. The reason for this is that the diffusing substance accumulates at the boundary or inside the inhomogeneities, so the concentration makes a jump. This phenomenon is known as the segregation effect. Belova and March [8, 9] introduce the segregation parameter into the Hart and Maxwell–Garnett equations to calculate the effective properties of a material consisting of grain boundaries and spherical grains. Knyazeva et al. [2] represent the Mori–Tanaka method and the Maxwell homogenization scheme in terms of tensors of contribution to diffusion, serving for calculating the effective diffusion coefficients of isotropic material consisting of spheroidal grains, which are inhomogeneities, and grain boundaries, which are a matrix. On the other hand, the effect of segregation was not taken into account in [2] at the stage when the fields were averaged. The effect of segregation was taken into account in [10] at all stages of solving the homogenization problem for a transversely isotropic material with pores, whose anisotropy is due to the geometry of the microstructure.

The goal of our paper is to compare two approaches to simulation of polycrystalline materials.

Within the first approach, the grains are simulated by inhomogeneities and the grain boundary by the matrix, and, vice versa, the grain boundary is simulated by inhomogeneities, and the grains by the material matrix within the second approach. The models are compared by constructing a tensor of effective diffusion coefficients $\mathbf{D}_{eff}$ using the results obtained in [10]. In this case, the tensor $\mathbf{D}_{eff}$ takes the same form for both models of material. The difference in the models is reflected in the quantitative values of the microstructural parameters used.

Problem statement

The goal we set is achieved in two stages. First, we select a model for describing the polycrystalline material (Fig. 1, I) that can best approximate the effective diffusion coefficients of the real material. Second, an expression should be constructed for the tensor $\mathbf{D}_{eff}$. The homogenization problem is solved for this purpose (Fig. 1, II). Let us now consider each of the stages in more detail.

Two models of a two-phase composite are considered to describe the polycrystalline material (Fig. 1):

matrix–grain boundary, inhomogeneities–grains (M1);

matrix–grains, inhomogeneities–grain boundary (M2).

The composite consists of a matrix of material and isolated inhomogeneities placed in it both models; however, the matrix of the material and the inhomogeneities have different physical properties.

Models M1 and M2 differ only in the values of microstructural parameters: the segregation parameter s and the ratio of semi-major axis of the spheroid γ (see Table). The distribution of heterogeneities is assumed to be isotropic.

The following boundary conditions are imposed at the interface between the matrix (+)/inhomogeneity (–) phases [8, 9]:

$$D_0 \left.\frac{\partial c(x)}{\partial n}\right|_{x\to\partial V_1+} = D_1 \left.\frac{\partial c(x)}{\partial n}\right|_{x\to\partial V_1-}, \tag{1}$$

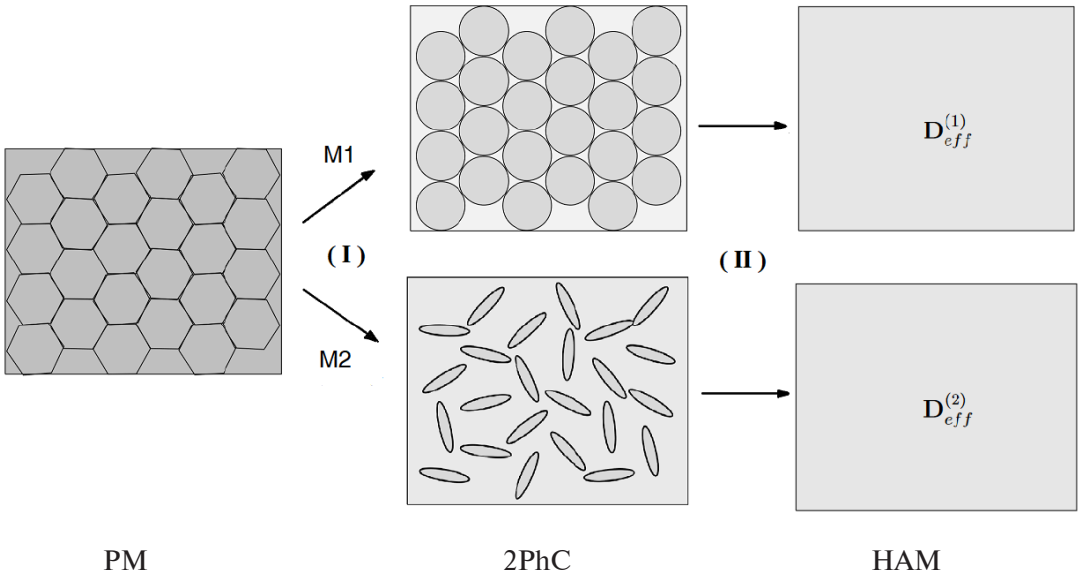

Fig. 1. Approximation scheme for polycrystalline material (PM) using Model 1 (M1) and Model 2 (M2) in two stages: modelling (I), homogenization (II); 2-phase composite (2PhC) and homogeneous anisotropic material (HAM) are shown; the corresponding tensors are given on the right

$$c(x)\big|_{x\to\partial V_1+} = sc(x)\big|_{x\to\partial V_1-}, \tag{2}$$

where D_0, D_1 are the diffusion coefficients of the material matrix and inhomogeneity, respectively; $c(x)$ is the concentration function with respect to the coordinate; ∂V_1 is the inhomogeneity boundary; **n** is the vector of the external normal to the inhomogeneity boundary, s is the segregation parameter.

Condition (1) stipulates that the fluxes at the interface be equal, while (2) describes the effect of segregation, i.e., the jump in concentration at the interface between the matrix and the inhomogeneity.

The segregation parameter s takes a value greater than unity in the model M1, and less than unity in the model M2. The reason for this is that the diffusing substance accumulates along the grain boundaries.

M1 considers spherical inhomogeneities, so $\gamma = 1$; the grain boundary in M2 is a highly oblate spheroid, so the parameter γ is taken in the range from 0.05 to 0.10.

The matrix and heterogeneities consist of an isotropic material with diffusion tensors taking the following form:

$$\mathbf{D}_0 = D_0\mathbf{E},\ \mathbf{D}_i = D_i\mathbf{E}, \tag{3}$$

where D_i is the diffusion coefficient of an ith heterogeneity, **E** is a single second-order tensor.

Table

Parameters of the models used and their values

Model	Segregation parameter s	Semi-major axes ratio γ for spheroid
1	$s > 1$	1.00
2	$s < 1$	0.05–0.10

$D_i < D_0$ for the model M1, since the diffusion coefficient of the grains is always less than that of the grain boundary. The opposite is true for the model M2: $D_i > D_0$.

After we select a model for describing the polycrystalline material, we construct an expression for the tensor of effective diffusion coefficients $\mathbf{D}_{eff}$. This requires a homogenization procedure, which consists in adopting a homogeneous continuous medium with anisotropic properties instead of an inhomogeneous medium [11].

The interaction between inhomogeneities is taken into account during homogenization. The Mori–Tanaka scheme is used for this purpose: its main principle is that each of the inhomogeneities is placed in a uniform field (either a concentration gradient or a diffusion flux acts as such a field in the context of the diffusion problem), equal to the average field with respect to the matrix of the material [12]. The Mori–Tanaka scheme is from the group of effective field methods, also including the widely used Maxwell and Kanaun–Levin schemes. However, unlike the latter two schemes, the Mori–Tanaka scheme does not have a singularity at a volume fraction of inhomogeneities equal to unity, so the model M1 can be used correctly, since the concentration of inhomogeneities in it is about 95–99%.

Contribution of isolated inhomogeneity

The contribution of isolated inhomogeneity to the effective properties of the material is determined following the steps similar to those described in our earlier paper [10]. The homogenization problem is solved introducing the concentrations and fluxes averaged over the volume. The averaging operation is denoted by the angle brackets and the subscript corresponding to the volume to be averaged.

It is assumed that the concentration $c(\mathbf{x})|_{\partial V} = \mathbf{G^0} \cdot \mathbf{x}$ is given at the boundary of the representative volume V considered. The concentration gradients $\langle \nabla c \rangle_V$ averaged over the representative volume V then amount to $\mathbf{G}^0$. At the same time, the flux $\langle \mathbf{J} \rangle_V$ $\langle \mathbf{J} \rangle_V$, also averaged over the representative volume V, depends on the microstructure of the material.

The concentration gradient $\langle \nabla c \rangle_V$ is composed of the mean concentration gradient $\langle \nabla c \rangle_m$ of the substance, distributed in the matrix, the mean concentration gradient $\langle \nabla c \rangle_{in}$ of the substance, distributed within the inhomogeneity with a volume V_1, and the substance accumulated at the interface between the matrix and the inhomogeneity as a result of the segregation effect evolving:

$$\mathbf{G}^0 = \langle \nabla c \rangle_V = (1 - \frac{V_1}{V}) \langle \nabla c \rangle_m + \frac{V_1}{V} \langle \nabla c \rangle_{in} + \frac{1}{V} \int_{\partial V_1} \mathbf{n}(c_0 - c_1) d(\partial V_1). \tag{4}$$

In view of condition (2), expression (4) is converted to the following form:

$$\mathbf{G}^0 = \langle \nabla c \rangle_V = (1 - \frac{V_1}{V}) \langle \nabla c \rangle_m + s \frac{V_1}{V} \langle \nabla c \rangle_{in}. \tag{5}$$

The flux $\langle \mathbf{J} \rangle_V$ is continuous upon crossing the interface and consists of two components:

$$\langle \mathbf{J} \rangle_V = (1 - \frac{V_1}{V}) \langle \mathbf{J} \rangle_m + \frac{V_1}{V} \langle \mathbf{J} \rangle_{in}. \tag{6}$$

Taking into account Fick's first law, expression (6) takes the following form:

$$\langle \mathbf{J} \rangle_V = -(1 - \frac{V_1}{V}) \mathbf{D}_0 \cdot \langle \nabla c \rangle_m - \frac{V_1}{V} \mathbf{D}_1 \cdot \langle \nabla c \rangle_{in}. \tag{7}$$

In view of (5), expression (7) is converted to the form

$$\langle \mathbf{J} \rangle_V = -\mathbf{D}_0 \cdot \langle \nabla c \rangle_V - \frac{V_1}{V} (\mathbf{D}_1 - s\mathbf{D}_0) \cdot \langle \nabla c \rangle_{in}. \tag{8}$$

Next, $\langle \nabla c \rangle_{in}$ is expressed in terms of $\langle \nabla c \rangle_V$:

$$\langle \nabla c \rangle_{in} = \mathbf{\Lambda}_c \cdot \langle \nabla c \rangle_V = \mathbf{\Lambda}_c \cdot \mathbf{G}^0. \tag{9}$$

The tensor $\mathbf{\Lambda}_c$ is the solution of the Eshelby problem for diffusion. The expression for this tensor is obtained in [10] and has the form:

$$\mathbf{\Lambda}_c = [s\mathbf{E} + \mathbf{P} \cdot (\mathbf{D}_1 - s\mathbf{D}_0)]^{-1}, \tag{10}$$

where $\mathbf{P}$ is the Hill tensor.

In view of (9), Eq. (8) is converted to the following form:

$$\langle \mathbf{J} \rangle_V = -\left(\mathbf{D}_0 + \frac{V_1}{V}(\mathbf{D}_1 - s\mathbf{D}_0) \cdot \mathbf{\Lambda}_c \right) \cdot \mathbf{G}^0 = -\mathbf{D}_{eff} \cdot \mathbf{G}^0. \tag{11}$$

Thus, the inhomogeneous material consisting of the matrix and the inhomogeneity was replaced by a homogeneous anisotropic material with an effective diffusion tensor $\mathbf{D}_{eff}$.

Mori–Tanaka method

This section covers a generic material consisting of the matrix and n inhomogeneities. The interaction of inhomogeneities is described by the Mori–Tanaka scheme [12], outlined in Fig. 2. Each of the inhomogeneities is regarded as isolated and placed in an effective uniform field of the concentration gradient $\mathbf{G}^{eff}$, different from the one applied ($\mathbf{G}^0$) and equal to the average field over the material matrix $\langle \nabla c \rangle_m$.

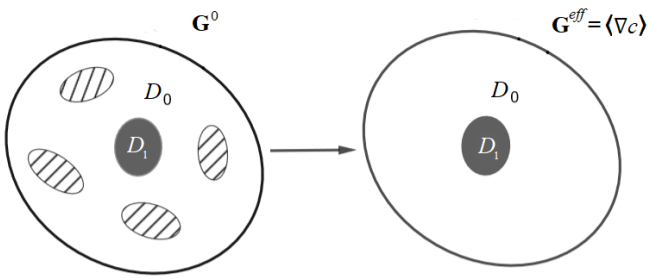

Fig. 2. Mori–Tanaka scheme:
interaction of isolated inhomogeneities (left) is taken into account by placing each of them in an effective field equal to the average over the material matrix (right)

The concentration gradient $\langle \nabla c \rangle_V$ is written as follows:

$$\mathbf{G}^0 = \langle \nabla c \rangle_V = \frac{1}{V}\sum_{i=1}^{n} V_i \langle \nabla c \rangle_{in}^i + (1-\varphi)\langle \nabla c \rangle_m + \frac{1}{V}\sum_{i=1}^{n} \int_{\partial V_i} \mathbf{N}_i (c_0 - c_i) d(\partial V_i), \tag{12}$$

where V_i, ∂V_i are the volume and boundary of an ith inhomogeneity; $\mathbf{N}_i$ is the normal to its boundary; φ is the volume fraction of inhomogeneities.

In view of boundary conditions (1) and (2), expression (12) is converted to the following form:

$$\mathbf{G}^0 = \langle \nabla c \rangle_V = s\frac{1}{V}\sum_{i=1}^{n} V_i \langle \nabla c \rangle_{in}^i + (1-\varphi)\langle \nabla c \rangle_m. \tag{13}$$

Expression (13) can be used to express $(1 - \varphi)\langle \nabla c \rangle_m$:

$$(1-\varphi)\langle \nabla c \rangle_m = \mathbf{G}^0 - s\frac{1}{V}\sum_{i=1}^{n} V_i \langle \nabla c \rangle_{in}^i. \tag{14}$$

Taking into account the Mori-Tanaka interaction, $\langle \nabla c \rangle^i_{in}$ is written as follows:

$$\langle \nabla c \rangle^i_{in} = \mathbf{\Lambda}^i_c \cdot \langle \nabla c \rangle_m , \tag{15}$$

where Λ^i_c is the concentration tensor for an ith heterogeneity.

The averaged flow is represented in the following form:

$$\langle \mathbf{J} \rangle_V = \frac{1}{V} \sum_{i=1}^{n} V_i \langle \mathbf{J} \rangle^i_{in} + (1-\varphi) \langle \mathbf{J} \rangle_m . \tag{16}$$

Next, expression (16) is transformed taking into account Fick's law:

$$\langle \mathbf{J} \rangle_V = -\frac{1}{V} \sum_{i=1}^{n} V_i \mathbf{D}_i \cdot \langle \nabla c \rangle^i_{in} - (1-\varphi) \mathbf{D}_0 \cdot \langle \nabla c \rangle_m . \tag{17}$$

In view of Eq. (14), expression (17) is converted to the following form:

$$\langle \mathbf{J} \rangle_V = -\mathbf{D}_0 \cdot \mathbf{G}^0 - \frac{1}{V} \sum_{i=1}^{n} V_i (\mathbf{D}_i - s\mathbf{D}_0) \cdot \langle \nabla c \rangle^i_{in} . \tag{18}$$

Relations (14) and (15) are used to obtain the expression for $\langle \nabla c \rangle^i_{in}$:

$$\langle \nabla c \rangle^i_{in} = \mathbf{\Lambda}^i_c \cdot [s \frac{1}{V} \sum_{i=1}^{n} V_i \mathbf{\Lambda}^i_c + (1-\varphi)\mathbf{E}]^{-1} \cdot \mathbf{G}^0 . \tag{19}$$

Next, form (18) is converted to the following form taking into account expression (19):

$$\langle \mathbf{J} \rangle_V = -\mathbf{D}_0 \cdot \mathbf{G}^0 - \frac{1}{V} \sum_{i=1}^{n} V_i (\mathbf{D}_i - s\mathbf{D}_0) \cdot \mathbf{\Lambda}^i_c \cdot [s \frac{1}{V} \sum_{i=1}^{n} V_i \mathbf{\Lambda}^i_c + (1-\varphi)\mathbf{E}]^{-1} \cdot \mathbf{G}^0 . \tag{20}$$

Taking into account Fick's law, we obtain the formula

$$\langle \mathbf{J} \rangle_V = -\mathbf{D}_{eff} \cdot \mathbf{G}^0 . \tag{21}$$

Equalities (20) and (21) imply that the expression for $\mathbf{D}_{eff}$ takes the following form:

$$\mathbf{D}_{eff} = \mathbf{D}_0 + \frac{1}{V} \sum_{i=1}^{n} V_i (\mathbf{D}_i - s\mathbf{D}_0) \cdot \mathbf{\Lambda}^i_c \cdot [s \frac{1}{V} \sum_{i=1}^{n} V_i \mathbf{\Lambda}^i_c + (1-\varphi)\mathbf{E}]^{-1} . \tag{22}$$

Next, we convert expression (22) taking into account the averaging and equality $\mathbf{D}_i = \mathbf{D}_1$:

$$\mathbf{D}_{eff} = \mathbf{D}_0 + \varphi(\mathbf{D}_i - s\mathbf{D}_0) \cdot \langle \mathbf{\Lambda} \rangle_c \cdot [s\varphi \langle \mathbf{\Lambda} \rangle_c + (1-\varphi)\mathbf{E}]^{-1} . \tag{23}$$

Effective diffusion tensor

The Hill tensor for spheroidal heterogeneities takes the following form [11]:

$$\mathbf{P} = \frac{1}{D_0} (f_0(\gamma)(\mathbf{E} - \mathbf{nn}) + (1 - 2f_0(\gamma))\mathbf{nn}), \tag{24}$$

where the function $f_0(\gamma)$ is expressed as

$$f_0(\gamma)=\frac{(1-g(\gamma))\gamma^2}{2(\gamma^2-1)},\ g(\gamma)=\begin{cases}\dfrac{1}{\gamma\sqrt{1-\gamma^2}}\arctan\left(\dfrac{\sqrt{1-\gamma^2}}{\gamma}\right), & \gamma<1\\ 1/3, & \gamma=1\\ \dfrac{1}{2\gamma\sqrt{1-\gamma^2}}\log\left(\dfrac{\gamma+\sqrt{\gamma^2+1}}{\gamma-\sqrt{\gamma^2+1}}\right), & \gamma>1.\end{cases} \tag{25}$$

The inverse second-order tensor is calculated by the Sherman–Morrison formula [14]. In general, it takes the following form:

$$\mathbf{B}^{-1}=(\mathbf{A}+\mathbf{n}_1\mathbf{n}_2)^{-1}=\mathbf{A}^{-1}-\frac{1}{1+\mathbf{n}_2\cdot\mathbf{A}^{-1}\cdot\mathbf{n}_1}(\mathbf{A}^{-1}\cdot\mathbf{n}_1\mathbf{n}_2\cdot\mathbf{A}^{-1}), \tag{26}$$

where $\mathbf{n}_1$, $\mathbf{n}_2$ are arbitrary vectors, **A**, **B** are second-order tensors.

In the case when **A** = **E**, Eq. (26) is converted to the form

$$\mathbf{B}^{-1}=(\mathbf{E}+\mathbf{n}_1\mathbf{n}_2)^{-1}=\mathbf{E}-\frac{1}{1+\mathbf{n}_2\cdot\mathbf{n}_1}\mathbf{n}_1\mathbf{n}_2. \tag{27}$$

We calculate the inverse tensor in expression (10) and obtain the following equation:

$$\left\langle[s\mathbf{E}+\mathbf{P}\cdot(\mathbf{D}_1-s\mathbf{D}_0)]^{-1}\right\rangle=A_1\mathbf{E}+A_2\left\langle\mathbf{nn}\right\rangle, \tag{28}$$

where

$$A_1=\frac{1}{s+\dfrac{f_0(D_1-D_0s)}{D_0}},$$

$$A_2=\frac{D_0(3f_0-1)(D_1-D_0s)}{(D_1-2D_1f_0+2D_0f_0s)(D_1f_0+D_0s-D_0f_0s)}.$$

In the case when there is some predominant distribution of heterogeneities by orientation, it can be taken into account using the distribution function of the following form:

$$\psi_1(\upsilon,\xi)=\frac{1}{2\pi}((\xi^2+1)\exp(-\xi\upsilon)-\frac{1}{2}\exp(-\xi\pi)),\ \upsilon\in[0,\pi], \tag{29}$$

where ξ is the parameter for the spread in orientations, υ is the zenith angle in the spherical coordinate system.

Another distribution function is considered in [15], taking the following form:

$$\psi_2(\upsilon,\xi)=\frac{1}{2\pi}((\xi^2+1)\exp(-\xi\upsilon)+\xi\exp(-\xi\frac{\pi}{2})),\ \upsilon\in[0,\frac{\pi}{2}]. \tag{30}$$

Fig. 3 shows the influence of the parameter ξ on the spread in inhomogeneity orientations. If ξ = 0, all inhomogeneities are randomly oriented, so there is no preferential direction. As ξ increases, the orientations of the inhomogeneities tend to the given preferential direction.

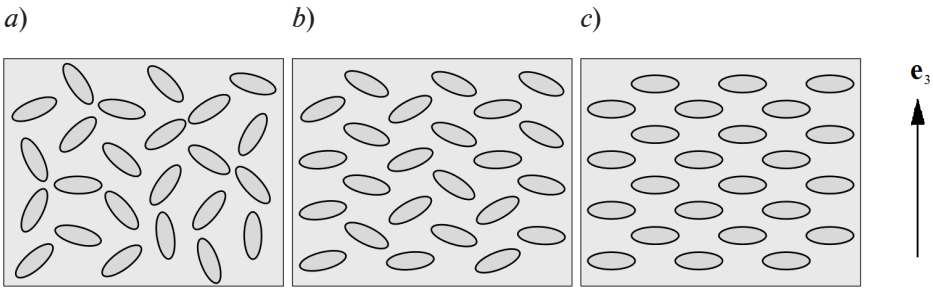

Fig. 3. Influence of parameter ξ on the spread in orientations of inhomogeneities relative to the predominant direction $\mathbf{e}_3$; **ξ = 0** (*a*), 7(*b*) 100 (*c*)

The orientation vector is given as follows in the spherical coordinate system:

$$\mathbf{n} = \cos(\theta)\sin(\upsilon)\mathbf{e}_1 + \sin(\theta)\sin(\upsilon)\mathbf{e}_2 + \cos(\upsilon)\mathbf{e}_3, \tag{31}$$

where $\mathbf{e}_1, \mathbf{e}_2, \mathbf{e}_3$ is the orthonormal basis; θ is the azimuthal angle in the spherical coordinate system.

The averaged tensor $\langle\mathbf{nn}\rangle$ accounting for the distribution function ψ_1 is calculated by the following formula:

$$\langle\mathbf{nn}\rangle = \int_0^{\pi}\int_0^{2\pi} \mathbf{nn}\psi_1(\upsilon,\xi)\sin(\varphi)d\theta d\upsilon. \tag{32}$$

As a result, we obtain the following expression for the dyad $\langle\mathbf{nn}\rangle$ (the preferred direction $\mathbf{e}_3$):

$$\langle\mathbf{nn}\rangle = \mathrm{N}_1\mathbf{e}_1\mathbf{e}_1 + \mathrm{N}_2\mathbf{e}_2\mathbf{e}_2 + \mathrm{N}_3\mathbf{e}_3\mathbf{e}_3. \tag{33}$$

The components of $\langle\mathbf{nn}\rangle$ take the following form:

$$\mathrm{N}_1 = \frac{1}{2\pi}\Big(\frac{6\pi}{\xi^2+9} - \frac{2\pi}{3(\xi^2+9)}\xi^2\exp(-\pi\xi)\Big), \tag{34}$$

$$\mathrm{N}_2 = \frac{1}{2\pi}\Big(\frac{6\pi}{\xi^2+9} - \frac{2\pi}{3(\xi^2+9)}\xi^2\exp(-\pi\xi)\Big), \tag{35}$$

$$\mathrm{N}_3 = \frac{1}{2\pi}\Big(\frac{6\pi}{\xi^2+9} + \frac{2\pi\xi^2}{\xi^2+9} + \frac{4\pi}{3(\xi^2+9)}\xi^2\exp(-\pi\xi)\Big). \tag{36}$$

In the case of the distribution function ψ_2, the tensor $\langle\mathbf{nn}\rangle$ is calculated from the formula

$$\langle\mathbf{nn}\rangle = \int_0^{\pi/2}\int_0^{2\pi} \mathbf{nn}\psi_2(\upsilon,\xi)\sin(\upsilon)d\theta d\upsilon. \tag{37}$$

The tensor $\langle\mathbf{nn}\rangle$ takes the form (33) but with different components:

$$\mathrm{N}_1 = \frac{1}{2\pi}\Big(\frac{1}{\xi^2+9}\Big(6\pi + 2\pi\xi\exp\Big(-\frac{\pi}{2}\xi\Big)\Big) - \frac{\pi}{3}\xi\exp\Big(-\frac{\pi}{2}\xi\Big)\Big), \tag{38}$$

$$\mathrm{N}_2 = \frac{1}{2\pi}\Big(\frac{1}{\xi^2+9}\Big(6\pi + 2\pi\xi\exp\Big(-\frac{\pi}{2}\xi\Big)\Big) - \frac{\pi}{3}\xi\exp\Big(-\frac{\pi}{2}\xi\Big)\Big), \tag{39}$$

$$\mathrm{N}_3 = \exp\Big(-\frac{\pi}{2}\xi\Big)\frac{\xi^2+3}{3(\xi^2+9)}\Big(\xi + 3\exp\Big(\frac{\pi}{2}\xi\Big)\Big). \tag{40}$$

The resulting expression for the tensor $\langle \mathbf{\Lambda} \rangle_c$ takes the following form:

$$\left\langle \mathbf{\Lambda} \right\rangle_c = \left\langle [s\mathbf{E} + \mathbf{P} \cdot (\mathbf{D}_1 - s\mathbf{D}_0)]^{-1} \right\rangle = A_1\mathbf{E} + A_2(\mathrm{N}_1\mathbf{e}_1\mathbf{e}_1 + \mathrm{N}_2\mathbf{e}_2\mathbf{e}_2 + \mathrm{N}_3\mathbf{e}_3\mathbf{e}_3). \quad (41)$$

The expression for $\mathbf{D}_{eff}$ (22) is converted to the following form taking into account Eq. (41):

$$\mathbf{D}_{eff} = D_0\mathbf{E} + (D_1 - sD_0)\varphi(B_1(\mathbf{e}_1\mathbf{e}_1 + \mathbf{e}_2\mathbf{e}_2) + B_2\mathbf{e}_3\mathbf{e}_3), \quad (42)$$

where the coefficients B_1 and B_2 follow the expressions:

$$B_1 = \frac{A_1 + A_2\mathrm{N}_1}{s\varphi(A_1 + A_2\mathrm{N}_1) + (1-\varphi)},$$

$$B_2 = \frac{A_1 + A_2\mathcal{N}_3}{s\varphi(A_1 + A_2\mathcal{N}_3) + (1-\varphi)}.$$

The constructed expression for the tensor of effective diffusion coefficients (42) is used for both models of polycrystalline material. The difference between the models is only in the numerical values of the microstructural parameters.

Results

Consider the components of the tensor $\mathbf{D}_{eff}$ as functions of various generalized microstructural parameters. The diffusion coefficient at the grain boundary is taken equal to $D_{gb} = 4\cdot10^{-2}$ m²/s, and the diffusion coefficient of the grain is taken equal to $D_{gr} = 9\cdot10^{-5}$ m²/s. The remaining microstructural parameters are given in the table above.

First, let us compare the influence of functions ψ_1 and ψ_2 (distributions of inhomogeneities by orientation) on the effective diffusion properties. The material is isotropic in the model M1, because the inhomogeneities are spherical, so the effective diffusion coefficients do not depend on the chosen distribution function. Fig. 4 shows the dependence for the components of the tensor $\mathbf{D}_{eff}$ on the scatter parameter ξ for model M2.

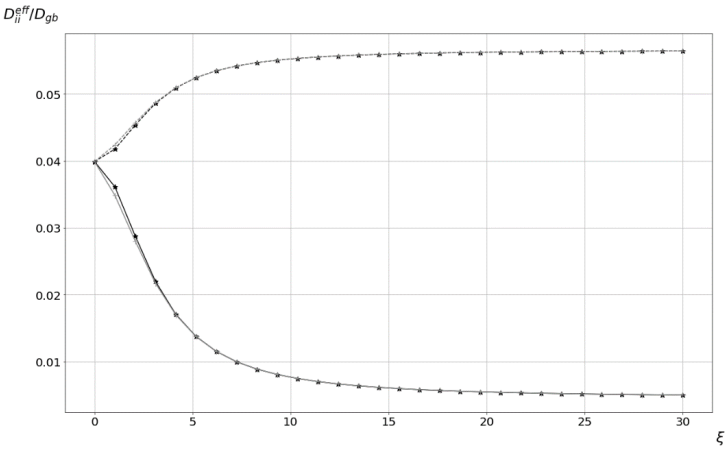

Fig. 4. Ratios D^{eff}_{11}/D_{gb} and D^{eff}_{33}/D_{gb} (components of the tensor $\mathbf{D}_{eff}$) as functions of the parameter ξ for the functions ψ_1 and ψ_2 (orientation distributions of inhomogeneities); model M2; $\gamma = 0.05$; $\varphi_{gr} = 0.5$; $s = 1$ (all 4 curves coincide)

The distribution functions ψ_1 and ψ_2 are found by Eqs. (29) and (30), respectively. Fig. 4 shows that the effective properties do not depend on the specific distribution function chosen to account for the spread in the orientation of the inhomogeneities. Next, we consider $\mathbf{D}_{eff}$ taking into account distribution function (29).

Notably, the chosen distribution function has no effect on the effective diffusion coefficients at $\xi = 0$, since this corresponds to the isotropic distribution of inhomogeneities. Suppose that the heterogeneities in the material are distributed isotropically ($\xi = 0$), so all components of the effective diffusion coefficient tensor $\mathbf{D}_{eff}$ are identical.

Fig. 5 shows the dependences of D^{eff}/D_{gb} on the grain volume fraction φ_{gr} for models M1 and M2. The dependences are plotted for volumes ranging from 0 to 1 to check whether the two models coincide in limiting cases at $s = 1$. The grain concentration φ_{gr} in real polycrystalline materials is close to unity.

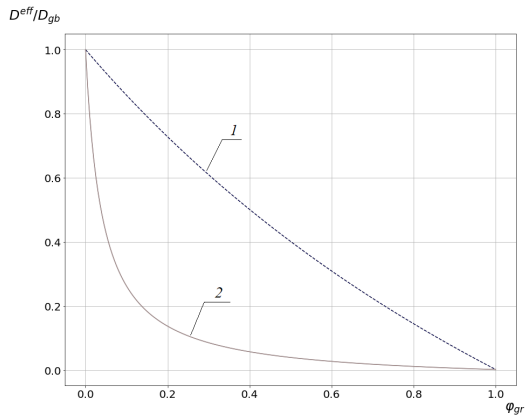

Fig. 5. Dependences of the ratio D^{eff}_{33}/D_{gb} (components of the tensor $\mathbf{D}_{eff}$) on the volume fraction of grains φ_{gr} for both models; $\gamma = 1.00$ for the model M1 (curve *1*) and $\gamma = 0.05$ for the model M2 (*2*); $s = 1.0$, $\xi = 0.0$

The two models coincide given the segregation parameter $s = 1$ at $\varphi_{gr} = 0$ and 1 (see Fig. 5). Furthermore, the behavior of the curves for models M1 and M2 is very different at any values of the volume fraction φ_{gr}, so the two models cannot be considered equivalent at the given values of parameters (see Table).

Fig. 6 shows the effect of the segregation parameter s on the effective diffusion coefficient at large volume fractions of the grains.

As evident from Fig. 6, variation in the segregation parameter has a more pronounced effect on the dependences for the model M2 than on those for the model M1. Both models show that the effective diffusion coefficient decreases with increasing segregation parameter. The segregation

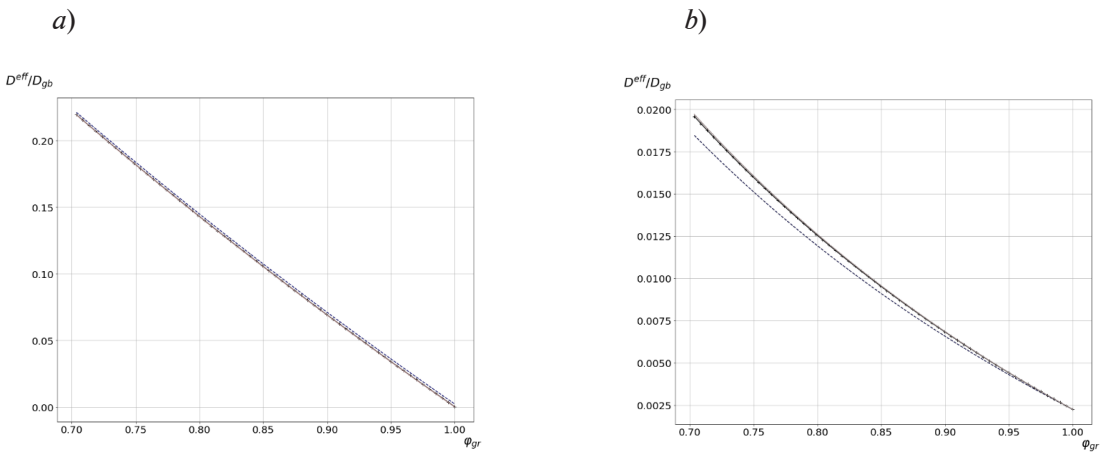

Fig. 6. Ratios D^{eff}_{33}/D_{gb} (components of the tensor $\mathbf{D}_{eff}$) as functions of the grain volume fraction φ_{gr} for models M1 (*a*) and M2 (*b*) at different values of the segregation parameter s: 1, 10, 100 (*a*) and 1, 0.1 and 0.01 (*b*);
curve $s = 1$ for M2 separated from the curves, which coincided; all curves coincided for M1

parameter has little influence on the effective diffusion coefficient in the model M1 at high concentrations of inhomogeneities.

Fig. 7 shows the dependence of D^{eff}_{33}/D_{gb} on the segregation parameter s with large volume fractions of grains (in the range from 95 to 99%). Evidently, the segregation parameter has little influence on the variation in the effective diffusion coefficient for both models, but a slight decrease in the diffusion coefficient is observed with increasing s.

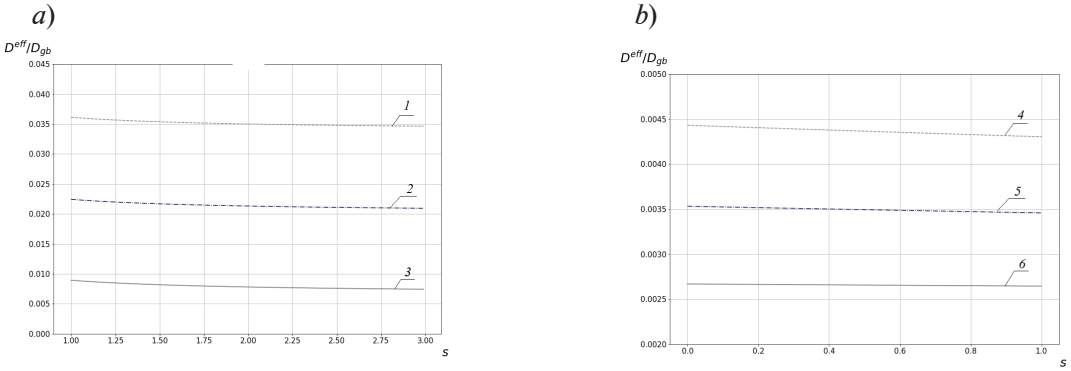

Fig. 7. Ratios D^{eff}_{33}/D_{gb} as functions of the segregation parameter s for models M1 (*a*) and M2 (*b*) at different values of the parameters γ and φ_{gr}; $\xi = 0{,}0$; $\gamma = 1.00$, $\varphi = 0.95$ (*1*), 0.97 (*2*), 0.99 (*3*) (*a*); $\gamma = 0.05$, $\varphi = 0.05$ (*4*), 0.03 (*5*), 0.01 (*6*) (*b*)

Verification of both models

This section compares the constructed mathematical models with the experimental data. Experimental data for the dependence of effective hydrogen diffusion coefficient in nickel on grain size d are given in [16].

The model M1 assumes spherical inhomogeneities to be grains with a diffusion coefficient $D_1 = 9\cdot10^{-14}$ m^2/s, and the grain boundary with $D_0 = 4\cdot10^{-10}$ m^2/s is taken as the matrix. The situation is reversed in the model M2: $D_0 = 9\cdot10^{-14}$ m^2/s, while $D_1 = 4\cdot10^{-10}$ m^2/s. The remaining microstructural parameters are given in the table.

The volume fraction of grain boundaries is calculated by the formula from [16]:

$$\varphi_{GB} = Ad^p,\ A = 8.138\cdot10^{-3},\ p = -0.636. \tag{43}$$

The volume fraction of grains is calculated by the following formula:

$$\varphi = 1 - \varphi_{GB} = 1 - Ad^p. \tag{44}$$

First we construct the dependence of D^{eff} on the grain size d for both models at $s = 1$.

It can be seen from Fig. 8 that the model M1 describes the experimental data fairly well. The approximation error of the experimental data is very large for the model M2, so only the model M1 is considered below.

Fig. 9 illustrates the influence of the segregation parameter s. Evidently, it is important that the segregation parameter is taken into account in the approximation of the effective diffusion coefficients. The best approximation of the experimental data is achieved at s values in the range from 1 to 2.

Thus, in practice, it is recommended to use the model M1 (matrix–grain boundaries, inhomogeneities–grains) rather than the model M2 (matrix–grains, inhomogeneities–grain boundaries) to approximate the diffusion coefficients of the polycrystalline material. We should note that a decrease in the values of effective diffusion coefficients is observed in the experimental data for grain sizes less than 0.1 μm, which can be associated with additional internal effects. It is established in [8] that the decrease in the value of the diffusion coefficient is due to an increase in the amount of solutes with a decrease in the grain size. Since this effect is not taken into account in the mathematical model of the material, both models also do not describe the effective diffusion properties for grain sizes less than 0.1 μm. Moreover, the segregation parameter does not significantly influence the effective diffusion coefficient in the case of spherical grains. The influence of the segregation parameter for spherical grains has not been investigated in this study; we plan to concentrate on this problem in our future research.

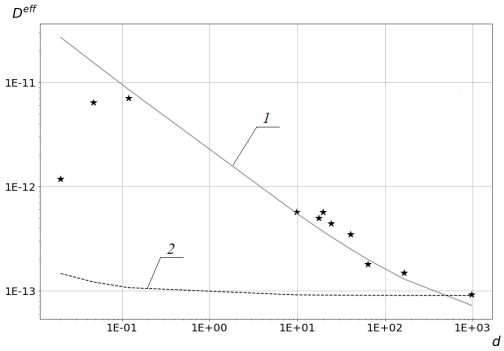

Fig. 8. Calculated (lines) and experimental (symbols) dependences of D^{eff} tensor components on d for models M1 (*1*) and M2 (*2*) at $s = 1$

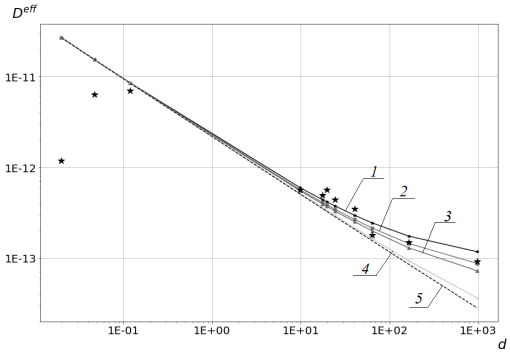

Fig. 9. Computational (lines) and experimental (symbols) dependences of the tensor component D^{eff} versus d for the model M1 at different s: 1.0 (*1*); 1.5 (*2*); 2.0 (*3*); 10 (*4*) and 100 (*5*)

Conclusion

The paper considers two approaches to describing polycrystalline material. The grains are simulated by inhomogeneities and the grain boundary by the matrix in the first case, and vice versa in the second case: the grain boundary is simulated by inhomogeneities, and the grains by the material matrix. The models used to approximate the effective diffusion coefficients of the polycrystalline material take into account the effect of segregation as well as the mutual effect of grains; the Mori–Tanaka scheme is applied. We have constructed an analytical approximation for the tensor of effective diffusion coefficients for the case of spheroidal inhomogeneities. We have verified the models using experimental data, establishing the importance of the segregation parameter for calculations of the effective diffusion coefficients.

REFERENCES

1. **Yakovlev Yu. A., Polyanskiy V. A., Sedova Yu. S., Belyaev A. K.,** Models of hydrogen influence on the mechanical properties of metals and alloys, PNRPU Mechanics Bulletin. (3) (2020) 136–160 (in Russian).

2. **Knyazeva A. G., Grabovetskaya G. P., Mishin I. P., Sevostianov I.** On the micromechanical modelling of the effective diffusion coefficient of a polycrystalline material, Phil. Mag. 95 (19) (2015) 2046–2066.

3. **Hart E. W.** Thermal conductivity, Acta Metallurgica. 5 (9) (1957) 597–605.

4. **Barrer R. M.,** Diffusion and permeation in heterogeneous media, In book: "Diffusion in polymers", Ed. by J. Crank and G. S. Park, Academic Press, London, 1968.

5. **Bell G. E., Crank J.** Influence of imbedded particles on steady-state diffusion, J. Chem. Soc. Farad. Trans. 70 (2) (1974) 1259–2732.

6. **Cussler E. L.,** Diffusion: mass transfer in fluid systems, Cambridge University Press, Cambridge, 2009.

7. **Zhang Y., Liu L.,** On diffusion in heterogeneous media, Am. J. Sci. 312 (9) (2012) 1028–1047.

8. **Belova I. V., Murch G. E.,** Diffusion in nanocrystalline materials, J. Phys. Chem. Solids. 64 (5) (2003) 873–878.

9. **Belova I. V., Murch G. E.,** The effective diffusivity in polycrystalline material in the presence of interphase boundaries, Phil. Mag. 84 (1) (2004) 17–28.

10. **Frolova K. P., Vilchevskaya E. N.,** Effective diffusivity of transversely isotropic material with embedded pores, Mater. Phys. & Mech. 47 (6) (2021) 937–950.

11. **Kachanov M., Sevostianov I.** Micromechanics of materials, with applications. Springer International Publishing AG (part of Springer Nature), Switzerland, 2018.

12. **Mori T., Tanaka K.** Average stress in matrix and average elastic energy of materials with misfitting inclusions, Acta Metallurgica. 21 (5) (1973) 571–574.

13. **Fricke H.,** A mathematical treatment of the electric conductivity and capacity of disperse systems. I. The electric conductivity of a suspension of homogeneous spheroids, Phys. Rev. 24 (5) (1924) 575–587.

14. **Sherman J., Morrison W. J.,** Adjustment of an inverse matrix corresponding to a change in one element of a given matrix, Ann. Math. Statistics. 21 (1) (1950) 124–127.

15. **Frolova K. P., Vilchevskaya E. N.,** Effective diffusion coefficient of a porous material applied to the problem of hydrogen damage, In book: “Advances in hydrogen embrittlement study”, Ed. by Polyanskiy V. A., Belyaev A. K., Book Ser. Advanced Structured Materials. Vol. 143, Springer International Publishing, Cham. (2021) 113–130.

16. **Oudris A., Creus J., Bouhattate J., et al.,** Grain size and grain-boundary effects on diffusion and trapping of hydrogen in pure nickel, Acta Materialia. 60 (19) (2012) 6814–6828.

СПИСОК ЛИТЕРАТУРЫ

1. **Яковлев Ю. А., Полянский В. А., Седова Ю. С., Беляев А. К.** Модели влияния водорода на механические свойства металлов и сплавов // Вестник Пермского национального исследовательского политехнического университета (ПНИПУ). Механика. 2020. № 3. С. 136–160.

2. **Knyazeva A. G., Grabovetskaya G. P., Mishin I. P., Sevostianov I.** On the micromechanical modelling of the effective diffusion coefficient of a polycrystalline material // Philosophical Magazine. 2015. Vol. 95. No. 19. Pp. 2046–2066.

3. **Hart E. W.** Thermal conductivity // Acta Metallurgica. 1957. Vol. 5. No. 9. Pp. 597–605.

4. **Barrer R. M.** Diffusion and permeation in heterogeneous media // Diffusion in polymers. Edited by J. Crank and G. S. Park. London: Academic Press, 1968. 259 p.

5. **Bell G. E., Crank J.** Influence of imbedded particles on steady-state diffusion // Journal of the Chemical Society, Faraday Transactions. 1974. Vol. 70. No. 2. Pp. 1259–2732.

6. **Cussler E. L.** Diffusion: mass transfer in fluid systems. Cambridge: Cambridge University Press, 2009. 631 p.

7. **Zhang Y., Liu L.** On diffusion in heterogeneous media // American Journal of Science. 2012. Vol. 312. No. 9. Pp. 1028–1047.

8. **Belova I. V., Murch G. E.** Diffusion in nanocrystalline materials // Journal of Physics and Chemistry of Solids. 2003. Vol. 64. No. 5. Pp. 873–878.

9. **Belova I. V., Murch G. E.** The effective diffusivity in polycrystalline material in the presence of interphase boundaries // Philosophical Magazine. 2004. Vol. 84. No. 1. Pp. 17–28.

10. **Frolova K. P., Vilchevskaya E. N.** Effective diffusivity of transversely isotropic material with embedded pores // Materials Physics and Mechanics. 2021. Vol. 47. No. 6. Pp. 937–950.

11. **Kachanov M., Sevostianov I.** Micromechanics of materials, with applications. Switzerland: Springer International Publishing AG (part of Springer Nature, 2018. 712 p.

12. **Mori T., Tanaka K.** Average stress in matrix and average elastic energy of materials with misfitting inclusions // Acta Metallurgica. 1973. Vol. 21. No. 5. Pp. 571–574.

13. **Fricke H.** A mathematical treatment of the electric conductivity and capacity of disperse systems. I. The electric conductivity of a suspension of homogeneous spheroids // Physical Review. 1924. Vol. 24. No. 5. Pp. 575–587.

14. **Sherman J., Morrison W. J.** Adjustment of an inverse matrix corresponding to a change in one element of a given matrix // The Annals of Mathematical Statistics. 1950. Vol. 21. No 1. Pp. 124–127.

15. **Frolova K. P., Vilchevskaya E. N.** Effective diffusion coefficient of a porous material applied to the problem of hydrogen damage // Advances in Hydrogen Embrittlement Study. Edited by Polyanskiy V. A., Belyaev A. K. Book Ser. Advanced Structured Materials. Vol. 143. Springer International Publishing, Cham., 2021. Pp. 113–130.

16. **Oudris A., Creus J., Bouhattate J., Conforto E., Berziou C., Savall C., Feaugas X.** Grain size and grain-boundary effects on diffusion and trapping of hydrogen in pure nickel // Acta Materialia. 2012. Vol. 60. No. 19. Pp. 6814–6828.

THE AUTHORS

PASHKOVSKY Dmitry M.
Peter the Great St. Petersburg Polytechnic University
29 Politechnicheskaya St., St. Petersburg, 195251, Russia
mr.vivivilka@icloud.com
ORCID: 0000-0002-2218-6649

FROLOVA Ksenia P.
Institute for Problems in Mechanical Engineering, RAS
61 Bolshoi Ave., V. Isl., St. Petersburg, 199178, Russia
kspfrolova@gmail.com
ORCID: 0000-0003-0376-4463

VILCHEVSKAYA Elena N.
Institute for Problems in Mechanical Engineering RAS
61 Bolshoi Ave., V. Isl., St. Petersburg, 199178, Russia
vilchevskaya_en@spbstu.ru
ORCID: 0000-0002-5173-3218

СВЕДЕНИЯ ОБ АВТОРАХ

ПАШКОВСКИЙ Дмитрий Максимович – *студент Физико-механического института Санкт-Петербургского политехнического университета Петра Великого.*
195251, Россия, г. Санкт-Петербург, Политехническая ул., 29
mr.vivivilka@icloud.com
ORCID: 0000-0002-2218-6649

ФРОЛОВА Ксения Петровна – *младший научный сотрудник Института проблем машиноведения РАН.*
199178, Россия, г. Санкт-Петербург, Большой проспект В. О., 61.
kspfrolova@gmail.com
ORCID: 0000-0003-0376-4463

ВИЛЬЧЕВСКАЯ Елена Никитична – *доктор физико-математических наук, ведущий научный сотрудник Института проблем машиноведения РАН.*
199178, Россия, г. Санкт-Петербург, Большой проспект В. О., 61.
vilchevskaya_en@spbstu.ru
ORCID: 0000-0002-5173-3218

Статья поступила в редакцию 08.04.2022. Одобрена после рецензирования 16.05.2022. Принята 16.05.2022.
Received 08.04.2022. Approved after reviewing 16.05.2022. Accepted 16.05.2022.

Original article
DOI: https://doi.org/10.18721/JPM.15313

INFLUENCE OF THE HYDROGEN SKIN EFFECT ON THE NATURE OF THE FRACTURE OF STEEL SPECIMENS

Yu. S. Sedova✉, *N. M. Bessonov*, *V. A. Polyanskiy*

Institute for Problems in Mechanical Engineering of the Russian Academy of Sciences,

St. Petersburg, Russia

✉ sedova.yus@mail.ru

Abstract. The influence of hydrogen saturation of steel specimens on the results of their standardized testing for resistance to hydrogen cracking has been carried out. The simulation took into account the hydrogen skin effect observed when metal samples being charged with hydrogen in various electrolyte solutions. The classical decohesion model of hydrogen embrittlement HEDE was used. It was shown that, despite the microscopic skin depth, the effect led to a dual fracture pattern, when the specimen's cross-sectional view exhibited both a hydrogen brittleness area and a normal destruction one. The comparison of calculated results with experimental ones showed the strong influence of the hydrogen skin layer on the results of standardized metal testing. This skin effect plays a significant role in the destruction propagation over a metal sample and should be taken into account when conducting industrial tests, simulations and experimental studies.

Keywords: hydrogen-induced cracking, decohesion, hydrogen charged sample, hydrogen diffusion, destruction

Funding: The reported study was funded by Russian Science Foundation (Project No. 18-19-00160)

Citation: Sedova Yu. S., Bessonov N. M., Polyanskiy V. A., Influence of the hydrogen skin effect on the nature of the fracture of steel specimens, St. Petersburg State Polytechnical University Journal. Physics and Mathematics, Vol. 15, No. 3. 169–184. DOI: https://doi.org/10.18721/JPM.15313

Научная статья
УДК 539.561
DOI: https://doi.org/10.18721/JPM.15313

ВЛИЯНИЕ ВОДОРОДНОГО СКИН-ЭФФЕКТА НА ХАРАКТЕР РАЗРУШЕНИЯ СТАЛЬНЫХ ОБРАЗЦОВ

Ю. С. Седова✉, *Н. М. Бессонов*, *В. А. Полянский*

Институт проблем машиноведения Российской академии наук,

Санкт-Петербург, Россия

✉ sedova.yus@mail.ru

Аннотация. Исследовано влияние насыщения водородом стальных образцов на результаты их стандартизованного тестирования на стойкость к водородному растрескиванию. При моделировании учтен водородный скин-эффект, который наблюдается при стандартизованном насыщении образцов водородом в различных растворах электролитов. Использована классическая декогезионная модель водородной хрупкости HEDE. Показано, что, несмотря на микроскопическую глубину скин-слоя, скин-эффект приводит к двойственному характеру разрушения, когда на изломе образца наблюдаются как площадки водородной хрупкости, так и области обычного разрушения. Сопоставление расчетных результатов с экспериментальными показало сильное влияние водородного скин-слоя на результаты стандартизованного тестирования металлов. Этот скин-эффект играет существенную роль в распространении процесса разрушения по металлическому образцу и должен приниматься во внимание при проведении промышленных испытаний, моделирования и экспериментальных исследований.

Ключевые слова: водородный скин-эффект, индуцированное растрескивание, декогезия, насыщение водородом, диффузия водорода

Финансирование: Исследование выполнено при финансовой поддержке гранта Российского научного фонда (проект №00160-19-18).

Ссылка для цитирования: Седова Ю. С., Бессонов Н. М., Полянский В. А. Влияние водородного скин-эффекта на характер разрушения стальных образцов // Научно-технические ведомости СПбГПУ. Физико-математические науки. 2022. Т. 15. № 3. С. 169–184. DOI: https://doi.org/10.18721/JPM.15313

Introduction

The so-called metallurgical dissolved hydrogen accumulates in metals and metal products during the manufacturing process. It negatively affects all mechanical and technological characteristics of metals, is one of the main causes of embrittlement, porosity and flaking in rolled products. Production facilities introduce different measures for monitoring the concentration of metallurgical hydrogen. It is maintained at a level of about $1{,}000{,}000^{-1}$ or less in steels and aluminum alloys.

The second source of dissolved hydrogen is an aggressive external environment to which metal parts are exposed during operation. Any corrosion process is accompanied by release of hydrogen and its absorption inside the metal. External mechanical loads and the presence of pure hydrogen in the environment can considerably accelerate hydrogen degradation of metal properties.

A system for standardized testing for resistance to hydrogen-induced cracking (HIC) has been developed and implemented in the manufacturing industry over the recent decades [1–3]. Typically, the procedure consists of an exposure phase (hydrogen saturation) of metal specimens

in a corrosive environment that lasts up to 100 h. The second phase consists of mechanical tests and microscopic studies of the specimens: the surfaces of fractures and cracks induced by hydrogen are recorded.

These tests allow to achieve high resistance to HIC in modern pipe steels. While hydrogen-induced cracks tended to evolve inside steel specimens tested by the procedures developed in the 1970s [4], modern steels are characterized by only minor microcracking. At the same time, the mechanical characteristics of the specimens considerably deteriorate after saturation with hydrogen, and high-strength steels are characterized by a proportional decrease in crack resistance [5, 6]. Numerous fractographic studies [7–10], carried out experimentally for steels fractured during mechanical tests, indicate the presence of two characteristic fracture regions: brittle and ductile. Modern alloys are widely used in various fields of energy and manufacturing industries. Therefore, the effect of their rapid degradation upon saturation with hydrogen should be investigated and mitigated.

The mean partial concentration of hydrogen atoms to matrix atoms in the metal increases to no more than 1:30,000 during HIC testing [11]. Furthermore, recent studies have observed a skin effect of hydrogen saturation in aqueous corrosive solutions during cathodic polarization, where all hydrogen absorbed by the metal is concentrated in a thin surface layer of specimens about 50–100 μm thick [12–15]. If the working diameter of the specimen is 8–10 mm, this layer can be attributed to layers with small thickness (the ratio of 1:100 is typical for theory of thin shells). Thus, from a mechanical perspective, we are dealing with a problem on the influence of a small parameter.

To date, several approaches have been proposed to describe hydrogen-induced degradation.

One of the first models was Hydrogen-Enhanced Decohesion (HEDE) [16]. It describes brittle fracture resulting from accumulation of hydrogen at the crack tip and development of hydrogen embrittlement without plastic deformations. At the microscopic level, the approach is based on the idea that interstitial hydrogen expands the metal lattice of crystals, thus contributing to a decrease in the adhesion strength of atoms [17]. From the standpoint of energy, hydrogen atoms lower the energy barrier for fracture, which leads to segregation of grains, or decohesion.

A fundamentally different approach to modeling hydrogen degradation of the mechanical properties of materials is taken within the model of hydrogen-enhanced localized plasticity (HELP) [18, 19]. Hydrogen dissolved in the metal is interpreted within this model as a chemical that reduces the energy required to initiate dislocations. It is assumed that ‘softening’ of the metal, or localized plasticity, is observed at the tip of the crack, where hydrogen is concentrated under the action of internal stresses.

The dual nature of the fracture observed in HIC testing is commonly interpreted by using a combination of both models: HELP + HEDE. Brittle HEDE mechanism is assumed to work if the local hydrogen concentrations in the tip of the crack are above a certain ‘switching threshold’, and HELP is assumed to apply for concentrations below the threshold one. One of the problems of this approach is the exponential increase (up to 100 times) in hydrogen concentration during plastic deformation, which directly follows from the equations of the HELP model [20]. Thus, if the models are sequentially ‘combined’, the localized plastic deformation induced by hydrogen should lead to a manifold increase in its local concentration, triggering a mechanism of brittle decohesion for the fracture.

In addition, the HELP model essentially describes an increase in ductility due to a decrease in the yield strength of the material. However, the bulk of the experimental evidence does not suggest a decrease in the yield point during specimen testing [6]. All of this indicates that existing experimental and theoretical data contradict the hypothesis that the HELP model is initiated, determining the principal fracture surface.

These HELP + HEDE paradoxes allow us to settle on a decohesion model of hydrogen cracking.

Description of the model

The modern concept of the HEDE-model comprises the following key elements:

equations of elastic or viscoelastic solid medium with hardening (in particular, for materials with hardening);

equations of diffusion describing the redistribution and accumulation of hydrogen;

dependences describing hydrogen degradation of cohesive parameters.

Hydrogen transport within a solid has been traditionally understood as a diffusive process, and the equation of Fick's second law [21] was used to describe it:

$$\frac{\partial C}{\partial t} = \nabla \cdot \left[D(T, \mathbf{r}) \nabla C \right], \tag{1}$$

where C is the hydrogen concentration, t is the time, $\mathbf{r}$ is the coordinate vector, D is the diffusion coefficient, T is the absolute temperature, ∇ is the nabla operator.

However, modern approaches typically introduce components accounting for the thermodynamic or chemical potential [22]:

$$\mu = \mu_0(T) + RT \ln C - V_H p.$$

In this case, Eq. (1) takes the form

$$\frac{\partial C}{\partial t} = \nabla \cdot \left[D(T, \mathbf{r}) \left(\nabla C - \frac{C V_H}{RT} \nabla p \right) \right], \tag{2}$$

and the following form accounting for the effect of mechanical stresses:

$$\frac{\partial C}{\partial t} = D \nabla^2 C - \frac{D V_H}{RT} \nabla C \cdot \nabla p - \frac{D C V_H}{RT} \nabla^2 p, \tag{3}$$

where p is the pressure in spherical stress tensor, V_H is the partial molar volume of hydrogen [23].

According to Gorsky's law [24], hydrogen tends to migrate to regions of maximum tensile stresses. An increase in its concentration in these regions unavoidably lowers the cohesion of the crack edges, which is what leads to decohesion [16]. The model characterizes this phenomenon by introducing the parameter θ for the degree to which the free surface of crack edges is filled with hydrogen atoms:

$$\theta = \frac{C}{C + \exp\left(-\frac{\Delta g_H}{RT} \right)}, \tag{4}$$

where Δg_H is the difference in Gibbs free energy for hydrogen between the state adsorbed inside the crystal lattice and the free state (established experimentally).

This expression was proposed by Serebrinsky [24] based on the thermodynamic relationship for the partial molar volume of hydrogen inside and on the surface of a single crystal, obtained by McLean [25].

Notably, if the partial volume of impurity is used in this relationship, accounting for the value of C (10^{-6}), expression (4) takes the form:

$$\theta = \frac{55.85 \cdot C \cdot 10^{-6}}{55.85 \cdot C \cdot 10^{-6} + \exp\left(-\frac{\Delta g_H}{RT} \right)}. \tag{5}$$

The value of the parameter θ allows calculating the specific energy $\gamma(\theta)$ of the free surface, depending on the sorption of hydrogen on it. Most existing studies use the formula proposed by Serebrinsky to describe this relationship [25]:

$$\gamma(\theta) = \left(1 - 1.0467\theta + 0.1687\theta^2 \right) \gamma(0), \tag{6}$$

where $\gamma(0)$ is the surface energy in the absence of hydrogen.

Next, the brittle fracture model takes into account the identity for energy

$$G = 2\gamma(\theta) = f(\sigma_{Zc}, \delta_c), \tag{7}$$

where G is the fracture energy; $f(\sigma_{Zc},\delta_c)$ is a linear function depending on the maximum cohesive stresses σ_{Zc} normal to the crack edges, and on the maximum relative displacements δ_c of the crack edges at which the bonds between them do not break (or decohesion does not occur).

The form of the function $f(\sigma_{Zc},\delta_c)$ is determined by the cohesive law.

Assuming the value of δ_c to weakly depend on the value of θ, the HEDE-model introduces the law of hydrogen degradation:

$$\sigma_{Zc}(\theta) = \left(1 - 1.0467\theta + 0.1687\theta^2\right)\sigma_Z(0), \tag{8}$$

where $\sigma_Z(0)$ are cohesive stresses, normal to the crack edges acting in the absence of hydrogen.

According to the criterion for initiation and propagation of the crack by the HEDE mechanism, the crack preserves its configuration as long as the level of elastic stresses normal to its edges and acting near the tip of the crack does not exceed the cohesive stresses bridging the crack. As soon as the hydrogen accumulated at the tip of the crack under the action of chemical potential reduces these stresses so that this condition is violated, the crack starts to grow, with a new free surface forming. On the other hand, this cracking produces a local increase in the level of normal stresses in the new position of the crack tip, in turn leading to an increase in the local hydrogen concentration. The cohesive stresses once more decrease to a value violating the condition for crack stability, and the process is repeated again and again.

On the other hand, the energy required for fracture can be expressed in terms of material parameters. For a crack opening normally, it can be written as

$$G = \frac{K_{Ic}^2}{\hat{E}}, \tag{9}$$

where K_{Ic} is the critical stress intensity factor acting in the vicinity of the crack tip; the quantity $K = E(1 - \nu^2)$ is either $K = E$ for the cases of plane stress or plane strain state, respectively (E is Young's modulus, ν is Poisson's ratio).

In view of identity (7), we can prove that a decrease in the specific energy of the free surface due to an increase in the hydrogen concentration also leads to a decrease in K_{Ic}:

$$\frac{K_{Ic}^2}{K_{Ic}^2(0)} = \frac{\gamma(\theta)}{\gamma(0)} = 1 - 1.0467\theta + 0.1687\theta^2.$$

Thus, the magnitude of the critical stress intensity factor (the parameter characterizing the crack resistance of the material) depends on the hydrogen concentration as

$$K_{Ic}(\theta) = \sqrt{1 - 1.0467\theta + 0.1687\theta^2}\, K_{Ic}(0), \tag{10}$$

where $K_{Ic}(0)$ is the experimentally established value of crack resistance in the material in the absence of hydrogen.

It follows that the presence of hydrogen dissolved in the material modifies the force criterion of Irvine fracture ($K_I = K_{Ic}$) [27, 28], so cracking becomes possible at a lower value of K_I.

Problem statement

We consider a problem on uniaxial stretching of a cylindrical rod with an elliptical notch, saturated with hydrogen. We refrained from using standard finite element packages with in-built modules for cohesive zone modeling and crack propagation, since specialized fictitious cohesive elements have to be introduced in them following a particular cohesive law. This means that a large number of additional model parameters have to be introduced and several additional assumptions have to be adopted.

The model was implemented with the C++ code developed in Microsoft Visual Studio, allowing to obtain numerical solutions to problems on the stress-strain state of bodies using the finite volume method.

The procedure comprised two consecutive stages.

Stage 1. The problem on the stress-strain state in a pre-stretched specimen is solved.

Stage 2. The diffusion problem on the redistribution of hydrogen along the rod is solved.

As part of the second stage, the cohesive stresses σ_{Zc} and the crack resistance parameter K_{Ic} were also calculated.

A system of equations (11)–(13) from linear elasticity theory was solved at the first stage of the problem. The system includes a differential equilibrium equation (11), equation for the linear strain tensor (12) and generalized Hooke's law (13):

$$\begin{cases} \nabla \cdot \boldsymbol{\sigma} + \mathbf{f} = 0, & (11) \\ \boldsymbol{\varepsilon} = \frac{1}{2}\left(\nabla \mathbf{u} + \mathbf{u}\nabla\right), & (12) \\ \boldsymbol{\sigma} = \lambda\theta\mathbf{E} + 2G\boldsymbol{\varepsilon}, & (13) \end{cases}$$

where $\boldsymbol{\sigma}$ is the Cauchy stress tensor; $\mathbf{f}$ is the body force intensity; $\mathbf{u}$ is the displacement vector; λ, G are the Lamé parameters; $\theta = \mathrm{tr}(\varepsilon)$ is the relative volume change for the hydrostatic pressure $p = 1/3\mathrm{tr}(\sigma)$.

A method proposed by Wilkins [28] was used to numerically solve Eq. (11).

The characteristics of the stress-strain state of the specimen obtained in the first step of the technique were recorded in the second stage. Eqs. (3), (5), (8) and (10) that we described earlier were solved.

$$\begin{cases} \dfrac{\partial C}{\partial t} = D\nabla^2 C - \dfrac{DV_H}{RT}\nabla C \cdot \nabla p - \dfrac{DCV_H}{RT}\nabla^2 p \\ \theta = \dfrac{55.85 \cdot C \cdot 10^{-6}}{55.85 \cdot C \cdot 10^{-6} + \exp\left(-\dfrac{\Delta g_H}{RT}\right)} \\ \sigma_{Zc}(\theta) = \left(1 - 1.0467\theta + 0.1687\theta^2\right)\sigma_Z(0) \\ K_{Ic}(\theta) = \sqrt{1 - 1.0467\theta + 0.1687\theta^2}\, K_{Ic}(0). \end{cases}$$

Eq. (3) was also numerically solved based on Wilkins's determination method [29].

The instantaneous SIF in the vicinity of the crack tip was calculated from the approximate Benthem–Koiter formula [30, 31], obtained for the case of a crack with the length c initiating in an edge notch in a cylindrical rod with the diameter D under the action of uniaxial tension σ^{∞}_{z}:

$$\sigma_{net} = \sigma_Z^{\infty}\left(\frac{D}{d}\right)^2. \quad (14)$$

The conditions for cracking were found based on the results obtained in the second stage by the criterion for cohesive stresses or the Irwin force criterion for fracture.

We selected the model relying on the experimental data to be able to compare and evaluate the results obtained by the finite-volume solution. We were guided by a recently published study [8], investigating the effect of hydrogen on the properties of chromoly steel. The article considers a specimen of 2.25Cr1Mo ferritic steel shaped as a cylindrical rod 9.0 mm in diameter with a radial notch 2.0 mm deep, 1.2 mm wide and with a rounding radius of 0.15 mm.

Fractographic images of the fracture surface obtained after tensile tests of the specimen pre-saturated with hydrogen by cathodic polarization revealed a circular region of brittle fracture w up to 1 mm wide and an internal region of ductile fracture.

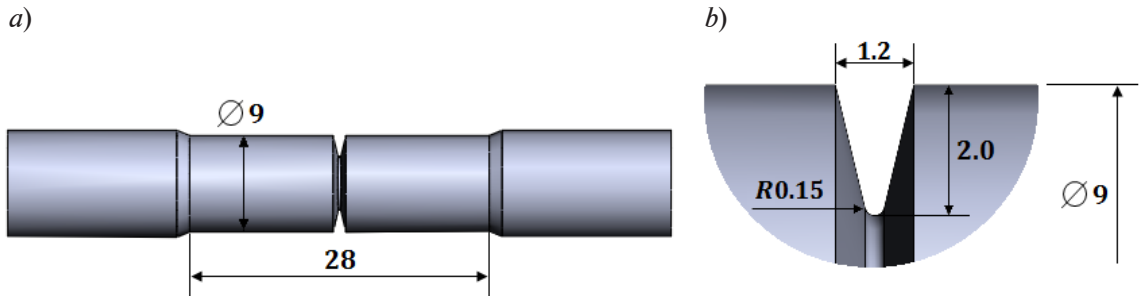

Fig. 1. Image of cylindrical steel specimen with radial notch (*a*) and its half cross-section at the notch root (*b*) (dimensions are given in mm)

We considered uniaxial tension of a cylindrical rod of the same geometry (Fig. 1), made of the same steel (the tensile load was 650 MPa). The computations were carried out in a two-dimensional axisymmetric formulation. By virtue of symmetry, the geometry of the modeled specimen was a quarter of the longitudinal section of the bar (Fig. 2).

The following properties of the 2.25Cr1Mo steel were used in the computations:

Physical properties of 2.25Cr1Mo steel

Yield strength σ_B	895 MPa
Flow stress σ_T	761 MPa
Density ρ	7,750 kg/m^3
Shear modulus μ	80 GPa
Poisson's ratio ν	0.3
Bulk modulus of elasticity K	140 GPa
Fracture toughness $K_{Ic}(0)$	64.1 MPa·m$^{1/2}$

Let us also give the values of the remaining computational parameters. The diffusivity was assumed to be constant, amounting to $D = 2\cdot10^{-11}$ m^2/s; the partial molar volume of hydrogen $V_H = 2\cdot10^{-6}$ m^3/mol [32]; the difference in Gibbs free energies for the state of hydrogen adsorbed inside the crystal lattice and its free state was $\Delta g_H = 30$ kJ/mol [32], the absolute temperature $T = 298$ K. The magnitude of the stresses included in Eq. (8), taking into account the recommendations from [33], was assumed to be $\sigma_z(0) = 30\ \sigma T$.

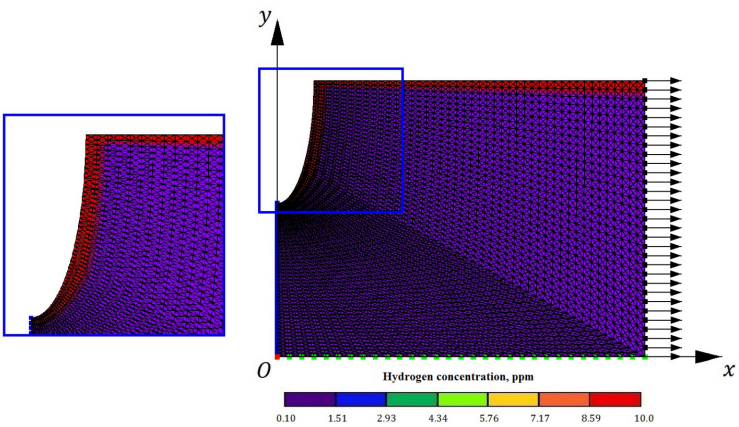

Fig. 2. Computational finite-volume model for a quarter of longitudinal section of the bar (see Fig. 1,*a*); geometry, boundary and initial conditions are shown the arrows indicate the direction of extension

The initial distribution of hydrogen over the specimen was established as follows: uniform background concentration $\tilde{c}_0 = 0.1 \cdot 10^{-6}$ throughout the region and the concentration $c_0 = 10 \cdot 10^{-6}$ in the surface layer with a thickness of one structural element ($t = 20$ μm). The latter characterizes the experimentally observed hydrogen concentration in metal specimens, accumulating on the surface. (hydrogen saturation due to the skin effect), see enlarged fragment in Fig. 2.

By virtue of symmetry, displacement along the horizontal axis *Ox* is prohibited for the left face, and displacement along the vertical axis *Oy* for the bottom face. A tensile stress σ acting along the axis *Ox* was applied to the right edge of the region.

The initiation and propagation of the crack was modeled as follows. After the characteristics of the body's stress-strain state are obtained, analysis of the diffusion problem on the redistribution of hydrogen over the specimen was performed at the second stage of the computational technique. The behavior of two inequalities was monitored in the analysis: $\sigma_{el} < \sigma_{Zc}(\theta)$ for stresses and $K_I < K_{Ic}(\theta)$ for SIFs at the nodes of the finite-volume mesh along the hypothetical line of crack propagation line (along the left face of the region). As soon as one of these inequalities was violated in the node due to an increase in hydrogen concentration or an increase in the level of elastic stresses, the restriction on displacements along the horizontal axis *Ox* was removed in this node, reproducing a broken bond with the node at the opposite edge of the crack. The node could then move freely under the applied load.

Results of finite-element modeling

Fig. 3 shows the dependence for the time range between the instants when the fracture criterion is satisfied in two consecutive nodes of the finite volume model. This is a time range necessary for hydrogen to redistribute under the influence of elastic stresses and subsequently accumulate in the given node, with the resulting decrease in cohesive stresses σ(θ) or the crack resistance parameter of the material $K_{Ic}(\theta)$.

It is evident from Fig. 3 that the criterion for bond breakage by the decohesion mechanism is instantly fulfilled in the first two nodes of the mesh. This is due to high content of hydrogen in the surface layer of the specimen, so the cohesive stresses bridging the nodes of the material are greatly reduced as a result, and fracture by the HEDE mechanism occurs at the first time step of the problem solution. The distributions of the components of elastic stresses acting along the horizontal axis and the hydrogen content in the vicinity of the crack tip at different times are shown in Figs. 4 and 5, respectively.

However, the time for diffusion increases with distance from the specimen surface, with the process reflected accordingly in the solution of the diffusion problem. A certain amount of time has to pass for hydrogen to be redistributed, diffused and accumulated in the current crack tip until the facture criterion is satisfied. For this reason, the dependence is shown by an increasing segment starting from the third node (see Figs. 4,*b* and 5,*b*), but the propagation of the crack still follows a HEDE fracture mechanism.

This scenario continues until the sixth node of the mesh. After that, elastic stresses (see Fig. 4,*c*) acting near the stress concentrator start to exert a considerable effect. Their values gradually increase, so it is sufficient to decrease the cohesive stresses initiated by hydrogen to a smaller degree to trigger the decohesion mechanism (see Fig. 5,*c*). Consequently, an ever shorter time is required to solve the diffusion problem.

Notably, the value of the crack resistance parameter also decreases substantially at this stage of monitoring due to the presence of hydrogen in the material, but it still turns out to be higher than the value of the SIF acting near the crack tip.

As seen from Fig. 3, the decreasing trend in the critical hydrogen concentration at which decohesion occurs continues with distance from the specimen surface. At the same time, the magnitude of elastic stresses acting at the tip of the crack becomes so large at a distance of about 0.97 mm (corresponding to the seventeenth node of the mesh) that the crack can propagate further even at a background value of hydrogen content.

After that, the crack extends to a considerable size, so that the SIF reaches a high value near its tip, immediately exceeding the crack resistance of the material (also reduced by the presence of hydrogen in the bar) in the next node, with fracture propagating by only 1.0 mm (see Fig. 4,*d* and 5,*d*). Evidently, as the crack grows further, the level of the active stresses only increases. This explains the observed continuous propagation of the main crack after switching of the fracture mechanism, which happens after the force criterion for fracture is satisfied.

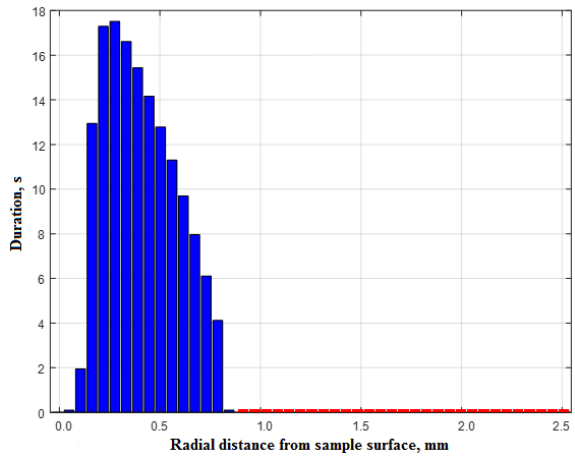

Fig. 3. Time required for the crack to propagate over 1 mesh spacing as a function of distance from the specimen surface
decohesion mechanism and crack resistance are shown in blue and red, respectively

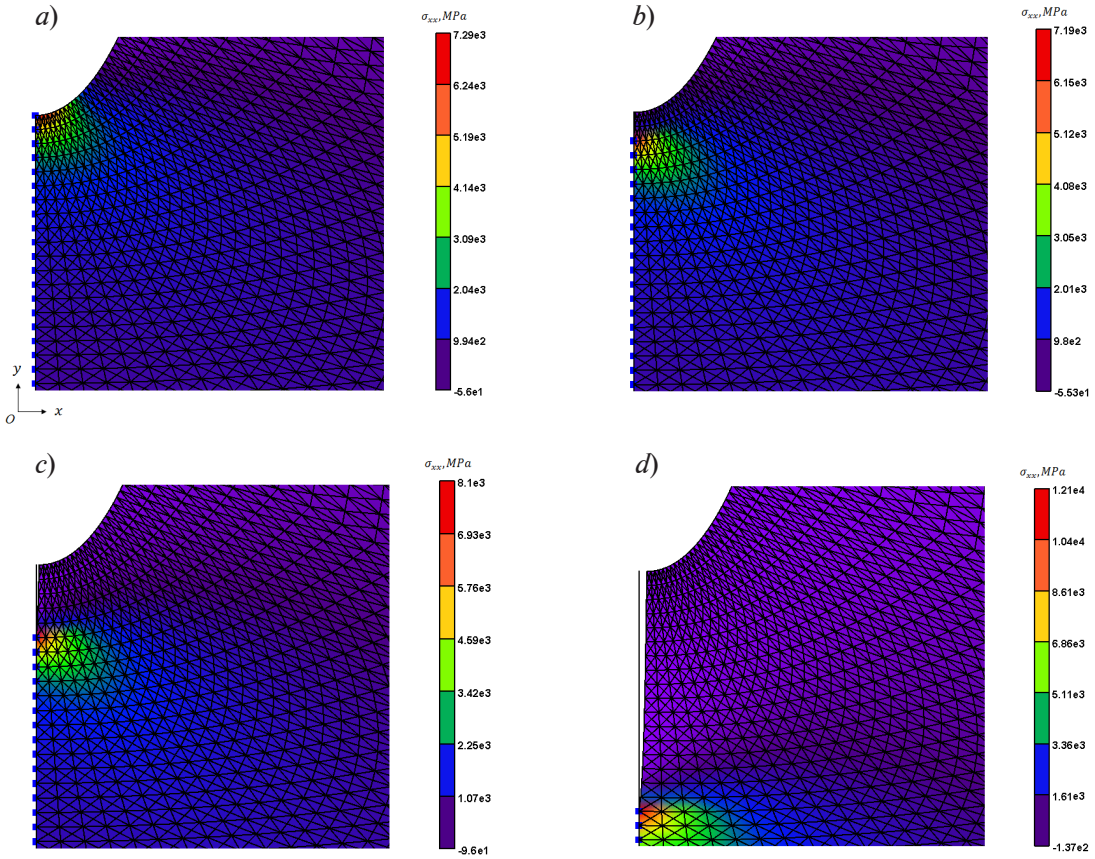

Fig. 4. Distributions of elastic stress components (MPa) acting in the horizontal direction at different time instants when decohesion is observed in the first (*a*), third (*b*), sixth (*c*) mesh nodes; switching of fracture mechanism (*d*)

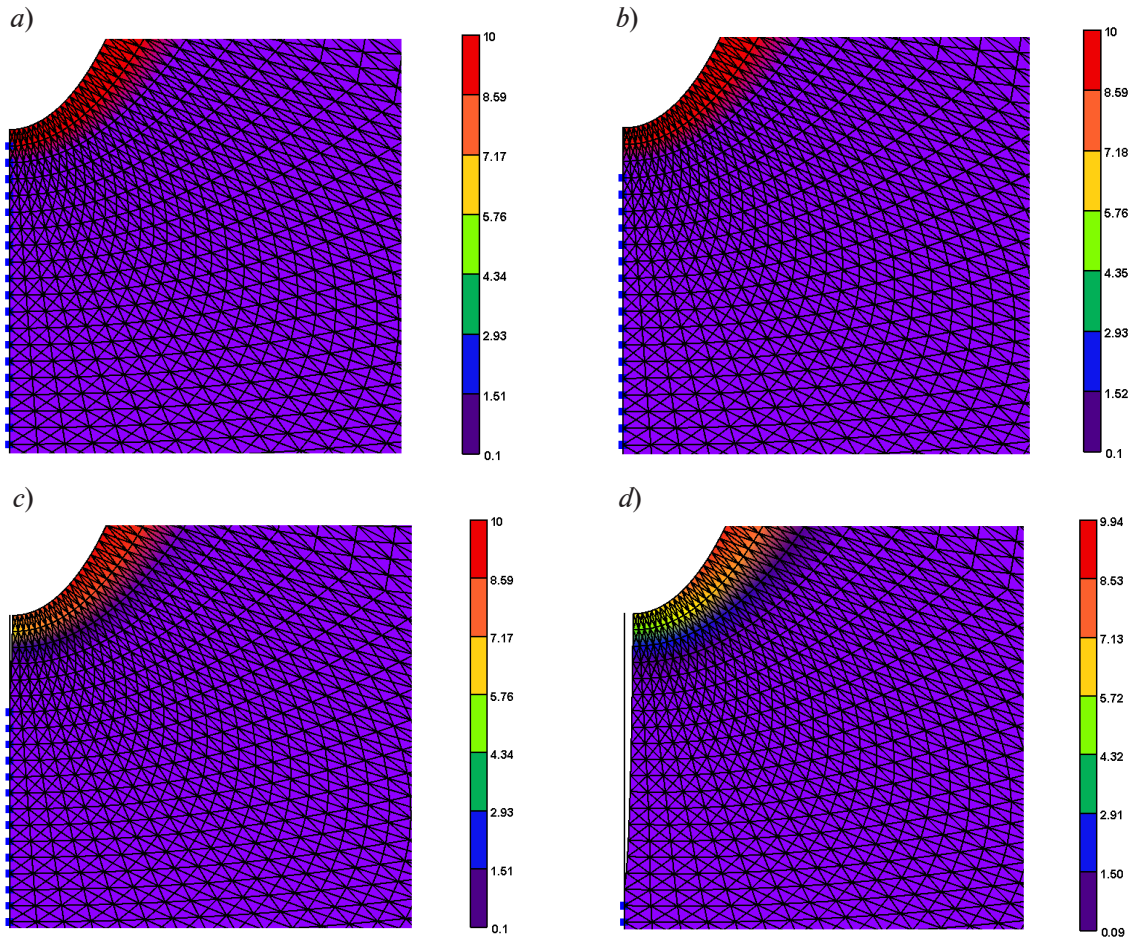

Fig. 5. Distribution of hydrogen concentration (10^{-6}) at the same instants as in Fig. 4

Fig. 6 shows the distribution of hydrogen concentration over the sample radius at crucial moments characterizing the evolution of the process from the initial state to propagation of the crack to half the specimen thickness. Apparently, as the crack propagates, hydrogen gradually redistributes from the surface of the specimen and moves deep into the material under the action of the chemical potential of the applied stresses. Importantly however, the penetration depth does not exceed 1 mm, because further fracture of steel occurs at the initial background hydrogen content, due to high stresses near the crack tip.

Thus, simulating the process allowed detecting and tracking the mechanism relating the saturation of specimens with hydrogen and the nature of fracture in the metal alloy under load (skin effect).

Results and discussion

Let us consider the finite-volume solution of the equations from the classical HEDE model for brittle fracture accounting for the skin effect of hydrogen saturation of the specimens. We adopt the approach of linear cracking theory and a classical model of hydrogen embrittlement. The computational results indicate that fracture follows the brittle decohesion mechanism at first, due to the high concentration of hydrogen in the surface layer. Hydrogen diffuses under the action of both the concentration gradient and the chemical potential along the crack propagation line, but its concentration in the moving crack tip drops to background values due to the slow progress of the diffusion process. At the same time, the balance between the length of the crack induced by hydrogen and the load level is important, since the crack can grow further after reaching a certain critical length with the background concentration of hydrogenby the standard cracking mechanism.

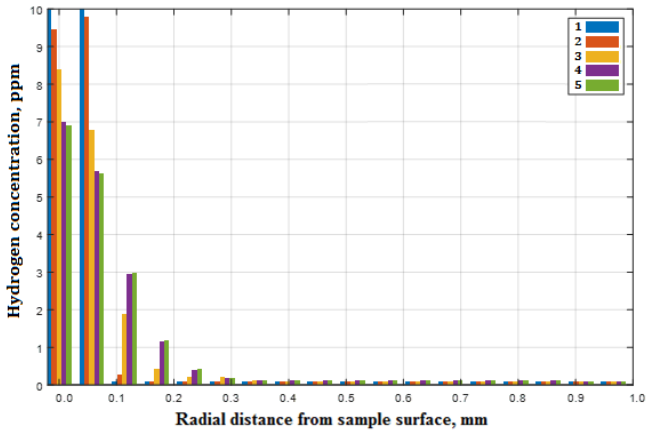

Fig. 6. Distribution of hydrogen concentration over the specimen radius (from the surface to the central axis) at crucial moments in the process: initial state (*1*), decohesion in the 3rd (*2*) and 6th (*3*) mesh nodes, switching of fracture mechanism (*4*) and crack extending to half the specimen thickness (*5*)

The images showing the regions with the distribution of hydrogen over the rod cross-section (Fig. 7) present a clear illustration for the evolution of the given process. Brittle fracture associated with increased hydrogen concentration is observed along the crack edges; sites of hydrogen embrittlement are detected in this region. Normal fracture occurs in the central part of the specimen, in accordance with the cracking theory.

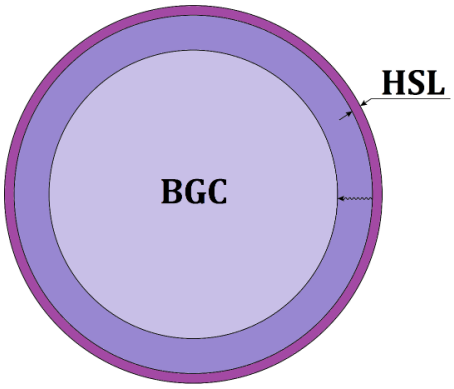

Fig. 7. Schematic representation of hydrogen redistribution regions within the specimen: HSL is the hydrogen skin layer; BHC is the normal (background) hydrogen concentration. The arrow indicates the direction of hydrogen diffusion during crack growth

The simulation results quantitatively and qualitatively agree with the experimental data presented in [8, 34]. The region of hydrogen-induced brittle fracture was 1 mm wide. We carried out computations varying the skin layer thickness, hydrogen concentration and the magnitude of the applied load. The results indicate that this thickness depends only on the level of load applied to the specimen (or the extension rate of the specimen): the larger it is, the smaller the hydrogen embrittlement region. This is qualitatively consistent with the experimental data [35].

Thus, the classical models we used allow describing the critical influence of the skin effect region (a small parameter) with a small volume on the fracture of specimens, relating the experimentally observed dual nature of the fracture in the specimens with the procedure used to saturate them with hydrogen. Our findings can serve to explain the differences between the results for testing steel specimens and for operation of parts and assemblies manufactured from the same steels in aggressive environments.

Conclusion

We have carried out finite-volume simulation for fracture in a cylindrical dumbbell-shaped steel specimen with an elliptical cutout saturated with hydrogen. The mechanism of hydrogen-enhanced decohesion (HEDE) was used as a model of hydrogen embrittlement. The skin effect from saturating the specimens with hydrogen, established experimentally, was taken into account.

The computational results indicate that fracture begins at the surface of the specimen as brittle, initiated by hydrogen. A crack then appears, and, as it reaches a certain length, continues to propagate naturally with typical background values of hydrogen concentration. This change in the nature of fracture produces a dual picture: regions of both hydrogen embrittlement and standard fracture are observed in the specimen cross-section.

Moreover, the simulations revealed that the skin effect in the distribution of hydrogen concentration may be the main reason behind the dual behavior of fracture; on the other hand, the general consensus is that this duality can be attributed to the simultaneously evolving HELP and HEDE mechanisms at the tip of the main crack.

The skin effect from hydrogen charging has a major influence on fracture of metal specimens despite its small depth, so it should definitely be taken into consideration in industrial tests, experimental studies, theoretical analysis, and simulation.

REFERENCES

1. ISO11114-4. Transportable gas cylinders – compatibility of cylinder and valve materials with gas contents – part 4: Test methods for selecting metallic materials resistant to hydrogen embrittlement. ISO 11114-4:2017 International Organization for Standardization, (2017). URL: https://www.iso.org/standard/64587.html (Date of the last access: 12.03.2022).

2. ISO16573. Steel-measurement method for the evaluation of hydrogen embrittlement resistance of high strength steels. ISO 16573:2015 International Organization for Standardization, (2015). URL: https://www.iso.org/standard/57128.html (Date of the last access: 12.03.2022).

3. ISO17081. Method of measurement of hydrogen permeation and determination of hydrogen uptake and transport in metals by an electrochemical technique. ISO 17081:2014 International Organization for Standardization (2014). URL: https://www.iso.org/standard/64514.html (Date of the last access: 12.03.2022).

4. **Giuliani L., Mirabile M., Sarracino M.,** Embrittlement kinetics of N 80 steel in H_2S environment, Metall. Mater. Trans. B. 5 (9) (1974) 2069–2073.

5. **Nagumo M., Yoshida H., Shimomura Y., Kadokura T.,** Ductile crack growth resistance in hydrogen-charged steels, Mater. Trans. 42 (1) (2001) 132–137.

6. **Koyama M., Tasan C. C., Tsuzaki K.,** Overview of metastability and compositional complexity effects for hydrogen-resistant iron alloys: Inverse austenite stability effects, Eng. Fract. Mech. 214 (2019) 123–133.

7. **Troiano A. R.,** The role of hydrogen and other interstitials in the mechanical behavior of metals, Metallogr. Microstruct. Anal. 5 (6) (2016) 557–569.

8. **Peral L. B., Zafra A., Fernández-Pariente I., et al.,** Effect of internal hydrogen on the tensile properties of different CrMo(V) steel grades: Influence of vanadium addition on hydrogen trapping and diffusion, Int. J. Hydrog. Energy. 45 (41) (2020) 22054–22079.

9. **Venezuela J., Hill T., Zhou Q., et al.,** Hydrogen-induced fast fracture in notched 1500 and 1700 MPa class automotive martensitic advanced high-strength steel, Corr. Sci. 188 (1 August) (2021) 109550.

10. **Duportal M., Oudriss A., Savall C., et al.,** On the implication of mobile hydrogen content on the surface reactivity of an austenitic stainless steel, Electrochim. Acta. 403 (20 January) (2022) 139684.

11. **Alekseeva E.**, **Belyaev A.**, **Zegzhda A., et al.,** Boundary layer influence on the distribution of hydrogen concentrations during hydrogen-induced cracking test of steels, Diagnostics, Resource and Mechanics of Materials and Structures. (3) (2018) 43–57 (in Russian).

12. **Polyanskiy V. A., Belyaev A. K., Alekseeva E. L., et al.,** Phenomenon of skin effect in metals due to hydrogen absorption, Contin. Mech. Thermodyn. 31 (6) (2019) 1961–1975.

13. **Martinsson A., Sandström R.,** Hydrogen depth profile in phosphorus-doped, oxygen-free copper after cathodic charging, J. Mater. Sci. 47 (19) (2012) 6768–6776.

14. **Wu R., Ahiström J., Magnusson H., et al.,** Charging, degassing and distribution of hydrogen in cast iron (report SKB R-13-45), Svensk Kärnbränslehantering AB, Swedish Nuclear and Waste Management Co., Stockholm, May 2015.

15. **Oriani R. A.,** A mechanistic theory of hydrogen embrittlement of steels, Berichte der Bundesgesellschaft für physikalische Chemie. 76 (8) (1972) 848–857.

16. **Troiano A. R.,** The role of hydrogen and other interstitials in the mechanical behavior of metals, Trans. ASM. 52 (1960) 54–80.

17. **Birnbaum H. K., Sofronis P.,** Hydrogen-enhanced localized plasticity – a mechanism for hydrogen-related fracture, Mater. Sci. Eng. A. 176 (1–2) (1994) 191–202.

18. **Sofronis P.**, **Birnbaum H. K.,** Mechanics of the hydrogen dislocation-impurity interactions. I. Increasing shear modulus, J. Mech. Phys. Solid. 43 (1) (1995) 49–90.

19. **Taha A., Sofronis P.,** A micromechanics approach to the study of hydrogen transport and embrittlement, Eng. Fract. Mech. 68 (6) (2001) 803–837.

20. **von Fick A.,** Ueber Diffusion, Annalen der Physik. 170 (1) (1855) 59–86.

21. **Shewmon P. G.,** Diffusion in solids, Mc Graw-Hill Book Co, Inc., New York, 1963.

22. **Kolachev B. A.,** Vodorodnaya khrupkost metallov [Hydrogen embrittlement of metals], Metallurgiya, Moscow, 1985 (in Russian).

23. **Gorsky W.,** Theorie der elastischen Nachwirkung in ungeordneten Mischkristallen (elastische Nachwirkung zweiter Art), Physikalische Zeitschrift der Sowjetunion. 8 (1935) 457–471.

24. **Serebrinsky S., Carter E. A., Ortiz M.,** A quantum-mechanically informed continuum model of hydrogen embrittlement, J. Mech. Phys. Solids. 52 (10) (2004) 2403–2430.

25. **McLean D.,** Grain boundaries in metals. Clarendon Press, London, 1957.

26. **Irwin G. R.,** Analysis of stresses and strains near the end of a crack traversing a plate, J. Appl. Mech. 24 (3) (1957) 361–364.

27. **Irwin G. R.,** Fracture, In book: Encyclopedia of Physics, Ed. by S. Flugge, Vol. 6: Elasticity and Plasticity, Springer Verlag, Berlin (1958) 551–590.

28. **Wilkins M. L.,** Computer simulation of dynamic phenomena, Springer Science & Business Media, Berlin, Heidelberg, 1999.

29. Stress intensity factors handbook, in 2 Vols. Editor-in-Chief Murakami Y. Vol. 2. The Society of Materials Science, Pergamon Press Oxford, New York, 1987.

30. **Benthem J. P., Koiter W. T.,** Asymptotic approximations to crack problems, In book: Methods of analysis and solutions of crack problems, Ed. by G. C. Sih, Book Series “Mechanics of Fracture”, Vol. 1. Springer, Dordrecht (1973) 131–178.

31. **Hirth J. P.,** Effects of hydrogen on the properties of iron and steel, Metallurg. Trans. A. 11 (6) (1980) 861–890.

32. **Tvergaard V., Hutchinson J. W.,** The relation between crack growth resistance and fracture process parameters in elastic-plastic solids, J. Mech. Phys. 40 (6) (1992) 1377–1397.

33. **Herms E., Olive J. M., Puiggali M.,** Hydrogen embrittlement of 316L type stainless steel, Mater. Sci. Eng. A. 272 (2) (1999) 279–283.

34. **Momotani Y., Shibata A., Terada D., Tsuji N.,** Effect of strain rate on hydrogen embrittlement in low-carbon martensitic steel, Int. J. Hydrog. Energy. 42 (5) (2017) 3371–3379.

СПИСОК ЛИТЕРАТУРЫ

1. ISO11114-4. Transportable gas cylinders – compatibility of cylinder and valve materials with gas contents – part 4: Test methods for selecting metallic materials resistant to hydrogen embrittlement. ISO 11114-4:2017 International Organization for Standardization, 2017. URL: https://www.iso.org/standard/64587.html (Дата последнего обращения: 12.03.2022).

2. ISO16573. Steel – measurement method for the evaluation of hydrogen embrittlement resistance of high strength steels. ISO 16573:2015 International Organization for Standardization, 2015. URL: https://www.iso.org/standard/57128.html (Дата последнего обращения: 12.03.2022).

3. ISO17081. Method of measurement of hydrogen permeation and determination of hydrogen uptake and transport in metals by an electrochemical technique. ISO 17081:2014 International Organization for Standardization, 2014. URL: https://www.iso.org/standard/64514.html (Дата последнего обращения: 12.03.2022).

4. **Giuliani L., Mirabile M., Sarracino M.** Embrittlement kinetics of N 80 steel in H_2S environment // Metallurgical and Materials Transactions B. 1974. Vol. 5. No. 9. Pp. 2069–2073.

5. **Nagumo M., Yoshida H., Shimomura Y., Kadokura T.** Ductile crack growth resistance in hydrogen-charged steels // Materials Transactions. 2001. Vol. 42. No. 1. Pp. 132–137.

6. **Koyama M., Tasan C. C., Tsuzaki K.** Overview of metastability and compositional complexity effects for hydrogen-resistant iron alloys: Inverse austenite stability effects // Engineering Fracture Mechanics. 2019. Vol. 214. 1 June. Pp. 123–133.

7. **Troiano A. R.** The role of hydrogen and other interstitials in the mechanical behavior of metals // Metallography, Microstructure & Analysis. 2016. Vol. 5. No. 6. Pp. 557–569.

8. **Peral L. B., Zafra A., Fernández-Pariente I., Rodrнguez C., Belzunce J.** Effect of internal hydrogen on the tensile properties of different CrMo(V) steel grades: Influence of vanadium addition on hydrogen trapping and diffusion // International Journal of Hydrogen Energy. 2020. Vol. 45. No. 41. Pp. 22054–22079.

9. **Venezuela J., Hill T., Zhou Q., Li H., Shi Z., Dong F., Knibbe R., Zhang M., Dargusch M. S., Atrens A.** Hydrogen-induced fast fracture in notched 1500 and 1700 MPa class automotive martensitic advanced high-strength steel // Corrosion Science. 2021. Vol. 188. 1 August. P. 109550.

10. **Duportal M., Oudriss A., Savall C., Renaud A., Labrugure-Sarroste C., Feaugas X.** On the implication of mobile hydrogen content on the surface reactivity of an austenitic stainless steel // Electrochimica Acta. 2022. Vol. 403. 20 January. P. 139684.

11. Алексеева Е. Л., Беляев А. К., Зегжда **А. С., Полянский А. М., Полянский В. А., Фролова К. П., Яковлев В. А.** Влияние пограничного слоя на распределение концентраций водорода при испытаниях сталей на стойкость к водородному растрескиванию // Diagnostics, Resource and Mechanics of Materials and Structures. 2018. № 3. С. 43–57.

12. **Polyanskiy V. A., Belyaev A. K., Alekseeva E. L., Polyanskiy A. M., Tretyakov D. A., Yakovlev Yu. A.** Phenomenon of skin effect in metals due to hydrogen absorption // Continuum Mechanics and Thermodynamics. 2019. Vol. 31. No. 6. Pp. 1961–1975.

13. **Martinsson A., Sandström R.** Hydrogen depth profile in phosphorus-doped, oxygen-free copper after cathodic charging // Journal of Materials Science. 2012. Vol. 47. No. 19. Pp. 6768–6776.

14. **Wu R., Ahiström J., Magnusson H., Frisk K., Martinsson E.** Charging, degassing and distribution of hydrogen in cast iron (report SKB R-13-45). Stockholm: Svensk Kärnbränslehantering AB. Swedish Nuclear and Waste Management Co., May 2015. 47 p.

15. **Oriani R. A.** A mechanistic theory of hydrogen embrittlement of steels // Berichte der Bundesgesellschaft für physikalische Chemie. 1972. Vol. 76. No. 8. Pp. 848–857.

16. **Troiano A. R.** The role of hydrogen and other interstitials in the mechanical behavior of metals // Transactions of the American Society of Metals (ASM). 1960. Vol. 52. Pp. 54–80.

17. **Birnbaum H. K., Sofronis P.** Hydrogen-enhanced localized plasticity – a mechanism for hydrogen-related fracture // Materials Science and Engineering A. 1994. Vol. 176. No. 1–2. Pp. 191–202.

18. **Sofronis P.**, **Birnbaum H. K.** Mechanics of the hydrogen dislocation-impurity interactions. I. Increasing shear modulus // Journal of the Mechanics and Physics of Solids. 1995. Vol. 43. No. 1. Pp. 49–90.

19. **Taha A., Sofronis P.** A micromechanics approach to the study of hydrogen transport and embrittlement // Engineering Fracture Mechanics. 2001. Vol. 68. No. 6. Pp. 803–837.

20. Фика закон // Физический энциклопедический словарь. Гл. ред. А. М. Прохоров. М.: Советская энциклопедия, 1984. С. 818.

21. **Шьюмон П.** Диффузия в твердых телах. М.: Металлургия, 1966. 196 с.

22. **Колачев Б. А.** Водородная хрупкость металлов. М.: Металлургия, 1985. 216 с.

23. **Gorsky W.** Theorie der elastischen Nachwirkung in ungeordneten Mischkristallen (elastische Nachwirkung zweiter Art) // Physikalische Zeitschrift der Sowjetunion. 1935. Bd. 8. S. 457–471.

24. **Serebrinsky S., Carter E. A., Ortiz M.** A quantum-mechanically informed continuum model of hydrogen embrittlement // Journal of the Mechanics and Physics of Solids. 2004. Vol. 52. No. 10. Pp. 2403–2430.

25. **McLean D.** Grain boundaries in metals. London: Clarendon Press, 1957. 346 p.

26. **Irwin G. R.** Analysis of stresses and strains near the end of a crack traversing a plate // Journal of Applied Mechanics. 1957. Vol. 24. No. 3. Pp. 361–364.

27. **Irwin G. R.** Fracture // Encyclopedia of Physics. Ed. by S. Flugge. Vol. 6. Elasticity and Plasticity. Berlin: Springer Verlag, 1958. Pp. 551–590.

28. **Wilkins M. L.** Computer simulation of dynamic phenomena Berlin, Heidelberg: Springer Science & Business Media, 1999. 246 p.

29. Справочник по коэффициентам интенсивности напряжений. Под ред. Ю. Мураками. Пер. с англ. В 2 тт. Т. 2. М.: Мир, 1990. 556 с.

30. **Benthem J. P., Koiter W. T.** Asymptotic approximations to crack problems // Methods of analysis and solutions of crack problems. Ed. by G. C. Sih. Book Series "Mechanics of Fracture". Vol. 1. Dordrecht: Springer, 1973. Pp. 131–178.

31. **Hirth J. P.** Effects of hydrogen on the properties of iron and steel // Metallurgical Transactions A. 1980. Vol. 11. No. 6. Pp. 861–890.

32. **Tvergaard V., Hutchinson J. W.** The relation between crack growth resistance and fracture process parameters in elastic-plastic solids // Journal of the Mechanics and Physics of Solids. 1992. Vol. 40. No. 6. Pp. 1377–1397.

33. **Herms E., Olive J. M., Puiggali M.** Hydrogen embrittlement of 316L type stainless steel // Materials Science and Engineering A. 1999. Vol. 272. No. 2. Pp. 279–283.

34. **Momotani Y., Shibata A., Terada D., Tsuji N.** Effect of strain rate on hydrogen embrittlement in low-carbon martensitic steel // International Journal of Hydrogen Energy. 2017. Vol. 42. No. 5. Pp. 3371–3379.

THE AUTHORS

SEDOVA Yuliya S.
Institute for Problems in Mechanical Engineering of the Russian Academy of Sciences
61 Bolshoy Ave., V. Isl.., St. Petersburg, 199178, Russia
sedova.yus@mail.ru
ORCID: 0000-0003-4397-6073

BESSONOV Nikolay M.
Institute for Problems in Mechanical Engineering of the Russian Academy of Sciences
61 Bolshoy Ave., V. Isl.., St. Petersburg, 199178, Russia
nickbessonov1@gmail.com.ru
ORCID: 0000-0001-6462-5980

POLYANSKIY Vladimir A.
Institute for Problems in Mechanical Engineering of the Russian Academy of Sciences
61 Bolshoy Ave., V. Isl.., St. Petersburg, 199178, Russia
vapol@mail.ru
ORCID: 0000-0002-1199-1028

СВЕДЕНИЯ ОБ АВТОРАХ

СЕДОВА Юлия Сергеевна – *стажер-исследователь Института проблем машиноведения Российской академии наук.*
199178, Россия, г. Санкт-Петербург, Большой проспект В. О., 61
sedova.yus@mail.ru
ORCID: 0000-0003-4397-6073

БЕССОНОВ Николай Михайлович – *доктор физико-математических наук, главный научный сотрудник Института проблем машиноведения Российской академии наук.*
199178, Россия, г. Санкт-Петербург, Большой проспект В. О., 61
nickbessonov1@gmail.com.ru
ORCID: 0000-0001-6462-5980

ПОЛЯНСКИЙ Владимир Анатольевич – *доктор технических наук, директор Института проблем машиноведения Российской академии наук.*
199178, Россия, г. Санкт-Петербург, Большой проспект В. О., 61
vapol@mail.ru
ORCID: 0000-0002-1199-1028

Received 31.03.2022. Approved after reviewing 30.06.2022. Accepted 01.07.2022.
Статья поступила в редакцию 31.03.2022. Одобрена после рецензирования 30.06.2022. Принята 01.07.2022.

RADIOPHYSICS

Original article
DOI: https://doi.org/10.18721/JPM.15314

SYNTHESIS OF WINDOW FUNCTIONS FOR REDUCING SYSTEMATIC ERRORS OF MULTIPLEXED FIBER-OPTIC SENSORS

A. A. Markvart✉, *L. B. Liokumovich*, *N. A. Ushakov*

Peter the Great St. Petersburg Polytechnic University, St. Petersburg, Russia

✉ markvart_aa@spbstu.ru

Abstract. In the paper, the systematic (bias) error of digital processing of the biharmonic signal of two multiplexed fiber-optic interferometers under spectral interrogation, when the registered spectral transfer function being processed through a discrete Fourier transform has been analyzed. The synthesis of a special weighted window function was put forward; this made it possible to reduce the systematic errors in determining the frequencies of a polyharmonic signal without a significant increase in the random (noise) error. The effectiveness of this approach was proven through numerical simulation and experimentally by comparison with the error when using standard Dolph – Chebyshev window. The proposed approach can be applied in any problems related to the estimation of frequencies and phases of polyharmonic signals.

Keywords: harmonic analysis, discrete Fourier transform, methodological error, window function, interferometer

Funding: The reported study was carried out as a part of the State Assignment for Fundamental Research (Subject Code FSEG-2020-0024).

Citation: Markvart A. A., Liokumovich L. B., Ushakov N. A., Synthesis of window functions for reducing systematic errors of multiplexed fiber-optic sensors, St. Petersburg State Polytechnical University Journal. Physics and Mathematics. 15 (3) (2022) 185–200. DOI: https://doi.org/10.18721/JPM.15314

Научная статья
УДК 535.3, 535-15, 535.417
DOI: https://doi.org/10.18721/JPM.15314

СИНТЕЗ ОКОННЫХ ФУНКЦИЙ ДЛЯ СНИЖЕНИЯ МЕТОДИЧЕСКИХ ОШИБОК МУЛЬТИПЛЕКСИРОВАННЫХ ВОЛОКОННО-ОПТИЧЕСКИХ ДАТЧИКОВ

А. А. Маркварт✉, *Л. Б. Лиокумович*, *Н. А. Ушаков*

Санкт-Петербургский политехнический университет Петра Великого,

Санкт-Петербург, Россия

✉ markvart_aa@spbstu.ru

Аннотация. Проведен анализ методической погрешности цифровой обработки бигармонического сигнала двух мультиплексированных волоконно-оптических интерферометров при спектральном опросе, когда регистрируемая спектральная передаточная функция обрабатывается посредством дискретного преобразования Фурье. Предложен синтез специальной весовой оконной функции, позволяющей снизить методические погрешности определения частот полигармонического сигнала без существенного увеличения случайной погрешности. Эффективность такого подхода доказана численным моделированием и экспериментально, путем сравнения с результатами применения стандартного окна Дольфа – Чебыш□ва. Предложенный подход может использоваться в любых задачах, связанных с оценкой частот и фаз полигармонических сигналов.

Ключевые слова: гармонический анализ, дискретное преобразование Фурье, методическая погрешность, оконная функция, интерферометр.

Финансирование: Работа выполнена в рамках Государственного задания на проведение фундаментальных исследований (код темы FSEG-2020-0024).

Ссылка для цитирования: Маркварт А. А., Лиокумович Л. Б., Ушаков Н. А. Синтез оконных функций для снижения методических ошибок мультиплексированных волоконно-оптических датчиков // Научно-технические ведомости СПбГПУ. Физико-математические науки. 2022. Т. 15. № 3. С. 185–200. DOI: https://doi.org/10.18721/JPM.15314

Introduction

Fiber-optic sensors are the focus of much attention in R&D, due to their high accuracy, immunity to electromagnetic interference, compact size, and capabilities for multiplexing and remote interrogation [1]. Such sensors can measure various physical impacts, such as temperature, stretching, pressure, etc., and have a wide range of applications, from monitoring buildings and structures to medical diagnostics.

One type of such sensors are interferometric fiber optic sensors [2]. Spectral interferometry is an effective widespread mechanism for interrogating these sensors. It involves recording and subsequently processing the dependence of the relative intensity level of the light S passed through a sensitive interferometer on the frequency f of this light; this dependence $S(f)$ is the spectral transfer function (SPF) of this interferometer [3].

Users generally tend to multiplex two or more interferometers connected to a single interrogation setup [4, 5]. Importantly, the STF of multiplexed interferometers contains sums of harmonic components with certain frequencies and phases characterizing each of the sensing elements; this can be confirmed experimentally.

The most common approach to processing STF applies the discrete Fourier transform (DFT) with analysis of the resulting harmonic components. However, the spectral leakage effect produces systematic errors in determining the frequencies and phases of harmonic components in STF and, consequently, errors in demodulation of signals from multiplexed sensors and their parasitic interference. Standard weight functions, e.g., Hamming, Kaiser, Blackman, Dolph–Chebyshev windows, are commonly used to reduce the level of these errors. [6, 7]. Their drawback is a decrease in spectral resolution and an increase in the influence of noise on measurements due to increased equivalent noise bandwidth (ENBW) of the window. Therefore, it is worth considering synthesis of specialized windows reducing demodulation errors without a significant deterioration in ENBW level. This approach was considered in [8–10] and used in radar systems. However, the algorithm proposed by the authors for synthesizing the window and finding the harmonic component frequencies of the signal is multi-iterative, which means that the windows have to be recalculated with any change in these frequencies. The frequencies of the harmonic components in STF only vary slightly in measurements using fiber optic interferometers. This allows avoiding iterative recalculation of windows, using a single weight window specifically synthesized for a particular scheme.

This paper proposes a method for reducing demodulation errors in signals from two multiplexed fiber-optic interferometric sensors by synthesizing a specialized weight window.

The proposed method has none of these drawbacks which are inherent in the existing methods for synthesizing windows.

Circuit description and general principles for synthesizing the special window

For certainty, we consider a circuit with two multiplexed sensing elements, which are the so-called extrinsic fiber Fabry–Perot interferometers (EFFPI), Fig. 1) [3, 8]. Each EFFPI is formed by the endface of a single-mode waveguide feed and a mirror with an air gap between them, with thicknesses L_1 and L_2 for the first and second EFFPI, respectively. The variations L_1 and L_2 from the measured quantity (deformation, temperature, etc.) are to be determined in the measurements. The radiation of the frequency (or wavelength) tunable laser passes through the circulator and is directed through the coupler to both EFFPIs, is s reflected from them, entering the photodetector through the coupler and the circulator.

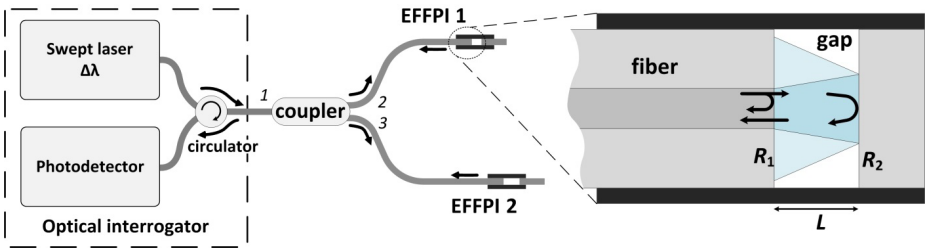

Fig. 1. Measuring circuit with multiplexed EFFPI:
Optical interrogator; swept laser; circulator; coupler with ports *1*, *2* and 3; fiber; interferometer gap with the width L; photodetector; R_1, R_2 are the reflectivities of the mirrors

We consider the case of low-finesse EFFPIs (valid for small R_1 and R_2), when multiply reflected waves can be omitted. If the difference in the lengths of the feeding fiber segments between the EFFPI and the coupler is greater than the coherence length of the radiation source, the STF is determined by the interference of beam pairs from each EFFPI [4, 11]:

$$S\left(f, L_1, L_2\right) = \overline{S} + S_1 \cos\left[\frac{4\pi L_1}{c} f + \gamma_1\left(L_1\right)\right] + S_2 \cos\left[\frac{4\pi L_2}{c} f + \gamma_2\left(L_2\right)\right], \quad (1)$$

where

$$\overline{S} = \alpha_{12}^2\left[R_1 + R_2\eta_1\right] + \alpha_{13}^2\left[R_1 + R_2\eta_2\right],$$

$$S_{1,2} = 2\alpha_{12,13}^2 \sqrt{R_1 R_2 \eta_{1,2}},$$

$$\eta_{1,2} = \frac{\pi^2 w_0 (f)^2}{L_{1,2}^2 c^2 / f^2 + \pi^2 w_0 (f)^2},$$

$$\gamma_{1,2} = \pi - \mathrm{arctg}\left(\frac{L_{1,2}}{z_R}\right),$$

$$z_R = \pi \cdot f \cdot w_0^2 (f) / c.$$

The following notations are adopted in Eq. (1): f, c are the frequency and speed of light; S is the mean STF level; $S_{1,2}$ are the amplitudes of interference components determined by mirrors $R_{1,2}$, coupling coefficients $\alpha_{12,13}$ of the coupler and light losses in the EFFPI due to divergence of light in the gap (losses are taken into account by the coefficients $\eta_{1,2}$); $\gamma_{1,2}$ are the phase shifts of waves; z_R is the Rayleigh length of the Gaussian beam; w_0 is the waist radius of the Gaussian beam.

The waves acquire a phase shift upon reflection from the external mirror, as well as due to divergence of light in the interferometer gap. The explicit form of expressions for $\eta_{1,2}$ and $\gamma_{1,2}$ is obtained via a Gaussian beam model for light in the interferometer gap [11] (z_R is Rayleigh length of the Gaussian beam); the waist radius of the Gaussian beam corresponds to the radius of the fiber mode spot. Notably, STF calculations in small frequency-tuning ranges used in practical interrogation devices generally neglect minor variations in the values of $\eta_{1,2}$, $\gamma_{1,2}$, z_R and w_0 due to variation in frequency f.

In practice, the interrogation system records a set of readouts $S_i = S(f_i, L_1, L_2)$, where i is the readout number. A uniform frequency step Δ is taken for further processing. If f_0 is the center of the frequency scanning range and N is the number of readouts, then

$$f_i = f_0 + [i - (N-1)/2] \cdot \Delta, \tag{2}$$

where i varies from 0 to $(N - 1)$ and the scanning range $\Delta f = \Delta \cdot (N - 1)$.

Demodulation of the obtained dependence $S(f)$ consists in finding the values of L_1 and L_2, which in turn amounts to estimating the frequencies and phases of the harmonic components of the following sequence:

$$v(i) = w(i)\left\{\overline{S} + S_1 \cos\left[\omega_1(L_1) \cdot i + \vartheta_1(L_1)\right] + S_2 \cos\left[\omega_2(L_2) \cdot i + \vartheta_2(L_2)\right]\right\}, \tag{3}$$

where $w(i)$ is the weighting window used; $\omega_{1,2}(L_{1,2})$ are the circular frequencies in radians; $\vartheta_{1,2}(L_{1,2})$ are the phases of harmonic components.

In view of expressions (1) and (2), we obtain:

$$\omega_{1,2}(L_{1,2}) = 4\pi\Delta \cdot L_{1,2}/c, \tag{4}$$

$$\vartheta_{1,2}(L_{1,2}) = 4\pi \cdot f_0 \cdot L_{1,2} / c - 2\pi \cdot \Delta \cdot (N-1) \cdot L_{1,2} / c + \gamma_{1,2}(L_{1,2}). \tag{5}$$

The Fourier transform of the sequence of counts (3) takes the form [6]:

$$\begin{aligned} V(\omega, L_1, L_2) &= \overline{S} \cdot W(\omega) + \\ &+ 0.5 \cdot S_1 \cdot \exp\left[j\vartheta_1(L_1)\right] \cdot W\left[\omega - \omega_1(L_1)\right] + 0.5 \cdot S_1 \cdot \exp\left[-j\vartheta_1(L_1)\right] \cdot W\left[\omega + \omega_1(L_1)\right] + \\ &+ 0.5 \cdot S_2 \cdot \exp\left[j\vartheta_2(L_2)\right] \cdot W\left[\omega - \omega_2(L_2)\right] + 0.5 \cdot S_2 \cdot \exp\left[-j\vartheta_2(L_2)\right] \cdot W\left[\omega + \omega_2(L_2)\right], \end{aligned} \tag{6}$$

where $W(\omega)$ is the Fourier transform of the window $w(i)$.

The frequencies $\omega_{1,2}$ are typically found by determining the positions $\omega_{1m,2m}$ of the peaks on the Fourier transform modulus V, and the phases $\vartheta_{1,2}$ are found by calculating the argument V in these peaks (taking into account the influence of the window). However, it can be seen from expression (3) that the first, third, fourth and fifth terms generate errors for the values of ω_1 and θ_1. This is because the second term with $W(0)$ required for estimating the magnitude of the quantity $|V(\omega)|$ and the argument V in the region ω_1 is supplemented by the terms with $W(\omega_1)$, $W(2\omega_1)$, $W(\omega_1 - \omega_2)$ and with $W(\omega_1 + \omega_2)$, distorting the result. Similarly, the first, second, third and fifth terms generate errors for the values of ω_2 and θ_2 found in region ω_2. To determine the frequencies and phases correctly, we should synthesize such a weight window w^{synt} whose Fourier transform W^{synt} could minimize the corresponding parasitic components in the required frequency frequency range, due to dips in W^{synt} in the regions ω_1, $2\omega_1$, $(\omega_1 + \omega_2)$, $(\omega_1 - \omega_2)$, ω_2, $2\omega_2$, $(\omega_2 - \omega_1)$. Furthermore, additional dips in W^{synt} should also be provide in the negative frequency range, so that the Fourier transform W^{synt} is symmetrical relative to zero, because the frequency estimate by the maxima of the Fourier transform $|V|$ of the sequence multiplied by the window w^{synt} is unbiased only in this case. The additional frequencies for the negative range are $-\omega_1$, $-2\omega_1$, $-(\omega_1 + \omega_2)$, $-\omega_2$, $-2\omega_2$.

Thus, the quantity W^{synt} should be minimized in the range of the above 12 frequencies, i.e., in the bands $\Delta\Omega_p$, $p = \pm1, \pm2, ..., \pm6$, accounting for the potential variation in the frequencies $\omega_{1,2}$ with respect to the variation in $L_{1,2}$, as well as the shift in the positions $\omega_{1m,2m}$ of the maxima $|V|$ due to spectral leakage and the influence of the noise from the measuring equipment. Denoting these variations in frequency as $\Delta\omega_1$ and $\Delta\omega_2$, we can write the following expressions for the zeros in W^{synt}:

$$\Delta\Omega_{\pm1} = \Delta\omega_1,\ \Delta\Omega_2 = {}_{2\pm}\Delta\omega_1,\ \Delta\Omega_{\pm3} = \Delta\omega_2,$$

$$\Delta\Omega_{\pm4} = 2\Delta\omega_2,\ \Delta\Omega_{\pm5} = \Delta\omega_1 + \Delta\omega_2,\ \Delta\Omega_{\pm6} = \Delta\omega_1 + \Delta\omega_2.$$

It is preferable to synthesize the required window $w^{synt}(i)$ based on one of the standard windows $w(i)$,, introducing an additional requirement for a minimum residual of the Fourier transforms $W^{synt}(\omega)$ and $W(\omega)$ of these windows outside these regions. In this case, the requirements for the window $w^{synt}(i)$ can be written as two conditions:

$$\begin{cases} \text{Condition 1:} \\ \left|W^{synt}(\omega)\right| \to \min \text{ for} \\ \quad \omega \in \pm\left[\omega_{1m} - \Delta\Omega_1/2;\ \omega_{1m} + \Delta\Omega_1/2\right] \cup \pm\left[2\omega_{1m} - \Delta\Omega_2/2;\ 2\omega_{1m} + \Delta\Omega_2/2\right] \cup \\ \quad\quad \cup \pm\left[\omega_{2m} - \Delta\Omega_3/2;\ \omega_{2m} + \Delta\Omega_3/2\right] \cup \pm\left[2\omega_{2m} - \Delta\Omega_4/2;\ 2\omega_{2m} + -\Delta\Omega_4/2\right] \cup \\ \quad\quad \cup \pm\left[\omega_{1m} - \omega_{2m} - \Delta\Omega_5/2;\ \omega_{1m} - \omega_{2m} + \Delta\Omega_5/2\right] \cup \\ \quad\quad \cup \pm\left[\omega_{1m} + \omega_{2m} - \Delta\Omega_6/2;\ \omega_{1m} + \omega_{2m} + \Delta\Omega_6/2\right]; \\ \text{Condition 2:} \\ \left|W^{synt}(\omega) - W(\omega)\right| \to \min \text{ for other } \omega. \end{cases} \tag{7}$$

Condition 1 gives the dips of W^{synt} at frequencies $\pm\omega_1$, $\pm2\omega_1$, $\pm\omega_2$, $\pm2\omega_2$, $\pm|(\omega_1 - \omega_2)|$, $\pm(\omega_1 + \omega_2)$. Notice that it is this condition (7) that is responsible for suppressing $W^{synt}(\omega)$ in the given frequency ranges and is in fact aimed at reducing the systematic error in finding the frequencies and phases of the harmonic components due to the parasitic effects described above.

The second condition can be interpreted as minimization of the broadening in the main Fourier transform lobe of the window. It prevents an increase in the ENBW value of the window, i.e., an increase in the random measurement error due to noise from the measuring equipment.

There are different approaches to tgenerating dips in the Fourier transform of a certain sequence of readouts. Such approaches are the best developed for antenna arrays, often involving synthesis of the discrete amplitude-phase distribution of currents over the elements of the antenna array to produce dips in the antenna's directivity pattern in the given directions [12–15]. We use the approach to solving this problem outlined in [15], as it is relatively simple. According to this

approach, the required Fourier transform of the window W^{synt} is represented as the difference of the initial W and compensating W^{comp} Fourier transforms:

$$W^{synt} = W - W^{comp}. \tag{8}$$

The window is synthesized by the following logic. For example, let the compensating transform W^{comp} be the window transform whose main lobe is frequency-shifted to the position ω_1 and is equal in amplitude to the magnitude of the initial transform W at this point. Then, a zero of the transform W^{synt} appears after subtraction at the point ω_1. Broad dips can be produced by generating a set of zeros at multiple points ω_k filling the regions with dips. The compensating Fourier image is composed as a sum [15]:

$$W^{\text{comp}}(\omega) = \sum_{k=1}^{K} H_k \cdot G(\omega - \omega_k), \tag{9}$$

where $G(\omega)$ are the basic functions; $\{\omega_k\}$ is a set of frequency points generating zeros in the Fourier transform of the synthesized window; $\{H_k\}$ are the coefficients before basis functions, calculated after the set $\{\omega_k\}$ is given.

The Fourier transform of a rectangular window is used as the basis function. The synthesized function W^{synt} is obtained by finding the set $\{\omega_k\}$. The coefficients $\{H_k\}$ are calculated from the condition that the value of the subtracted function W^{comp} be equal to the value of the initial function W at each of the points of the set $\{\omega_k\}$. This condition can be written in the following matrix form:

$$\left[W(\omega_k)\right] = \left[W^{\text{comp}}(\omega_k)\right] \cdot \left[H_k\right]. \tag{10}$$

Then the coefficients $\{H_k\}$ can be found using the expression

$$\left[H_k\right] = \left[W^{\text{comp}}(\omega_k)\right]^{-1} \cdot \left[W(\omega_k)\right]. \tag{11}$$

After these coefficients are calculated, the search window $w^{synt}(i)$ is found by an inverse Fourier transform with respect to W^{synt}, or, in view of the theorem on the frequency shift of a Fourier transform, using the expression

$$w^{\text{comp}}(i) = \sum_{k=1}^{K} H_k \cdot g(i) \cdot \exp\left[j\omega_k i\right]. \tag{12}$$

where $g(i)$ is the inverse Fourier transform of the basis function $G(\omega)$.

Method for finding the optimal set $\{\omega_k\}$

The crucial step within the proposed approach is to select the set $\{\omega_k\}$ to best satisfy condition (7). A simple version was used in [15, 16], with an equidistant distribution of a certain number of points ω_k in the regions assumed to have dips in the Fourier transform W^{synt}. However, this choice may be far from optimal. Multiparameter optimization is actually required, where the parameters optimized include not only the values of ω_k but also the number of points K in the set. To solve the problem, we consider some target function M. It is logical to introduce minimization of the highest levels of $|W^{synt}|$ in the regions with dips into this function, as well as the regularization term r, depending on the magnitude of ENBW:

$$\begin{cases} M = \max\left|W^{\text{synt}}\left[\omega_{1\text{m}} - \Delta\Omega_1/2;\, \omega_{1\text{m}} + \Delta\Omega_1/2\right]\right| + \max\left|W^{\text{synt}}\left[2\omega_{1\text{m}} - \Delta\Omega_2/2;\, 2\omega_{1\text{m}} + \Delta\Omega_2/2\right]\right| + \\ + \max\left|W^{\text{synt}}\left[\omega_{2\text{m}} - \Delta\Omega_3/2;\, \omega_{2\text{m}} + \Delta\Omega_3/2\right]\right| + \max\left|W^{\text{synt}}\left[2\omega_{2\text{m}} - \Delta\Omega_4/2;\, 2\omega_{2\text{m}} + \Delta\Omega_4/2\right]\right| + \\ + \max\left|W^{\text{synt}}\left[\left|\omega_{1\text{m}} - \omega_{2m}\right| - \Delta\Omega_5/2;\, \left|\omega_{1\text{m}} - \omega_{2m}\right| + \Delta\Omega_5/2\right]\right| + \\ + \max\left|W^{\text{synt}}\left[\omega_{1\text{m}} + \omega_{2m} - \Delta\Omega_6/2;\, \omega_{1\text{m}} + \omega_{2m} + \Delta\Omega_6/2\right]\right| + \\ + r\left\{\text{ENBW}\left(w^{\text{synt}}\right)\right\}. \end{cases} \tag{13}$$

As mentioned above, an increase in the depth of the dips is accompanied by the increase in ENBW, therefore, we should aim to compromise between these values, that is, between the systematic and random errors; the required balance can be regulated by selecting the function $r\{\mathrm{ENBW}(w^{synt})\}$. It is preferable to select the actual points ω_k in regions that are slightly wider (by k times) than $\Delta\Omega_p$, i.e., with the width of $k\cdot\Delta\Omega_p$.

In this paper, we used a genetic optimization algorithm [17] to find the set $\{\omega_k\}$, since it is well suited for a problem where the target function defined by expression (13) is considerably nonlinear with multiple discontinuities. The optimization procedure was carried out in the MATLAB software package using the built-in ga function with a random set $\{\omega_k\}$ in the first generation [18]. In view of the symmetry requirements for W^{synt}, the set $\{\omega_k\}$ was taken to be symmetric with respect to zero. The enerations had a length of $K/2$ because the values of ω_k were optimized in the region of positive frequencies due to symmetry. The minimization function was programmed so that not only the position ω_k but also the value of K was optimized. On the one hand, the higher K, the deeper the dips W^{synt} formed; on the other hand, however, the condition number of the matrix $[\underline{W}^{comp}(\omega_k)]$ is reduced, producing computational errors and incorrect results. The initial value of K and the population size were selected empirically. The remaining parameters of the ga function were selected by default.

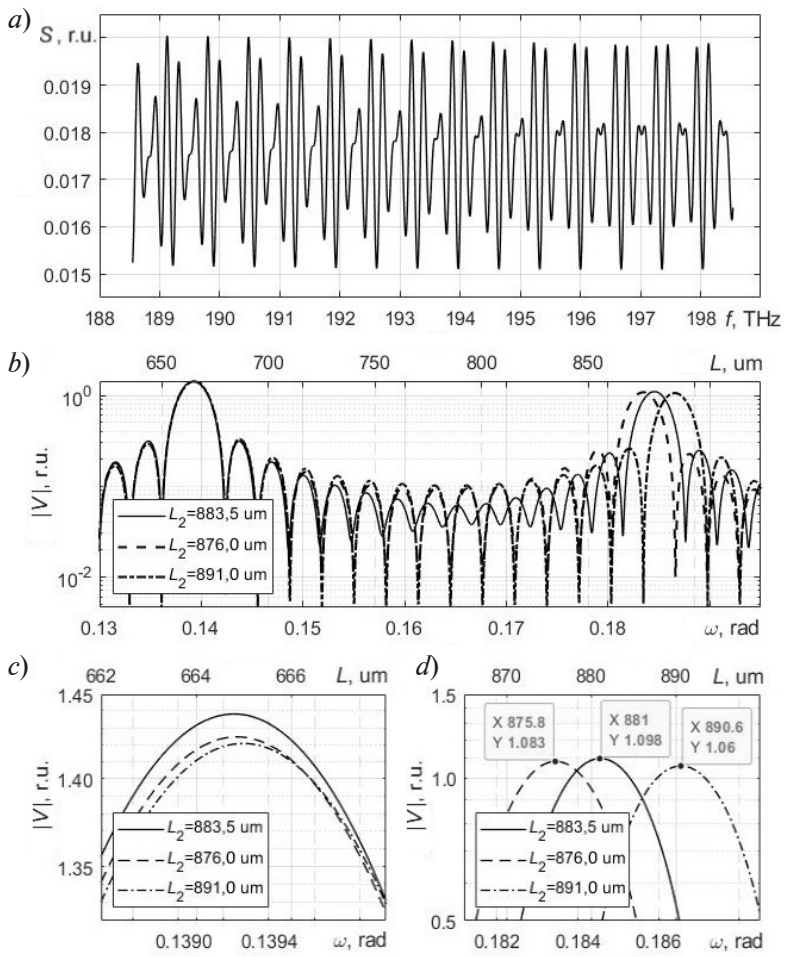

Fig. 2. Numerical simulation of biharmonic signal from two multiplexed fiber-optic interferometers: *a* shows the STF frequency dependence for the circuit; *b* shows the dependences $|V(\omega)|$; *c*, *d* show fragments of $|V(\omega)|$; L_1 = 664.8 μm, L_2 = 883.5 μm (*a*); L_1 = 664.8 μm, the values of L_2 are given in the captions (*b*–*d*)

Demonstration of the proposed approach based on simulation

To illustrate the results of the proposed approach and reduce the systematic error of signal demodulation from multiplexed EFFPIs, we carried out numerical simulation in the MATLAB software package. The spectral transfer function $S(f)$ was calculate by Eq. (1) in the frequency range $\Delta f = 9.99$ THz with the center of the frequency scanning range $f_0 = 193.54$ THz (this corresponds to the range from 1510 to 1590 nm in the wavelength scale), the frequency step $\Delta = 5$ GHz and readout number $N = 2000$. The mirror reflectivities $R_{1,2} = 3.5\%$ were used as the parameters of the multiplexed EFFPIs. The value $w_0 = 5.2$ μm (corresponding to the mode field diameter (MFD) of a standard single-mode fiber for a wavelength of 1550 nm), assumed to be fixed, was selected for the Gaussian beam radius used in expression (1). Based on these values, we calculated a set of readout sequences $S(f)$ (5001 sequences); the gap L_1 of the first EFFPI was taken to be constant, with $L_1 = 664.8$ μm, and the gap L_2 of the second EFFPI was linearly increased from one STF to another in the range from 861 to 906 μm at a step of 10 nm. Notice that the given simulation parameters were selected based on the experimental data (described and analyzed below). Fig. 2, *a* shows a graph of the calculated STF for $L_2 = 883.5$ μm.

The mean STF was found from the calculated readouts, with the sequence then centered for subsequent signal processing. This was done to minimize the parasitic effect from the constant component of STF on the results of signal processing by DFT. Next, a 200,000-point DFT $V(\omega)$ was calculated for each centered STF. A rectangular single window $w(i) = 1$ was chosen as the initial one, where $i = 1, 0, N - 1$. Its Fourier transform is found by the following formula:

$$W(\omega) = \frac{\sin(\omega N/2)}{\sin(N/2)} \exp\left[-j\omega(N-1)/2\right]. \quad (14)$$

Fig. 2,*b* shows variation in $|V(\omega)|$ for three values of L_2: 876.0, 883.5 and 891.0 μm at $L_1 = 664.8$ μm. In addition to the frequency scale in radians, a scale L values in μm was added to the figure for convenience (recalculated using expression (4)). Evidently, the position of the maxima $|V(\omega)|$ deviates from the given values of L_1 and L_2, pointing to the systematic error in determining the gap lengths.

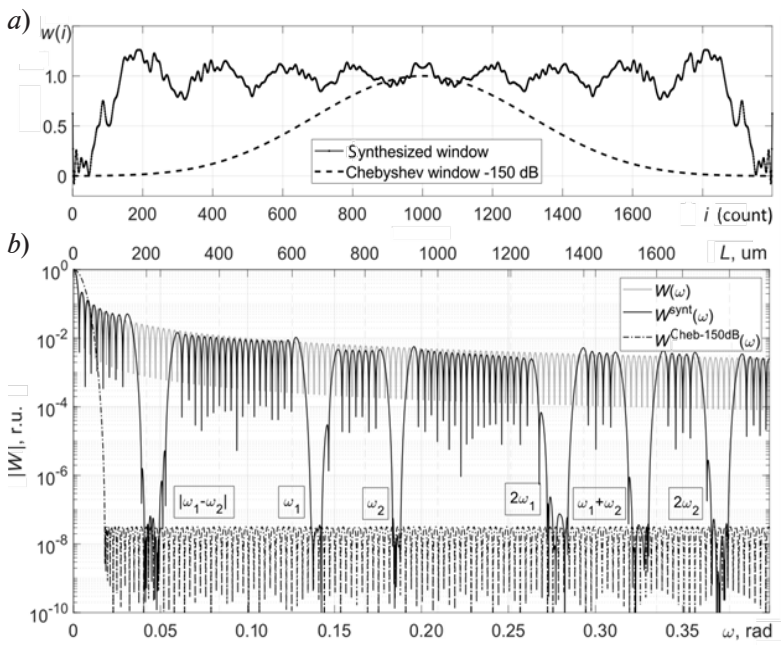

Fig. 3. Comparison of dependences for the window we synthesized and the standard Dolph–Chebyshev window: *a* shows the dependences of *w* on the readout number; *b* shows the normalized dependences of the Fourier transform magnitude. for $w(i)$, $w^{synt}(i)$ and $w^{\text{Cheb-150dB}}(i)$

Next, following the above algorithm, we synthesized the window w^{synt} satisfying condition (7). The Fourier transform function of a rectangular window was selected as the basis for calculating the window by Eqs. (8), (9), i.e., $G(\omega) = W(\omega)$. To find the optimal set $\{\omega_k\}$, the function $r\{\mathrm{ENBW}(w^C)\}$ in condition (13) was take to equal zero, since in this case the value of the ENBW window during synthesis was close to unity.

The window w^{synt} was synthesized assuming that the sensor gap varied within the range of 15 μm with the centers L_{10} = 664.8 μm, L_{20} = 883.5 μm. The following parameters in condition (13) were selected for these parameters of the optical circuit:

circular frequencies $\omega_1 = 0.1392$ rad and $\omega_2 = 0.1851$ rad;
frequency bands $\Delta\omega_1 = \Delta\omega_2 = 0.0034$ rad.

These values of the bands correspond to the above gap variation range plus a margin of 1 μm, taken to account for the potential displacement due to systematic error (the displacement was estimated from the data in Fig. 2, *b*–*d*). The following parameters were adopted for genetic optimization:

population size 500; number of points in the set $\{\omega_k\}$ $K/2 = 90$;
coefficient $k = 2$.

Fig. 3 shows graphs of the synthesized window (weight function) $w^{synt}(i)$ and the Fourier-transformed $W^{Synt}(\omega)$ obtained with this window. Apparently, six deep dips were obtained at the level of at least $3\cdot10^{-8}$ relative to the maximum of the main lobe. Outside the dip region, the dependence $W^{Synt}(\omega)$ is close to the Fourier transform of the rectangular window $W(\omega)$ shown in this figure. The main lobe broadened insignificantly in this case. The ENBW value for w^{synt} was 1.0737, compared to a unit ENBW (1.000) for a rectangular window.

Notably, the same nulls in the side lobes can be obtained using standard windows. For example, it is convenient to compare the synthesized window with the Dolph–Chebyshev window, since the latter allows setting an arbitrary level for the side lobes, which are located at the same level in the entire frequency band. To obtain dips at a level of about $3\cdot10^{-8}$, we should use the Dolph–Chebyshev window with a side lobe level of -150dB (we denote it as $w^{\text{Cheb-150dB}}$, and its Fourier transform as $W^{\text{Cheb-150dB}}$), whose ENBW value is 1.9814, which is 1.8 times higher than that of the synthesized window $w^{synt}(\omega)$. Moreover, the optimization algorithm apparently reduced the level of $K/2$ to 58 from the initial value of 90, indicating that it was chosen correctly.

The set of functions $S(f)$ was used to calculate the corresponding dependences $V(\omega)$. Then, the positions of L_{1m} and L_{2m} of two main maxima were found for each $V(\omega)$, taking into account expression (4). They were found by interpolating the parabola at the three maximum points $|V(\omega)|$ in the region of the peak and determining its vertex. Similarly, the positions of the two main maxima L_{1m}^{synt} and L_{2m}^{synt} were found for all $V(\omega)$. The maxima were recalculated from the set of STF and multiplied by the window w^{synt}. In addition, the positions of peaks in $L_{1m}^{\text{Cheb-150dB}}$ and $L_{2m}^{\text{Cheb-150dB}}$ were found for $|V(\omega)|$ by multiplying STF by the window $w^{\text{Cheb-150dB}}$. The results are shown in Fig. 4.

It is clear from the graphs in Fig. 4, *a* and *c* that the systematic error in determining L_1 and L_2 with a rectangular window has a pronounced oscillating character. The period of rapid oscillations is associated with the variation in L, resulting in a phase shift of the harmonic by 2π in the sequence $v(i)$. The period of slow oscillations is due to displacement of the parasitic side lobe system relative to the frequency of the target maximum $V(w)$.

Importantly, the oscillations were successfully reduced by five orders of magnitude for the selected gap variation range using the synthesized window: this can be seen from comparing the graphs in Fig. 4, *a* and *b*, as well as Fig. 4, *c* and *d*.

The window $w^{\text{Cheb-150dB}}$ yields the same reduction (see Fig. 4, *b* and *d*), eliminating the drawback of the standard window that consists in increased ENBW value, since no noise was introduced in this simulation.

Experimental demonstration of the proposed approach

The proposed approach was tested through an experiment using the scheme discussed above (see Fig. 1). Each EFFPI was constructed using two patch cords with SMF-28 fiber, spliced with APC-type (tapered) connectors on one side and UPC-type (straight) connectors on the other.

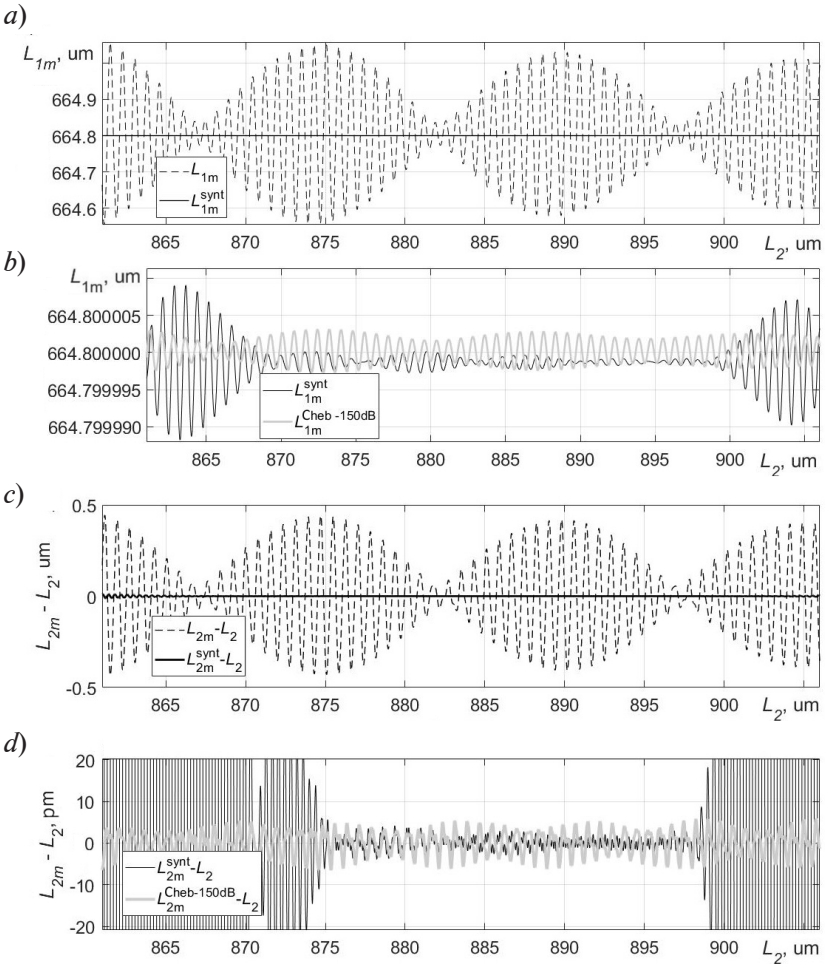

Fig. 4. Positions of the main maxima as function of given L_2 value: L_{1m} and L_{1m}^{synt} (*a*), L_{1m}^{synt} and $L_{1m}^{\text{Cheb-150dB}}$ (*b*), $L_{2m} - L_2$ and $L_{2m}^{synt} - L_2$ (*c*), $L_{2m}^{synt} - L_2$ and $L_{1m}^{\text{Cheb-150dB}} - L_2$ (*d*)

The straight ends of the patchcords were combined with a gap in a standard connector plug. Thus, the reflection coefficients at the quartz/air boundary were $R \approx \%3.5$. One of the patchcords was connected to a 50:50 coupler, and the other was left free; the parasitic reflections of light from this end of the patchcord were negligible (due to the tapered end). The first port of the coupler was connected to the optical interrogator NI-PXIe-4844, which was capable of detecting STF in the range of 1510–1590 nm with a uniform wavelength step of 4 pm. The appearance of the experimental setup is shown in Fig. 5,*a*.

The gap of the first EFFPI was set to approximately $L_1 = 664.8$ μm during the experiment, and subsequently left unchanged. The gap of the second EFFPI was slowly reduced from 906 to 861 μm. The recorded STFs were then interpolated from a uniform wavelength scale to a uniform optical frequency scale with the range $\Delta f = 9.99$ THz, the band center $f_0 = 193.54$ THz, the frequency step $\Delta = 5$ GHz and the number of readouts $N = 2000$. Fig. 5, *b* shows an example of the obtained $S(f)$ for the values $L_1 \approx 664.8$ μm and $L_2 \approx 906$ μm. The mean value was found from the obtained STF readouts; the sequence was then centered and its Fourier transform $V(\omega)$ determined by DTF. Fig. 5,*c* shows an example of the resulting function $|V(\omega)|$ for the same values of L_1 and L_2.

The positions L_{1m} and L_{2m} of the two main maxima $|V(\omega)|$ were found for each dependence $V(\omega)$. The function $V(\omega)$ was also determined for the STF multiplied by the synthesized window w^{synt} (the same as in the simulation), and the positions of the two main maxima L_{1m}^{synt} and L_{2m}^{synt} were found. The computational results are shown in Fig. 6,*a* and *b*.

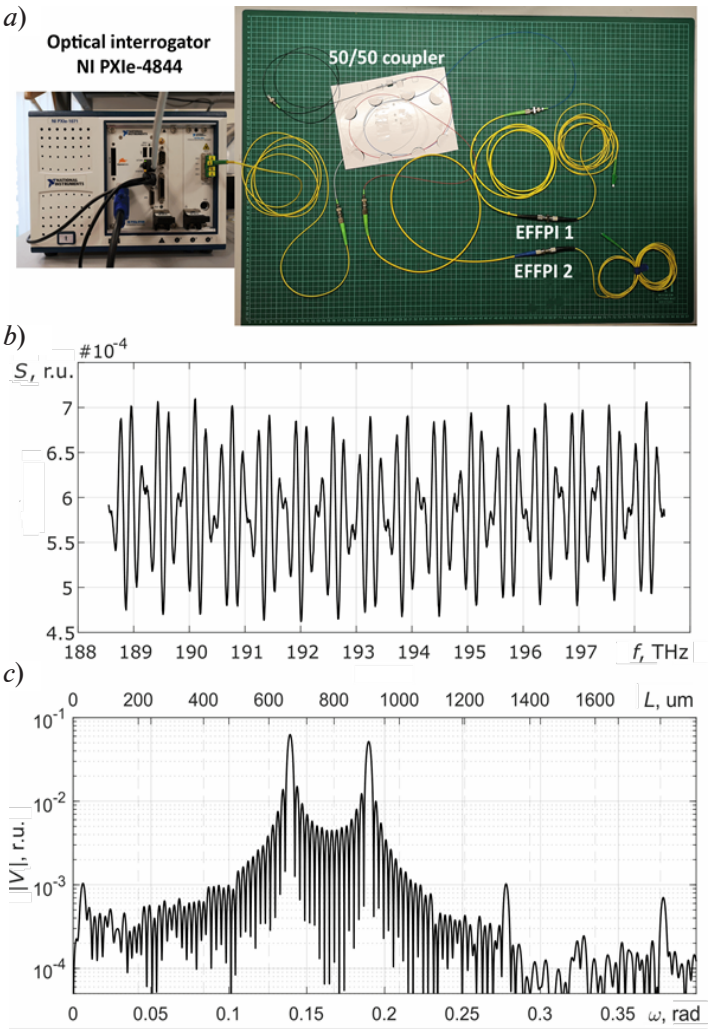

Fig. 5. Photograph of experimental setup (*a*) and examples of experimental data obtained: dependencies $S(f)$ (*b*) and $|V(\omega)|$ (*c*) for $L_1 \approx 664.8$ μm and $L_2 \approx 906$ μm

Table

Error estimation: comparison of results in the presence of noise-generated error

Window (weight function)	σ_{L1m}, nm	ENBW value
Rectangular	8.3. (noise only)	1.0000
	121	
Synthesized	9.0	1.0737
Dolph–Chebyshev: –60 dB	17.0	1.5180
–70 dB	13.4	1.6336
–80 dB	14.0	1.7432
–90 dB	15.0	1.8445
–100 dB	16.1	1.9414

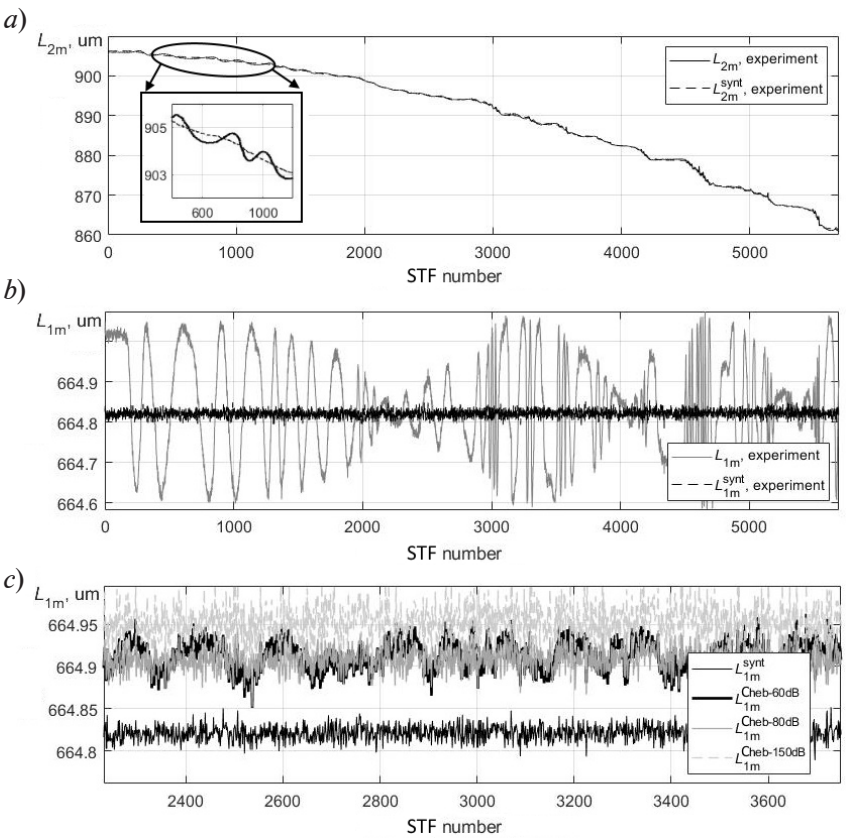

Fig. 6. Processed experimental dependences on the STF number: positions of the main peaks L_{2m} and L_{2m}^{synt} (*a*), L_{1m} and L_{1m}^{synt} (*b*), L_{1m}^{synt}, $L_{1m}^{\text{Cheb-60dB}}$, $L_{1m}^{\text{Cheb-80dB}}$, $L_{1m}^{\text{Cheb-150dB}}$ (*c*)

As seen from Fig. 6, *a*, the value of L_{2m} decreases from one STF to another; the reason for non-uniform variation in L_{2m} is that the gap L_2 was decreased manually. As predicted by the simulation results, this decrease is accompanied by an oscillating error of finding the value of L_{1m}, as can be clearly seen in Fig. 6, *b*. A synthesized window allowed to virtually suppress the oscillating error, which follows from the nature of the L_{1m}^{synt} curve in the same figure. Moreover, suppression of the oscillating error is also clear from comparing the L_{2m} and L_{2m}^{synt} curves (see the inset in Fig. 6,*a*).

Unlike the simulation results, noise is observed in the experiment, which demonstrates the advantage of the synthesized window over the standard ones.

Let us analyze the results obtained for suppressing the systematic error in the presence of the noise-induced error. As noted earlier, the advantage of the synthesized window is a slight increase in the ENBW value compared to standard windows. The analysis was carried out for the values found for L_{1m}. The RMS error of L_{1m} upon variation in L_2 (i.e., in the presence of oscillations due to systematic error) with a rectangular window was σ_{L1m} = 121 nm. The RMS error of L_{1m}^{synt} with the synthesized window was $\sigma_{L1msynt}$ = 9 nm. Thus, the RMS error of the values of L_{1m} found with varying L_2 decreased by 13 times, starting to depend mainly on the noise from the measuring equipment.

Only the noise error can be estimated for the region where the value of L_2 remained unchanged (the first 100 STFs recorded). In this case, the values obtained are σ_{L1m_noise} = 8.2 nm and $\sigma_{L1msynt}$ = 8.7 nm, i.e., the noise increment is insignificant (by only 1.06 times). Recall that the ENBW value of the synthesized window is 1.07 times higher than that of the rectangular one. These results are summarized in Table.

In addition to the presented analysis, let us compare the effectiveness of the approach using a synthesized window with the standard one considering the example of the Dolph–Chebyshev window. To this end, we additionally defined the values of L_{1m}^{Cheb}using Dolph–Chebyshev windows

with different levels of side lobes (three dependences of this type are shown in Fig. 6,*c*). As seen from the figure, the systematic error prevails over the noise error at the level of -60 dB, becoming less noticeable against the increased noise error at the level of -80 dB; it is not detected at all at the level of -150 dB. The results for this analysis of the quantity L_{1m}^{Cheb} are also given in Table. The obtained data indicate that the minimum value of RMS error (σ_{L1m}) among the L_{1m}^{Cheb} found is observed for the level of -70 dB and is equal to $\sigma_{L1m\text{Cheb}}$ = 13.4 nm. This level reflects the trade-off between systematic bias and noise figure. In this particular case, a synthesized window yielded RMS deviations that were 1.49 times better than for the measurements carried out with a standard Dolph–Chebyshev window at -70 dB. Notably, the ENBW value of the synthesized window was lower by 1.52 times.

Fig. 6 shows that the values of *L* found experimentally have different constant offsets with different windows, which was not observed in numerical simulations and, generally speaking, is a factor of the constant error in demodulation. One possible reason for the difference is that the noise present in the recorded STFs is not white; the other option is that additional parasitic harmonics (for example, from parasitic interferometers in the fiber-optic channel) may be present in the signal and exert some influence. However, search for the causes of this effect is a subject for separate study and is beyond the scope of our paper.

Conclusion

We have analyzed the problems of signal demodulation in interferometric fiber-optic systems with multiplexed interferometric sensors during spectral interrogation with the recorded STF processed by DTF. Both simulation and experiments confirmed the presence of a considerable systematic error in measuring the frequencies of harmonic components of STF. A specially synthesized weight window is proposed as a solution for reducing the systematic error without a significant increase in the noise error. A specific example was considered numerically and experimentally to confirm the effectiveness of the proposed approach compared to the standard Dolph–Chebyshev window. The procedure proposed can be used in any problems related to estimation of frequencies and phases of polyharmonic signals.

REFERENCES

1. **Udd E., Spillman. Jr. W. B.** (Eds.), Fiber optic sensors: An introduction for engineers and scientists, 2nd ed., John Wiley & Sons Inc., New York, 2011.
2. **Liokumovich L. B.**, Volokonno-opticheskiye interferometricheskiye izmereniya [Fiber optic interferometric measurements], Polytech. University Press, St. Petersburg, 2007 (in Russian).
3. **Ushakov N., Liokumovich L.** Resolution limits of extrinsic Fabry – Perot interferometric displacement sensors utilizing wavelength scanning interrogation // Appl. Optics. 53 (23) (2014) 5092-5099.
4. **Ushakov N. A., Liokumovich L. B.,** Multiplexed extrinsic fiber Fabry –Pérot interferometric sensors: resolution limits, J. Lightwave Technol. 33 (9) (2015) 1683–1690.
5. **Ushakov N. A., Markvart A. A., Liokumovich L. B.,** Pulse wave velocity measurement with multiplexed fiber optic Fabry – Pérot interferometric sensors, IEEE Sens. J. 20 (19) (2020) 11302–11312.
6. **Oppenheim A. V., Schafer R. W.,** Discrete-time signal processing, 2nd ed., Pearson Education, London, 2007.
7. **Dvorkovich V. P., Dvorkovich A. V.,** Okonnyye funktsii dlya garmonicheskogo analiza signalov [Window functions for harmonic signal analysis, 2nd ed.], Tekhnosfera Publishing, Moscow, 2016 (in Russian).
8. **Baranov I. V., Ezerski V. V.,** Minimization to inaccuracy of the measurement of the distance under digital processing signal in FM radar for industrial application], Bulletin of Ryazan State Radioengineering University. (24) (2008) 55–60.
9. **Davydochkin V. M.,** Vesovyye funktsii i algoritmy dlya povysheniya tochnosti otsenki chastoty i amplitudy vyborki garmonicheskogo signala na fone signalopodobnykh pomekh, Avtoref. dis. kand. tekhn. nauk [Weighting functions and algorithms for improving the accuracy of estimating the frequency and amplitude of a harmonic signal sample against the background of signal-like noise], Synopsis of Thesis for Cand. Techn. Sci., Ryazan, 2008.

10. **Davydochkin V. M., Davydochkina S. V.,** Window functions for the digitial adaptive harmonic analysis of the signals with the miltimodal spectrum, J. Radioengineering. (9) (2009) 11–20 (in Russian).

11. **Markvart A. A., Liokumovich L. B., Ushakov N. A.,** Estimating the measurement resolution of an arbitrary finesse fiber-optic Fabry – Perot interferometer via Cramer – Rao bound, St. Petersburg Polytechnical State University Journal. Physics and Mathematics. 14 (4) (2021) 172–189.

12. **Zelkin E. G., Sokolov V. G.,** Metody sinteza antenn: Fazirovannyye antennyye reshetki i antenny s nepreryvnym raskryvom [Antenna synthesis methods: Phased antenna array and antennas with continuous aperture], Sovetskoye Radio Publishing, Moscow, 1980 (in Russian).

13. **Mangoud M. A.-A., Elragal H. M.,** Antenna array pattern synthesis and wide null control using enhanced particle swarm optimization, Progr. Electromagn. Res. B. 17 (2009) 1–14.

14. **Vendik O. G., Kalinin S. A., Kozlov D. S.**, Phased array with controlled directivity pattern, Techn. Phys. 58 (10) (2013) 1507–1511.

15. **Kozlov D. S.,** Interferentsionnoye formirovaniye diagrammy napravlennosti fazirovannoy antennoy reshetki s podavleniyem izlucheniya v zadannom napravlenii s uchetom vzaimnogo vliyaniya izluchateley. Avtoref. dis. kand. fiz.-mat. nauk [Interference beamforming of a phased antenna array with suppression of radiation in a given direction, taking into account the mutual influence of emitters], Synopsis of Thesis for Cand. Phys.-Math. Sci., St. Petersburg, 2016.

16. **Markvart A. A., Ushakov N. A., Liokumovich L. B.**, Application of weight window synthesis in a discrete Fourier transform to reduce demodulation errors of signals of multiplexed fiber-optic sensors, In book: Proc. 24-th Int. Conf. "Digital Signal Processing and its Applications" (DSPA-2022), Publ. by A. S. Popov Russian Scientific and Technical Society of Radio Engineering, Electronics and Communications Press. (24) (2022) 177–182.

17. **Sivanandam S. N., Deepa S. N.,** Introduction to genetic algorithms, Berlin, Heidelberg, Springer, 2008.

18. MathWorks Help Center. Genetic Algorithm, https://www.mathworks.com/help/gads/genetic-algorithm.html, Accessed June 01, 2022.

СПИСОК ЛИТЕРАТУРЫ

1. Волоконно-оптические датчики. Вводный курс для инженеров и научных работников. Под ред. Э. Удда. Пер. с англ. М.: Техносфера, 2008. 520 с.

2. Лиокумович **Л. Б.** Волоконно-оптические интерферометрические измерения. СПб.: Изд-во Политехнического ун-та, 2007. 110 с.

3. **Ushakov N., Liokumovich L**. Resolution limits of extrinsic Fabry – Perot interferometric displacement sensors utilizing wavelength scanning interrogation // Applied Optics. 2014. Vol. 53. No. 23. Pp. 5092–5099.

4. **Ushakov N. A., Liokumovich L. B.** Multiplexed extrinsic fiber Fabry – Perot interferometric sensors: resolution limits // Journal of Lightwave Technology. 2015. Vol. 33. No. 9. Pp. 1683–1690.

5. **Ushakov N. A., Markvart A. A., Liokumovich L. B.** Pulse wave velocity measurement with multiplexed fiber optic Fabry – Pérot interferometric sensors // IEEE Sensors Journal. 2020. Vol. 20. No. 19. Pp. 11302–11312.

6. **Оппенгейм А., Шафер Р.** Цифровая обработка сигналов. 3-е изд. Пер. с англ. М.: Техносфера, 2007. 1048 с.

7. **Дворкович В. П., Дворкович А. В.** Оконные функции для гармонического анализа сигналов. 2-е изд. М.: Техносфера, 2016. 217 с.

8. **Баранов И. В., Езерский В. В.** Минимизация погрешности измерения расстояния при цифровой обработке сигналов частотных дальномеров промышленного применения // Вестник Рязанского государственного радиотехнического университета. 2008. № 24. С. 55–60.

9. **Давыдочкин В. М.** Весовые функции и алгоритмы для повышения точности оценки частоты и амплитуды выборки гармонического сигнала на фоне сигналоподобных помех. Автореф. дис. канд. техн. наук. Рязань: Академия права и управления ФСИН, 2008. 16 с.

10. **Давыдочкин В. М., Давыдочкина С. В.** Весовые функции для цифрового адаптивного гармонического анализа сигналов с многомодовым спектром // Радиотехника. 2009. № 9. С. 11–20.

11. **Маркварт А. А., Лиокумович Л. Б., Ушаков Н. А.** Соотношение Рао – Крамера для оценки разрешающей способности измерений с волоконно-оптическим интерферометром Фабри – Перо произвольной добротности // Научно-технические ведомости СПбГПУ. Физико-математические науки. 2021. Т. 14. № 4. С. 172–189.

12. **Зелкин Е. Г., Соколов В. Г.** Методы синтеза антенн: фазированные антенные решетки и антенны с непрерывным раскрывом. М.: Советское радио, 1980. 294 с.

13. **Mangoud M. A.-A., Elragal H. M.** Antenna array pattern synthesis and wide null control using enhanced particle swarm optimization // Progress in Electromagnetics Research B. 2009. Vol. 17. Pp. 1–14.

14. **Вендик О. Г., Калинин С. А., Козлов Д. С.** Фазированная антенная решетка с управляемой формой диаграммы направленности // Журнал технической физики. 2013. Т. 83. № 10. С. 117–121.

15. **Козлов Д. С.** Интерференционное формирование диаграммы направленности фазированной антенной решетки с подавлением излучения в заданном направлении с учетом взаимного влияния излучателей. Автореф. дис. канд. физ.-мат. наук. СПб: ЛЭТИ, 2016. 16 с.

16. Маркварт **А. А., Ушаков Н. А.,** Лиокумович **Л. Б.** Применение синтеза весовых окон в дискретном преобразовании Фурье для снижения ошибок демодуляции сигналов мультиплексированных волоконно-оптических датчиков // Сборник трудов 24-й Международной конференции «Цифровая обработка сигналов и ее применение» (DSPA-2022). Вып. 24. М.: Изд-во РНТОРЭС имени А. С. Попова, 2022. С. 177–182.

17. **Sivanandam S. N., Deepa S. N.** Introduction to genetic algorithms. Berlin, Heidelberg: Springer, 2008. 442 p.

18. MathWorks Help Center. Genetic Algorithm. Режим доступа: https://www.mathworks.com/help/gads/genetic-algorithm.html (Дата обращения: 01.06.2022).

THE AUTHORS

MARKVART Aleksandr A.
Peter the Great St. Petersburg Polytechnic University
29 Politechnicheskaya St., St. Petersburg, 195251, Russia
markvart_aa@spbstu.ru
ORCID: 0000-0001-8080-0830

LIOKUMOVICH Leonid B.
Peter the Great St. Petersburg Polytechnic University
29 Politechnicheskaya St., St. Petersburg, 195251, Russia
leonid@spbstu.ru
ORCID: 0000-0001-5988-1429

USHAKOV Nikolai A.
Peter the Great St. Petersburg Polytechnic University
29 Politechnicheskaya St., St. Petersburg, 195251, Russia
n.ushakoff@spbstu.ru
ORCID: 0000-0002-3480-2779

СВЕДЕНИЯ ОБ АВТОРАХ

МАРКВАРТ Александр Александрович – *ассистент Высшей школы прикладной физики и космических технологий Санкт-Петербургского политехнического университета Петра Великого.*
195251, Россия, г. Санкт-Петербург, Политехническая ул., 29
markvart_aa@spbstu.ru
ORCID: 0000-0001-8080-0830

ЛИОКУМОВИЧ Леонид Борисович – *доктор физико-математических наук, профессор Высшей школы прикладной физики и космических технологий Санкт-Петербургского политехнического университета Петра Великого.*
195251, Россия, г. Санкт-Петербург, Политехническая ул., 29
leonid@spbstu.ru
ORCID: 0000-0001-5988-1429

УШАКОВ Николай Александрович – *кандидат физико-математических наук, доцент Высшей школы прикладной физики и космических технологий Санкт-Петербургского политехнического университета Петра Великого.*
195251, Россия, г. Санкт-Петербург, Политехническая ул., 29
n.ushakoff@spbstu.ru
ORCID: 0000-0002-3480-2779

Received 20.06.2022. Approved after reviewing 16.08.2022. Accepted 16.08.2022.
Статья поступила в редакцию 20.06.2022. Одобрена после рецензирования 16.08.2022. Принята 16.08.2022.

MECHANICS

Original article
DOI: https://doi.org/10.18721/JPM.15315

FUNCTIONALLY GRADED WEDGE WEAKENED BY A SEMI-INFINITE CRACK

V. V. Tikhomirov✉

Peter the Great St. Petersburg Polytechnic University, St. Petersburg, Russia

✉ victikh@mail.ru

Abstract. In the paper, the problem of a semi-infinite antiplane interface crack located between two functionally graded wedge-shaped regions has been considered. The shear modules of the materials' regions are quadratic functions of the polar angle. This kind of functional inhomogeneity made it possible to express all the components of the elastic field through a single harmonic function. Using the Mellin integral transform, the problem was reduced to the Wiener – Hopf scalar equation, for which an exact solution was obtained. The influence of gradients of elastic properties of materials on the stress intensity coefficient at the crack tip and the singularity value at the angular point of the structure was studied.

Keywords: functionally graded wedge, antiplane interface crack, stress singularity

Citation: Tikhomirov V. V., Functionally graded wedge weakened by a semi-infinite crack, St. Petersburg State Polytechnical University Journal. Physics and Mathematics. 15 (3) (2022) 201–213. DOI: https://doi.org/10.18721/JPM.15315

Научная статья
УДК 539.3
DOI: https://doi.org/10.18721/JPM.15315

ФУНКЦИОНАЛЬНО-ГРАДИЕНТНЫЙ КЛИН, ОСЛАБЛЕННЫЙ ПОЛУБЕСКОНЕЧНОЙ ТРЕЩИНОЙ

В. В. Тихомиров✉

Санкт-Петербургский политехнический университет Петра Великого,

Санкт-Петербург, Россия

✉ victikh@mail.ru

Аннотация. Рассматривается задача о полубесконечной антиплоской интерфейсной трещине, находящейся между двумя функционально-градиентными клиновидными областями. Модули сдвига материалов областей являются квадратичными функциями полярного угла. Такой вид функциональной неоднородности позволяет выразить все компоненты упругого поля через одну гармоническую функцию. С помощью интегрального преобразования Меллина проблема сведена к скалярному уравнению Винера – Хопфа, для которого получено точное решение. Изучено влияние градиентов упругих свойств материалов на коэффициент интенсивности напряжений в вершине трещины и показатель сингулярности в угловой точке структуры.

Ключевые слова: функционально-градиентный клин, антиплоская интерфейсная трещина, сингулярность напряжений

Ссылка для цитирования: Тихомиров В. В. Функционально-градиентный клин, ослабленный полубесконечной трещиной // Научно-технические ведомости СПбГПУ. Физико-математические науки. 2022. Т. 15. № 3. С. 201–213. DOI: https://doi.org/10.18721/JPM.15315

Introduction

Functionally graded materials (FGM) are composites whose mechanical and physical properties reflect the characteristics of their spatially variable microstructure [1, 2]. The concept of FGM was first introduced in the 1980s in Japan, finding wide application in the aerospace and nuclear industries, electronics, optoelectronics, construction and other fields as materials for energy conversion and as biomaterials [3]. Simulations consider FGM as heterogeneous materials, assuming the variation in their properties to be continuous, while their microstructure is not taken into account in this case.

Analysis of stress field singularities in such materials is one of the fundamental problems in linear fracture mechanics [4]. Due to the gradient of elastic properties, the classical nature of stress singularity (square-root in the case of cracks and simple power-law in the case of sharp notches) can be modified in the FGM [5, 6].

Numerous studies have considered fracture in FGM in the plane and antiplane formulations. Confining ourselves to antiplane problems, we should note that one of the first studies in this direction [7] established that the jump in the derivative of the shear modulus (preserving its continuity) does not affect the singularity exponent at the crack tip.

Singular fields in layered structures with functionally graded elements which have defects such as cracks oriented along or perpendicular to the gradient of the shear modulus were considered in [8–11]. The stress-strain state of wedge-shaped regions with gradient properties, including multi-material wedges and sharp notches were described in [5, 6, 12–14].

The dependence of the FGM shear modulus on the coordinates is selected in analytical models from a class of functions for which the equilibrium equations have analytical solutions. Linear or exponential dependences are typically used for the shear modulus. If the elastic module varies arbitrarily, the piecewise linear and piecewise exponential models can be applied [15, 16]. A quadratic dependence of the shear modulus on the polar angle was proposed in an earlier study [13] for gradient material, allowing to express all the components of the elastic field in terms of a single harmonic function under the conditions of an antiplane problem. This approach was used for singularity analysis in the apex of a multi-material wedge [14].

Based on the results obtained in [13], we consider the stress state of a composite wedge with gradient properties varying quadratically in the transverse direction, weakened by a semi-infinite antiplane crack. The effect from the increase and decrease in the stress intensity factor (SIF) at the tip of the crack has been analyzed, as well as the variations in the singularity exponent in the corner of the wedge due to gradient elastic properties of materials, compared to a homogeneous structure.

Problem statement

Consider a semi-infinite mode III interface crack located between two wedge-shaped regions Ω_1 and Ω_2 with the angles α_1 and α_2 (Fig. 1):

$$\Omega_1 = \{(r,\theta): 0 < r < \infty, 0 < \theta < \alpha_1\},\ \Omega_2 = \{(r,\theta): 0 < r < \infty, -\alpha_2 < \theta < 0\},$$

where r, θ are the polar coordinates.

It is assumed that the materials in these regions are functionally graded, and their shear moduli μ_1 and μ_2 are functions of the polar angle. In this case, the functional dependences $\mu_k(\theta)$ (k = 1, 2) are such that the elastic moduli are the same on the ray $\theta = 0$, equal to μ_0, taking the values μ_* at the boundaries $\theta = \alpha_1$ and $\theta = -\alpha_2$.

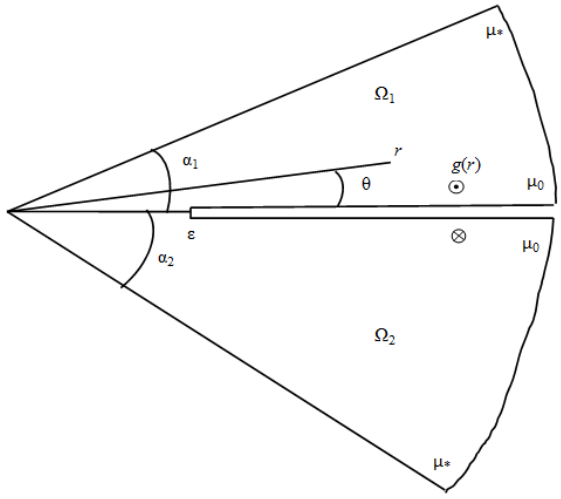

Fig. 1. Functionally graded wedge with semi-infinite interface crack under longitudinal shear: μ_1, μ_2 are the shear moduli at the boundaries of the regions Ω_1 and Ω_2 with graded materials; α_1, α_2, θ, r, ε are the geometric parameters; $g(r)$ is a self-balanced load applied to the edges of the crack

We assume that the tip of crack is located at a distance ε from the apex of a composite wedge. A self-balanced load $g(r)$ is applied to the edges of crack. The contact of materials outside the crack is assumed to be perfect.

The equilibrium equations take the following form in the regions Ω_k with shear moduli varying in the transverse direction

$$\frac{\partial^2 w_k}{\partial r^2}+\frac{1}{r^2}\frac{\partial^2 w_k}{\partial \theta^2}+\frac{1}{r}\frac{\partial w_k}{\partial r}+\frac{1}{\mu_k(\theta)r^2}\frac{d\mu_k}{d\theta}\frac{\partial w_k}{\partial \theta}=0, \tag{1}$$

and the stresses are expressed in terms of displacements $\tilde{w}_k$ by the following formulas:

$$\tau_{\theta zk}=\frac{\mu_k}{r}\frac{\partial w_k}{\partial \theta},\ \tau_{rzk}=\mu_k\frac{\partial w_k}{\partial r}\ \ (k=1,2). \tag{2}$$

Consider a quadratic functional dependence of the shear modulus in FGM on the polar angle, proposed and tested in [12]:

$$\mu_k(\theta)=(a_k\theta+b_k)^2, \tag{3}$$

where the coefficients in this case take the form

$$a_k=(\sqrt{\mu_*}-\sqrt{\mu_0})/\alpha_k,\ b_1=-b_2=\sqrt{\mu_0}.$$

Therefore, the shear modulus of the composite is continuous at the interface $\theta = 0$, and its derivative with respect to the angle θ has a discontinuity.

Searching for displacements in the regions Ω_k in the form

$$w_k(r,\theta)=\frac{1}{a_k\theta+b_k}\tilde{w}_k(r,\theta) \tag{4}$$

from Eqs. (1), we obtain that the functions $\tilde{w}_k(r,\theta)$ are harmonic:

$$\frac{\partial^2 \tilde{w}_k}{\partial r^2} + \frac{1}{r^2}\frac{\partial^2 \tilde{w}_k}{\partial \theta^2} + \frac{1}{r}\frac{\partial \tilde{w}_k}{\partial r} = 0. \tag{5}$$

Using Eqs. (2), we arrive at the following representations for the stresses:

$$\tau_{\theta zk} = -\frac{a_k}{r}\tilde{w}_k(r,\theta) + \frac{a_k\theta + b_k}{\mathrm{r}}\frac{\partial \tilde{w}_k}{\partial \theta}, \tag{6}$$

$$\tau_{rzk} = (a_k\theta + b_k)\frac{\partial \tilde{w}_k}{\partial r}.$$

Solutions of Eqs. (1) at the interface $\theta = 0$ must satisfy mixed conditions

$$\tau_{\theta z1}(r,+0) = \tau_{\theta z2}(r,-0),\ w_1(r,+0) = w_2(r,-0)\ (0 \le r \le 1), \tag{7}$$

$$\tilde{\tau}_{\theta z1}(r,+0) = \tilde{\tau}_{\theta z2}(r,-0) = g(r)\ (1 \le r < \infty),$$

as well as boundary conditions at the edges of the wedge

$$\tau_{\theta z1}(r,\alpha_1) = 0,\ \tau_{\theta z1}(r,-\alpha_2) = 0\ (0 \le r < \infty). \tag{8}$$

Reducing the problem to the Wiener–Hopf equation and its solution

We search for the solution of problem (1)–(8) in the regions Ω_k in the form of Mellin integrals:

$$w_k(r,\theta) = \frac{1}{2\pi i}\int_L W_k(p,\theta) r^{-p} dp\ (k = 1,2), \tag{9}$$

$$W_k(p,\theta) = [A_k(p)\sin p\theta + B_k(p)\cos p\theta]/(a_k\theta + b_k).$$

According to Eqs. (6), stresses are defined by expressions

$$\tau_{\theta zjk}(r,\theta) = \frac{1}{2\pi i}\int_L T_{\theta zjk}(p,\theta) r^{-p-1} dp, \tag{10}$$

$$T_{\theta zjk}(p,\theta) = -a_k[A_k(\mathrm{p})\sin p\theta + B_k(\mathrm{p})\cos p\theta] +$$
$$+(a_k\theta + b_k)p[A_k(p)\cos p\theta - B_k(p)\sin p\theta].$$

According to the regularity conditions, the integration path L is located parallel to an imaginary axis in the strip

$$-\delta_1 < \mathrm{Re}\, p < \delta_2\ (\delta_1, \delta_2 > 0).$$

The quantities $A_k(p)$ and $B_k(p)$ are found from boundary conditions (7) and (8).

Following the scheme implemented in [17], we come to the inhomogeneous Wiener–Hopf equation:

$$F(p)[T_+(p) + G_-(p)] + \mu_0\varepsilon^{-1}W_-(p) = 0\ (p \in L), \tag{11}$$

where

$$T_+(p) = \int_0^1 \tau_{\theta z1}(\varepsilon\rho,+0)\rho^p d\rho,\ G_-(p) = \int_1^\infty g(\varepsilon\rho)\rho^p d\rho,$$

$$W_-(p)=\int_1^\infty \frac{\partial}{\partial\rho}[w_1(\varepsilon\rho,+0)-w_2(\varepsilon\rho,-0)]\rho^p d\rho.$$

Functions $G_-(p)$ and $W_-(p)$ are regular and do not have zeros in in the half-plane Ω_-left from the path L, while $T_+(p)$ does not have zeros in the right half-plane Ω_+ [18]. An imaginary axis can be selected as the path L.

The coefficient of Eq. (11) takes the form

$$F(p)=\mathrm{ctg}(\alpha_1 p)\frac{v(\alpha_1 p)}{u(\alpha_1 p)}+\mathrm{ctg}(\alpha_2 p)\frac{v(\alpha_2 p)}{u(\alpha_2 p)}, \tag{12}$$

where

$$u(x)=1+m^{-1}(m-1)^2x^{-2}[1-x\mathrm{ctg}(x)], \tag{13}$$

$$v(x)=1+(m-1)x^{-1}\mathrm{tg}(x),\ m=\sqrt{\mu_0/\mu_*}.$$

The parameter m characterizes the relative shear stiffness of the material on the crack line compared to the material on the sides of wedge. The crack is located in the region of locally soft composite material at $0 < m < 1$, and in the region of the locally rigid material at $1 < m < \infty$. The case $m = 1$ corresponds to homogeneous material in the regions Ω_k. The expression given in [17] is obtained from Eqs. (12) and (13) for the coefficient of problem (11).

To factorize function (12), let us represent it in the following form:

$$F(p)=\frac{2}{p}K(p), \tag{14}$$

$$K(p)=X(p)\Phi(p),\ X(p)=p\mathrm{ctg}(\alpha_1 p),$$

$$\Phi(p)=\frac{1}{2}F_1(p)F_2(p),\ F_1(p)=\frac{v(\alpha_1 p)}{u(\alpha_1 p)},$$

$$F_2(p)=1+\mathrm{tg}(\alpha_1 p)\mathrm{ctg}(\alpha_2 p)\frac{u(\alpha_1 p)v(\alpha_2 p)}{u(\alpha_2 p)v(\alpha_1 p)}.$$

Notice that the function $F_2(p) = 2$ at $\alpha_1 = \alpha_2$, while the function $F_1(p) = 1$ for a homogeneous medium.

Factorization of the function $X(p)$ is carried in an elementary way [18]:

$$X(p)=X_+(p)X_-^{-1}(p), \tag{15}$$

$$X_+(p)=\sqrt{\frac{\pi}{\alpha_1}}\frac{\Gamma(1+p\alpha_1/\pi)}{\Gamma(1/2+p\alpha_1/\pi)},\ X_-(p)=\sqrt{\frac{\alpha_1}{\pi}}\frac{\Gamma(1/2-\alpha_1 p/\pi)}{\Gamma(1-\alpha_1 p/\pi)}.$$

The function $\Phi(it)$ is continuous on the imaginary axis of the function at $p = it$, has no zeros and poles, its index is zero and it exponentially tends to unity at $t \to \infty$. Therefore, in accordance with the data from [18],

$$\Phi(p)=\frac{\Phi_+(p)}{\Phi_-(p)},\ \Phi_\pm(p)=\exp\left[-\frac{1}{2\pi i}\int_L\frac{\ln\Phi(t)}{t-p}dt\right]\ (p\notin L). \tag{16}$$

Because the function $\Phi(p)$ is even, analytic functions (16) in the regions Ω_+ and Ω_- can be represented as

$$\Phi_{\pm}(p) = \exp\left[\frac{p}{\pi}\int_0^{\infty}\frac{\ln\Phi(i\xi)}{\xi^2+p^2}d\xi\right].$$

Using Eqs. (14)–(16), regrouping the terms in Eqs. (11) and applying Liouville's theorem [18], we obtain:

$$\Phi_+(p)X_+(p)T_+(p)+Q_+(p) = -\frac{\mu_1 p}{2\varepsilon}W_-(p)\Phi_-(p)X_-(p)-Q_-(p) = J(p), \tag{17}$$

where

$$Q_{\pm}(p) = \mp\frac{1}{2\pi i}\int_L \frac{Q(t)}{t-p}dt,\ Q(t) = \frac{t}{2}\Phi_-(t)X_-(t)F(t)G_-(t). \tag{18}$$

Estimating the terms in equality (16) with $p \to \infty$, we can conclude that the unified analytic function is $J(p) = const = C$. Let us find this constant from Eq. (17) at $p = 0$. In view of Eq. (18), we find that

$$C = C_* G_-(0) - \frac{1}{4\pi i}\int_L \Phi_-(\mathrm{t})X_-(p)F(t)G_-(t)dt, \tag{19}$$

$$C_* = \Phi_+(0)X_+(0) = \sqrt{\frac{3m^2(\alpha_1+\alpha_2)}{2\alpha_1\alpha_2(m^2+m+1)}}.$$

To calculate the integral in Eq. (19), we use Cauchy's residue theorem. The poles of the integrand in the left half-plane are the poles of $F(t)$. It follows from representation (12) that they are determined by the negative roots of the equation

$$mx^2\sin x + (m-1)^2(\sin x - x\cos x) = 0,$$

lying in the intervals

$$-(n+0.5)\pi < -x_n < -n\pi\ (n = 1, 2, \ldots).$$

There are two groups of poles: $t_{nj} = -x_n/\alpha_j$ ($j = 1, 2$).

We assume that concentrated forces with the magnitude T_0 are applied to the edges of the crack at a distance r_0 from the apex of the wedge. In this case,

$$g(r) = -T_0\delta(r-r_0),$$

where $\delta(r - r_0)$ is the Dirac delta function, while

$$G_-(p) = -T_0/\varepsilon(r_0/\varepsilon)^p.$$

As a result, we obtain from Eq. (19) that

$$C = \frac{T_0}{\varepsilon}\left[C_* + \frac{1}{2}\sqrt{\frac{\alpha_1}{\pi}}\sum_{j=1}^{2}\sum_{n=1}^{\infty}a_{nj}\left(\frac{\varepsilon}{r_0}\right)^{x_n/\alpha_j}\right], \tag{20}$$

where

$$a_{nj} = \frac{1}{\alpha_j} \frac{\Gamma(1/2 - \alpha_1 t_{nj}/\pi)}{\Gamma(1 - \alpha_1 t_{nj}/\pi)} \Phi_-(t_{nj}) b(x_n),$$

$$b(x_n) = \frac{x_n \cos x_n + (m-1)\sin x_n}{x_n \cos x_n + (m + m^{-1})\sin x_n}.$$

Using the procedure based on Abel-type theorem [18] (used in [17]), we conclude that the asymptotic expansion of the stresses on the crack line with $r \to \varepsilon - 0$ takes the form

$$\tau_{\theta z1}(r) \sim C\sqrt{\frac{\varepsilon}{\pi}} \frac{1}{\sqrt{\varepsilon - r}}. \tag{21}$$

We define the stress intensity factor (SIF) at the crack tip by the formula

$$K_{\text{III}} = \lim_{r \to \varepsilon - 0} \sqrt{2\pi(\varepsilon - r)}\tau_{\theta z1}(r).$$

Then, using asymptote (21), we obtain:

$$K_{\text{III}}(\alpha_1, \alpha_2, m, \varepsilon/r_0) = \sqrt{2\varepsilon}C. \tag{22}$$

To examine the effect from the gradient of the material, we introduce a normalized SIF of the form

$$N = K_{III} / K_{III}^0,$$

where K_{III}^0 is the SIF at the tip of the crack located in a homogeneous wedge.

According to [17], in the case of geometric symmetry, i.e., at $\alpha_1 = \alpha_2 = \alpha$, such a SIF takes the form

$$K_{\text{III}}^0 = T_0 \sqrt{\frac{2}{\alpha\varepsilon}} \frac{r_0^{\pi/(2\alpha)}}{\sqrt{r_0^{\pi/\alpha} - \varepsilon^{\pi/\alpha}}}. \tag{23}$$

It follows from Eqs. (20)–(23) that the crack behaves unsteadily at small distances between the crack tip and the angular point of the wedge in both a homogeneous and a gradient material, since $K_{\text{III}} \to \infty$ at $\varepsilon \to 0$.

The dependence of the normalized SIF at the tip of the crack located in the composite functionally graded half-plane at $\alpha_1 = \alpha_2 = \pi/2$ on the relative distance ε/r_0 for different values of relative shear stiffness is shown in Fig. 2. If $m < 1$, the gradient of elastic properties produces a significant decrease in the magnitude of SIF compared to homogeneous material. At the same time, a decrease in the parameter m produces increasing differences in SIF values for the inhomogeneous and homogeneous cases. Conversely, the stiffening of the material along the ray $\theta = 0$ ($m > 1$) produces an increase in the SIF at the tip of the crack. These trends in the behavior of the normalized SIF occur at all other wedge opening angles (Fig. 3).

Stress singularity in the tip of the wedge

We examine the stress fields at the tip of the wedge for $r \to 0$. The tangential stresses along the ray $\theta = 0$ take the form

$$\tau_{\theta zj}(r, 0) = \frac{1}{2\pi i} \int_L [T_+(p) + G_-(p)] \left(\frac{r}{\varepsilon}\right)^{-p-1} dp. \tag{24}$$

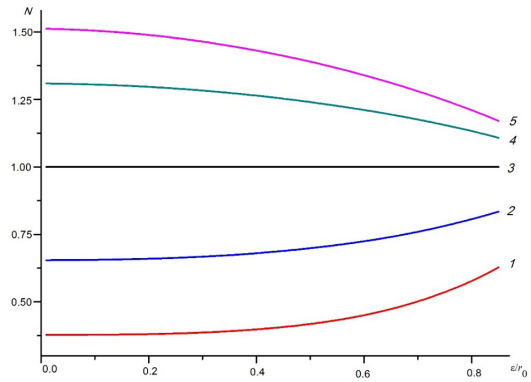

Fig. 2. Dependences of normalized SIF in the tip of the crack located in the gradient half-plane $\alpha_1 = \alpha_2 = 90°$, on the parameter ε/r_0 for different values of the relative shear stiffness m: 0.25 (*1*), 0.50 (*2*), 1.0 (*3*), 2.0 (*4*), 4.0 (*5*)

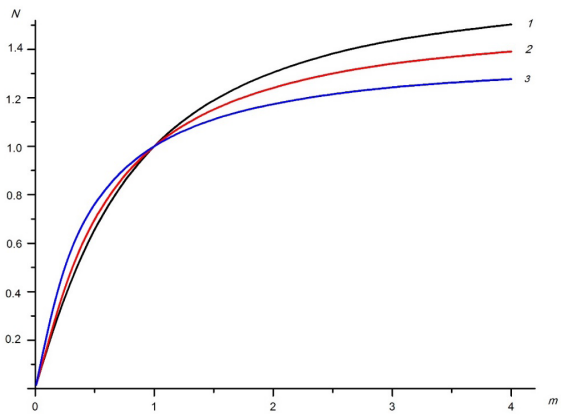

Fig. 3. Dependences of normalized SIF at the crack tip on the relative shear stiffness m at $\varepsilon/r_0 = 0.5$ for different values of the angle $\alpha = \alpha_1 = \alpha_2$: 30° (*1*), 90° (*2*), 180° (*3*)

Using Eq. (11) and Eqs. (14), (17) for the integrand, we obtain the following representation:

$$T_+(p) + G_-(p) = \frac{2\left[C + Q_-(p)\right]}{pK_-(p)F(p)}.$$

Based on this representation and using Eqs. (12), (13) and (24), we obtain the following expression for the stresses in the segment $0 < r < \varepsilon$ at $\theta = 0$

$$\tau_{\theta zj}(r,0) = \frac{1}{m\pi i}\int_L Y(p)\frac{u_*(\alpha_1 p)u_*(\alpha_2 p)}{\Delta(p)}\left(\frac{r}{\varepsilon}\right)^{-p-1} dp, \tag{25}$$

where

$$Y(p) = \frac{C + Q_-(p)}{p^2 X_-(p)\Phi_-(p)},$$

$$u_*(x) = mx^2 \sin x + (m-1)^2(\sin x - x\cos x),$$

$$v_*(x) = x\cos x + (m-1)\sin x.$$

The poles of the integrand in Eq. (25), lying in the half-plane to the left of the path L, are determined by the roots of the equation

$$\Delta(p) = \alpha_1 u_*(\alpha_2 p) v_*(\alpha_1 p) + \alpha_2 u_*(\alpha_1 p) v_*(\alpha_2 p) = 0. \tag{26}$$

The function $\Delta(p)$ is an integer function that has a fourth-order zero at $p = 0$. However, this point is a removable singularity at $m > 0$, and the imaginary axis can be taken as the path L in equality (25). Because the function $\Delta(p)$ is even, each positive root p_k of Eq. (26) corresponds to the negative root $p_{-k} = -p_{-k}$. Since this function does not change its form if α_1 is replaced with α_2 and α_2 with α_1, it is sufficient to consider the case when $\alpha_1 \geq \alpha_2$ next.

Applying the residue theorem for the negative poles of the integrand to integral (25), we obtain the representation of stresses at $r \to 0$ in the form

$$\tau_{\theta zj}(r,0) = D_1(p_1, \alpha_1, \alpha_2, m)\left(\frac{r}{\varepsilon}\right)^{\gamma_1} + D_2(p_2, \alpha_1, \alpha_2, m)\left(\frac{r}{\varepsilon}\right)^{\gamma_2} + \ldots, \tag{27}$$

where $\gamma_k = -1 + p_k$ ($k = 1, 2, \ldots$).

It is evident that the stresses at the tip of the wedge are singular if the roots $0 < p_k < 1$ exist for the given values of the parameters α_1, α_2 and m.

In the case of a geometrically symmetric structure, where $\alpha_1 = \alpha_2 = \alpha$, it follows from Eqs. (25) and (26) that the numbers p_k are the roots of the equation

$$v_*(x) = x\cos x + (m-1)\sin x = 0 \ (x = \alpha p, \ \alpha \leq \pi). \tag{28}$$

This equation has no complex roots, and there is a single root in the interval $(0, \pi)$ for any $0 < m < \infty$, so that $0 < x_1 \leq \pi/2$ for $m \leq 1$ and $\pi/2 < x_1 < \pi$ for $m > 1$. As the relative shear stiffness parameter m decreases from unity to zero, the first root of $p_1 = x_1/\alpha$ also decreases from $\pi/(2\alpha)$ to zero. With the magnitude of m changing from unity to infinity (i.e., when the middle section of the wedge is stiffened), this root increases from $\pi/(2\alpha)$ to π/α. The dependence of the singularity exponent $\gamma = \gamma_1$ on the angle α is given in Fig. 4. Evidently, the singularity in the apex of the wedge can only be weak at $m \geq 1$ ($0 < |\gamma| < 1/2$) and occurs only for angles α greater than 90°, the same as in homogeneous material. With an increase in the parameter m, this exponent becomes smaller compared with the homogeneous case, and the range of angles at which the singularity occurs is narrowed down. In contrast to the homogeneous case, the half angles of the wedge opening at which the singularity appears become sharp, and the singularity itself can be both weak and strong ($1/2 < |\gamma| < 1$).

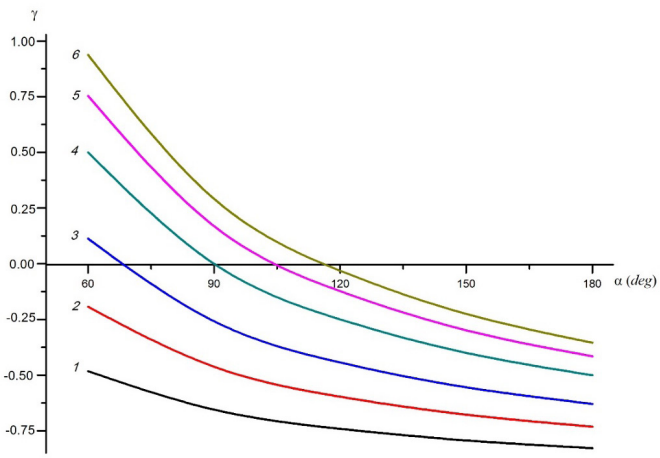

Fig. 4. Dependences of the singularity exponent γ at the tip of the functionally graded wedge on the angle $\alpha = \alpha_1 = \alpha_2$ for different values of the relative stiffness parameter m: 0.10 (*1*), 0.25 (*2*), 0.50 (*3*), 1.0 (*4*), 2.0 (*5*), 4.0 (*6*)

Analyzing the general situation when $\alpha_1 > \alpha_2$ and $\alpha_1 + \alpha_2 \leq 2\pi$, let us consider a number of limiting cases.

In the case of a homogeneous wedge ($m = 1$), it follows from Eqs. (25) and (26) that the characteristic equation takes the form $\sin(\alpha_1 + \alpha_2)p = 0$, where the first root determines the classical singularity

$$\gamma_1 = -1 + \pi/(\alpha_1 + \alpha_2),$$

appearing provided that $\alpha_1 + \alpha_2 > \pi$.

Given high values of the parameter m, Eq. (26) can be written as

$$\alpha_1 f(\alpha_2 p)\sin\alpha_1 p + \alpha_1 f(\alpha_1 p)\sin\alpha_2 p = 0, \tag{29}$$

$$f(x) = \sin x - x\cos x. \tag{30}$$

The first positive zero x_* of function (30) lies in the interval $(\pi, 3\pi/2)$, while $f(x) > 0$ for $0 < x < x_*$ and $f(x) < 0$ for $x_* < x < 2\pi$. It follows then that Eq. (29) has no roots in the interval (0, 1) at $m >> 1$ and angles $0 < \alpha_2 < \alpha_1 \leq \pi$, so there is no singularity at the corner point. Eq. (29) has a single root $1/2 < p_1 < 1$ for angles $x_* \leq \alpha_1 < 2\pi$ and $0 < \alpha_2 < 2\pi - x_*$ ($x_* = 1.4302967\pi$) and large values of m, generating a weak singularity at the corner point. The presence of the root $p_1 < 1$ at $\pi < \alpha_1 < x_*$ is checked numerically.

In the case where the relative stiffness $m \to 0$, Eq. (26) takes the form

$$f(\alpha_1 p) f(\alpha_2 p) = 0, \tag{31}$$

and the function $u_*(\alpha_1 p)u_*(\alpha_2 p)/\Delta(p)$ included in integral (25) tends to unity. However, in reality, the low values of the parameter $m = \sqrt{\mu_0/\mu_*}$ must exceed a certain value $m_* > 0$. At the same time, the limit equation (31) indicates that the first root is located near zero at sufficiently small m. Additionally, another second root of Eq. (26), which is less than unity, exists in the case of sharp notches where the angles satisfy the conditions $x_* \leq \alpha_1 < 2\pi$, $0 < \alpha_2 < 2\pi - x_*$. For example, there are two roots at $\alpha_1 = 3\pi/2$, $\alpha_2 = \pi/6$ and $m = 0.10$: $p_1 = 0.3379652$ and $p_2 = 0.9599646$. Asymptote (27) contains two singular terms. Notably, the singularity generated by the second root is very weak. Numerical analysis indicates that this property is also preserved for other values of the structure parameters.

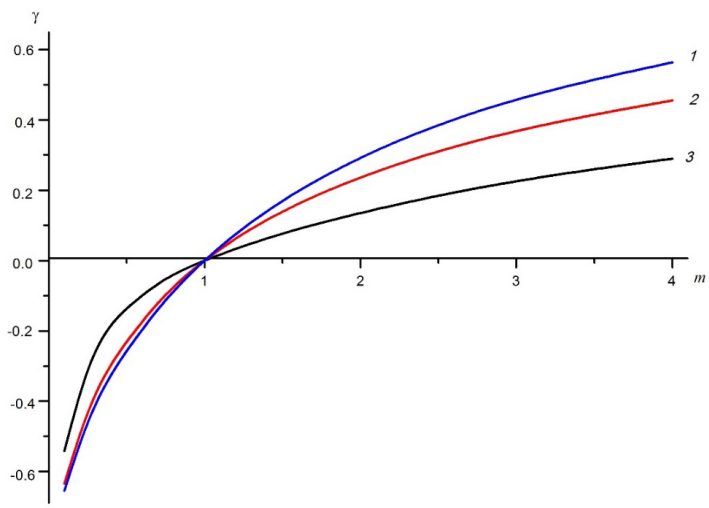

Fig. 5. Dependences of singularity exponent γ at the point $r = 0$ of the functionally graded half-plane on the relative shear stiffness m for different angles: $\alpha_1 = \alpha_2 = 90°$ (*1*); $\alpha_1 = 120°$, $\alpha_2 = 60°$ (*2*); $\alpha_1 = 150°$, $\alpha_2 = 30°$ (*3*)

Next, let us consider two particular cases in more detail. The first one is the case of a functionally graded half-plane with a semi-infinite notch when $\alpha_1 + \alpha_2 = \pi$ ($\alpha_1 \geq \alpha_2$). The analysis indicates that no stress singularity can be detected at $m \geq 1$, while the asymptotic expansion of stresses at the point $r = 0$ has one singular term at $m < 1$. Fig. 5 shows the dependence of the quantity $\gamma_1 = \gamma$ on the relative shear stiffness for different angles α_1 and α_2. Evidently, the inhomogeneity of the material at $m < 1$ produces singular stresses at the smooth half-plane boundary at the point $r = 0$. At the same time, the singularity can be both weak and strong (for fairly low m). The asymmetric position of the crack weakens the singularity to some extent.

In the case of a functionally graded plane with two notched cracks ($\alpha_1 + \alpha_2 = 2\pi$, $\alpha_1 \geq \alpha_2$), Eq. (26) can have one or two roots in the interval (0, 1). For example, if the cracks are collinear ($\alpha_1 + \alpha_2 = \pi$), there is only one root in this interval generating a strong stress singularity at the tip of the unloaded fracture at $m < 1$ and a weak singularity at $m > 1$. In the case of orthogonal cracks, when $\alpha_1 = 3\pi/2$, $\alpha_2 = \pi/2$, the characteristic equation has only one root $1/2 < p_1 < 1$ at $m > 1$, and two roots at $m < 1$: $0 < p_1 < 1/2 < p_2 < 1$. Here the second root is very close to unity and determines a weak singularity.

Conclusion

We used the Wiener–Hopf method to obtain an accurate solution to the problem on the equilibrium of a functionally graded composite wedge weakened by a semi-infinite longitudinal-shear interface crack whose edges are loaded with self-balanced forces. It was assumed that the gradient properties of materials quadratically depend on the angular coordinate. We have considered the effect of the structural parameter on the SIF in the tip of the crack. It is established that the crack becomes unstable as the distance from the crack tip to the wedge corner point tends to zero. The gradient properties of materials can considerably affect the magnitude of SIF. If the middle section of the wedge where the crack is located is relatively softer than the regions near its edges, the SIF decreases substantially compared to its value in the homogeneous material. Conversely, the stiffening of this region tends to increase the SIF compared to the homogeneous case.

The problem of stress singularity at the tip of the functionally graded wedge has a number of peculiarities compared to the case of a homogeneous structure. Unlike homogeneous material, no stress singularity appears at the tip with sufficiently high values of relative shear stiffness, even in the cases of sharp notches. On the other hand, the stresses at the tip can grow indefinitely in functionally graded wedges with sharp opening angles and a soft middle section. Moreover, the relative stiffnesses less than unity correspond to such opening angles of the wedge-shaped region at which the asymptotic expansion of stresses near its tip has two singular terms.

REFERENCES

1. **Jin Z.-H., Batra R. C.**, Some basic fracture mechanics concepts in functionally graded materials, J. Mech. Phys. Sol. 44 (8) (1996) 1221–1235.

2. **Abotula A., Kidane A., Chalivendra V. B., Shukla A.,** Dynamic curving cracks in functionally graded materials under thermomechanical loading, Int. J. Solids Struct. 49 (4) (2012) 583–593.

3. **Mostefa A. H., Merdai S., Mahmoudi N.**, An overview of functionally graded materials 'FGM', In book: Proceedings of the Third International Symposium on Materials and Sustainable Development, Ed. by Abdelbaki B., Safi B., Saidi M. Springer Cham (2018) 267–278.

4. **Carpinteri A., Paggi M.,** Asymptotic analysis in linear elasticity: from the pioneering studies by Westerhardt and Irwin until today, Eng. Fract. Mech. 76 (12) (2009) 1771–1784.

5. **Carpinteri A., Paggi M.,** On the asymptotic stress field in angularly nonhomogeneous materials, Int. J. Fract. 135 (1–4) (2005) 267–283.

6. **Cheng C. Z., Ge S. Y., Yao S. I., et al.,** Singularity analysis for a V-notch with angularly inhomogeneous elastic properties, Int. J. Solids Struct. 78–79 (1) (2016) 138–148.

7. **Erdogan F.,** Crack problems for bonded nonhomogeneous materials under antiplane shear loading, J. Appl. Mech. 52 (4) (1985) 823–828.

8. **Erdogan F., Ozturk M.,** Periodic cracking of functionally graded coatings, Int. J. Eng. Sci. 33 (15) (1995) 2179–2195.

9. **Jin Z.-H., Batra R. C.,** Interface cracking between functionally graded coatings and a substrate under antiplane shear, Int. J. Eng. Sci. 34 (15) (1996) 1705–1716.

10. **Li Y.-D., Lee K. Y.,** An antiplane crack perpendicular to the weak/microdiscontinuos interface in a bi-FGM structure with exponential and linear nonhomogeneities, Int. J. Fract. 146 (4) (2007) 203–211.

11. **Pan H., Song T., Wang Z.,** An analytical model for collinear cracks in functionally graded materials with general mechanical properties, Compos. Struct. 132 (15) (2015) 359–371.

12. **Linkov A., Rybarska-Rusinek L.,** Evaluation of stress concentration in multi-wedge systems with functionally graded wedges, Int. J. Eng. Sci. 61 (1) (2012) 87–93.

13. **Tikhomirov V. V.,** Stress singularity in a top of the composite wedge with internal functionally graded material, St. Petersburg State Polytechnical University Journal. Physics and Mathematics. (3 (225)) (2015) 96–106.

14. **Makhorkin M. I., Skrypochka T. A., Torskyy A. R.,** The stress singularity in a composite wedge of functionally graded materials under antiplane deformation, Math. Model. Comput. 2020. Vol. 7 (1) (2020) 39–47.

15. **Wang Y.-S., Huang G.-Y., Dross D.,** On the mechanical modeling of functionally graded interfacial zone with Griffith crack: antiplane deformation, J. Appl. Mech. 70 (5) (2003) 676–680.

16. **Guo L.-C., Noda N.,** Modeling method for a crack problem of functionally graded materials with arbitrary properties – piecewise-exponential model, Int. J. Solids Struct. 44 (15) (2007) 6768–6790.

17. **Tikhomirov V. V.,** A semi-infinite crack of mode III in the bimaterial wedge, St. Petersburg State Polytechnical University Journal. Physics and Mathematics. (2(242)) (2016) 126–135.

18. **Noble B.**, Method based on the Wiener – Hopf technique for solution of partial differential equations, Pergamon Press, New York, London, 1958.

СПИСОК ЛИТЕРАТУРЫ

1. **Jin Z.-H., Batra R.C.** Some basic fracture mechanics concepts in functionally graded materials // Journal of Mechanics and Physics of Solids. 1996. Vol. 44. No. 8. Pp. 1221–1235.

2. **Abotula A., Kidane A., Chalivendra V. B., Shukla A.** Dynamic curving cracks in functionally graded materials under thermomechanical loading // International Journal of Solids and Structures. 2012. Vol. 49. No. 4. Pp. 583–593.

3. **Mostefa A. H., Merdai S., Mahmoudi N.** An overview of functionally graded materials 'FGM' // Proceedings of the Third International Symposium on Materials and Sustainable Development. Edited by Abdelbaki B., Safi B., Saidi M. Springer Cham, 2018. Pp. 267–278.

4. **Carpinteri A., Paggi M.** Asymptotic analysis in linear elasticity: from the pioneering studies by Westerhardt and Irwin until today // Engineering Fracture Mechanics. 2009. Vol. 76. No. 12. Pp. 1771–1784.

5. **Carpinteri A., Paggi M.** On the asymptotic stress field in angularly nonhomogeneous materials. // International Journal of Fracture. 2005. Vol. 135. No. 1–4. Pp. 267–283.

6. **Cheng C. Z., Ge S. Y., Yao S. I., Niu Z. R., Recho N.** Singularity analysis for a V-notch with angularly inhomogeneous elastic properties // International Journal of Solids and Structures. 2016. Vol. 78–79. No. 1. Pp. 138–148.

7. **Erdogan F.** Crack problems for bonded nonhomogeneous materials under antiplane shear loading // Journal of Applied Mechanics. 1985. Vol. 52. No. 4. Pp. 823–828.

8. **Erdogan F., Ozturk M.** Periodic cracking of functionally graded coatings // International Journal of Engineering Science. 1995. Vol. 33. No. 15. Pp. 2179–2195.

9. **Jin Z.-H., Batra R. C.** Interface cracking between functionally graded coatings and a substrate under antiplane shear // International Journal of Engineering Science. 1996. Vol. 34. No. 15. Pp. 1705–1716.

10. **Li Y.-D., Lee K. Y.** An antiplane crack perpendicular to the weak/microdiscontinuos interface in a bi-FGM structure with exponential and linear nonhomogeneities // International Journal of Fracture. 2007. Vol. 146. No. 4. Pp. 203–211.

11. **Pan H., Song T., Wang Z.** An analytical model for collinear cracks in functionally graded materials with general mechanical properties // Composite Structures. 2015. Vol. 132. No. 15. Pp. 359–371.

12. **Linkov A., Rybarska-Rusinek L.** Evaluation of stress concentration in multiwedge systems with functionally graded wedges // International Journal of Engineering Science. 2012. Vol. 61. No 1. Pp. 87–93.

13. **Тихомиров В. В.** Сингулярность напряжений в вершине композитного клина с внутренним функционально-градиентным материалом // Научно-технические ведомости СПбГПУ. Физико-математические науки. 2015. № 3 (225). С. 96–106.

14. **Makhorkin M. I., Skrypochka T. A., Torskyy A. R.** The stress singularity order in a composite wedge of functionally graded materials under antiplane deformation // Mathematical Modelling and Computing. 2020. Vol. 7. No. 1. Pp. 39–47.

15. **Wang Y.-S., Huang G.-Y., Dross D.** On the mechanical modeling of functionally graded interfacial zone with Griffith crack: antiplane deformation // Journal of Applied Mechanics. 2003. Vol. 70. No. 5. Pp. 676–680.

16. **Guo L.-C., Noda N.** Modeling method for a crack problem of functionally graded materials with arbitrary properties – piecewise-exponential model // International Journal of Solids and Structures. 2007. Vol. 44. No. 15. Pp. 6768–6790.

17. **Тихомиров В. В.** Полубесконечная трещина моды III в биматериальном клине // Научно-технические ведомости СПбГПУ. Физико-математические науки. 2016. № 2 (242). С. 126–135.

18. **Noble B.** Method based on the Wiener – Hopf technique for solution of partial differential equations. New York, London: Pergamon Press, 1958. 246 p.

THE AUTHOR

TIKHOMIROV Victor V.
Peter the Great St. Petersburg Polytechnic University
29 Politechnicheskaya St., St. Petersburg, 195251, Russia
victikh@mail.ru
ORCID: 0000-0001-9655-5817

СВЕДЕНИЯ ОБ АВТОРЕ

ТИХОМИРОВ Виктор Васильевич – *кандидат физико-математических наук, заместитель директора по образовательной деятельности Института прикладной математики и механики Санкт-Петербургского политехнического университета Петра Великого.*
195251, Россия, г. Санкт-Петербург, Политехническая ул., 29
victikh@mail.ru
ORCID: 0000-0001-9655-5817

Received 29.04.2022. Approved after reviewing 30.08.2022. Accepted 30.08.2022.
Статья поступила в редакцию 29.04.2022. Одобрена после рецензирования 30.08.2022. Принята 30.08.2022.

Journal

**ST. PETERSBURG STATE POLYTECHNICAL UNIVERSITY JOURNAL:
PHYSICS AND MATHEMATICS**

Vol. 16, No. 1.2, 2023

Founder and publisher: Peter the Great St. Petersburg Polytechnic University

The journal is registered with the Federal Service for Supervision of Communications,
Information Technology and Mass Media (Roskomnadzor).
Certificate ПИ ФС77-51457 issued 19.10.2012.

All papers presented are final author versions
Peer review is under responsibility of the Organizing Committee

Phone 8 (812) 294-22-85

Website https://physmath.spbstu.ru/

E-mail: physics@spbstu.ru

Typesetting by A.S. Kolgatina

Published 15.05.2023. Format 60x84/8. Digital print.
Printer's sheets Print circulation 1000. Order ID